UNIVERSITAT DE BARCELONA

Dynamic behaviour of salt rocks: exploring the interplay between deformation and recrystallization with full-field numerical simulations

Baoqin Hao

Departament de Mineralogia, Petrologia i Geologia Aplicada
Facultat de Ciències de la Terra
Universitat de Barcelona

Dynamic behaviour of salt rocks: exploring the interplay between deformation and recrystallization with full-field numerical simulations

PhD Thesis

Baoqin Hao

To obtain the degree of doctor from the University of Barcelona
Thesis conducted within the framework of the Doctoral Program in Earth Sciences

Supervisors:
Dr. Enrique Gómez Rivas (Universitat de Barcelona)
Dr. Albert Griera Artigas (Universitat Autònoma de Barcelona)
Dr. María Gema Llorens Verde (Geo3BCN-CSIC)

Tutor:
Dr. Juan Diego Martín Martín (Universitat de Barcelona)

Barcelona, September 2024

This thesis has been carried out at the Department of Mineralogy, Petrology and Applied Geology of the Faculty of Earth Sciences, University of Barcelona. This thesis was funded by the Ph.D. scholarship (CSC-202006930010) from the China Scholarship Council. This PhD project was also funded by DGICYT Spanish Projects PID-2020-118999GB-I00 (Ministerio de Ciencia e Innovación/Agencia Estatal de Investigación/10.13039/501100011033), PID2021-122467NB-C21 (Ministerio de Ciencia e Innovación/Agencia Estatal de Investigación/10.13039/501100011033/FEDER), and the 2021 SGR 00349 “Geologia Sedimentària” and 2021 SGR 00410 “Modelització Geodinàmica de la Litosfera” consolidated research groups (Agència de Gestió d’Ajuts Universitaris i de Recerca).

Acknowledgements

Throughout this intense and enriching PhD journey, I have been fortunate to receive invaluable support from many people, to whom I would like to express my sincerest gratitude. This work would not have been possible without the help, both direct and indirect, of those who contributed to the development of this thesis.

First and foremost, I would like to extend my heartfelt thanks to my supervisors, Enrique Gómez-Rivas, Albert Griera Artigas, and María-Gema Llorens Verde. They have been guiding lights, helping me navigate the complex wilderness of science. Their insightful advice, vast knowledge, and patient guidance were essential in shaping this work. I am also especially grateful to Paul Bons, whose practical advice and problem-solving skills made many difficult tasks seem much easier. Their dedication and attention to detail greatly improved the quality of this research.

I would also like to thank Yuanchao for his active for his active contributions to the peer-reviewed papers and code discussions, which advanced my PhD project. My thanks also go to Ricardo Lebensohn for his valuable code and his interest in my work, even though we never had the chance to meet.

I am grateful to Juan Diego Martín-Martín, who made my time at the University of Barcelona much smoother by providing everything I needed to settle in quickly. Thanks as well to the professors, postdocs, and staff throughout the Department of Mineralogy, Petrology, and Applied Geology for their support and guidance. Special thanks to Anna, Irene, Telm, Meri, Elisabet and Gisbert who shared many lunches, coffee breaks, and desserts with me, and helped me explore and enjoy life in Spain.

A special thank you to Cristina and Ari for assisting me in testing rock sample properties, even though this part of the work was ultimately not included in my PhD thesis. Your help was greatly appreciated.

To my friend and colleague, Victoriano Pineda González, who sadly passed away in a mining accident towards the end of his PhD, I offer my deepest respect. He was a man of great integrity and joy. I hope our work on the deformation of salt rocks can help prevent such tragedies in the future.

My sincere thanks also go to my friends and colleagues: Dani, Xiaolong, Gabriel, Oriol, Eloi, Claudia, Pedro, Joaquin, Saipeng, Haofu, Jingjing, Gustavo, Nuria, Xuan, Congcong, Jun, Yin, Yetong, Wentao, Ming, Yue, Xuefeng, Julia, Llanos and John, and many others. I am truly grateful to them for the fun plans, the beers, the jokes, and the encouragement. Without them, my time in Barcelona would not have been nearly as enjoyable and memorable. A special thanks to Ying for the wonderful moments we shared in this city. They have all deepened my understanding of friendship, love, and happiness.

Last but not least, I would like to thank my family, including my parents, Mr. Hao and Mrs. Zhang, and my sister Ruohan, for their unwavering support and encouragement. Despite the distance, their love has been a constant source of strength throughout this journey.

Table of contents

Abstract

Rock salt, primarily composed of halite, flows in a viscous manner in the solid state under a wide range of geological conditions, strongly affecting the dynamic evolution of sedimentary basins and orogens. The macroscopic physical properties of rock salt are governed by the deformation mechanisms that operate at the microscale and the resulting anisotropy, as rock salt is fundamentally a polycrystalline aggregate. Understanding how microscale deformation mechanisms, like dislocation glide and recrystallization processes (including intracrystalline recovery, subgrain rotation, and grain boundary migration), control the microstructural evolution of polycrystalline aggregates under different temperatures and deformation conditions is crucial for grasping the mechanical behavior of rock salt. Moreover, the interaction between different mineral phases significantly influences grain boundary kinetics, adding complexity to the rock's microstructural evolution. The overarching aim of this PhD thesis is to systematically analyze and quantify the development of microstructures in rock salt (halite) under different deformation conditions through full-field numerical simulations. The specific objectives are to (i) understand the impact of dynamic recrystallization on pure rock salt, (ii) examine the influence of deformation kinematics on pure rock salt microstructural evolution, and (iii) quantify the effect of a second hard phase on the dynamic recrystallization of polymineralic rock salt. Additionally, the thesis presents the calibration and validation of a state-of-the-art numerical method to simulate rock salt dynamic recrystallization. These objectives are addressed using full-field numerical simulations of halite based on the ELLE-VPFFT approach. The thesis is structured into three main studies. The first one couples dislocation glide and dynamic recrystallization (DRX) processes to simulate the evolution of pure halite polycrystalline aggregates under simple shear deformation, successfully replicating the microstructural evolution observed in laboratory torsion experiments at temperatures

ranging from 100 to 300°C. The second study explores simulations across different temperatures and deformation kinematics, in both pure and simple shear boundary conditions. The third study presents simulations incorporating a second hard phase in the halite polycrystalline aggregate, which affects the deformation and recrystallization of halite. The results of the three studies are discussed in an integrated manner. The pure halite deformation models show that temperature governs the competition between grain size reduction driven by dislocation glide and subgrain rotation recrystallization (SGR) at low temperatures, while grain growth produced by grain boundary migration (GBM) dominates at higher temperatures. This leads to either a grain size reduction or increase. When GBM dominates, larger and more equidimensional grains are observed, complicating strain localization assessment from grain morphology, compared to models deformed at lower temperatures. Despite these differences, the crystallographic preferred orientation (CPO) remains consistent across all the modelled temperatures in simple shear. Additionally, the relationship between subgrain misorientation and finite strain follows a power law with a universal exponent of 2/3 at low strain. However, dynamic recrystallization processes produce a progressive deviation from this relationship at high strain. This deviation can be quantified by the average and skewness of the subgrain misorientation distribution, highlighting the need for precise calibration when inferring finite strain or temperature from microstructures. The results also illustrate how the kinematics of deformation control the development of micro-shear bands and the spread direction of crystallographic preferred orientation. Simple shear deformation features a discontinuous evolution of high strain-rate bands, which activate and deactivate periodically, thus causing variation of strain localization and the formation of asymmetric subgrain boundary orientations relative to the grain shape preferred orientation. In contrast, pure shear deformation results in steady high strain-rate bands and more distributed deformation, producing symmetric conjugate subgrain boundaries, small grain bands, and higher grain aspect ratios compared to

simple shear scenarios. At high strain, the CPO allows distinguishing between coaxial and non-coaxial deformation and determining the sense of shear. Finally, the presence of a second hard phase under dynamic recrystallization significantly influences halite microstructures, amplifying strain localization. When there is a second hard phase, the steady grain size of the halite matrix is significantly smaller than in single-phase systems, and the CPO intensity of halite is weaker compared to that of pure halite aggregates. The pinning effect of second phases restricts GBM, limiting grain growth, while promoting SGR and strain localization, resulting in further grain size reduction. The load transfer and strain partitioning within polymineralic aggregates are also affected by the second phase content, altering the intensity of the matrix CPO. Therefore, caution is advised when using steady-state recrystallized grain size to predict differential stresses in polymineralic rocks, as smaller grain sizes may lead to overestimated stresses. Finally, the methods and results presented in this PhD thesis are not restricted to rock salt polymineralic aggregates but are applicable to other rocks deformed predominantly by crystal-plastic processes in the Earth's crust or mantle.

Resum

Les roques salines (o sals), compostes principalment d'halita, es comporten com un fluid viscós en estat sòlid en diversos contextos i condicions geològiques, jugant un paper fonamental a l'evolució dinàmica de moltes conques sedimentàries i orògens. A nivell macroscòpic, les propietats físiques de les roques salines depenen dels mecanismes de deformació que actuen a microescala, ja que aquestes roques es comporten essencialment com agregats policristal·lins, resultant en el desenvolupament d'anisotropia. Per comprendre el comportament mecànic de les sals, és crucial entendre com els mecanismes de deformació a la microescala, com el lliscament de dislocacions i els processos de recristal·lització (incloent-hi la recuperació intracristal·lina, la rotació de subgrans i la migració de vores de gra) controlen l'evolució microestructural dels agregats policristal·lins sota diferents condicions de temperatures i deformació. A més, la interacció entre diferents fases minerals influeix significativament a la cinètica de les vores de gra, afegint-hi complexitat a l'evolució microestructural de la roca. L'objectiu principal d'aquesta tesi doctoral consisteix en analitzar i quantificar sistemàticament el desenvolupament de microestructures en roques salines (halita) sota diferents condicions de deformació a partir de simulacions numèriques de tipus "full-field". Els objectius específics són: (i) analitzar la influència de la recristal·lització dinàmica en el desenvolupament de microestructures en roques compostes per halita pura, (ii) examinar l'impacte de la cinemàtica de deformació a l'evolució microestructural de roques compostes per halita pura, i (iii) quantificar l'efecte de la presència d'una segona fase competent en la recristal·lització dinàmica de roques salines polimineràliques. Així mateix, a la tesi presenta el calibratge i la validació del mètode numèric "full-field" basat en la plataforma ELLE-VPFFT per simular la recristal·lització dinàmica de roques. La tesi s'estructura en tres estudis principals. El primer acobla la simulació del lliscament de dislocacions i dels processos de recristal·lització dinàmica per estudiar l'evolució d'agregats policristal·lins d'halita pura deformats en cisalla simple. Les

simulacions reprodueixen amb èxit l'evolució microestructural observada en experiments de torsió a temperatures que varien entre 100ºC i 300°C. El segon estudi explora simulacions d'halita a diferents temperatures i condicions cinemàtiques de deformació, en particular per a casos de cisalla pura i cisalla simple. El tercer estudi presenta simulacions d'agregats policristal·lins d'halita que incorporen una segona fase competent, la qual cosa afecta la deformació i la recristal·lització principal de l'agregat. Els resultats dels tres estudis es discuteixen de manera integradora. Els models de deformació d'halita pura mostren que per temperatures baixes la reducció de la mida de gra es afavorida com conseqüència del lliscament de dislocacions i la recristal·lització per rotació de subgrans (SGR). En canvi, a temperatures més elevades la recristal·lització per migració de vores de gra (GBM) és dominant i produeix un augment de la mida de gra. En situacions on domina la recristal·lització per migració de vores de gra, s'observen grans de mides majors i més equidimensionals, cosa que complica l'avaluació de la localització de la deformació a partir de la morfologia dels grans, en comparació amb els models deformats a temperatures més baixes. Tot i aquestes diferències, l'orientació preferent cristal·logràfica (CPO) que es forma en condicions de cisalla simple és independentment de la temperatura. A més, la relació entre la misorientació intracristal·lina i la deformació finita segueix una llei potencial amb un exponent universal de 2/3, per a condicions de baixa deformació finita. Malgrat això, els processos de recristal·lització dinàmica produeixen una desviació progressiva d'aquesta relació per a deformacions finites més elevades. Es pot quantificar aquesta desviació utilitzant la mitjana i l'asimetria de la distribució de la misorientació intracristal·lina. Aquests resultats demostren que és necessari realitzar un calibratge precís del sistema abans de poder quantificar la deformació finita o la temperatura de deformació a partir de l'anàlisi de les microestructures resultants. Els resultats també demostren com la cinemàtica de la deformació controla el desenvolupament de microbandes de cisalla i l'orientació preferent cristal·logràfica. Per a condicions de cisalla

simple, es produeixen bandes amb una elevava taxa de deformació interna (*i.e.*, "strain-rate"). Aquestes bandes s'activen i desactiven periòdicament, mostrant una evolució discontínua i causant variacions tant en la localització de la deformació com a la formació d'orientacions de les vores dels subgrans asimètriques respecte l'orientació preferent de la forma dels grans (SPO). En contrast, la deformació per cisalla pura dona lloc a la creació de bandes d'alta taxa de deformació interna amb orientacions constants i a una deformació més distribuïda. Aquest procés resulta en la formació de vores de subgrans conjugats simètrics, bandes de grans de mida petita i grans amb una elongació major que en els casos de cisalla simple. Aquestes observacions aporten criteris per poder diferenciar entre condicions de deformació coaxial/no-coaxial i el sentit de cisalla analitzant la microestructura i la CPO. Finalment, la presència d'una segona fase competent controla de manera significativa les microestructures d'halita que es formen, amplificant la localització de la deformació, així com la recristal·lització dinàmica del material. Quan hi ha una segona fase competent en el sistema, la mida de gra de la matriu quan arriba a l'estat estacionari és significativament menor i la intensitat de la CPO de la matriu és més feble amb comparació de sistemes monofàsics. Els grans de la segona fase també restringeixen el creixement dels grans d'halita per GBM, mentre que es promou la rotació rígida dels grans i un increment de la heterogeneïtat de la deformació. Per tant, es recomana precaució alhora d'utilitzar la mida de gra recristal·litzat per predir la magnitud de l'esforç diferencial en roques polimineràliques, ja que les mides de gra més petites poden resultar en una sobreestimació dels esforços. Finalment, els mètodes i resultats presentats en aquesta tesi doctoral no són restringits a l'estudi d'agregats polimineràlics de roca salines, sinó que també es poden aplicar a altres roques deformades per processos de plasticitat cristal·lina a l'escorça o al mantell terrestre.

Resumen

Las rocas salinas (o sales), compuestas principalmente por halita, se comportan como un fluido viscoso en estado sólido en diversos contextos y condiciones geológicas, y juegan un papel fundamental en la evolución dinámica de muchas cuencas sedimentarias y orógenos. A nivel macroscópico, las propiedades físicas macroscópicas de las rocas salinas dependen de los mecanismos de deformación que actúan a microescala, ya que estas rocas se comportan esencialmente como agregados policristalinos, resultando en el desarrollo de anisotropía. Para comprender el comportamiento mecánico de las sales, es crucial entender cómo los mecanismos de deformación a la microescala, como el deslizamiento de dislocaciones y los procesos de recristalización (incluyendo la recuperación intracristalina, la rotación de subgranos y la migración de bordes de grano), controlan la evolución microestructural de los agregados policristalinos bajo diferentes condiciones de temperatura y deformación. Además, la interacción entre diferentes fases minerales influye significativamente en la cinética de los límites de grano, añadiendo complejidad a la evolución microestructural de la roca. El objetivo principal de esta tesis doctoral radica en analizar y cuantificar sistemáticamente el desarrollo de microestructuras en rocas salinas (halita) bajo diferentes condiciones de deformación mediante simulaciones numéricas de tipo "full-field". Los objetivos específicos son: (i) analizar la influencia de la recristalización dinámica en el desarrollo de microestructuras en rocas compuestas por halita pura, (ii) examinar el impacto de la cinemática de deformación en la evolución microestructural de rocas compuestas por halita pura, y (iii) cuantificar el efecto de la presencia de una segunda fase competente en la recristalización dinámica de rocas salinas poliminerálicas. Asimismo, en esta tesis doctoral se presenta la calibración y validación del método numérico "full-field" basado en la plataforma ELLE-VPFFT para simular la recristalización dinámica de rocas. La tesis se estructura en tres estudios principales. El

primero acopla la simulación del deslizamiento de dislocaciones y de los procesos de recristalización dinámica para estudiar la evolución de agregados policristalinos de halita pura deformados en cizalla simple. Las simulaciones reproducen con éxito la evolución microestructural observada en experimentos de torsión de laboratorio a temperaturas que varían entre 100°C y 300°C. El segundo estudio explora simulaciones de halita a diferentes temperaturas y condiciones cinemáticas de deformación, en particular en casos de cizalla pura y cizalla simple. El tercer estudio presenta simulaciones de agregados policristalinos de halita que incorporan una segunda fase competente, lo que afecta a la deformación y recristalización del principal del agregado. Los resultados de los tres estudios se discuten de manera integrada. Los modelos de deformación de halita pura muestran que a temperaturas bajas se produce una reducción del tamaño de grano como consecuencia del deslizamiento de dislocaciones y de la recristalización por rotación de subgranos (SGR). En cambio, a temperaturas más elevadas domina la recristalización por migración de bordes de grano (GBM) y se produce un aumento del tamaño de grano. En situaciones en las que domina la recristalización por migración de bordes de grano, se observan granos más grandes y más equidimensionales, lo que complica la evaluación de la localización de la deformación a partir de la morfología de los granos, en comparación con los modelos deformados a temperaturas más bajas. A pesar de estas diferencias, la orientación preferente cristalográfica (CPO) que se forma en condiciones de cizalla simple es independiente de la temperatura. Además, la relación entre la misorientación intracristalina y la deformación finita sigue una ley potencial con un exponente universal de 2/3, para condiciones de baja deformación finita. Sin embargo, los procesos de recristalización dinámica producen una desviación progresiva de esta relación a deformaciones finitas más elevadas. Se puede cuantificar esta desviación utilizando el promedio y la asimetría de la distribución de la misorientación intracristalina. Estos resultados demuestran que es necesario realizar una calibración precisa del sistema para poder inferir la deformación finita o la

temperatura de deformación a partir del análisis de las microestructuras resultantes. Los resultados también demuestran cómo la cinemática de la deformación controla el desarrollo de microbandas de cizalla y la dirección de propagación de la orientación preferente cristalográfica. Para condiciones de cizalla simple, se producen bandas con alta tasa de deformación interna (*i.e.*, "strain-rate"). Estas bandas se activan y desactivan periódicamente, mostrando una evolución discontinua y causando variaciones tanto en la localización de la deformación como en la formación de orientaciones de los límites de grano asimétricos respecto a la orientación preferente de la forma de los granos (SPO). En contraste, la deformación por cizalla pura da lugar a la creación de bandas de alta tasa de deformación interna con orientaciones constantes y una deformación más distribuida. Este proceso resulta en la formación de límites de subgranos conjugados simétricos, bandas de granos de pequeño tamaño y granos con una elongación mayor que en los casos de cizalla simple. Estas observaciones aportan criterios para poder distinguir entre condiciones de deformación coaxial y no coaxial y determinar el sentido de la cizalla analizando la microestructura y la CPO. Finalmente, la presencia de una segunda fase competente controla de manera significativa las microestructuras de halita que se forman, amplificando la localización de la deformación, así como la recristalización dinámica del material. Cuando hay una segunda fase dura en el sistema, el tamaño de grano constante de la matriz de halita es significativamente más pequeño que en los sistemas monofásicos, y la intensidad de la CPO de la halita es más débil en comparación con la que se forma en agregados de halita pura. Los granos de la fase dura producen un efecto de anclaje o bloqueo, restringiendo el crecimiento de los granos de halita por GBM, mientras que se promueve la rotación de subgranos y la localización de la deformación. Así, se produce una mayor reducción del tamaño de grano. Los resultados muestran que la presencia de una segunda fase mineral más dura altera la intensidad de la CPO de la matriz de halita. Por lo tanto, se recomienda precaución al utilizar el tamaño de grano recristalizado en condiciones

estacionarias para predecir la magnitud del esfuerzo diferencial en rocas poliminerálicas, ya que los tamaños de grano más pequeños pueden llevar a una sobreestimación del esfuerzo. Finalmente, los métodos y resultados presentados en esta tesis doctoral no están restringidos al estudio de agregados poliminerálicos de roca de sal, sino que también se pueden aplicar a otras rocas deformadas por procesos cristal-plásticos en la corteza o el manto terrestres.

1 Introduction

1.1 Flow of rock salt

Evaporites, including rock salt, are commonly found in sedimentary sequences, and exhibit unique physical properties compared to other rock types, such as low density, low permeability, low strength, and high ductility. Due to these properties, rock salt flows in a viscous manner in the solid state under low stress, undergoing ductile deformation near or at the Earth's surface (Carter et al., 1993; Weijermars et al., 1993). Consequently, the deformation behaviour of rock salt relative to its surrounding rocks leads to complex tectonic structures, such as salt diapirs, salt walls and salt welds, and induces the folding and faulting of encasing rocks (e.g., Canérot et al., 2005; Jackson & Talbot, 1986). Rock salt, primarily composed of halite (NaCl), typically acts as a detachment level in thrust systems, accommodating significant horizontal shortening in orogenic belts and significantly affects the overall deformation style and dynamic evolution of orogens (Jackson & Hudec, 2017). Additionally, salt deposits control the deposition and distribution of other sedimentary rocks within sedimentary basins, producing halokinetic structures (e.g., Canérot et al., 2005; Mohr et al., 2005; Rowan et al., 2019). Furthermore, the mineral halite has been extensively used as an analogue of silicate rocks and metals in deformation experiments. This use stems from the particular mechanical properties of halite, which facilitate the study of deformation mechanisms at laboratory spatial and temporal scales. Specifically, halite exhibits deformation behaviour that is akin to that of crustal rocks, but at substantially lower confining pressures and temperatures (e.g., Drury & Urai, 1990). Halite also plays a crucial role in terms of subsurface energy, as subsurface salt bodies often serve as seals for fluid migration and create structural traps in oil and gas reservoirs (Hudec & Jackson,

2007). Besides, salt rock, as well as other evaporites, is key for the energy transition, since artificial caverns in salt are used for the storing Geo-energy products like hydrogen or compressed air (Duffy et al., 2018). These storage sites experience loading and unloading cycles, which also impact the properties of the host rock. Therefore, enhancing our understanding of the deformation and rheology of rock salt under various conditions is crucial both for fundamental science and also for addressing key societal challenges such as achieving a decarbonized economy.

The viscous flow of rock salt in collisional settings and its interaction with deformation zones can lead to a variety of salt structures. The simplest scenario, based on the channel flow model, assumes a blend of Couette (laminar-type) and Poiseuille (pipe-type) flows (Godin et al., 2006; Sarkarinejad et al., 2018). As shown in Fig. 1.1a, Couette flow between moving rigid plates induces uniform simple shear in the channel (Godin et al., 2006; Grujic, 2006). This flow type typically occurs in salt layers that act as detachments for thrusts (Fig. 1.1b) (e.g., McClay et al., 2004). In Poiseuille flow, the highest velocity is reached at the channel centre, resulting in opposing senses of shear at the top and bottom (Fig. 1.1a) (Godin et al., 2006; Sarkarinejad et al., 2018). Poiseuille flow is expected to occur during salt flow into growing salt diapirs or anticlines (Fig. 1.1c) (Fossen, 2010). In the Poiseuille flow channel, the central part typically undergoes pure shear deformation (e.g., central diapir stem) (Hudec & Jackson, 2007), while the peripheral regions predominantly experience simple shear (e.g., edge of the salt body) (Fossen, 2010). Generally, deformation of salt bodies features both rotation and flattening components, quantified by the kinematic vorticity number, which normalizes the curl of flow velocity relative to stretching (Means et al., 1980; Truesdell, 1953). Recent studies based on natural rock samples (Langille et al., 2010; Michels et al., 2015; P. Skemer et al., 2010), experiments (Boneh & Skemer, 2014a), and numerical models (Llorens et al., 2017, 2022) reveal that the spatial and temporal evolution of kinematic conditions governs the deformation

of polycrystalline aggregates and their resulting structures and textures. However, accurately quantifying kinematic vorticity and finite strain from the rock microstructures is challenging due to the complex natural deformation processes that affect the rock. Analytical methods rely on homogeneous steady-state flow models, subject to necessary assumptions whose practical application is not always straightforward (Xypolias, 2010). Moreover, dynamic recrystallization in viscoplastic deformation significantly affects the use of paleopiezometers in polycrystalline aggregates (Stipp et al., 2010).

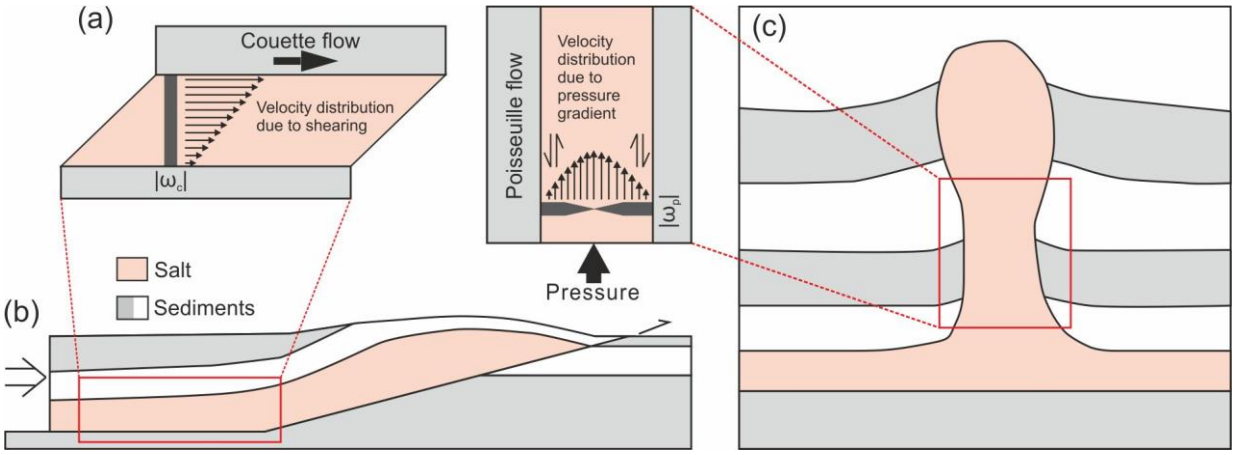

Figure. 1.1. Sketch of the flow pattern in a salt channel flow. (a) Couette flow (left) with velocity profile (arrows) and kinematic vorticity (dark bar, ω_c) caused by shearing; Poiseuille flow (right) with velocity profile (arrows) and kinematic vorticity (dark bar, ω_p) caused by pressure gradient within the channel, after Godin et al. (2006) and Sarkarinejad et al. (2018). The kinematic vorticity numbers are visually indicated by the width of a black bar. A wider segment of the bar indicates a higher component of simple shear, whereas a narrower segment indicates a greater component of pure shear. The diagrams display only the absolute magnitude of the kinematic vorticity, without distinguishing between positive (sinistral simple shear) and negative (dextral simple shear) directions. (b) Couette flow can occur in a salt layer beneath the sliding overburden, after Hudec and Jackson (2007). (c) In stem of salt diapir, a Poiseuille flow can occur as salt moves into a salt structure. The central salt within the diapir stem flows faster than the salt along the boundary due to boundary drag restrictions. Poiseuille flow results in a predominant pure shear component at the centre of the channel and a significant simple shear component at its margins (Sarkarinejad et al., 2018).

Rock deformation microstructures provide insights into the geological evolution of a rock, providing reliable information about its rheology and deformation mechanisms that operate.

Grain size and morphology, alongside the pattern and intensity of crystallographic preferred orientation (CPO, also called texture), are frequently utilized to determine rock deformation mechanisms (e.g., Barabasch et al., 2023; Desbois et al., 2010), deformation kinematics (e.g., Boneh & Skemer, 2014; Michels et al., 2015; Sarkarinejad et al., 2018) and physical conditions under which rocks deform (e.g., Stipp et al., 2010; Sundberg & Cooper, 2008). This highlights the value of detailed microstructural and textural analysis, encompassing evaluations of grain size, shape, distribution, and CPO intensity.

1.2 Microdynamic processes of rock salt

1.2.1 Deformation mechanisms of halite

The microdynamic evolution of rock salt is governed by various deformation mechanisms primarily controlled by temperature, stress/strain rate, confining pressure and water content, among others (e.g., Bourcier et al., 2013; Carter & Heard, 1970; Franssen, 1994; Franssen & Spiers, 1990; ter Heege et al., 2005a, 2005b; Hunsche & Hampel, 1999; Linckens et al., 2016; Wenk et al., 2009). At low temperature and high deviatoric stress, rock salt undergoes (semi-) brittle failure, characterized by microcrack formation and propagation, and intergranular sliding (Peach et al., 2001; Peach & Spiers, 1996). As confining pressure and temperature increase, cracking is suppressed, and halite deformation becomes dominated by dislocation creep (e.g., Urai et al., 2008). When brine is present, dislocation creep can be accompanied by dissolution-precipitation creep (Spiers et al., 1988, 1990), which involves mass transfer around grain boundaries. The focus of the current study is on dislocation creep and the effects of dynamic recrystallization and dissolution-precipitation creep has not been included.

Crystals undergo internal deformation when crystallographic defects, such as vacancies and dislocations, migrate and interact within the crystal lattice. This leads to permanent strain

known as crystal plasticity, typically without causing brittle failure (Poirier, 1985). The primary deformation mechanism is the glide of dislocations along specific directions on specific crystallographic planes, known as slip systems. The activation of these systems for dislocation glide depends on reaching the critical resolved shear stress (CRSS), which is influenced by the local orientation and magnitude of the stress field. As shown in Fig. 1.2, deformation experiments on halite single crystals have identified three active slip systems: $\{110\} < \bar{1}10 >$, {100} <011>, and $\{111\} < \bar{1}10 >$ (Carter & Heard, 1970; Guillope & Poirier, 1979). Halite crystals exhibit mechanical anisotropy, with the CRSS for harder slip systems being 1 to 5 times greater than that for the most readily activated, the $\{110\} < \bar{1}10 >$ slip system (Carter & Heard, 1970). The macroscopic properties of halite polycrystalline aggregates are influenced by the mechanical anisotropy of individual halite crystals within the aggregate. According to the von Mises criterion, deformation in polycrystals requires five independent slip systems to compensate for strain incompatibilities (Mises, 1928). Only two of the six $\{110\} < \bar{1}10 >$, three of the six {100} <011>, and five of the twelve $\{111\} < \bar{1}10 >$ slip systems are independent. Therefore, during deformation, besides the $\{110\} < \bar{1}10 >$ slip system, activating additional slip systems is theoretically necessary for dislocation glide.

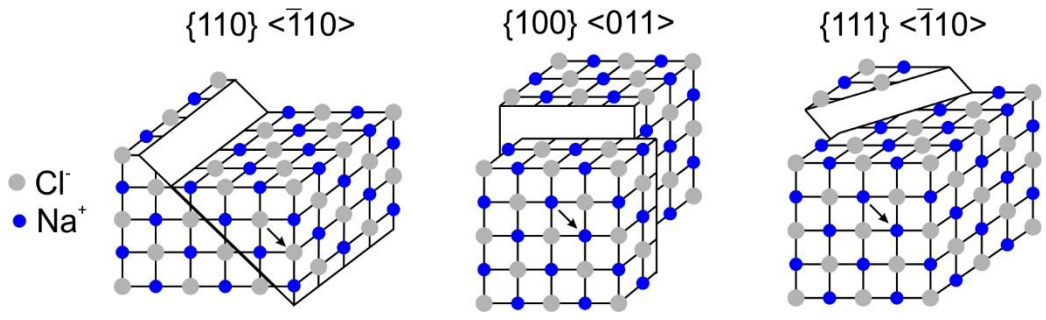

Figure. 1.2. Crystal structure of halite and its slip systems.

Intracrystalline recovery counteracts dislocation glide and reorganizes the subgrain boundary (low-angle grain boundaries, LAGBs) of rocks (Urai, Means, et al., 1986), reducing internal strain energy by decreasing dislocation density and tangles through several processes: (i)

annihilation of dislocations with opposite signs when they meet each other, (ii) climb of edge dislocations through vacancy diffusion, (iii) polygonization forming lower energy configurations such as regular arrays or LAGBs, and (iv) cross-slip, where screw dislocations glide onto a new plane oblique to their original path (Poirier, 1976).

1.2.2 Dynamic recrystallization of halite

Dynamic recrystallization (DRX) processes accompany dislocation creep, altering rock salt microstructure through changes in grain size, grain boundary network, and shape preferred orientation (SPO) (e.g., Desbois et al., 2010; Franssen, 1994; Guillope & Poirier, 1979; ter Heege et al., 2004; Mansouri et al., 2019; Schléder & Urai, 2007). Depending on the balance of driving forces involved, DRX can lead to either grain size reduction or grain growth. Grain size reduction occurs through subgrain rotation recrystallization (SGR), where dislocation generation, migration and reorganization increase local misorientation within the crystal lattice forming subgrain boundaries, which may finally evolve to form high-angle grain boundaries (HAGBs) and the formation of new and smaller grains (Gomez-Rivas et al., 2020; Urai et al., 1986). Grain size increases through grain boundary migration (GBM), a recrystallization process by which grain boundaries move via atom diffusion across the boundary between grains. There are several driving forces for GBM in rocks (e.g., Bons et al., 2008). GBM driven by the reducing the difference in stored strain energy (*i.e.*, associated with dislocation densities) across the boundaries is known as strain-induced GBM. In strain-induced GBM, grain boundaries migrate from grains with low dislocation density to neighbouring grains with high dislocation density due to the strain energy differences. GBM driven by the reduction of the grain-boundary surface energy is called boundary energy-induced GBM (Karato, 2008; Weaire & Rivier, 1984). In boundary energy-induced GBM, grain boundaries of large grains overgrow smaller ones, driven by the reduced grain curvature, resulting in grain growth (Karato, 2008).

The final microstructure and grain size depend on the competition of the interacting processes between grain size growth and reduction (Franssen, 1994; Leitner et al., 2011; Gomez-Rivas et al., 2020 and references therein).

1.2.3 Subgrain misorientation

Plastic strain correlates with the probability density of subgrain misorientation angles in polycrystalline aggregates dominated by dislocation creep (Hughes et al., 1997, 1998, 2003; Hughes & Hansen, 2018; Pennock et al., 2002; Pennock & Drury, 2005). A scaling behaviour linking mean subgrain misorientation to finite strain was proposed based on metal deformation experiments (Hughes et al., 1997), and its physical basis was confirmed by Pantleon (1997, 1998, 2001). Pennock et al. (2002, 2005) confirmed that this scaling behaviour extends to halite, identifying a power-law relationship between the mean subgrain misorientation and natural strain for low finite strain (up $\varepsilon = 0.54$). Their findings align with numerical simulations results by Mika & Dawson (1999) and Gomez-Rivas et al. (2017). This strain gauge could be valuable for structural analysis if it is further tested and generalized across materials subjected to various dynamic recrystallization processes at different temperatures. However, the impact of grain boundary migration on the probability density of subgrain misorientation angles remains unassessed, despite its significant role in the mechanical behaviour of wet rock salt in a wide range of conditions, and also of dry rock salt at relatively high temperatures (Leitner et al., 2011; Trimby et al., 2000). GBM reduces intragranular heterogeneities and significantly alters the microstructure of polycrystalline aggregates (Urai, Means, et al., 1986), in a way that subgrain misorientation and the grain boundary network may not clearly reflect the strain a volume of rock has experienced (Llorens et al., 2016a).

1.3 Deformation and recrystallization of polymineralic salt rock

Monomineralic aggregates have been extensively studied to understand micro-scale deformation, by means of the study of natural rocks, as well as experimental and numerical methods (Drury & Urai, 1990; Linckens et al., 2016; Pennacchioni et al., 2010; Piazolo et al., 2019; Wenk et al., 1989). Polymineralic rocks, which comprise a significant portion of the Earth's crust, are also of keen interest due to their complex deformation and metamorphic behaviour. Ongoing research continues to explore the dynamics of microstructure evolution and CPO development in these rocks, with the interplay of different minerals adding complexity to their deformation processes (e.g., Cyprych et al., 2016; Fei et al., 2023; Herwegh et al., 2011; Herwegh & Berger, 2004; Jessell et al., 2009; Linckens et al., 2011; Marques et al., 2010, 2011a, 2011b).

The microstructural evolution of monomineralic polycrystalline aggregates is governed by DRX processes, which involves a competition between (i) grain growth that is predominantly driven by GBM and (ii) grain refinement, typically dominated by SGR. The second phase restricts grain growth of the matrix by limiting grain boundary mobility, significantly impacting the microstructure (Brodhag & Herwegh, 2010; Evans et al., 2001). The presence of a second phase act as a stabilizer by pinning grain boundaries, depending on their grain size (d_s) and volume fraction (f_s), thus influencing the matrix grain size (Herwegh & Berger, 2004). The steady-state grain size of matrix can be expressed by the Zener parameter ($Z = d_s/fs$; Herwegh et al., 2011; Smith, 1948).

Second phases in polymineralic rocks not only modulate grain size but also influence the CPO within the matrix. The CPO reflects the alignment of mineral crystals and links directly to the rock's deformation history. In polymineralic aggregates, the presence of second phases often results in a weaker CPO compared to monomineralic aggregates deformed under similar

conditions (e.g., Cyprych et al., 2016). The second phase inhibits grain growth by fixing grain boundaries. This pinning effect can shift deformation mechanisms from grain-size insensitive creep, such as dislocation creep, to grain-size sensitive (GSS) creep mechanisms like grain boundary sliding and diffusion creep (e.g., Desbois et al., 2010; Linckens et al., 2011; Miranda et al., 2016; Skemer et al., 2010; Závada et al., 2015). Increasing the contribution of GSS mechanisms decreases the CPO intensity (Bestmann & Prior, 2003; Kilian et al., 2011; Schléder & Urai, 2007). Additionally, the interaction between the second phases and the matrix affects the load transfer and strain partitioning (Handy, 1994; Takeda & Griera, 2006), altering the intensity and orientation of the CPO (e.g., Austin et al., 2014; Cyprych et al., 2016). Overall, research on the impact of second phases on the matrix CPO remains sparse.

Despite the importance of understanding the deformational behaviour of polymineralic rocks and their resulting microstructure and texture in interpreting lithospheric rheology, the dynamics of grain size evolution and CPO development are not fully understood. Advanced numerical modelling allows visualizing the evolution of the rock and quantifying deformation processes, including the influence of second phases. This could enhance our understanding of how these minerals influence microstructural formation and improve our insights into geological processes across different scales, leading to better predictions of polymineralic rock behaviour.

1.4 Numerical simulations of rock salt

Insights into halite deformation and rheology are mostly derived from laboratory experiments using natural or synthetic rock salt and from the observation of naturally deformed samples. However, these natural samples capture only a static stage of deformation and potentially reworking by posterior annealing processes, while laboratory experiments face limitations in

terms of the length and time scales that can be achieved in the lab, which result in a limited range of sample lengths and strain rates (e.g., Franssen, 1994; Heege et al., 2005b; Picard et al., 2018). Numerical simulations overcome these limitations and effectively complement natural and experimental approaches. They enable achieving significantly higher finite strains at lower strain rates in polycrystalline aggregates and allow exploring multiple scenarios of diverse deformation conditions by varying parameters like sample size, strain rate, boundary conditions and temperature, among others. Accordingly, they allow systematic investigations of the study system. Numerical simulations also are useful to study the influence of deformation mechanisms in isolation and also how they interact when they are coupled (Amelirad & Assempour, 2022; Bons et al., 2008; Eisenlohr et al., 2013; Lebensohn, 2001; Otsuka et al., 2018; Pokharel et al., 2014). Various numerical approaches can be used to simulate the dynamic recrystallization in polycrystalline materials. Notably, Signorelli & Tommasi (2015) integrated the viscoplastic self-consistent approach (VPSC, Lebensohn & Tomé, 1993; Liu et al., 2005; Wenk et al., 1991) with a subgrain formation probability model to account for subgrain rotation effects on CPO evolution. In this approach, each grain is regarded as an inhomogeneity in a viscoplastic homogeneous effective medium, and therefore it does not take into account the intragranular heterogeneities for the simulation of DRX processes. Radhakrishnan & Sarma (2008) used a combined finite element (FEM) and Monte-Carlo (MC) approach to simulate DRX and resulting CPOs in metals. However, the FEM's requirement for high-resolution meshing to analyze the heterogeneous deformation of the microstructure in detail restricts its scalability, due to the computational time constraints (e.g., Roters et al., 2010). Moreover, the MC approach produces random microstructural changes, making the final structures and textures heavily reliant on nucleation criteria and difficult to constrain length and time scales or quantitatively external variables such as temperature or strain rate. The D-Rex method (Kaminski et al., 2004; Kaminski & Ribe, 2001) uses a kinematic constraint model

to simulate DRX, introducing parameters for nucleation and grain boundary migration without accounting for inter-grain mechanical interactions. However, all these methods face challenges in accurately simulating the evolution of rock strain localization, grain boundary networks, grain sizes, or textures.

To explicitly simulate the microstructural evolution of polycrystalline aggregates during deformation, the full-field formulation was used by using Fast Fourier Transforms (FFT, Moulinec & Suquet, 1994) overcomes previous limitations. Initially designed to predict the mechanical properties of composite materials (Moulinec & Suquet, 1998), it was later adapted for polycrystalline single-phase aggregates by Lebensohn (2001) to efficiently model the spatial evolution of viscoplastic deformation. The Viscoplastic Full-Field Transform code (VPFFT, Lebensohn et al., 2003; Lebensohn & Rollett, 2020) and the numerical software platform ELLE (Bons et al., 2008) were integrated to facilitate large-strain full-field simulations of dislocation creep (Griera et al., 2011, 2013). The numerical scheme comprises a variety of dynamic recrystallization processes, including intracrystalline recovery, grain nucleation, and grain boundary migration, by mapping misorientations between local lattice orientations on a regular grid. This full-field numerical modelling approach has been widely applied to study the microdynamic evolution of polycrystals such as 1h ice and halite, as well as multiphase anisotropic rocks (e.g., Finch et al., 2022; Gomez-Rivas et al., 2017; Hao et al., 2023; Llorens et al., 2016a; 2016b; 2017, 2022; Ran et al., 2022; Steinbach et al., 2016; Yu et al., 2024).

1.5 Objectives of the PhD thesis

The previous sections underscore the need for further research into the microdynamic processes of monomineralic and polymineralic rock salt. With advancements in computing power,

numerical simulations have evolved as a crucial complement of laboratory experiments and field studies of evaporite deformation. Numerical simulations overcome the limitation of temperature, strain rate and scale inherent to laboratory experiments, and allow visualizing the progressive evolution of the microstructure and texture of digital samples deformed at various strain rates and boundary conditions. Based on a state-of-the-art numerical modelling approach, this PhD thesis sets out three main objectives:

(1) Understand the interplay between rock deformation by dislocation glide and dynamic recrystallization in pure rock salt

A large proportion of halite-dominated rocks in the Earth's subsurface undergo viscoplastic deformation in a regime controlled by dynamic recrystallization, processes that have not been fully modelled to date, and which typically result in anisotropic systems. For the first time, this study incorporates the explicit simulation of subgrain rotation and grain boundary migration into numerical models of viscoplastic deformation in polycrystalline halite. The specific aims in that sense are to (a) calibrate the numerical modelling approach by comparing the simulations with torsion experiments of synthetic pure rock salt at various temperatures, and (b) investigate how dynamic recrystallization impacts the resulting microstructures and textures of rock salt at various temperatures.

(2) Address the influence of the kinematics of deformation on rock salt dynamic recrystallization and resulting microstructures and textures

The primary goal is to quantify and evaluate the effect of the kinematics of deformation on the resulting microstructures and textures by studying two endmembers of boundary conditions: pure shear and simple shear, representing coaxial and non-coaxial deformation paths, respectively. We focus on comparing the evolution of SPOs and CPOs in both pure shear and simple shear, and the associated development of strain localization. We specifically focus on

capturing indicators for determining the deformation kinematics at the microscale from microstructures and textures.

(3) Quantify the influence of a second hard phase on the deformation and dynamic recrystallization of polymineralic salt rock

Most evaporite rocks are polymineralic and, for example, halite-dominated rocks typically contain a second hard phase (such as carbonate or clastic grains). It is therefore crucial to understand how the presence of a second hard phase impacts the deformational behaviour of rock salt and to predict the behaviour of such two-phase systems in the subsurface. We examine how a second hard phase influences rock salt matrix deformation, including dynamic recrystallization processes. Special focus is placed on how its content affects strain rate distribution/evolution and microstructural properties such as grain size, grain shape and CPO and in two-phase polycrystalline aggregates deformed at various temperatures.

Finally, the PhD thesis presents the development, calibration and validation of a full-field numerical method to simulate rock salt deformation. This is essential for conducting the scientific studies described above. Specifically, this project aims to develop a comprehensive numerical approach that explicitly simulates the microdynamic evolution of polycrystalline and multiphase materials during viscoplastic deformation by dislocation creep and dynamic recrystallization, based on the study of halite deformation.

1.6 Organization of the PhD thesis

This PhD thesis is organized in seven chapters, exploring the control of microscale deformation mechanisms, like dislocation glide and recrystallization processes (including intracrystalline recovery, subgrain rotation, and grain boundary migration), on the microstructural evolution of polycrystalline aggregates under various temperatures and deformation conditions.

Chapter 1 provides an introduction to the importance of understanding the dynamic behaviour of salt rocks controlled by various deformation mechanisms. It also introduces the main challenges in modelling the complex viscoplastic behaviour of halite polycrystalline aggregates at multiple scales and presents the motivation for using full-field numerical simulations to address these challenges.

Chapter 2 introduces the methodology used in subsequent chapters. It details the development and implementation of ELLE-VPFFT full-field numerical method on deformation and recrystallization, and explains the data structure, program flow, and computational techniques used.

Chapter 3 presents the results of full-field numerical simulations of coupled dislocation glide and dynamic recrystallization processes of pure halite polycrystalline aggregates under simple shear deformation, successfully replicating the microstructural evolution observed in laboratory torsion experiments at temperatures ranging from 100 to 300°C.

Chapter 4 explores the effects of varying temperatures and deformation kinematics on the evolution of microstructure and texture of polycrystalline halite, considering both pure and simple shear boundary conditions.

Chapter 5 investigates the impact of a second hard phase within halite polycrystalline aggregates on deformation and recrystallization, focusing on how variations in second-phase content affect the development of grain size and crystallographic preferred orientation in the halite matrix.

Chapter 6 comprehensively discusses how temperature, deformation kinematics and second-phase presence affect polycrystalline aggregate deformation, dynamic recrystallization, and resulting microstructure. It also specifically discusses the application and limitations of subgrain misorientation for strain estimation, the Zener parameter for grain size estimation,

and summarizes the main indicators from microstructure and texture to distinguish deformation kinematics.

Chapter 7 recaps the main conclusions of this work.

1.7 Publications

This PhD thesis has contributed to three scientific articles. One of them is published, another one is in review for publication, and the third one is in preparation for publication at the time of submission of this PhD thesis. These articles are included in Appendices 1 to 2. Additionally, conference publications related to this research are presented in Appendix 3.

First-author publications from this PhD project:

[1] **Hao, B.**, Llorens, M. -G., Griera, A., Bons, P. D., Lebensohn, R. A., Yu, Y., & Gomez-Rivas, E. (2023). Full-Field Numerical Simulation of Halite Dynamic Recrystallization From Subgrain Rotation to Grain Boundary Migration. *Journal of Geophysical Research: Solid Earth*, *128*(12). https://doi.org/10.1029/2023JB027590

[2] **Hao, B.**, Griera, A., Llorens, M. -G., Bons, P. D., Lebensohn, R. A., Yu, Y., & Gomez-Rivas, E. (2024). The influence of kinematics of deformation on polycrystalline halite dynamic recrystallization: full-field simulation of simple shear versus pure shear. *Journal of Structural Geology, in review.*

[3] **Hao, B.**, Griera, A., Llorens, M. -G., Bons, P. D., Lebensohn, R. A., Yu, Y., & Gomez-Rivas, E. (2024). Influence of a second phase on the shearing and recrystallization of halite polycrystalline aggregates. *In preparation for submission.*

Other co-authored publication not included in this thesis:

[4] Yu, Y., Griera, A., Gomez-Rivas, E., Bons, P. D., García-Castellanos, D., **Hao, B.**, & Llorens, M. -G. (2024). Dynamic recrystallization of olivine during simple shear: Evolution of microstructure and crystallographic preferred orientation from full-field numerical simulations. *Geochemistry, Geophysics, Geosystems, 25, e2023GC011212*. https://doi.org/10.1029/2023GC011212

Conference presentations from this PhD project:

[1] Hao, B., Llorens, M.-G., Griera, A., Bons, P.D., and Gomez-Rivas, E. Full-field numerical simulation of polycrystalline halite dynamic recrystallization under simple shear conditions. Electron Backscatter Diffraction 2022 (EBSD 2022), New York, United States, June 2022.

[2] Hao, B., Llorens, M.-G., Griera, A., Bons, P. D., and Gomez-Rivas, E.:Full-field numerical simulation of dynamic recrystallization in polycrystalline halite, 23rd International Conference on Deformation mechanisms, Rheology and Tectonics (DRT). Catania, Italy. July 2022.

[3] Hao, B., Llorens, M.-G., Griera, A., Bons, P. D., Lebensohn, R. A., Yu, Y., and Gomez-Rivas, E.: Full-Field Numerical Simulation of Halite Dynamic Recrystallization From Subgrain Rotation to Grain Boundary Migration, EGU General Assembly 2024, Vienna, Austria, 14–19 Apr 2024, EGU24-3225, https://doi.org/10.5194/egusphere-egu24-3225, 2024.

[4] Hao, B., Llorens, M.-G., Griera, A., Bons, P. D., Lebensohn, R. A., Yu, Y., and Gomez-Rivas, E.: Dynamic recrystallization during visco-plastic deformation of halite polycrystals: full-field simulation of simple shear versus pure shear, 24th International Conference on Deformation mechanisms, Rheology and Tectonics (DRT). Barcelona, Spain. July 2024.

2 Methodology

We employ the Viscoplastic Fast Fourier Transform algorithm (VPFFT; Lebensohn, 2001; Lebensohn et al., 2008; Lebensohn & Rollett, 2020) to simulate viscoplastic deformation of polycrystalline aggregates. This code is coupled with the multi-scale and multi-purpose numerical simulation platform ELLE (Bons et al., 2008; http://www.elle.ws), which allows incorporating dynamic recrystallization processes. The VPFFT-ELLE approach has been widely used to simulate a variety of microstructural processes, such as static grain growth (Jessell et al., 2003; Roessiger et al., 2011), dynamic recrystallization (Gomez-Rivas et al., 2017; Llorens et al., 2016a, 2016b, 2017; Steinbach et al., 2016, 2017), strain localization (Griera et al., 2011; de Riese et al., 2019a), rotation of rigid objects in anisotropic rocks (Griera et al., 2013; Ran et al., 2019), folding (Hu et al., 2024) and deformation of multiphase materials (Finch et al., 2020, 2022; Jessell et al., 2009; Llorens et al., 2019; Ran et al., 2018; Steinbach et al., 2017), among other studies. A comprehensive introduction to the ELLE principles and modelling approach can be found in the textbook of Bons et al. (2008), with updates on more recent developments available in the review by Piazolo et al. (2019).

2.1 Data structure and program flow

In ELLE, a 2D polycrystalline aggregate (Fig. 2.1a) is discretized in two data layers as shown in Fig. 2.1b: (i) a set of unconnected nodes (*unodes*) that constitute the periodic grid for storing physical properties within grains, and (ii) a contiguous set of polygons referred to as *flynns*, defined by boundary nodes (*bnodes*) connected by straight boundary segments. These boundary nodes can be moved to simulate GBM. The *unode* resolution can be varied at will, but there is always a compromise between resolution and computational time. Accordingly,

numerical models in this thesis use a 256 × 256 grid of *unodes* to map crystallographic orientations, creating a unit cell with 65,536 discrete *unodes*. Each *unode* represents the smallest unit with homogeneous lattice orientation, along with local parameters such as dislocation density or local stress. The information stored in these *unodes* is used to calculate viscoplastic deformation with the VPFFT module and DRX processes in ELLE.

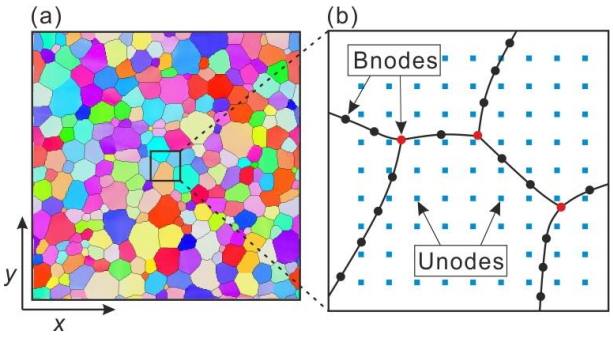

Figure 2.1. (a) Initial microstructure used in this study, and (b) maximization showing the discretization in two layers of unconnected nodes (*unodes*) and boundary nodes (*bnodes*) used in the numerical approach. Each color in (a) represents a different crystallographic orientation.

The VPFFT-ELLE method uses an operator-splitting approach where each process is executed sequentially in a loop, representing a small increment of time (Bons et al., 2008). Each loop starts with the application of viscoplastic deformation (VPFFT) for a given deformation kinematics according to a velocity gradient tensor (Table 2.1). Subsequently, the microstructure goes through the DRX subloop, which includes intracrystalline recovery, polygonization and GBM processes (Fig. 2.2). Additionally, supplementary routines handle data management, data conversion, and topology checks (Fig. 2.2). The VPFFT-ELLE approach requires periodic boundaries, resulting in the continuous connection of the left-right and upper-lower sides of the model unit cell (Jessell et al., 2001). The "reposition" process relocates any areas that have moved out of the rectangular unit cell back into it after each VPFFT step. This process is only necessary for simple shear simulations as the initial square model here deforms into a parallelogram. The main advantage of this method is that it facilitates

the visualization of microstructures even up to very high strain (Fig. 2.2), as shown in Finch et al. (2020), which reached a finite shear strain of 18.

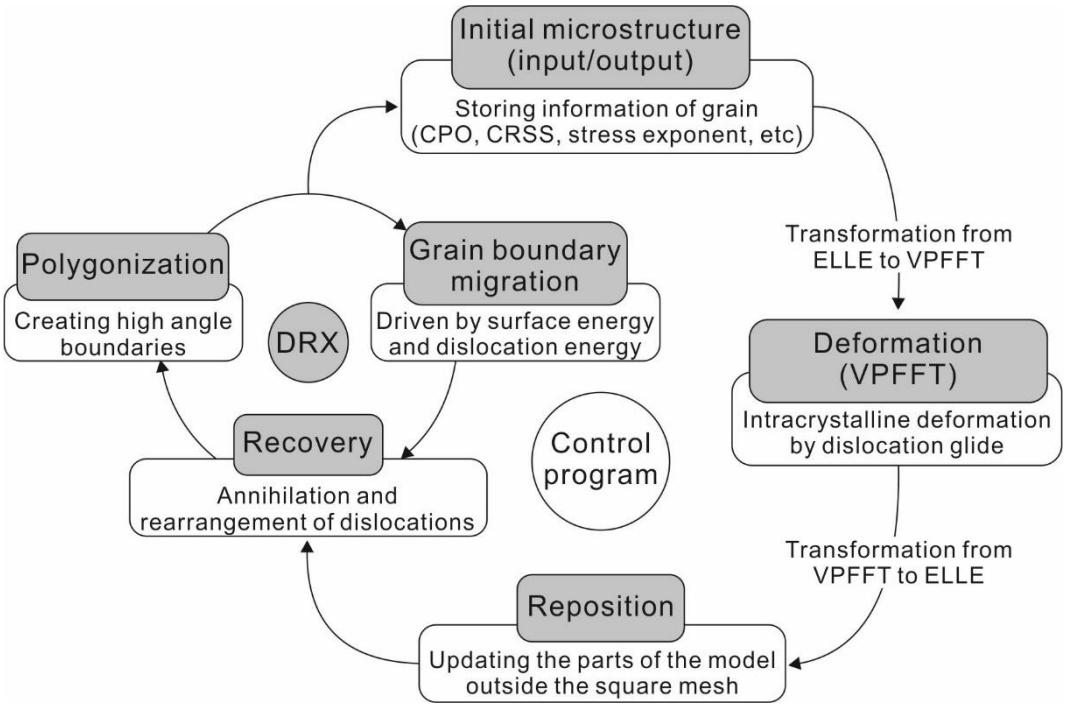

Figure 2.2. Loop showing the process workflow for one simulation time step. The initial microstructure is first subjected to viscoplastic deformation (VPFFT), followed by reposition, and a subloop of dynamic recrystallization processes (DRX). The DRX subloop includes polygonization, grain boundary migration (GBM) and intracrystalline recovery.

2.2 VPFFT - viscoplastic deformation by dislocation glide

The VPFFT (Viscoplastic Fast Fourier Transform algorithm) (Lebensohn, 2001) is an outstanding and widely used method for solving problems in the field of micromechanics. The approach is based on the application of Green functions to transform and solve the mechanical problem using the fast Fourier transform algorithm. The approach minimizes the average local work rate under the constraints of compatibility and equilibrium by finding an admissible stress and strain rate field. A detailed explanation of the VPFFT method can be found in Lebensohn (2001) and Lebensohn & Rollett (2020), and its implementation in ELLE is described by Griera et al. (2013). The VPFFT is a spectral method that discretizes the polycrystalline aggregate into

a periodic rectangular grid composed of Fourier points. This approach assumes that the crystalline deformation of the polycrystalline aggregate is only achieved by glide of dislocations along predefined slip systems of the crystal. The calculation of stress $\sigma^{'}(\mathbf{x})$ and strain rate $\dot{\varepsilon}_{ij}(\mathbf{x})$ at each Fourier point obeys a non-linear viscous rate-dependent power law based on the strength of the different slip systems. The constitutive equation is given by:

$$\dot{\varepsilon}_{ij}(\mathbf{x}) = \sum_{s=1}^{N_s} m_{ij}^{s}(\mathbf{x})\dot{\gamma}^{s}(\mathbf{x}) = \dot{\gamma}_0 \sum_{s=1}^{N_s} m_{ij}^{s}(\mathbf{x}) \left| \frac{m^{s}(\mathbf{x}) : \sigma^{'}(\mathbf{x})}{\tau^{s}(\mathbf{x})} \right|^{n} \operatorname{sgn}\left(m^{s}(\mathbf{x}) : \sigma^{'}(\mathbf{x}) \right) \qquad (1)$$

where N_s is the total number of slip systems within the crystal, m_{ij}^{s} and $\dot{\gamma}^{s}$ are the symmetric Schmid tensor and shear strain rate, which encodes the orientation of slip system (*s*), expressed in a sample reference frame, *i.e.*, varying from material point to material point, depending on local Euler angles. The scalar τ^{s} is the critical resolved shear stress (CRSS) of slip system (*s*). The constant $\dot{\gamma}_0$ is the reference strain rate, and *n* is the stress exponent. The symbol ":" indicates double contraction of second-order tensors.

In our model, viscoplastic deformation of halite is accommodated by three sets of slip systems based on the cubic symmetry: $\{110\} < \bar{1}10 >, \{100\} < 011 >$ and $\{111\} < \bar{1}10 >$ (Carter and Heard, 1970). Here we use an exponent of $n = 7$ for all the slip systems (Table 2.1). The interpreted stress exponent (*n*) obtained from torsion experiments ranges from 4.5 to 5.4 (Armann, 2008), which is consistent with the *n* values (4.1-13.2) obtained from other experiments (Carter et al., 1993; Franssen, 1994; Marques et al., 2013; Wawersik & Zeuch, 1986). In order to be consistent with previous halite viscoplastic simulations (e.g., Gomez-Rivas et al., 2017) all simulations presented here are carried out with $n = 7$ (which is based on Wenk et al., 2009). The abbreviation "FFT" in VPFFT stands for "Fast Fourier Transform" and refers to the spectral solver used by the code. This approach requires a rectangular grid of 2^m by 2^m elements, with the *m* whole number being greater than one. A further requirement is that

the model is wrapping in both the *x* and *y* directions to maintain periodic boundary conditions. The model that describes the polycrystalline aggregate with variations in lattice orientation resolved down to the scale of individual elements can thus be regarded as a unit cell that is infinitely repeated in all directions. For a given state of the microstructure and applied deformation (e.g., pure shear or simple shear), VPFFT calculates the stress field and all resulting kinematics fields (velocity, strain rate, rigid-body and lattice rotation-rate fields) that are applied to the model for small increments of strain, by updating the microstructure in ELLE.

2.3 ELLE - dynamic recrystallization (DRX) process

The DRX subloop, called after each VPFFT step (Fig. 2.2), launches intracrystalline recovery, polygonization, and GBM processes. The intracrystalline recovery process is driven by the reduction of the local misorientation and associated energy of dislocation densities, and reproduces the annihilation of dislocations and their rearrangement into low-angle grain boundaries (LAGBs; also known as subgrain boundaries) (Borthwick et al., 2014; Gomez-Rivas et al., 2017). The polygonization module updates the grain network topology in order to generate new high-angle grain boundaries (HAGBs) if the misorientation angle of a cluster of *unodes* (*i.e.*, subgrain) is higher than a predefined threshold. The movement of HAGBs is applied by the GBM code (Becker et al., 2008; Llorens et al., 2016a, 2016b), which calculates their displacement based on the grain boundary energy and the intragranular strain stored energy as driving forces.

2.3.1 Intracrystalline recovery

This module simulates intracrystalline recovery, reproducing the annihilation of dislocations and their rearrangement into LAGBs. This approach assumes that intracrystalline heterogeneities in the lattice orientation produces a local increase in the effective interface

energy of low-angle boundaries following the Read-Schockley model (e.g., Borthwick et al., 2014). The reduction of local misorientation produces a reduction of the free energy of the system. The approach assumes that the rotation rate of the *unode* or crystallite is proportional to the torque (Randle, 1993), and follows a linear viscous rate law (*i.e.*, linear relationship between shear stress and strain rate) (Gomez-Rivas et al., 2017). For a random *unode* chosen, the module only considers the first-neighbour *unodes* belonging to the same grain (*i.e.*, *unodes* with a local misorientation angle lower than HAGB). The routine calculates for each *unode* the local misorientation and boundary energy to the neighbour *unodes* following the Read-Schockley equation (Read & Shockley, 1950). Then, a small increment of the lattice orientation (in our simulations 0.02º) of the reference *unode* is applied using sample directions as rotation axis to calculate the gradient of energy reduction. The reference *unode* crystal orientation is changed towards the value that accounts for the maximum energy reduction. For a detailed description of the recovery module, the reader is referred to Borthwick et al. (2014) and Gomez-Rivas et al. (2017) (including the supplementary material of the latter publication).

2.3.2 Polygonization

In the polygonization process, new grains are defined as clusters of *unodes*, in a way that the misorientation between them and that of adjacent clusters is greater than a predefined misorientation threshold (HAGB), which is set to 10º following Pennock et al. (2005). The polygonization routine detects *unode* clusters with misorientation higher than the predefined threshold and inserts new boundary nodes between them to segment the pre-existing grain. Specifically, the approach uses Voronoi tessellations of the *unode* layer clipped to the pre-existent grain boundaries to define new positions of *bnodes* from a cluster of critical *unodes*. The new grain is therefore defined as a small part of a pre-existent grain and, therefore, preserves the topology of the grain network. Two main restrictions are imposed in this approach:

(1) island grains (*i.e.*, new grains within old grains) are not allowed to prevent topology misfits and (2) a minimum of four *unodes* are required to create a new grain to prevent numerical instabilities due lack of information inside the new grain. The reader is referred to Steinbach et al. (2016) for a more detailed description of this numerical process.

2.3.3 Grain boundary migration (GBM)

The GBM code used in this contribution is the same as the one described in Llorens et al. (2016a, 2016b, 2017) and Steinbach et al. (2016). This subsection provides an overview of the process, but a more detailed explanation of the approach and its implementation can be found in Becker et al. (2008), Roessiger et al. (2014) and Llorens et al. (2016a).

2.3.3.1 Single phase GBM

The GBM code is based on the front-tracking method, which moves the boundary nodes (*bnodes*) to achieve a reduction of Gibb's free energy (Becker et al., 2008). This direction is determined using four orthogonal trial positions close to the current *bnode* position and determining the gradient of energy reduction in x and y directions. In general, the *bnode* is moved over a small distance (Δl) for a small-time increment (Δt) with:

$$\Delta l = v\Delta t \tag{2}$$

The velocity of a grain boundary (v) is calculated from the grain boundary mobility (M) and driving stress (ΔF):

$$v = M\Delta F\vec{n} \tag{3}$$

where $\vec{n}$ is the unit vector perpendicular to the boundary. M has an exponential relationship with temperature (T), which is calculated from the grain boundary migration activation energy (Q), the intrinsic mobility (M_0), and the universal gas constant (R):

$$M = M_0 exp^{(-Q/RT)} \tag{4}$$

The driving forces used to move HAGBs are the reduction of grain boundary energy and intragranular strain energy. The driving stress (ΔF) can be expressed as:

$$\Delta F = \Delta H - \frac{2J}{r} \quad (5)$$

where J is the boundary energy and r is the local radius of curvature of the grain boundary. ΔH is the differential strain stored energy across a grain boundary, which is calculated from the shear modulus (G, assumed to be isotropic), the Burgers vector (b) and the difference in dislocation density ($\Delta\rho$):

$$\Delta H = \Delta\rho G|b|^2 \quad (6)$$

In the area swept by the grain boundary movement, the dislocation density ρ is set to 0. All parameters involved in GBM are listed in Table 2.1.

2.3.3.2 Two phase GBM

In polyphase aggregates, the content of each phase imposes a requirement of mass conservation. In the model, the absence of mass transfer between second-phase minerals implies that the cross-sectional area of each second-phase grain (or cluster) must be conserved. Theoretically, the movement of grain boundaries between halite and the second phase (*i.e.*, HS boundaries) should be restricted to uphold mass conservation. However, this restriction would immobilize the HS boundary nodes in the model, preventing any geometrical changes of the second-phase grains. Therefore, the approach permits movements that maintain the overall fraction of the second phase while allowing shape alterations. This approach can locally break the mass conservation requirement. An additional energy term is introduced to account for changes in local energy resulting from the area reduction/expansion of the second phase (Roessiger et al.,

2014). For the HS boundaries, total local energy (E_{total}) at a given *bnode* position (k) is calculated as follows:

$$E_{total}(k) = J(k) + c\left(\frac{A_k - A_0}{A_0}\right)^2 \quad (7)$$

where A_0 is the initial area of second-phase grain, and A_k is its area for a trial *bnode* at position k. The constant c, acting as a compressibility factor, determines the permissible area deviation. This factor influences the rate at which area variation is achieved between the two phases. For further details, see Roessiger et al. (2014) and Steinbach et al. (2016).

In polyphase models like halite with a second hard phase, three types of boundaries are present: halite-halite (HH), second phase-second phase (SS), and halite-second phase (HS) boundaries. The properties of HH boundaries, boundary energy (J_{HH}), intrinsic mobility ($M_{0(HH)}$), and grain boundary migration activation energy (Q_{HH}), are well-defined from static grain growth experiments (Piazolo et al., 2006; Sun & Bauer, 1970). For the second-phase mineral, we have presumed a scenario with slower grain boundary mobility than halite, with its intrinsic mobility ($M_{0(SS)}$) set at 0.2 times that of halite ($M_{0(HH)}$). The intrinsic mobility of HS boundaries ($M_{0(HS)}$) is set at 0.02 times that of halite, indicating a condition of very low mobility (Roessiger et al., 2014). The dihedral angle (ω) between HH and SS boundaries (wetting angle) is defined by their respective boundary energies,

$$\omega = 2\cos^{-1}\left(\frac{J_{HH}}{J_{SS}}\right) \quad (8)$$

Here we assume that the halite grains and the second-phase grains are similar in shape with a dihedral angle of ω = 120°, thus setting $J_{HH} = J_{SH} = J_{SS}$.

Table 2.1. Input properties of numerical simulations

Symbol	Explanation	Input value
n_H	Stress exponent of halite (Carter & Heard, 1970)	7
n_S	Stress exponent of second phase (e.g., calcite; Evans et al., 2001; Renner et al., 2002)	5
b	Burgers vector (Frost & Ashby, 1982)	3.9×10^{-10} m
G	Shear modulus	7.1×10^{9} Pa
$M_{0(HH)}$	Intrinsic mobility of halite–halite boundaries (Piazolo et al., 2006)	1.5×10^{-7} m^4 J^{-1} s^{-1}
$M_{0(SS)}$	Intrinsic mobility of second phase–second phase boundaries	3.0×10^{-8} m^4 J^{-1} s^{-1}
$M_{0(HS)}$	Intrinsic mobility of halite–second phase boundaries	3.0×10^{-9} m^4 J^{-1} s^{-1}
J_{HH}	Halite–halite interface boundary energy (Piazolo et al., 2006)	0.36 J m^{-2}
J_{HS}	Halite–second phase interface boundary energy	0.36 J m^{-2}
Q	Grain boundary migration activation energy (Piazolo et al., 2006)	4.7×10^{4} J mol^{-1}
c	Compressibility factor (Steinbach et al., 2016)	0.1
α_{hagb}	Critical minimum misorientation for high-angle boundaries (Pennock et al., 2005)	10°
Velocity gradient tensor	Static grain growth	$\begin{bmatrix}0 & 0 & 0\\ 0 & 0 & 0\\ 0 & 0 & 0\end{bmatrix}$
	Dextral simple shear	$\begin{bmatrix}0 & 0.03 & 0\\ 0 & 0 & 0\\ 0 & 0 & 0\end{bmatrix}$
	Pure shear	$\begin{bmatrix}0.015 & 0 & 0\\ 0 & -0.015 & 0\\ 0 & 0 & 0\end{bmatrix}$
	Two-phase simple shear	$\begin{bmatrix}0 & 0.03 & 0\\ 0 & 0 & 0\\ 0 & 0 & 0\end{bmatrix}$

2.4 Data analysis and visualization

Crystallographic orientation maps, including grain and subgrain boundary network maps, and pole figures, were plotted using the texture calculation toolbox MTEX (http://mtex.googlecode.com; Bachmann et al., 2010; Mainprice et al., 2011). This approach allows to postprocess numerical simulations in a similar way than that of EBSD analyses of natural and experimental samples, facilitating the comparison of numerical with natural or experimental microstructures. The routine to plot pole figures is based on the orientation distribution function (ODF) calculated from the three Euler angles stored at each *unode* of the model. MTEX allows to calculate the Schmid factor using the crystallographic orientation data and the applied stress tensor. The misorientation axis of an individual grain is a pole to arcs that best fits the patterns of the dispersion of orientations within a grain (Mainprice et al., 2015). Using these pole figures and subgrain boundary traces, a boundary trace analysis can be performed to determine the active slip systems (Barrie et al., 2008; Linckens et al., 2016; Mainprice et al., 2015; Prior et al., 2002; Reddy et al., 2007).

We quantify the strain heterogeneity using the localization factor (*F*) as originally defined by Sornette et al. (1993) and later implemented in ELLE by Gomez-Rivas (2008):

$$F = 1 - \frac{1}{N_u}\frac{(\sum \dot{\varepsilon}_{vM})^2}{\sum \dot{\varepsilon}_{vM}{}^2} \tag{9}$$

where N_u represents the total number of *unodes*, $\dot{\varepsilon}_{vM}$ is the von Mises strain rate, which is calculated as a function of the symmetric strain-rate tensor $\dot{\varepsilon}_{ij}$:

$$\dot{\varepsilon}_{vM} = \sqrt{\frac{2}{3}\dot{\varepsilon}_{ij}\dot{\varepsilon}_{ij}} \tag{10}$$

F varies from 0 to 1, representing the full spectrum between totally homogeneous deformation and maximum localization, respectively.

The relative contribution of the rigid rotation and flattening rates are quantified using the kinematic vorticity number (W_k), as defined by Truesdell (1953) and Tikoff & Fossen (1995) and Truesdell (1953):

$$W_k = \frac{2\omega}{\sqrt{2(\dot{s}_1^2 + \dot{s}_2^2 + \dot{s}_3^2)}} \tag{11}$$

where $\dot{s}_1$, $\dot{s}_2$ and $\dot{s}_3$ represent the eigenvalues of the stretching tensor (*i.e.*, the symmetric matrix of the velocity gradient tensor), while ω is the angular velocity vector of the spin tensor (*i.e.*, the skew-symmetric matrix of the velocity gradient tensor). For irrotational deformations, such as pure shear, $W_k = 0$. For a rigid rotation without stretching, W_k approaches ∞. For simple shear deformation, $W_k = 1$ (*i.e.*, similar stretching and rotation rates).

The resolved shear stress (τ) is related to the applied stress (σ_a) by Schmid factor (m):

$$\tau = \sigma_a m = \sigma_a(\cos(\lambda)\cos(\varphi)) \tag{12}$$

where λ is the angle between the stress direction and the slip direction, and φ is the angle between the stress direction and the normal to the slip plane (Schmid & Boas, 1950). The Schmid factor predicts the likelihood of slip systems in crystalline materials under applied stress. If m is zero, no resolved shear stress acts on the specific slip system. The maximum value of m is 0.5.

3 Halite polycrystalline dynamic recrystallization from subgrain rotation to grain boundary migration

3.1 Summary

Full-field numerical modelling is a useful method to gain understanding of rock salt deformation at multiple scales, but it is quite challenging due to the anisotropic and complex plastic behaviour of halite, together with dynamic recrystallization (DRX) processes. This chapter presents novel outcomes of full-field numerical simulations that couple dislocation glide with dynamic recrystallization in halite polycrystalline aggregates during simple shear deformation, focusing on subgrain rotation (SGR) and grain boundary migration (GBM) processes. The results demonstrate that the numerical approach successfully replicates the evolution of pure halite microstructures from laboratory torsion deformation experiments at 100-300°C. Temperature determines the competition between (a) grain size reduction controlled by dislocation glide and SGR (at low temperature) and (b) grain growth associated with GBM (at higher temperature), while the resulting CPOs are similar for all cases.

3.2 Model setup and comparison with laboratory experiments

The setup of our DRX simulations (Tables 3.1 & 3.2; DRX_100, DRX_200 and DRX_300) is similar to those of the laboratory torsion experiments of Armann et al. (2008), to allow a direct comparison. This includes the initial grain size, boundary conditions, temperature ranges, and strain rates. The numerical suffixes indicate the temperature at which the simulation was carried out. The initial average grain diameter of our model is 212 μm. The starting material is considered isotropic, as the initial distribution of grain lattice orientations is random (Fig. 2.1a). A detailed summary of all the input parameters for the simulations is presented in Tables 2.1 & 3.1.

Table 3.1. Input properties of numerical simulations

Symbol	Explanation	Input value
L	Unit length	3 cm
Δt	Time step per simulation step	100 s
$\Delta\gamma$	Incremental shear strain per simulation step	0.03
$\tau_{\{110\}}$-$\tau_{\{100\}}$-$\tau_{\{111\}}$	Critical resolved shear stress of $\{110\}<\bar{1}10>$, $\{100\}<011>$ and $\{111\}<\bar{1}10>$ slip systems at different temperatures (Carter and Heard, 1970)	1-3-2
Velocity gradient tensor	Static grain growth (G10_100/200/300)*	$\begin{bmatrix}0 & 0 & 0\\ 0 & 0 & 0\\ 0 & 0 & 0\end{bmatrix}$
	Dextral simple shear (DRX_100/200/300)*	$\begin{bmatrix}0 & 0.03 & 0\\ 0 & 0 & 0\\ 0 & 0 & 0\end{bmatrix}$

Note. * indicates the simulation names, with suffixes denoting the temperatures.

We simulated the microdynamic evolution of polycrystalline halite at different temperatures (100°C, 200°C and 300°C) under dextral simple-shear deformation up to a finite shear strain of $\gamma = 4$, by the application of shear strain increments of $\Delta\gamma = 0.03$ in each time step. Initially, a set of simulations that activate the DRX subloop with 5 times recovery, 20 polygonization, and 10 times GBM per deformation time step (Table 3.2) were performed for comparison with the experiments. In order to check the equivalent time and influence of GBM, a set of

simulations without deformation and with only GBM (static grain growth) were carried out (see G10 simulations in Table 3.2). In these simulations, only the boundary energy was used as a driving force to calculate grain boundary displacement. By activating each module in turn, the microstructure undergoes a loop of deformation processes within a constant time step (Δt = 100 s). The simulation goes through a total of 133 loops up to shear strain of 4, so the equivalent total time is 13,300 s and the shear strain rate is $\dot{\gamma} = 3 \times 10^{-4}\, s^{-1}$ for all simulations.

Table 3.2. Numerical simulation setup

Simulation name	Temperature (°C)	Recovery/ Polygonization/ GBM/VPFFT steps*	Initial average grain size (μm)	Final average grain size (μm)	Equivalent final time(s)/ Shear strain	Strain rate (s^{-1})
G10_100	100	0/0/10/0	212	212	13,300/0	0
G10_200	200	0/0/10/0	212	223	13,300/0	0
G10_300	300	0/0/10/0	212	299	13,300/0	0
*DRX*_100	100	5/20/10/1	212	92	13,300/4	3×10^{-4}
*DRX*_200	200	5/20/10/1	212	135	13,300/4	3×10^{-4}
*DRX*_300	300	5/20/10/1	212	303	13,300/4	3×10^{-4}

Note. * indicates the number of subloops of the different processes during one simulation step. The suffix of the simulation name indicates the temperature.

As stated, above, to calibrate our numerical approach, we compared our DRX simulation results (DRX_100, DRX_200, DRX_300) with torsion experiments of synthetic rock salt by Armann (2008). The halite polycrystalline aggregate used in the experiments of Armann (2008) (with a water content of 35 ppm, determined by FTIR) consisted of isotropic polygonal crystals with an initial average grain size of 216 μm. Cylindrical samples with a diameter of 15 mm were cored from the starting material and dried at atmospheric pressure and 110°C for at least 24 hours before testing (following the protocol by Marques et al., 2013). The torsion experiments were conducted in a temperature-controlled triaxial deformation Paterson rig

(Paterson & Olgaard, 2000). Shear strain rate and shear strain increase linearly in the torsion experiments from the sample's central axis to the outer circumference, and any position of the sample can be regarded as undergoing approximate simple shear deformation. The experiments of Armann (2008) were carried out at three sets of constant twist rates, corresponding to nominal strain rates of 3×10^{-3}, 3×10^{-4} and 3×10^{-5} s^{-1}, respectively. The samples were deformed up to a shear strain of eight at 100°C, 200°C and 300°C, with a constant confining pressure of 250 MPa. The reader is referred to Armann (2008) and Marques et al. (2013) for a more detailed description of their experimental setup.

3.3 Results

3.3.1 Static grain growth

Static grain growth is simulated as GBM-driven exclusively by grain boundary energy reduction (without considering GBM induced by dislocation stored strain energy; Karato, 2008; Weaire & Rivier, 1984). The kinetics of this process can be defined by the average area A from an initial area A_0 (Bons & Urai, 1992; Olgaard & Evans, 1988):

$$A - A_0 = MJt \tag{13}$$

where M is the grain boundary mobility according to equation (4), J is the grain boundary energy and t is time. The total time is equivalent to the duration of the experiments of Armann (2008) (approx. 13,300 s). We assumed surface and grain boundary energies are equal, implying a strong binding energy between surfaces (e.g., Rohrer, 2011). The simulations only including static grain growth (G10_100, G10_200 and G10_300 simulations) are used to test the validity of the setup of the GBM model, by comparing it with the theoretical calculation following equation (13). As shown in Fig. 3.1, and taking G10_300 as an example, the average grain diameter (as a proxy of grain size) in the simulation increases from 212 to 299 μm after

13,300s, while that following the theoretical calculation raised to 303 μm for the same time (Table 3.2 & Fig. 3.1, red lines). The diameter-time curves for G10_100 and G10_200 simulations are also in agreement with the theoretical curves (Fig. 3.1, blue and green lines). Compared with the significant grain growth of the G10_200 and G10_300 simulations, those of the G10_100 simulation do not change during the limited equivalent time. This reveals that the ratio GBM/VPFFT of 10 steps is correct, and validates the selected GBM parameters for our simulations (Tables 2.1 & 3.1).

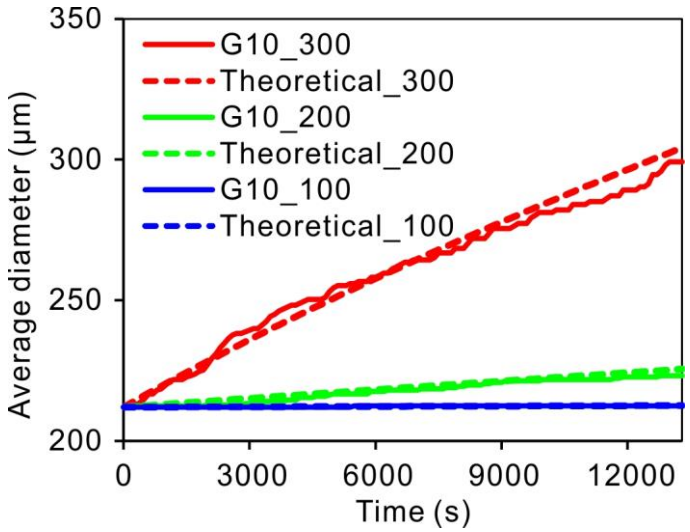

Figure 3.1. Evolution of the average grain size for simulations with only GBM (G10 simulations, solid lines) compared with the theoretical calculation (dashed lines) at temperatures of 100 (blue), 200 (green) and 300°C (red).

Analysis of the grain boundary orientation distribution of slightly deformed polycrystalline aggregates of synthetic rock salt using EBSD reveals that grain boundaries show a preference for {110} planes, which may be related to the anisotropy of the grain boundary energy (Pennock et al., 2009). Our study assumes that all planes per unit length have the same grain boundary energy (*i.e.*, isotropic) and, therefore, we refer to grain boundary migration driven by isotropic grain boundary energy (and dislocation energy) as isotropic grain boundary migration to distinguish it from natural and synthetic rock experiments. Fig. 3.2l-n shows the

microstructure of the simulations with static grain growth driven by grain boundary energy at an equivalent time of 10,000 s (G10_100, G10_200 and G10_300 simulations). All static grain growth simulations produce classical foam texture patterns, similar to the starting mineral aggregate (Fig. 3.1a), which is coherent with the isotropic boundary energy setup considered in these simulations.

3.3.2 Microstructure evolution

Simulations DRX_100, DRX_200 and DRX_300 represent systems in which dislocation creep and dynamic recrystallization processes (*i.e.*, intracrystalline recovery, polygonization and GBM) are coupled at various temperatures (100°C, 200°C and 300°C). At low temperatures (100°C and 200°C) grain boundaries tend to be elongated and parallel to the stretching direction, showing a shape-preferred orientation (SPO) oblique to the shear plane (Fig. 3.2f-g, b). As expected, the angle between the SPO and the shear plane gradually decreases with progressive deformation, and at a shear strain of three, the foliation already lies at a low angle with respect to the shear plane (approximately 17º, Fig. 3.2i-j, b). At high temperature (300°C), elongated grains parallel to the stretching direction and SPO are still visible, but their aspect ratio is lower, and grains are larger and more equidimensional than those of the low-temperature models at a similar shear strain (100°C and 200°C) (Fig. 3.2k, b). At low temperatures, the initial grain size (Fig. 3.2a) decreases significantly with increasing strain due to polygonization of new (recrystallized) grains (Fig. 3.2i-j, Table 3.2), and an intense network of LAGBs can be recognized within relict grains, as shown in Fig. 3.2i-j. The density of the LAGB network gradually increases with progressive strain, revealing a general trend of increasing intergranular heterogeneities with deformation (Fig. 3.2i-j). However, increasing GBM weakens this trend, resulting in a lower density of LAGBs (e.g., Fig. 3.2k).

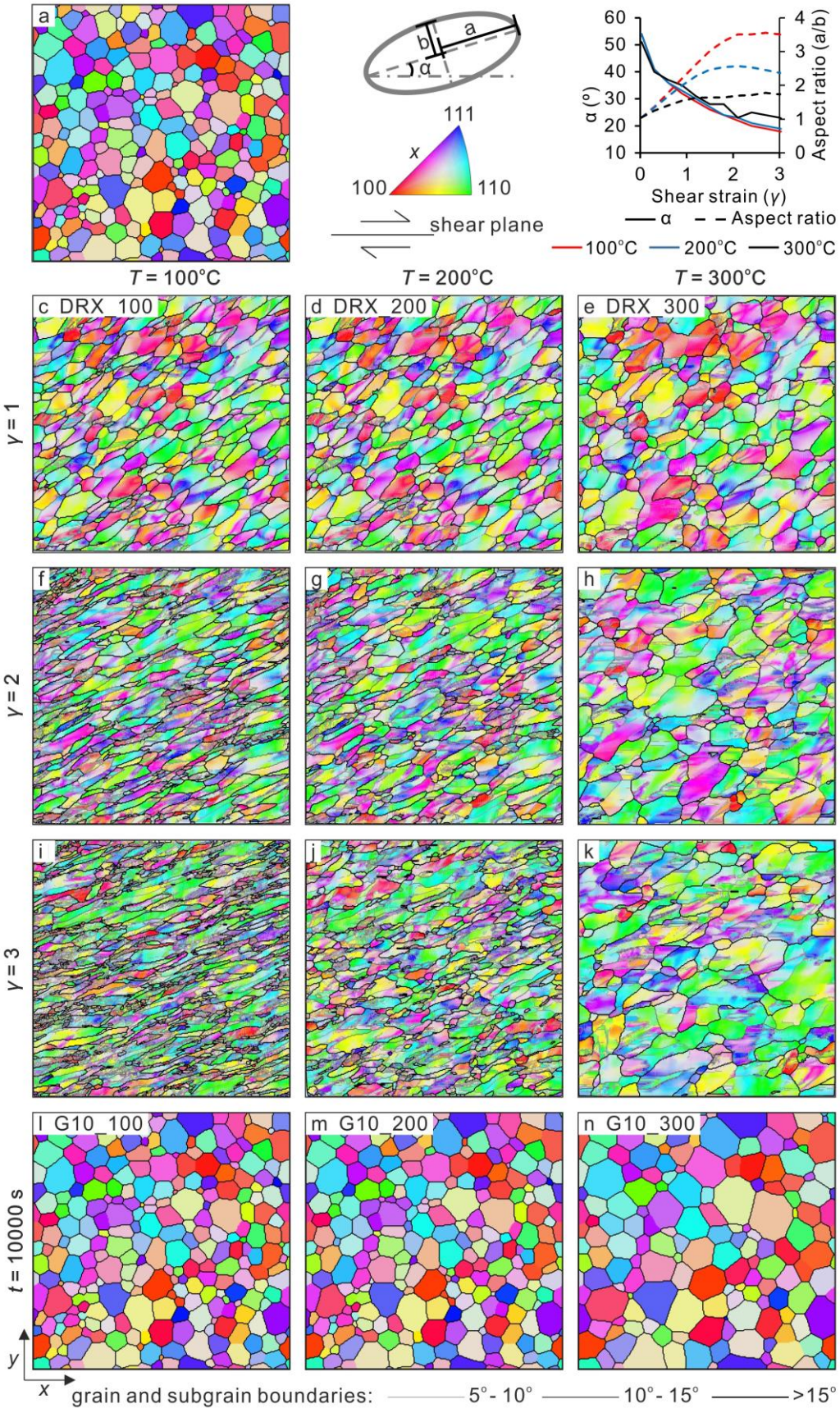
a
b
a
α
111
x
100
110
shear plane
60
50
40
30
20
10
α (°)
4
3
2
1
0
Aspect ratio (a/b)
0
1
2
3
Shear strain (γ)
α
Aspect ratio
100°C
200°C
300°C
T = 100°C
T = 200°C
T = 300°C
c DRX_100
d DRX_200
e DRX_300
f
g
h
i
j
k
l G10_100
m G10_200
n G10_300
γ = 1
γ = 2
γ = 3
t = 10000 s
y
x
grain and subgrain boundaries:
5°- 10°
10°- 15°
>15°

Figure 3.2. Crystallographic orientation and grain and subgrain boundary network maps of simulations with fully activated DRX at different shear strains (γ = 1, 2, 3) at (c, f, i) 100°C, (d, g, j) 200°C and (e, h, k) 300°C, and simulations with only GBM at a time t = 10,000s and at (l) 100°C, (m) 200°C and (n) 300°C, respectively. The initial microstructure is shown in (a). Crystal lattice orientations are plotted as inverse pole figure colors with respect to the horizontal *x*-axis (the shear direction). (b) Evolution of average shape-preferred orientation (solid lines indicate the angle between the major axis and the shear direction, while dashed lines the aspect ratio) with shear strain from γ = 0.03 to γ = 3 at 100°C (red lines) 200°C (blue lines) and 300°C (black lines).

A close look at the evolution of the grain boundary network more clearly reveals the effect of temperature on DRX. A detail of the grain boundary map of a small area of the simulations is shown in Fig. 3.3 for the 100ºC (DRX_100) and 300°C (DRX_300) cases. Increasing temperature accelerates grain boundary migration and reduces the number of LAGBs. At low shear strain (γ = 0.3) the microstructures show similar grain boundary and subgrain boundary networks regardless the temperature (Fig. 3.3a, d, red circle). With progressive strain grains split into multiple new grains at 100°C because of the increase in local misorientation of the LAGBs (Fig. 3.3b-c). However, at 300°C and for an equivalent region of grains to that of the 100°C case, there is a tendency of the grains with stronger substructure heterogeneities to disappear before they accumulate enough misorientation to split and produce new grains. The effect of GBM at high temperature is observed in Fig. 3.3d-f, where the boundaries of grains containing no or few low-angle grain boundaries move towards grains with higher subgrain heterogeneities, so that the substructures rich of grains are consumed and eventually disappear (Fig. 3.3f, red arrow). A similar process is visible in the blue circles of Fig. 3.3.

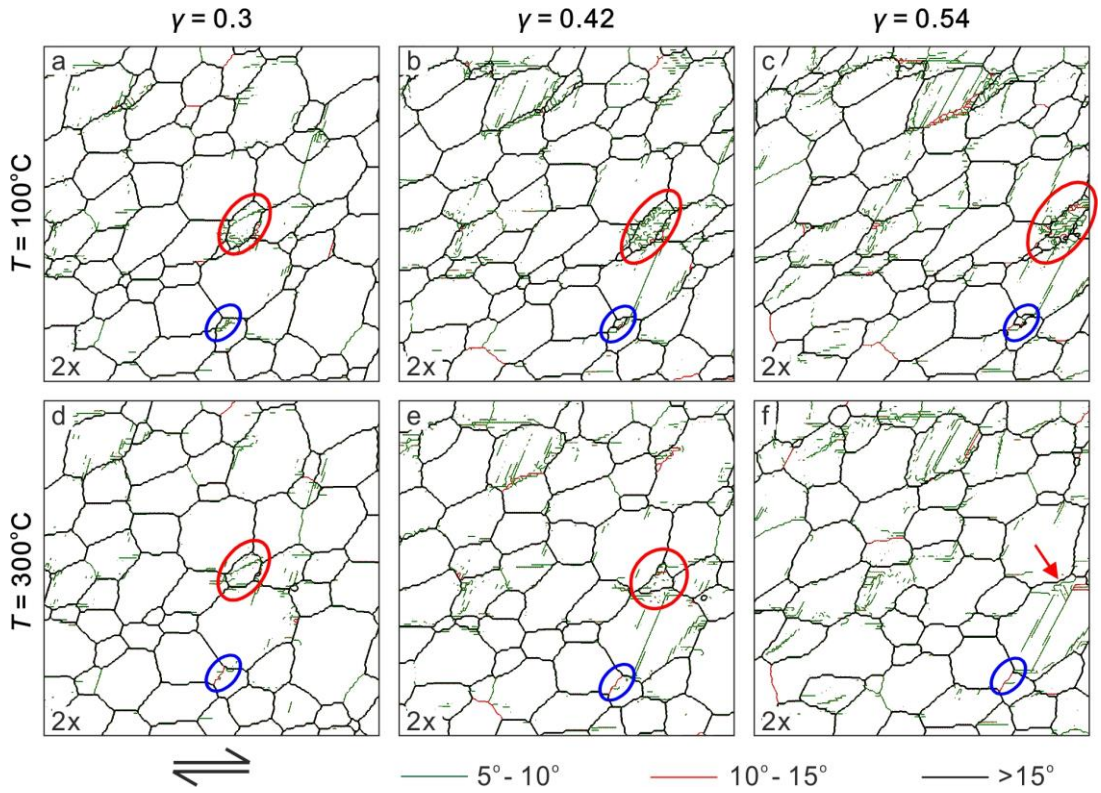

Figure 3.3. Comparison of the details of the grain boundary evolution of a selected grain with fully activated DRX at shear strains of γ = 0.3, 0.42 and 0.54 at 100°C (a-c) and 300°C (d-f), respectively.

The evolution of grain size distribution during progressive deformation is shown in Fig. 3.4, where the frequencies of grain size fractions are represented by different colors. The statistical results show that the grain size distribution in the logarithmic scale is always unimodal at different temperatures. At 100 and 200°C (Fig. 3.4a, b) the grain size distribution shifts towards smaller grain sizes. Specifically, the proportion of small grains gradually increases with progressive deformation (Fig. 3.4, log grain size ranges between 1.4-2.0), while the proportion of large grains gradually decreases (Fig. 3.4, log grain size ranges between 2.0-2.6), revealing that the grain refinement process dominated by SGR induces grain size reduction. The situation at 300°C is different because the grain size distribution reveals larger grain sizes and is stable for the logarithmic grain-size range of 2.4 to 2.6, remaining constant at around 30% with increasing shearing (Fig. 3.4c). The grain size distribution of the 200°C model is more uniform than that of the 100°C case at high strain (γ > 2), possibly due to the large effective mobility of

GBM at higher temperatures. The population of small grains remain essentially unchanged with increasing shear strain at 300°C (Fig. 3.4c, log grain size ranges between 1.2-1.6), which is different from that of the low-temperature models (100 and 200°C), whose proportions gradually increase.

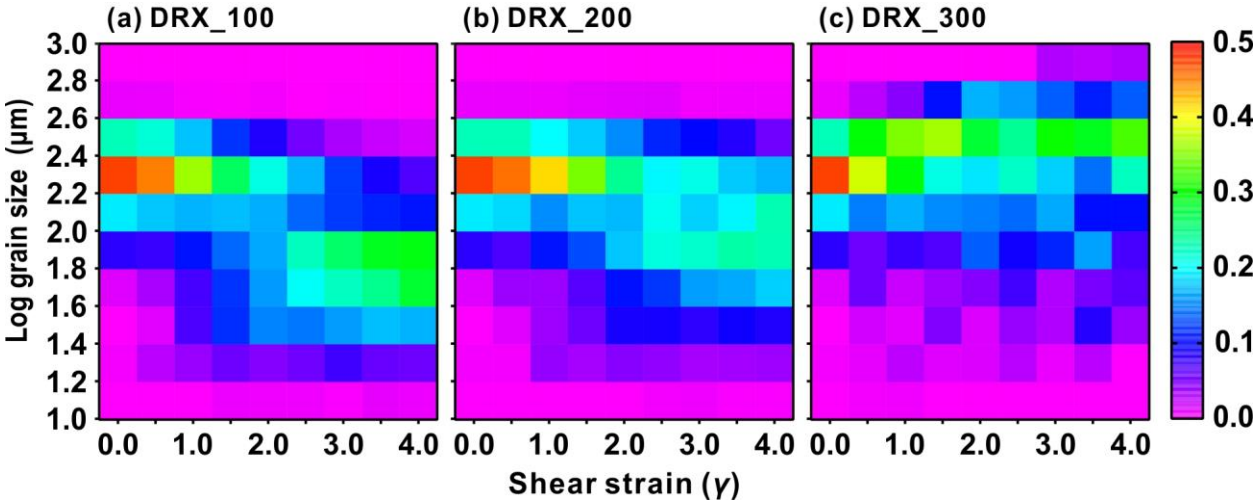

Figure 3.4. Evolution of grain size distribution with progressive strain for the simulations with fully activated DRX (DRX_100/200/300). The grain size corresponds to the equivalent grain size (in logarithmic form, log10).

3.3.3 Crystallographic Preferred Orientation (CPO) evolution

The crystallographic preferred orientation maps of DRX simulations (Table 3.2) at different shear strains (γ =1, 2, 3) and different temperatures (T = 100, 200, 300°C) are shown in Fig. 3.2 while the pole figures of the crystallographic preferred orientations (CPOs) are plotted in Fig. 3.5. As shown in Figs. 3.2 & 3.5, the CPO evolution with progressive strain is very similar regardless the temperature. Pole figures show the progressive evolution and intensity of the initial random distribution of crystallographic orientations (Fig. 3.5a), which in all cases evolve to form a {100} maximum CPO approximately perpendicular to the shear plane and two maxima at approximately 45º to it (Fig. 3.5d-g-j). At low strain (γ = 1), the {100} pole figure shows two maxima. One of these maxima is obliquely oriented to the shear plane with the opposite sense of shear, and the other one is approximately perpendicular to it (γ = 1, Fig. 3.5b-

e-h). For the same shear strain, the {110} and {111} pole figures show a weak hexagonal symmetry (Fig. 3.5b-e-h). The {110} CPO evolves with shear strain to form two maxima parallel to the shear plane and the other four maxima oriented at 45º from it (Fig. 3.5d-g-j). The {111} CPO evolves towards a pattern with four maxima at 45º to the shear direction. The {110} and {111} CPO intensity increases when temperature raises (compare Figs. 3.5d, g & j). However, the intensity of the final {100} CPO oriented perpendicular to the shear plane is reduced while the intensity of the two maxima oblique to the shear plane increases (Fig. 3.5d-g-j). Dynamic recrystallization does not change the CPOs, but shows a reduction of dispersion of crystallographic axes and strengthening of the maxima (Fig. 3.5).

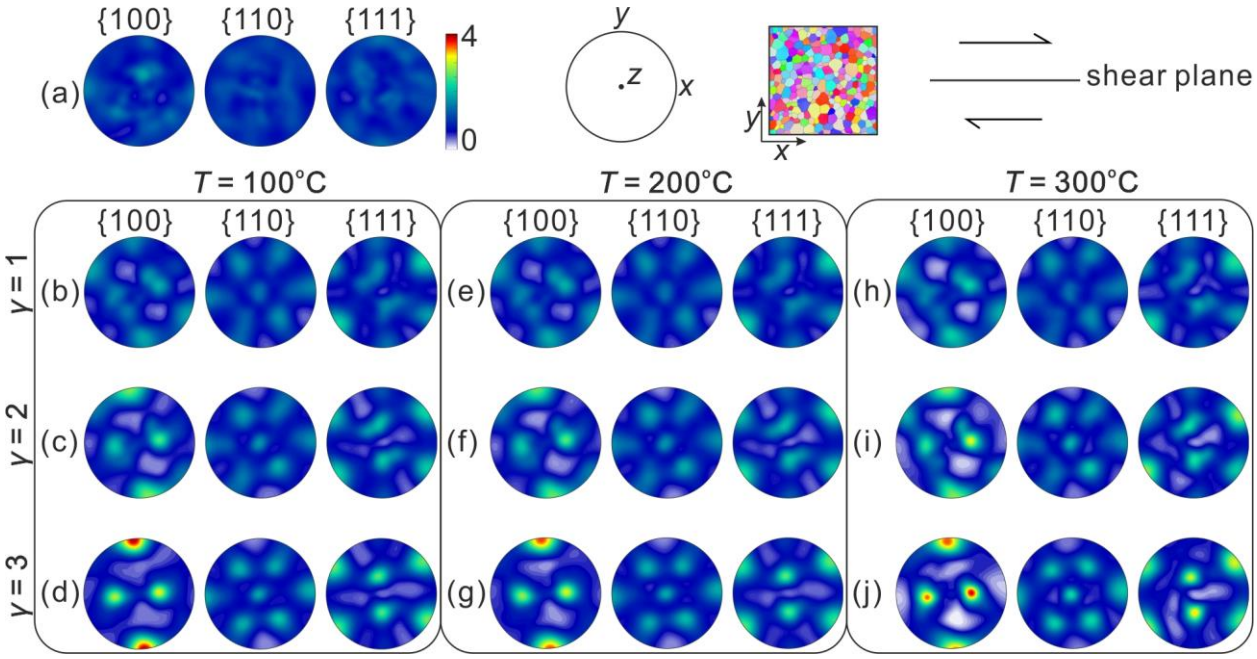

Figure 3.5. Pole figures of the crystallographic preferred orientations (CPOs) during deformation, where the shear sense is dextral and the shear plane is horizontal. The stereoplots of (a) correspond to the initial stage. Stereograms of the three groups of columns show the CPO evolution for the simulations with fully activated DRX (DRX_100/200/300) at different shear strains (γ = 1, 2, 3) at (b-d) 100°C, (e-g) 200°C and (h-j) 300°C, respectively.

3.4 Discussion

One of the objectives of this study is to investigate the microstructural evolution of halite aggregates in simple shear viscoplastic deformation including dynamic recrystallization (DRX) at different temperatures and compare numerical predictions with torsion experiments. We calibrate and corroborate that full-field DRX simulations can reproduce results from the experiments of Armann (2008). Specifically, the grain size statistics (Figs. 3.4 & 3.6), microstructures and crystallographic orientation maps (Fig. 3.2 & 3.5) of our numerical models can be directly compared with those from the pure halite torsion experiments of Armann (2008) and Marques et al. (2013) at the same temperature range (Figure 3.6). The simulations presented here also match the numerical results from VPSC simulations of Wenk et al. (2009) and full-field simulations of Gomez-Rivas et al. (2017), expanding the range of simulation conditions to include grain boundary migration recrystallization during halite deformation.

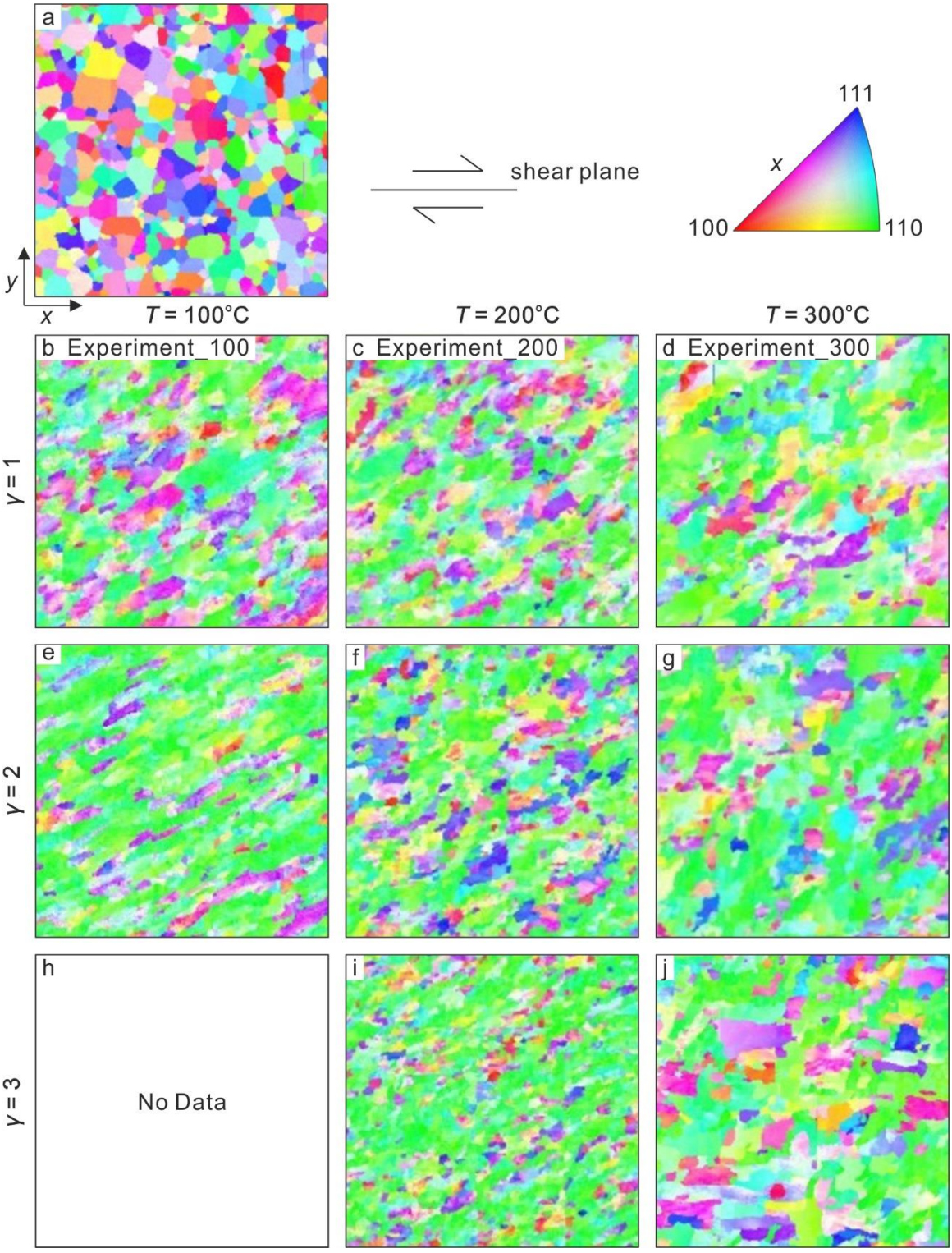

Figure 3.6. Crystallographic orientation maps of the experiments of Armann (2008) at different shear strains (γ = 1, 2, 3) at 100°C (b, e, h), 200°C (c, f, i) and 300°C (d, g, j), respectively. The initial orientation is shown in (a). Crystal lattice orientations are plotted as inverse pole figure colors with respect to the horizontal *x* axis (*i.e.*, shear direction). Figure modified from Armann (2008).

3.4.1 Effect of temperature on the evolution of microstructures

Under static conditions, when grain growth is purely driven by isotropic grain boundary energy reduction (Eq. 6) (G10 simulations), the resulting microstructure is a typical foam texture (e.g., Weaire & Rivier, 1984) similar to those reported for undeformed rock salt after heating experiments by Bestmann et al. (2005). Under dynamic recrystallization conditions (DRX simulations), we can observe how temperature determines the balance between grain size reduction/growth, significantly affecting the microstructure evolution of halite polycrystalline aggregates at a constant shear strain rate. When the microstructure is deformed at high-temperature conditions (300°C), GBM produces a larger average grain size than that of the initial microstructure, while the models run at lower temperatures (100 and 200°C) (Table 3.2, Fig. 3.7a-b) grain size reduction is observable (Armann, 2008). Moreover, there are more equidimensional grains at 200°C than at 100°C (Fig. 3.2b), showing that temperature-dependent GBM strongly affects the grain shapes. The transition from low (100°C and 200°C) to high temperature (300°C) in our numerical microstructures is comparable with that taking place in quartz deformation experiments from regime II to regime III of Stipp et al. (2002). Regime II is dominated by SGR, in which a portion of low-angle grain boundaries (LAGBs) eventually evolves to high-angle grain boundaries (HAGBs), and with the formation of new grains due to the gradual increase of dislocations within grains as a result of dislocation movement and reorganization (Hirth & Tullis, 1992; Urai, Means, et al., 1986). Regime III is characterized by a significant increase in grain boundary mobility at higher temperatures and large recrystallized grains (Stipp et al., 2010).

The grain size evolution of the laboratory experiments of Armann (2008) *versus* our simulations at 100°C, 200°C and 300°C at a shear strain rate of $3 \times 10\text{-}4\ s^{-1}$ is shown in Fig. 3.7 (grain size mean and standard deviation). The numerical simulation average grain size at

different temperatures is basically consistent with that of the torsion experiments. It gradually decreases with increasing shear strain for the low-temperature systems (100°C and 200°C) (Fig. 3.7a-b), while it increases when the temperature is higher (300°C) (black line in Fig. 3.7c). The reduction rate of the grain diameter standard deviation of simulations is significantly lower than the estimated value of the experiments (Armann, 2008). This reveals that the grain size distribution in our simulations during progressive strain is more inhomogeneous than that in experiments (Armann, 2008). One of the reasons may be that the discontinuous GBM processes affected by grain boundary pinning may limit the growth of large grains in laboratory experiments (Guillope & Poirier, 1979; Lücke & Stüwe, 1971), while impurity pinning processes are not included in our simulations. Deformation annealing experiments of rock salt (Piazolo et al., 2006) convincingly show that GBM is sensitive to changes in solute impurities or substructure when the temperature is lower than 400°C.

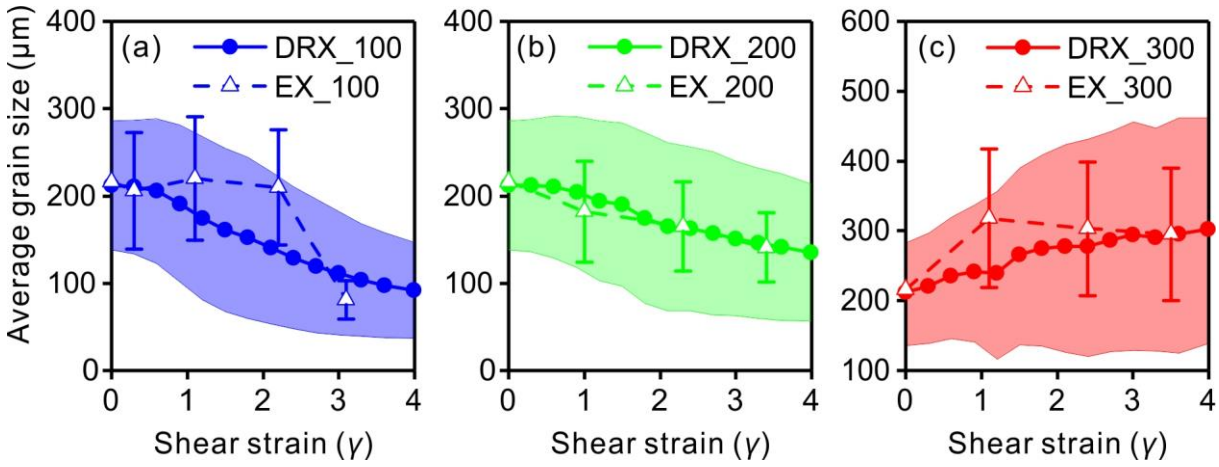

Figure 3.7. Comparison of the evolution of the average grain size (solid lines) with its standard deviation (shaded areas) for simulations (DRX_100/200/300) run in this study at (a) 100°C, (b) 200°C and (c) 300°C with laboratory experiments of Armann (2008) (dashed lines with error bars, EX_100/200/300) at the same temperatures. All the models and experiments were run at shear strain rate of $3 \times 10\text{-}4\ s^{-1}$.

Our results reveal that grains with a large number of subgrain boundaries are consumed by grains with no or few low-angle grain boundaries (Fig. 3.3). This is a phenomenon similar to

that described from halite laboratory experiments (Armann, 2008; ter Heege et al., 2005b) and borehole sample observations (Henneberg et al., 2020; Schléder & Urai, 2005; Thiemeyer et al., 2016). Our simulations assume that the rate of GBM has an exponential relationship with temperature. As expected, the GBM rate increases rapidly with increasing temperature and dominates rock salt deformation, potentially resulting in a microstructure reset (Franssen, 1994; Leitner et al., 2011).

3.4.2 Effect of temperature on the evolution of crystallographic preferred orientation

The numerical CPO evolution (Fig. 3.5b-g) at low temperature is similar to those of the rock deformation experiments at 100°C and 200°C of Armann (2008) (Fig. 3.8), and to numerical simulations by Wenk et al. (2009). However, the models at higher temperature (300°C) (Fig. 3.5h) differ from the experimental results of Armann (2008) (see discussion in the next paragraph below). Strong CPOs develop rapidly with progressive deformation for the whole series of experiments, regardless of whether GBM was active or not (Fig. 3.5). The initial randomly distributed CPOs quickly evolve into a pole to {100} sub-perpendicular to the shear plane at a lower strain of 2 (Fig. 3.5c-f-i). The {100} maximum then gets rotated according to the sense of shear up to becoming perpendicular to the shear plane at high shear strain ($\gamma = 3$) (Fig. 3.5d-g-j). The results of our simulations show that isotropic GBM has a very limited effect on the CPOs, with the only effect that there is less scattering and more intense pole of lattice orientation in higher temperature systems (Fig. 3.5). This agrees with many other studies on 1h polar ice (e.g., Llorens et al., 2016a, 2016b, 2017).

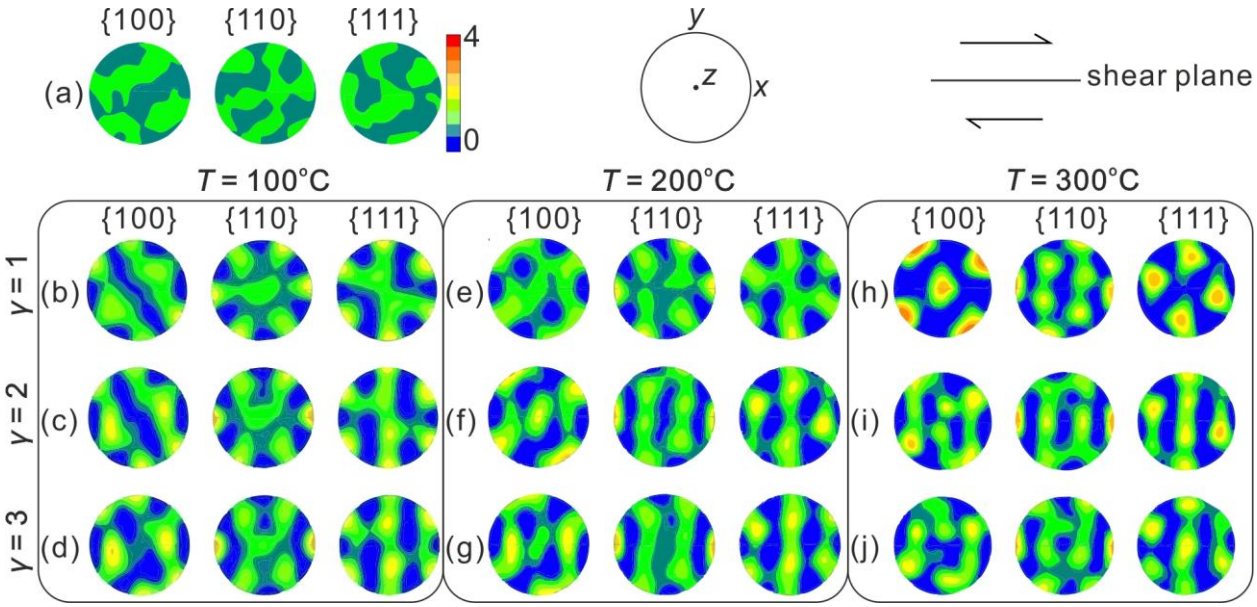

Figure 3.8. Pole figures of the crystallographic preferred orientations (CPOs) from torsion experiments (Armann, 2008). The stereoplots of (a) correspond to the initial stage. Stereograms of the three groups of columns show the CPO evolution for the torsion experiments at different shear strains (γ = 1, 2, 3) at (b-d) 100°C, (e-g) 200°C and (h-j) 300°C, respectively.

When the temperature is high (300°C) a particular CPO (Fig. 3.8h) that is accompanied by two {100} maxima at 45° between the shear plane and the shear plane normal was observed in torsion experiments (Armann, 2008) at low strain, which our simulations do not reproduce. Armann (2008) refers to it as grain growth CPO and suggests that it is produced by static annealing after deformation ceased in the experiments. Borthwick & Piazolo (2010) carried out thermal annealing experiments (>300°C) on a pre-deformed single crystal halite and found that annealing resulted in a change of the rotation axis of some part of LAGBs and an increase of the LAGBs. Static annealing experiments of olivine aggregates by Boneh et al. (2017) revealed that [100] poles rotate 10-15° from the original direction during annealing by discontinuous grain growth, in a sample almost composed of porphyroblasts that distinctly have a different CPO from that of the matrix of small grains. The CPO difference between large strain-free grains and surrounding matrix grains was also observed in recrystallized vein quartz (Stöckhert & Duyster, 1999) and chromite (Ghosh et al., 2017). Large free grains are visible in the

reflected light micrograph of the experimental microstructure corresponding to the grain growth CPO of Armann (2008) (see Fig. 6.6a of Armann, 2008), which means that discontinuous grain growth took place at high temperature. Therefore, the formation of such CPOs may be is influenced by the discontinuous grain growth with anisotropic grain boundary energy (Piazolo et al., 2006) or by the preferred elimination of high-energy grain boundaries during grain growth (Dillon & Rohrer, 2009; Pennock et al., 2009).

4 Influence of the kinematics of deformation on polycrystalline halite dynamic recrystallization: simulation of simple shear versus pure shear

4.1 Summary

Rock salt, composed mainly of halite, flows plastically over a wide range of geological conditions, strongly impacting the dynamic evolution of sedimentary basins and orogens. Understanding how dislocation creep, which involves dislocation glide, intracrystalline recovery and dynamic recrystallization, influences the microstructure and rheology of halite under various deformation kinematics and temperatures is crucial for enhancing knowledge of salt flow dynamics. This chapter focuses on studying the difference in the viscoplastic deformation of polycrystalline halite under simple shear and pure shear conditions up to a natural strain of ε = 1.5 at temperatures ranging from 100°C to 300°C.

4.2 Model setup

To assess the effect of deformation kinematics and temperature on rock salt deformation, two numerical series were implemented for simple shear (Table 4.1; SSH_100, SSH_200 and SSH_300) and pure shear (PSH_100, PSH_200 and PSH_300), with numerical suffixes denoting different temperatures (100°C, 200°C and 300°C). We use a pure halite polycrystalline aggregate, with a cell size of $L \times L$ (3×3 cm^2) for simple shear and a $L \times 2L$ (3×6 cm^2) cell for pure shear. Both deformation kinematics with an initial average grain size of 212 μm, and are modelled in increments of $\Delta\varepsilon = 0.015$ up to natural strain of $\varepsilon = 1.5$ at temperatures of 100°C, 200°C and 300°C. A natural strain of $\varepsilon = 1.5$ corresponds to 78 % shortening in pure shear, or a shear strain of $\gamma = 3$ in simple shear. All simulations employ a constant time step of 100 s, resulting in a natural strain rate of 1.5×10^{-4} s^{-1}. The input parameters for the simulations are detailed in Tables 2.1 and 4.1.

Table 4.1. Input properties of numerical simulations.

Symbol	Explanation	Input value
L	Unit length	3 cm
Δt	Time step per simulation step	100 s
$\Delta\varepsilon$	Incremental natural strain per simulation step	0.015
$\tau_{\{110\}}$-$\tau_{\{100\}}$-$\tau_{\{111\}}$ (100°C)	Critical resolved shear stress of $\{110\}<\bar{1}10>, \{100\}<011>$ and $\{111\}<\bar{1}10>$ slip systems at different temperatures (Carter and Heard, 1970)	4.2-18.0-12.2
$\tau_{\{110\}}$-$\tau_{\{100\}}$-$\tau_{\{111\}}$ (200°C)		3.1-8.2-7.6
$\tau_{\{110\}}$-$\tau_{\{100\}}$-$\tau_{\{111\}}$ (300°C)		2.0-4.0-4.0
Velocity gradient tensor	Dextral simple shear (SSH_100/200/300)*	$\begin{bmatrix} 0 & 0.03 & 0 \\ 0 & 0 & 0 \\ 0 & 0 & 0 \end{bmatrix}$
	Pure shear (PSH_100/200/300)*	$\begin{bmatrix} 0.015 & 0 & 0 \\ 0 & -0.015 & 0 \\ 0 & 0 & 0 \end{bmatrix}$

Note. * indicates the simulation names. Suffixes in the simulation names denote the temperatures.

4.3 Results

4.3.1 Microstructure evolution

Viscoplastic deformation leads to the development of a SPO due to grain elongation along the stretching direction (Fig. 4.1b-d). In simple shear simulations, the grain aspect ratio increases gradually with strain, reaching a maximum approximately at a natural strain of 1.0, then stabilizing (Fig. 4.2a). However, in pure shear simulations it increases steadily with strain (Fig. 4.2a). Under simple shear, the angle between the grain SPO and the horizontal shear plane gradually decreases as strain increases (Fig. 4.2b). Under pure shear, the grain SPO aligns parallel to the *x*-axis or the direction of maximum stretching, as expected (Fig. 4.1e-g & 4.2b). As temperature increases, the higher intensity of GBM reduces grain elongation, resulting in larger and more equidimensional grains (Figs. 4.1 & 4.2a).

At low temperatures (100°C and 200°C), qualitative variations in the grain boundary network between two deformation kinematics are observed at a natural strain of $\varepsilon = 1.0$ (Fig. 4.1). The bands of (recrystallized) small grains (also known as shear bands) are observed subparallel to the grain SPO. In simple shear models, these bands appear at low angle to the shear direction (Fig. 4.1b, c). In pure shear models, these bands align diagonally relative to the maximum stretching direction (Fig. 4.1e, f). At high temperature (300°C), subgrain boundaries are visible within some grains, although they are significantly less numerous than in lower temperature models. The bands of small grains are barely visible at 300°C (Fig. 4.1d, g).

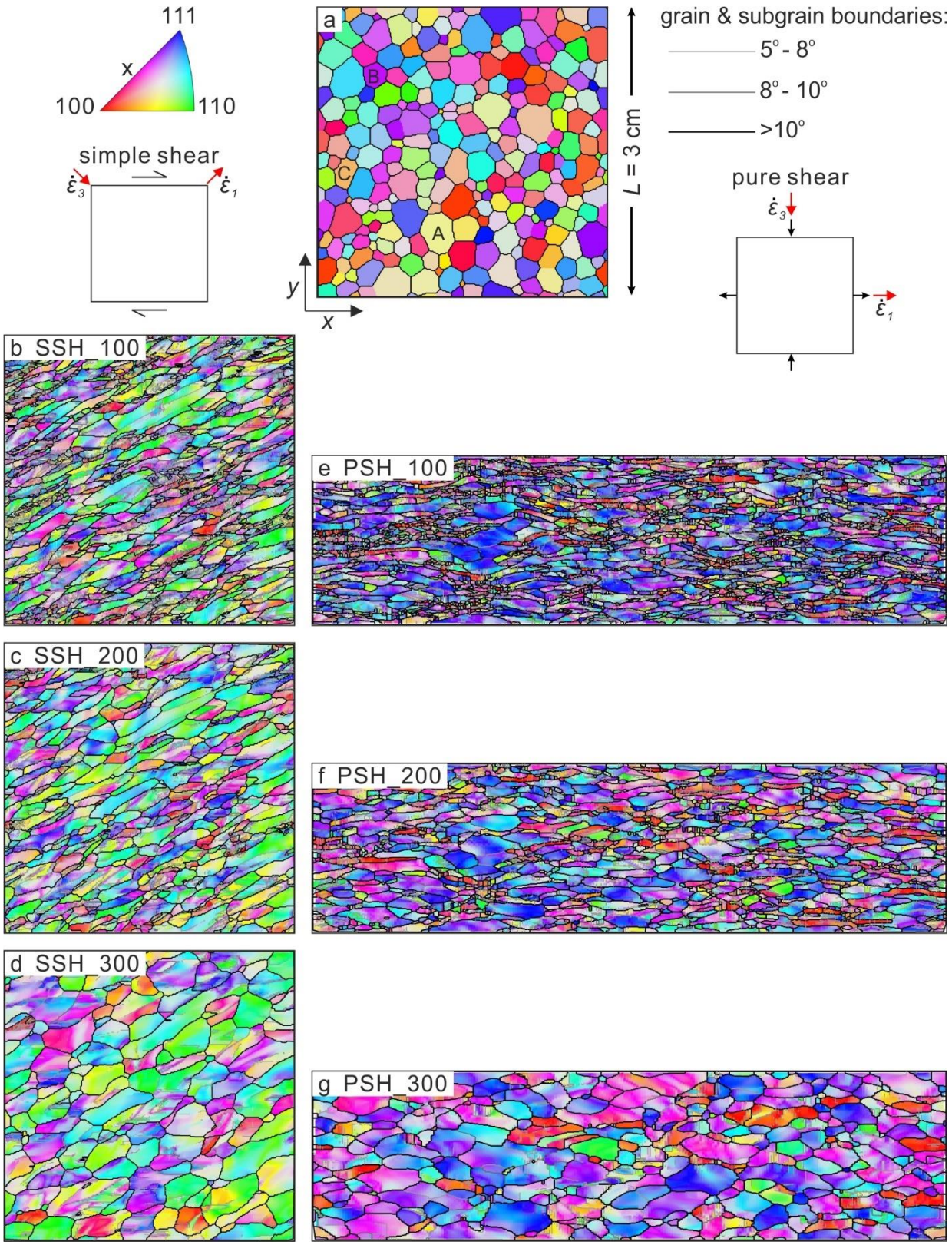

Figure 4.1. Crystallographic orientation and grain and subgrain boundary network maps at a natural strain of ε = 1.0 for simulations deformed in simple shear (b-d) and pure shear (e-g). Please note that the size of images corresponding to pure shear simulations (e-g) is displayed as 0.8 times that of the original images. The initial microstructure for simple shear simulations is a square model with a side

length of one unit (L = 3 cm) (a). The initial model size for pure shear simulations is doubled vertically ($2L$). Crystal lattice orientations are plotted with inverse pole figure (IPF) colors with respect to the horizontal x-axis. Grains and subgrains are delimited by black and grey lines, respectively.

Rose diagrams displaying the orientation distribution of subgrain boundaries at natural strains of ε = 0.3 and 0.6 are shown in Fig. 4.2c-f. Conjugate preferred orientations are observed in both deformation kinematics, along with an additional maximum at a low angle to the grain SPO (red lines in Fig. 4.2c-f). In simple shear models, the frequencies of conjugate directions are asymmetric, with increased asymmetry at higher strain (Fig. 4.2c, e). In pure shear models, the frequencies of conjugate directions remain nearly symmetric throughout the deformation (Fig. 4.2d, f). The orientation distribution normalized based on the subgrain boundary lengths is shown in Fig. 4.3. These figures are strongly similar to those showing just the orientation distribution, though some orientations slightly vary. Subgrain boundaries that are nearly perpendicular to the grain SPO appear more frequently in Fig. 4.2, yet are less prominent in Fig. 4.3, suggesting these subgrain boundaries are more numerous yet shorter.

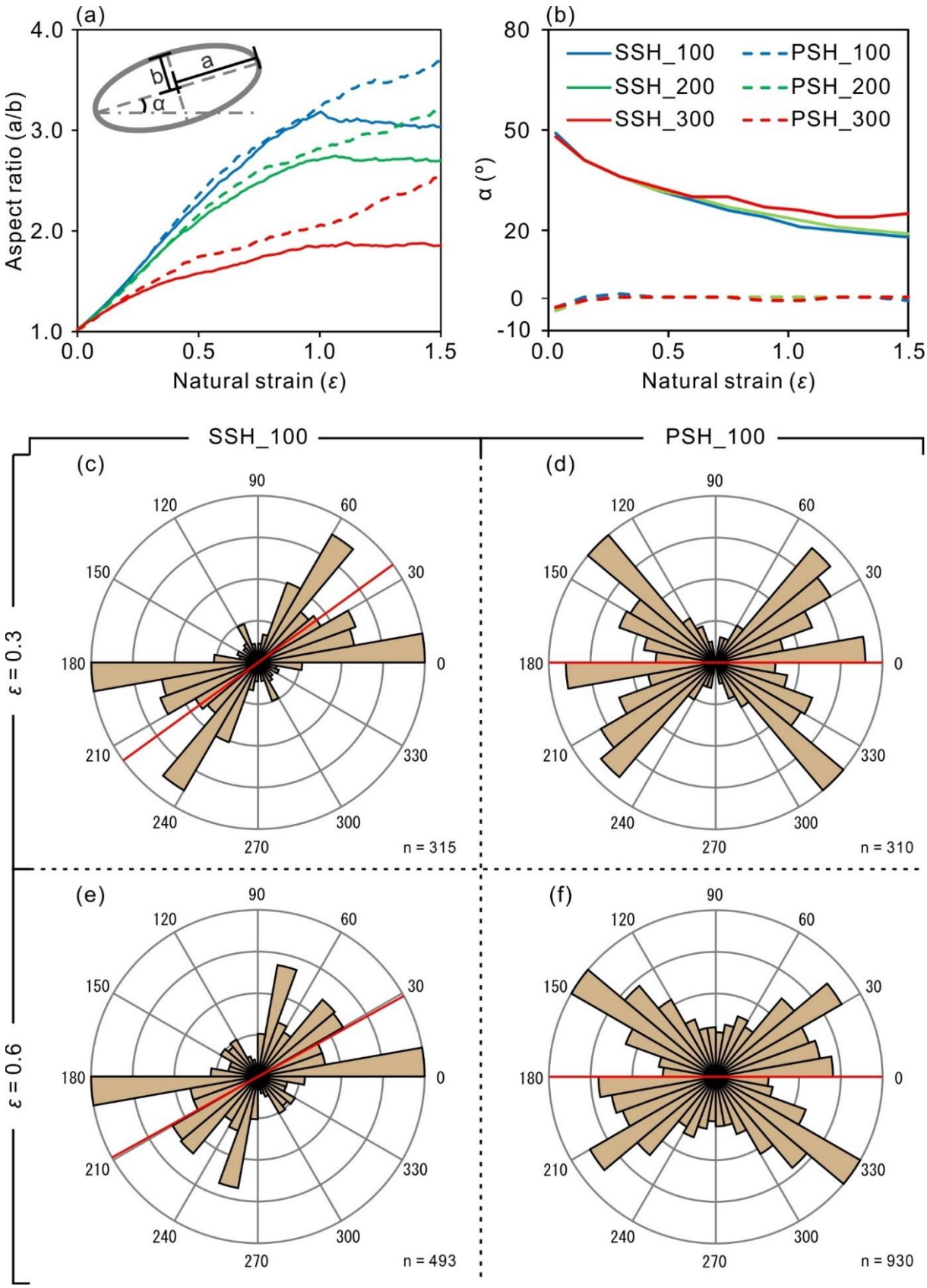

Figure 4.2. Evolution of the average shape preferred orientation (a) and aspect ratio (b) of grains with natural strain. Simulations deformed in simple shear (SSH_100/200/300) are marked in solid lines,

while pure shear simulations (PSH_100/200/300) are marked with dashed lines. Color lines indicate temperature, being 100°C, 200°C and 300°C shown in blue, green and red, respectively. (c-f) Rose diagrams displaying orientations of subgrain boundaries at a natural strain of ε = 0.3 and 0.6 in simulations deformed under simple shear and pure shear at 100°C. Red lines in rose diagrams represent the grain SPO. Diagrams are normalized to the orientation with maximum frequency.

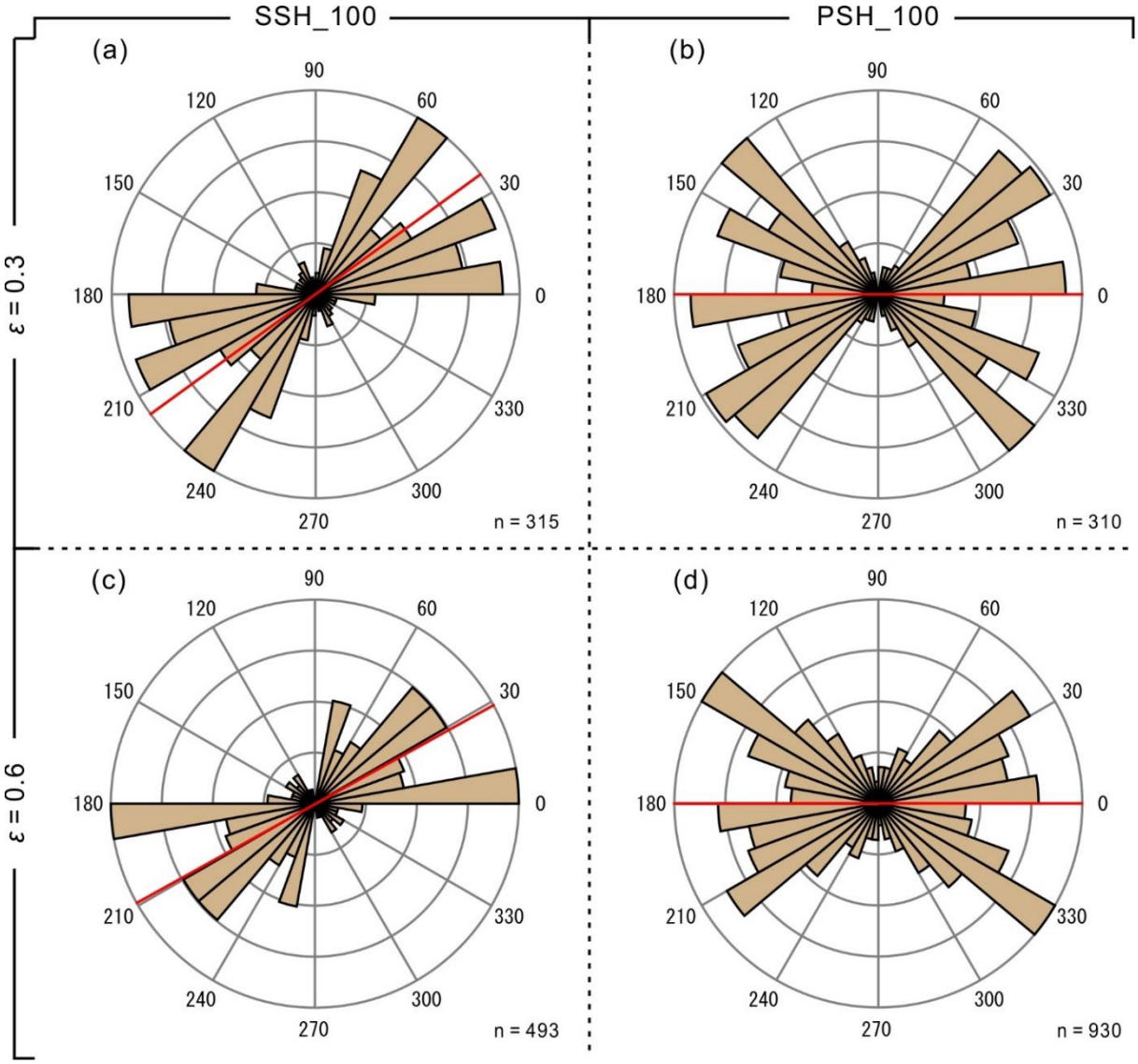

Figure 4.3. Rose diagrams displaying the orientations of subgrain boundary at a natural strain of ε = 0.3 and 0.6, from simulations under simple shear and pure shear at 100°C. The orientation distribution frequencies are normalized to the length of subgrain boundaries. Red lines in rose diagrams indicate the grain SPO.

The evolution of the average grain size and its standard deviation during progressive deformation in simple shear simulations is similar to that of pure shear at the same temperature, with only slight variations at high strain (Fig. 4.4). For instance, the grain size and its standard deviation under simple shear is marginally larger than that under pure shear at a finite strain of 1.5 at 200°C and 300°C, whereas the reverse holds true at 100°C (Fig. 4.4). The proportion of small grains gradually increases with strain (Fig. 4.5, logarithmic grain size ranging between 1.2 and 2.0) while the proportion of large grains gradually decreases (Fig. 4.5, logarithmic grain size ranging between 2.0 and 2.6) at 100°C and 200°C. The grain size distribution evolution is characterized by a gradual increase in the proportion of large grains at 300°C (Fig. 4.5, logarithmic grain size ranging between 2.0 and 2.6). At 200°C and 300°C, simple shear produces a more dispersed grain distribution than that of pure shear deformation at high strain ($\varepsilon > 1.0$), with a higher proportion of both large and small grains (Fig. 4.5), leading to a larger standard deviation of the average grain size (Fig. 4.4b, c).

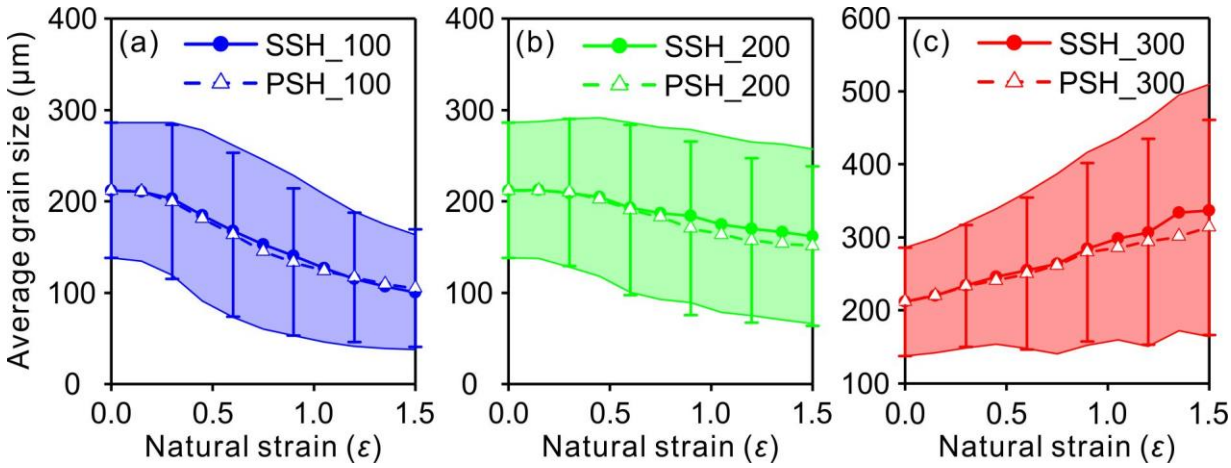

Figure 4.4. Evolution of the average grain size with its standard deviation (a-c) with natural strain. Simulations deformed in simple shear (SSH_100/200/300) are marked in solid lines and shaded areas, while pure shear simulations (PSH_100/200/300) are marked with dashed lines and error bars. Color lines indicate temperature, being 100°C, 200°C and 300°C shown in blue, green and red, respectively.

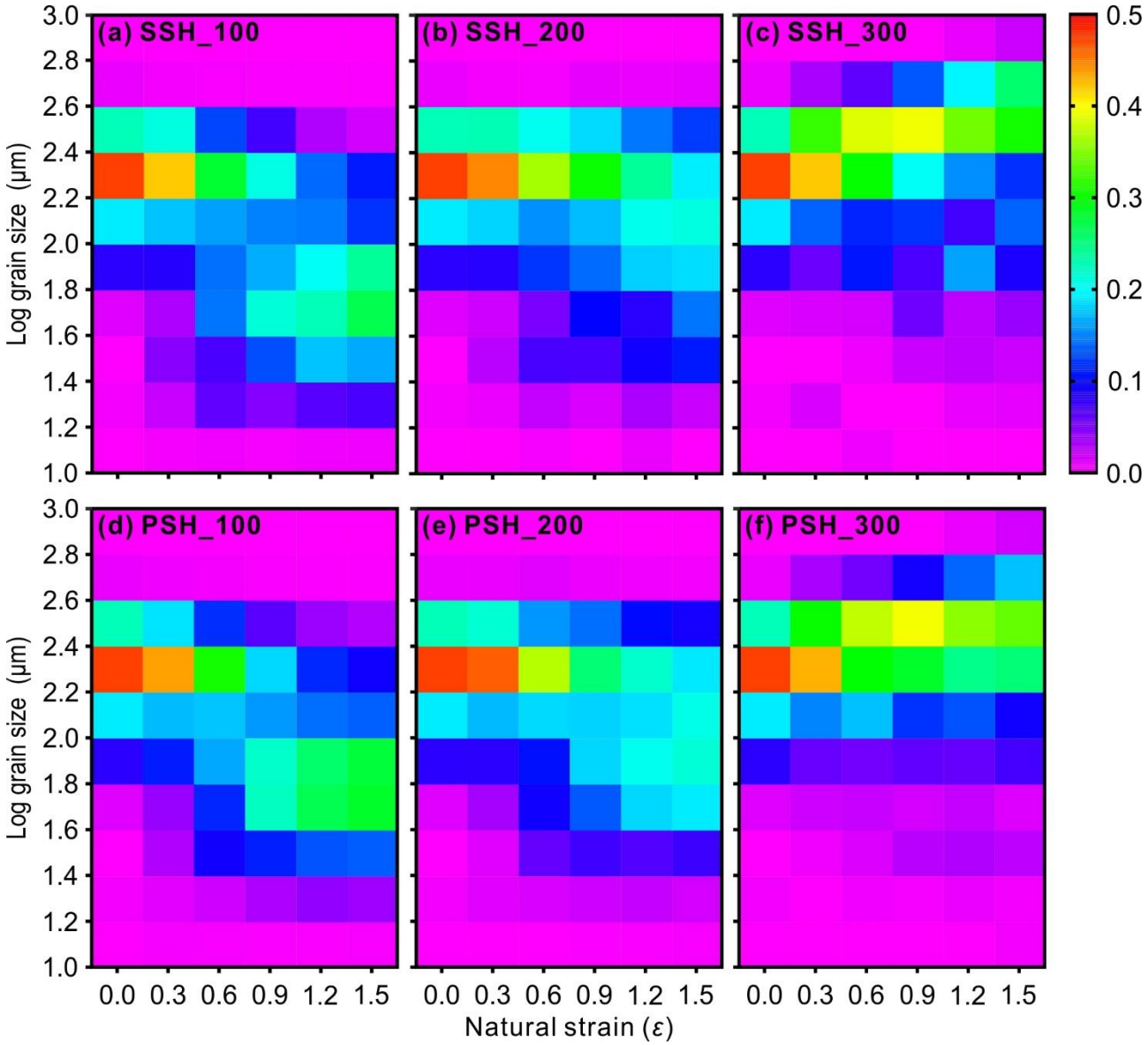

Figure 4.5. Comparison of the evolution of grain size distribution with natural strain increasing for simulations deformed in simple shear (SSH100/200/300) at (a) 100°C, (b) 200°C and (c) 300°C with that of simulations deformed in pure shear at the same temperatures (PSH_100/200/300, d-f). The grain size corresponds to the equivalent grain size (in logarithmic form, $\log_{10}$). The color bars indicate the frequency of grain size fractions (0.0-0.5).

Fig. 4.6 shows the details of the subgrain boundaries and crystal orientation of three selected grains (indicated as A, B and C in Fig. 4.1a) at low strain (ε = 0.3), comparing them under simple shear and pure shear deformation conditions. The kinematics of deformation affects the morphology of subgrain boundaries and the dispersion of crystallographic orientation. Under simple shear, grain A exhibits subgrain boundaries aligned subparallel to the maximum

stretching direction. Under pure shear, grain A instead develops two small subgrains with differing crystallographic orientations from the parent grain. Grain B develops subgrains oblique to the maximum stretching direction when is deformed under pure shear. Similar to Grain B, grain C also develops a subgrain boundary oblique to the direction of maximum stretching, when is affected by pure shear.. Under simple shear deformation, grains B and C do not exhibit an evident substructure, but lattice bending occurs. The 100 pole figures of selected grains show the dispersion of crystallographic orientations around the <100> misorientation axis due to the deformation (Fig. 4.6). The dispersion of orientations increases as the natural strain increases from 0.15 to 0.3. The direction of spread of the crystallographic orientations around the <100> axis is correlated with the deformation kinematics. Simple shear deformation results in clockwise spreading of the crystallographic orientations along the best fitting fibre, whereas pure shear deformation leads to clockwise and/or counterclockwise spreading directions (Fig. 4.6, red arrows in pole figures).

Fig. 4.6 displays the initial Schmid factors (*m*, see section 2.4 for its definition) for different slip systems in selected grains. The initial Schmid factors for the various slip systems within the grains at the onset of deformation ($\varepsilon = 0$) are calculated using the theoretical applied stress and the crystallographic orientations of the individual grains. Under simple shear, the initial Schmid factors for the $\{110\} < \bar{1}10 >$, {100} <011> and $\{111\} < \bar{1}10 >$ slip systems in grain A are 0.112, 0.449 and 0.318, respectively. Under pure shear, the initial Schmid factors for these three slip systems in grain A are 0.423, 0.254 and 0.492, respectively, distinctly different from those under simple shear. Similar deformation responses are observed in grains B and C, with comparable changes in their initial Schmid factors under both simple and pure shear conditions.

Additionally, Fig. 4.6 shows the distribution of slip system activity in selected grains at natural strain of $\varepsilon = 0.3$. The $\{110\} < \bar{1}10 >$ (green tones), $\{111\} < \bar{1}10 >$ (blue tones), and {100}

<011> (red tones) slip systems all contribute to the deformation of the grains. Different deformation kinematics within the same grain produce varied slip system activity distributions. In simple shear the upper half of grain A shows activation of the $\{111\} < \bar{1}10 >$ and {100} <011> slip systems, while the lower half shows activation of the $\{110\} < \bar{1}10 >$ slip system. Under pure shear, the same grain is primarily dominated by the $\{110\} < \bar{1}10 >$ slip system, with smaller regions dominated by the $\{111\} < \bar{1}10 >$ and {100} <011> slip systems. Under simple shear, the distribution of the three slip systems in grain B appears random. Under pure shear, grain B displays a green band inclined toward the direction of maximum stretching, indicating dominated by the $\{110\} < \bar{1}10 >$ slip system. Most of grain C shows activation of the $\{110\} < \bar{1}10 >$ slip system under both simple shear and pure shear conditions.

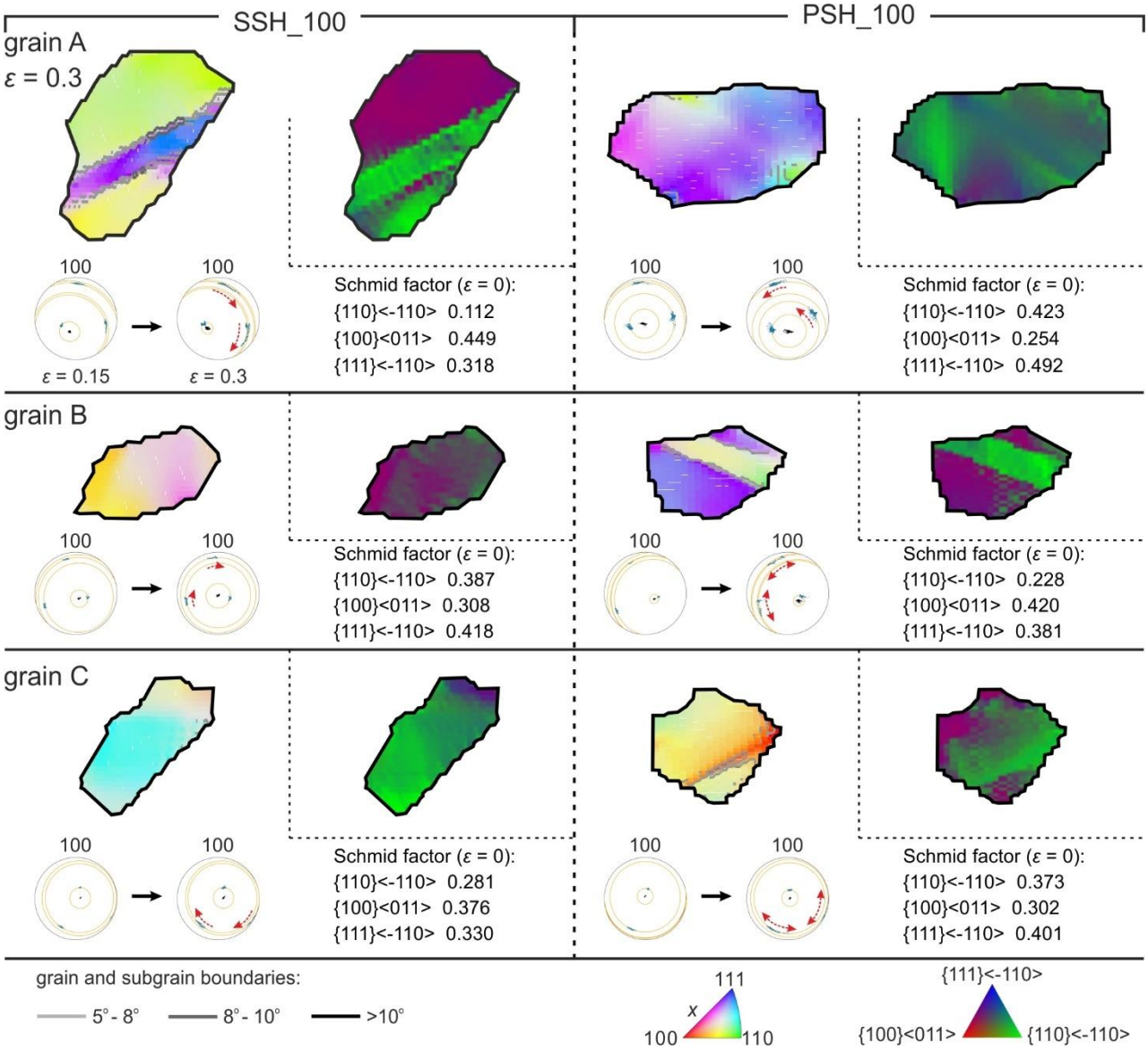

Figure 4.6. Crystallographic orientation, subgrain boundary network, distribution of the slip system activity and calculated initial Schmid factor of selected grains (see grains A, B and C in Fig. 4.1a for their original orientation and geometry) at a natural strain of $\varepsilon = 0.3$. Left-hand column shows the results for simulations deformed in simple shear (SSH_100) and the right-hand column results under pure shear (PSH_100), both at 100°C. The crystallographic orientations are plotted in 100 pole figures, where every point represents the orientation of a crystallite inside the grain. The evolution of orientations dispersion with increasing strain (from 0.15 to 0.3) is marked in red arrows. Orange arcs and black points are the best fitting fibre with a specific misorientation axis for given orientations (Mainprice et al., 2015). Crystallographic orientations are plotted with inverse pole figure (IPF) colors with respect to the horizontal *x* axis. The initial Schmid factor was calculated using crystallographic orientation of selected grains and the applied stress tensor at the onset of deformation ($\varepsilon = 0$).

4.3.2 CPO evolution

The pole figures of Fig. 4.7 illustrate the evolution of the CPO throughout simple *versus* pure shear deformation at the different modelled temperatures (T = 100°C, 200°C and 300°C). At a natural strain ε = 0.5, {100} CPO features six maxima that are orthogonally symmetric with respect to the maximum shortening strain rate axis ($\dot{\varepsilon}_3$ axis) both in simple shear and pure shear simulations. Under simple shear, three {100} maxima slightly rotate synthetically, aligning with the applied shearing sense, while the other three maxima diminish and eventually disappear with progressive deformation (Fig. 4.7b-g). With increasing strain, simple shear tends to create a marginally stronger fabric compared to pure shear, attributed to a higher concentration of the maxima (see M index comparison between pure and simple shear in Fig. 4.7). At the final strain of 1.5, the simple shear CPO exhibits a {100} maximum that is nearly parallel to the *y* axis, with two additional maxima in the XZ plane approximately 45º to the *x*-axis. The evolution of {110} and {111} CPOs during incremental deformation is akin to that of {100} CPO, where simple shear CPOs rotate according to the synthetic shear direction, while the pure shear CPOs remain static. Although both the {110}and {111} pole figures show mild hexagonal symmetry, the dispersion of crystallographic axes in simple shear CPOs is less than that in pure shear CPOs. In simple shear, a higher temperature modestly increases the CPO strength without changing its orientation (Fig. 4.7). However, the CPO strength in pure shear simulations decreases with increasing temperature.

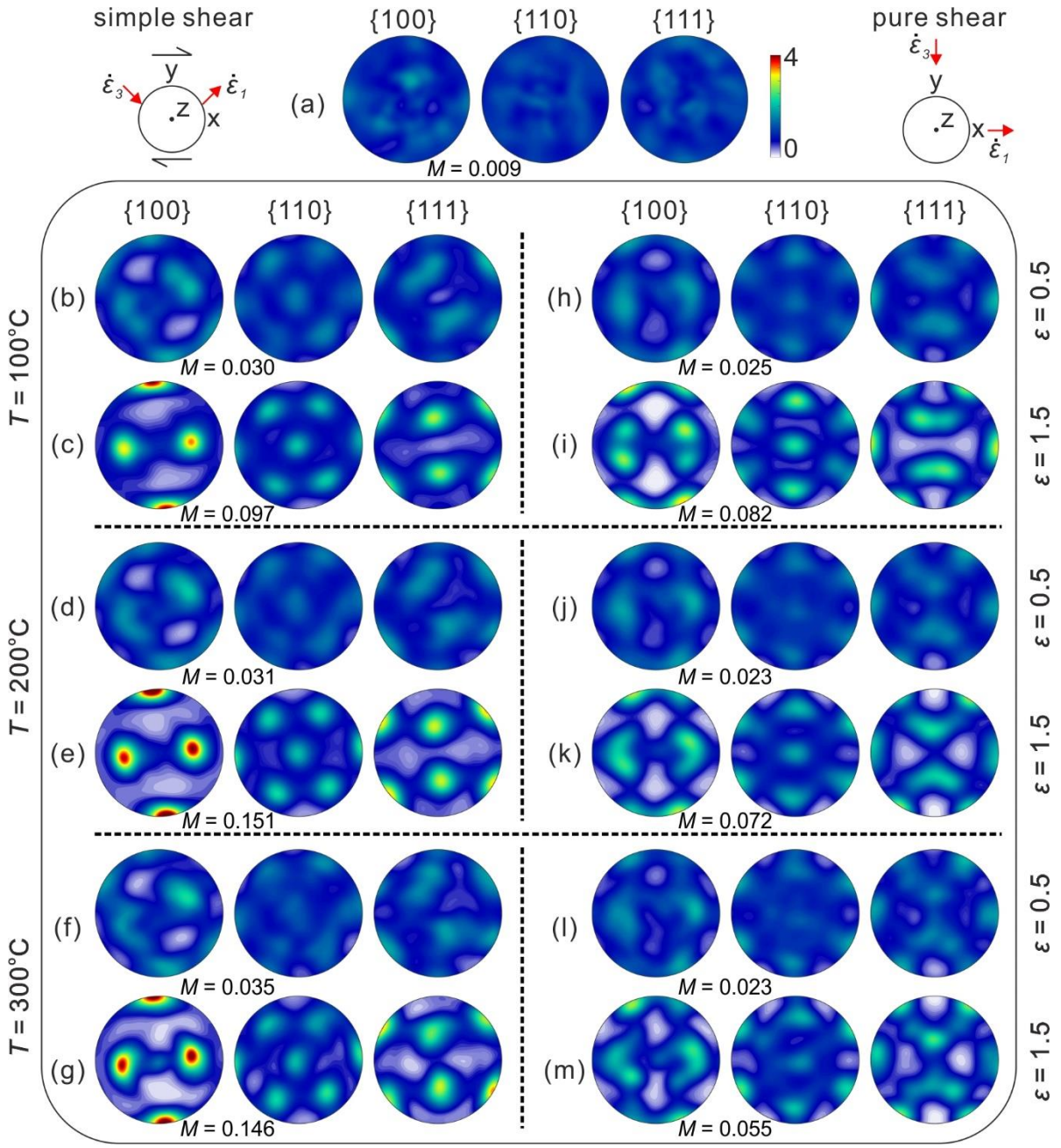

Figure 4.7. Pole figures of crystallographic preferred orientations at natural strain of ε = 0.5 and 1.5, for simulations performed at temperatures of 100°C (b-c-h-i), 200°C (d-e-j-k) and 300°C (f-g-l-m). Left-hand column shows results under simple shear, and right-hand column under pure shear deformation. The initial CPO is shown in (a). The CPO intensity is quantified as the M index (misorientation index) from the ODF (Skemer et al., 2005).

4.3.3 Slip system evolution and distribution

Fig. 4.8 shows the evolution of the activity of the slip systems during deformation for all simulations presented. In all instances, the CRSS is defined as a temperature-dependent

constant (Table 4.1). At 100°C, roughly 50% of the deformation is accommodated by the softest $\{110\} < \bar{1}10 >$ system, 20% by the hardest {100} <011> system, and approximately 30% by the $\{111\} < \bar{1}10 >$system at the onset of deformation. However, at 200°C and 300°C, the $\{111\} < \bar{1}10 >$ slip system becomes less active and accommodates approximately only 14%-19% of strain, remaining almost constant throughout the simulation. The kinematics of deformation clearly influence this behaviour: for pure shear the $\{110\} < \bar{1}10 >$ system activity experiences a slight decrease with increasing strain at all temperatures, while that of the {100} <011> system slightly increases (see dashed lines in Fig. 4.8). However, in simple shear, the equilibrium of activity between the softest $\{110\} < \bar{1}10 >$ and hardest {100} <011> systems is disrupted at moderate strains, with the activity of the hardest system surpassing that of the softest system (Fig. 4.8b, c). Temperature clearly affects this dynamic, with the hardest system surpassing the softest earlier at higher temperatures (ε = 0.6; Fig. 4.8c) than at lower temperatures (ε = 1; Fig. 4.8b).

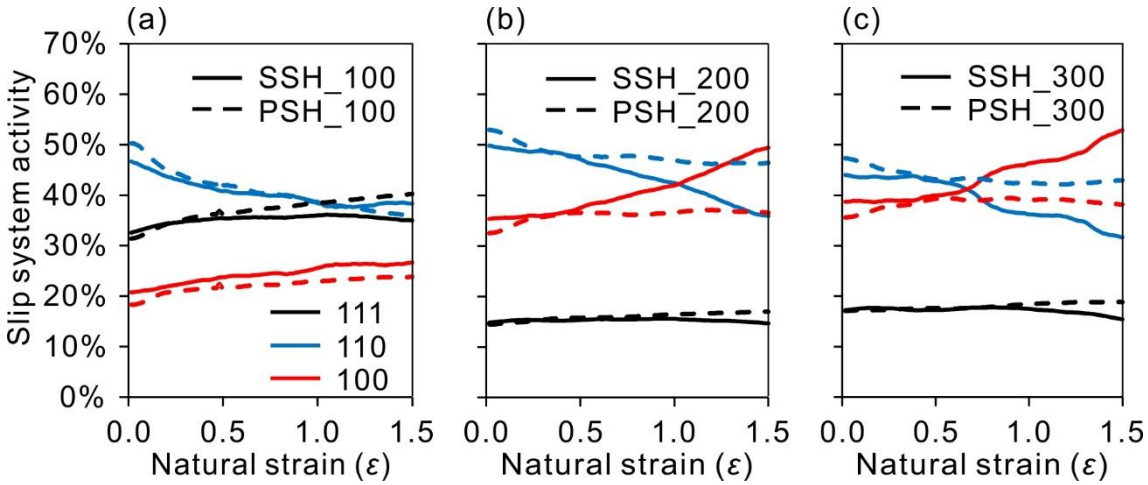

Figure 4.8. Evolution of the average relative slip system activity ($\{110\} < \bar{1}10 >, \{100\} < 011 >$ and $\{111\} < \bar{1}10 >$ with natural strain for simulations at 100°C (a) and 200°C (b) and 300°C (c).

Maps illustrating the distribution of the slip system activity at a natural strain of 1.0 reveal the dominance of the $\{110\} < \bar{1}10 >$ and $\{111\} < \bar{1}10 >$ slip systems, significantly influencing the entire sample at 100°C (green and blue tones in Fig. 4.9a, c) while at 300°C the dominant

slip systems are $\{110\} < \bar{1}10 >$ and {100} <011> (green and red tones in Fig. 4.9b, d). This is consistent with the results shown in Fig. 4.8.

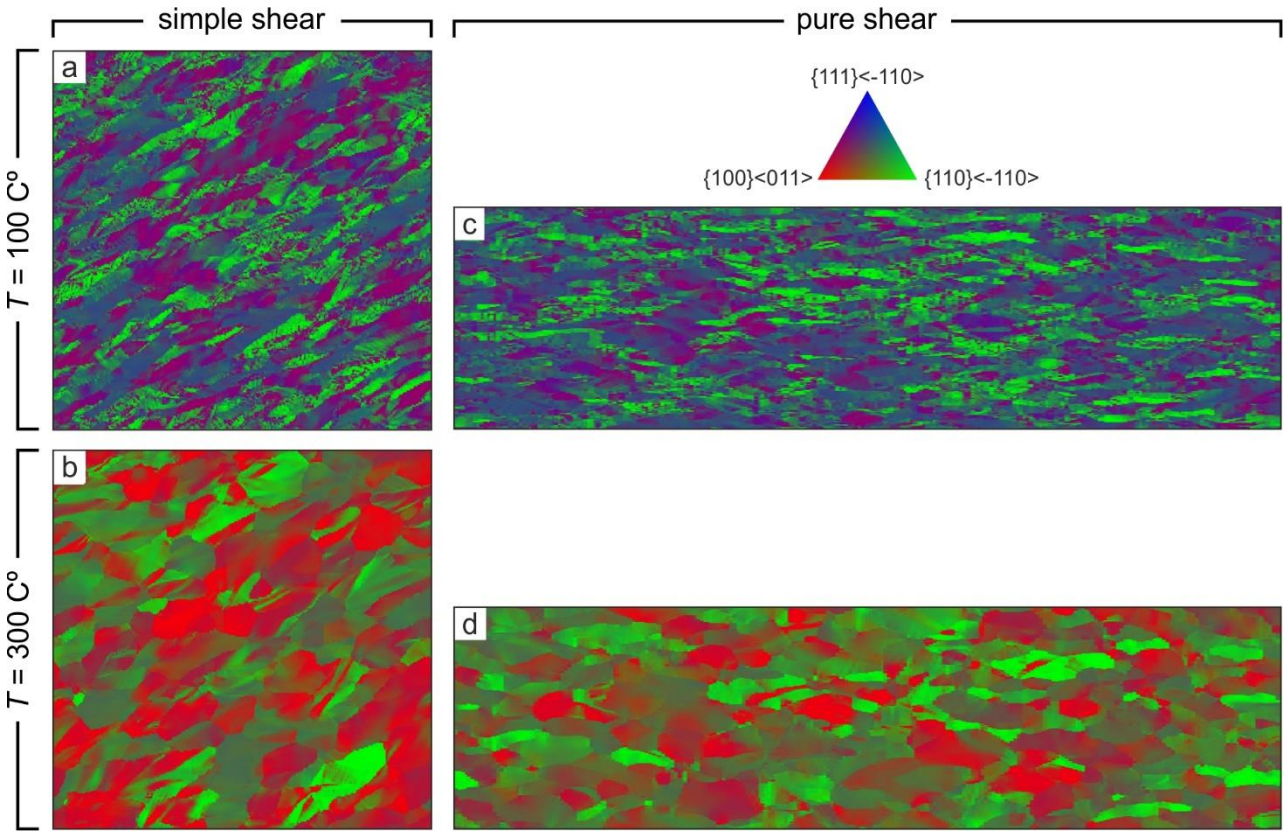

Figure 4.9. Maps of the distribution of slip system activity at a natural strain of ε = 1.0 for simulations performed at temperatures of 100°C (a, c) and 300°C (b, d). Left-hand column shows results under simple shear, and the right-hand column under pure shear deformation. Please note that the size of images corresponding to pure shear simulations (e-g) is displayed as 0.8 times that of the original images.

4.3.4 Strain localization

Regardless the temperature, for simple shear deformation most of the high strain-rate bands are almost parallel to the horizontal shear plane (*x*-axis), while a smaller portion of high strain-rate bands are nearly perpendicular to it (Fig. 4.10a, b). For pure shear deformation, conjugate high strain-rate bands are symmetrically orientated relative to the vertical *y*-axis (Fig. 4.10c, d). As expected, due high temperature GBM reduces the intensity and number of high strain-rate bands in both simple shear and pure shear simulations (Fig. 4.10b, d). At low temperature, the high strain-rate bands can be recognized by the regions rich in small grains. However, GBM

produces large and equidimensional grains, masking the high-strain bands, even reaching a point where they cannot be identified from the microstructure.

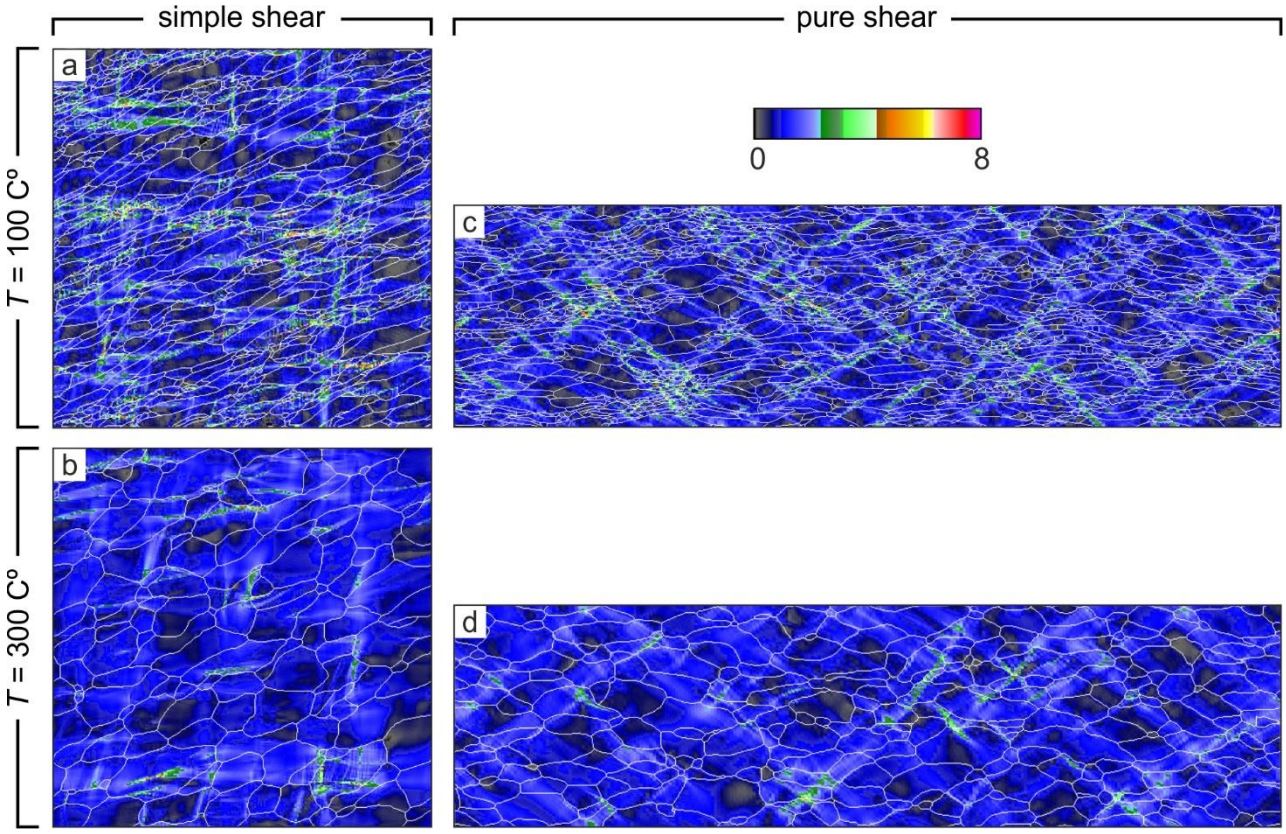

Figure 4.10. Maps of the von Mises strain-rate field at a natural strain of ε = 1.0 for simulations deformed in simple shear (a, b) and pure shear (c, d) at 100°C (a, c) and 300°C (b, d), respectively. Please note that the size of images corresponding to pure shear simulations (c, d) is displayed as 0.8 times that of the original images.

As depicted in Fig. 4.11a, the localization factor (*F*, see section 2.4 for its definition) in simple shear simulations exhibits a quasi-periodic evolution, with a trend remaining relatively stable or mildly intensified. However, the factor of the pure shear simulations displays a steadily decreasing trend with progressive deformation, resulting in more homogeneous deformation. As shown in Fig. 4.11b, the intragranular inhomogeneity can be quantified by the average dislocation density. At the same temperature, simple shear results in a higher dislocation density than pure shear as the strain increases.

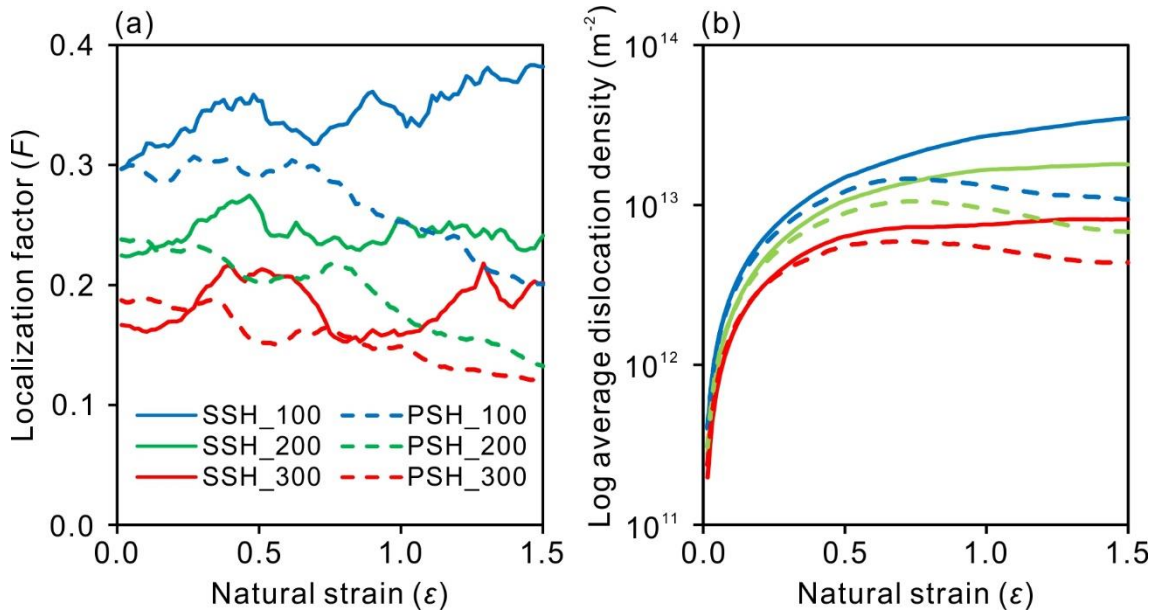

Figure 4.11. Evolution of the localization factor *F* (a) and average dislocation density (b; plotted in logarithmic form, log10) with natural strain for simulations deformed in simple shear (solid lines) and pure shear (dashed lines) at 100°C (blue lines), 200°C (green lines) and 300°C (red lines).

4.4 Discussion

The flow of salt and the resulting development of diverse tectonic structures are a complex phenomenon (Hudec & Jackson, 2007). Shear zones, dominated by non-coaxial deformation, have been observed within salt bodies and along their perimeter (Fossen, 2010; Jackson et al., 2015; Miralles et al., 2000; Talbot & Jackson, 1987). The central portion of a diapir stem is anticipated to experience pure shear deformation (Hudec & Jackson, 2007; Christopher J. Talbot & Pohjola, 2009). Hence, comprehending the distinct behaviour of halite under varying deformation kinematics is crucial.

4.4.1 Effect of deformation kinematics of salt flow on the evolution of microstructures

The simulation results reveal that the boundary kinematics slightly affect the halite grain size evolution (Fig. 4.4), but they significantly influence the SPO (Fig. 4.2a) during viscoplastic deformation, primarily due to strain heterogeneity. Regardless the temperature, simple shear

deformation results in a higher degree of strain localization than pure shear deformation (Fig. 4.11a), leading to higher dislocation density (Fig. 4.11b). Higher dislocation density contributes to the formation of new LAGBs and HAGBs, accelerating SGR thus resulting in grain size reduction (Fig. 4.5). Additionally, it also enhances the driving force for grain boundary migration at high temperature, accelerating GBM and eventually resulting in grain size increase (Fig. 4.5). The evolution pattern of the strain-rate field affects the microstructure. During progressive deformation, simple shear produces small grain bands subparallel to the grain SPO, whereas in pure shear simulations, such bands are conjugate and symmetric oblique to the grain SPO (Fig. 4.1). Simple shear results in highly variable strain-rate bands, creating distinct and dynamic deformation domains. Finch et al. (2020) also observed this phenomenon in their simulations of simple shear deformation of granitoid rocks. Given the high variability of strain-rate bands, in simple shear, a grain may initially elongate, subsequently move and rotate passively with progressive deformation, and then shorten. In contrast, pure shear simulations show a steady evolution of the strain-rate bands, resulting in the continuous deformation of grains. Consequently, pure shear deformation yields a larger average grain aspect ratio compared to simple shear deformation (Fig. 4.2a). The influence of salt deformation patterns on grain size and morphology is key for understanding the kinematics of deformation and estimating finite strain in salt tectonics (e.g., in salt diapirs; Sarkarinejad et al., 2018). For instance, at a natural strain of $\varepsilon = 1.5$ flow pattern differences alone can cause grain aspect ratio variations of up to 20% (Fig. 4.2a). Experiments of high-strain plastic deformation of metals underscore the impact of the kinematics of deformation on the stability of shear band evolution (Cao et al., 2018). Simple shear is characterized by the discontinuous evolution of shear bands and early strain localization, while pure shear involves the continuous evolution of shear bands, resulting in variations in the grain boundary network (Segal, 2002).

4.4.2 Effect of deformation kinematics of salt flow on the evolution of crystallographic preferred orientation (CPO)

One goal of this study is to provide systematic details of the evolution of halite CPOs with a view to deciphering deformation kinematics from the textures. Our study reveals that the CPOs evolve as anticipated under both simple shear and pure shear deformation conditions, and can be directly compared with halite torsion experiments, such as those carried out by Armann (2008) at temperatures of 100°C and 200°C, as well as pure shear experiments (e.g., Kern, 1977; Skrotzki et al., 1995). The CPOs resulting from simple shearing are generally associated with a monoclinic symmetry, whereas the CPOs from pure shear exhibit an orthotropic symmetry (Wenk et al., 1987). In our study, the {100} CPO pattern is similar for both the simple and pure shear cases at low strain (e.g., Fig. 4.12, ε = 0.5). In this scenario, the CPO displays six {100} maxima orthogonally symmetric to the maximum shortening axis ($\dot{\varepsilon}_3$), implying that the deformation kinematics have little impact on the CPO evolution of halite at low strains. As deformation progresses, the {100} CPO intensity under pure shear gradually increases without altering the pattern (Fig. 4.12). Meanwhile, in simple shear cases, the {100} CPO undergoes rotation following the sense of shear (clockwise here). Eventually, it culminates in a {100} maximum subperpendicular to the shear plane and two {100} maxima oblique to the shear direction (Fig. 4.12). The primary reason for this contrast is that once crystal lattices attain a stable orientation, for a specific dominant set of slip systems in alignment with the imposed pure shear deformation, further rotation is prevented. However, simple shear CPOs continuously rotate, leading to a stronger texture compared to pure shear (Fig. 4.12). Wenk et al. (2009) similarly noted the continuous regeneration and rotation of CPOs in simple shear using the viscoplastic self-consistent (VPSC) simulations of halite, even at shear strains as high as 35. Therefore, our study illustrates that the CPOs may serve as a sensitive indicator of the strain path in rock salt. This enables differentiating between simple

and pure shear, determining the sense of shear and identifying the non-coaxial deformation component. The same applies to minerals such as calcite (e.g., Wenk et al., 1987) and quartz (e.g., Morales et al., 2014).

4.4.3 Slip systems

The ELLE-VPFFT method allows calculating the evolution of the average relative slip system activity with natural strain at different temperatures (Fig. 4.8), a parameter not directly quantifiable from rock deformation experiments. The results reveal the contributions of slip systems to strain, and whether these contributions increase or decrease as the CPOs develop. Our study indicates that variations in CRSS due to their temperature dependency result in notable differences in the relative contribution of slip systems to strain at the onset of deformation. Specifically, the $\{111\} < \bar{1}10 >$ slip system accommodates 30% of strain at 100°C, decreasing to less than 20% at 200°C and 300°C. Despite the substantial alteration in slip system activity, its impact on the CPOs evolution remains minor. Previous studies on viscoplastic deformation of halite reported similar CPOs, despite varying CRSS and inconsistent contributions from slip systems at the onset of deformation (e.g., Wenk et al., 2009; Gomez-Rivas et al., 2017). These studies commonly observe a gradual decrease in the contribution of the softest $\{110\} < \bar{1}10 >$ slip system with increasing strain, while the contribution of the harder {100} <011> slip system increases during progressive deformation. In simple shear simulations at higher temperatures, the activity of the {100} <011> slip system increases significantly after moderate strains (Fig. 4.8b & c), enhancing the alignment of {100} lattice orientations (Fig. 4.12). Fig. 4.12 shows that the deformation of yellow grains primarily involves the $\{110\} < \bar{1}10 >$ slip system, showing high strain-rate shear bands with high dislocation densities. Conversely, deformation of orange grains is predominantly governed by the {100} <011> slip system, exhibiting lower dislocation density. With increasing strain, more

intense GBM eliminates high strain-rate bands, attributable to high temperatures and differences in stored strain energy along grain boundaries. This prompts the deformation/growth of grains with unfavourably oriented lattices where the {100} <011> slip system is activated (similarly to ice models of Llorens, et al., 2016a). Pure shear deformation results in lower strain localization and dislocation density (Fig. 4.11), causing the slip systems to change slower compared to simple shear cases (Fig. 4.8).

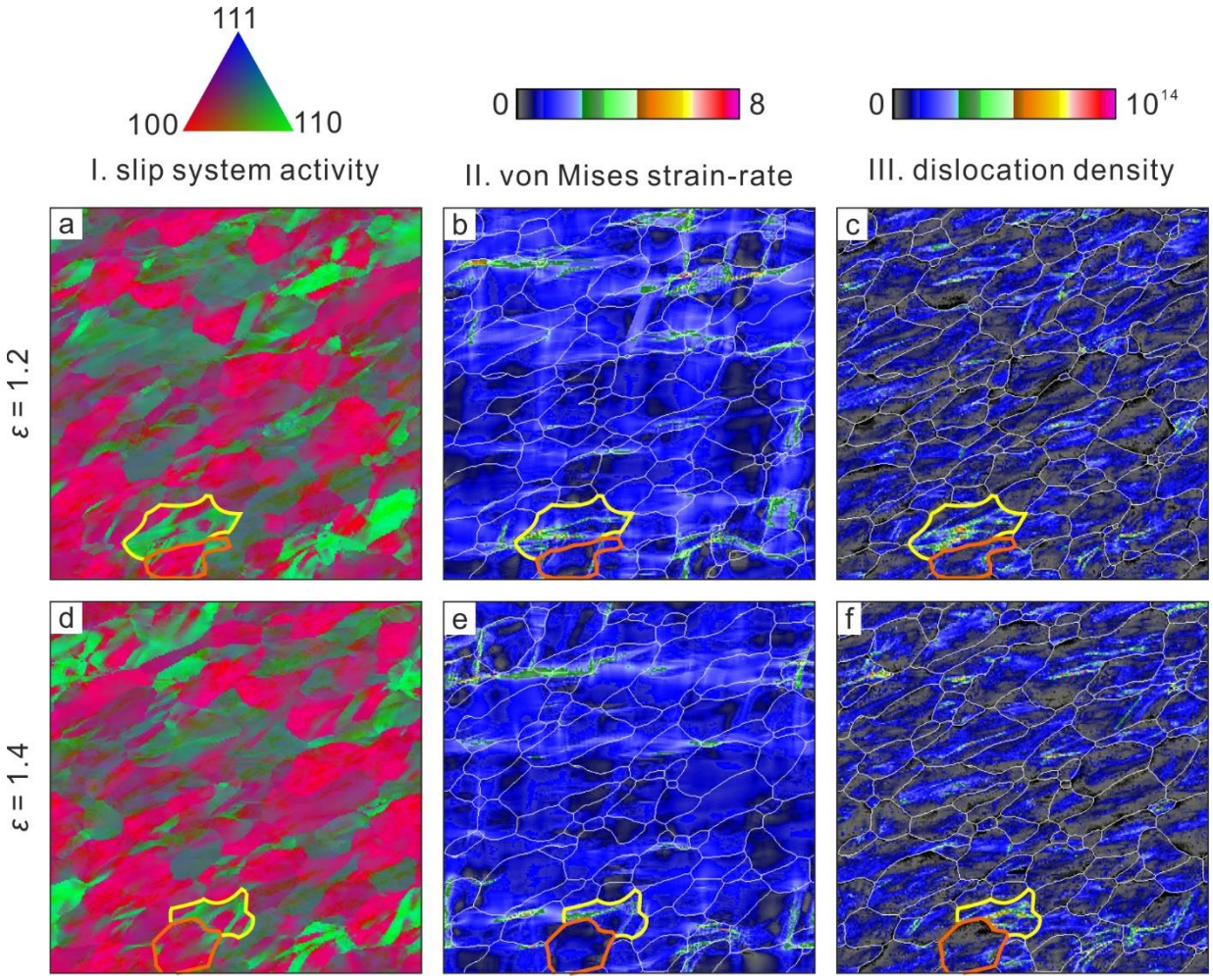

Figure 4.12. Distribution of slip system activity (column I), Maps of the von Mises strain-rate field (column II) and Maps of the dislocation density distribution (column III) at natural strain of ε = 1.2 (a-c) and 1.4 (d-f) for simulations deformed in simple shear at 300°C.

To identify active slip systems, a boundary trace analysis was conducted using crystallographic orientation data (Barrie et al., 2008; Linckens et al., 2016; Prior et al., 2002; Reddy et al., 2007). For the analysis, it is assumed that subgrain boundaries are ideal tilt boundaries, formed by the

accumulation of edge dislocations (Fig. 4.13a). The rotation axis and the pole to the slip plane are within the subgrain boundary plane and are perpendicular to the slip direction (Fig. 4.13a, b). From the crystallographic orientation data, the slip direction and the pole to the slip plane can be derived using the subgrain boundary trace and the rotation axis (misorientation axis). Fig. 4.13c-e shows the boundary trace analysis of several selected grains with distinct subgrain boundaries from Fig. 4.6. In simple shear simulations at the onset of deformation, the initial Schmid factors for the $\{110\} < \bar{1}10 >$, {100} <011> and $\{111\} < \bar{1}10 >$ slip systems in grain A are 0.112, 0.449 and 0.318, respectively, indicating potential activity for all of them. The boundary trace analysis reveals that both the pole to the slip plane and the slip direction align with the <110> axes, suggesting activation of the $\{110\} < \bar{1}10 >$ slip system. Maps of the distribution of slip systems indicate that all three slip systems contribute to grain deformation, particularly $\{110\} < \bar{1}10 >$ and $\{111\} < \bar{1}10 >$ (Fig. 4.6). The slip system analysis of grains B and C deformed in pure shear is similar to that of the grain A. Although the initial Schmid factors suggest substantial stress acting on the {100} <011> and $\{111\} < \bar{1}10 >$ systems for all three grains, boundary trace analyses only confirm activation of the $\{110\} < \bar{1}10 >$ system. Linckens et al. (2016) found divergent results between the two approaches in their experiments of polycrystalline halite deformation. Our simulations confirm that all three slip systems are active in these grains (Fig. 4.6). The von Mises criterion requires five independent slip systems for homogeneous deformation in polycrystals (Mises, 1928). Since only two of the six $\{110\} < \bar{1}10 >$ systems are independent, other systems must be activated to meet this criterion. Despite their lower Schmid factors, the $\{110\} < \bar{1}10 >$ systems activate significantly due to their lower critical resolved shear stress (CRSS; Carter & Heard, 1970). This underscores the importance of considering CRSS when using Schmid factors to predict slip system activity.

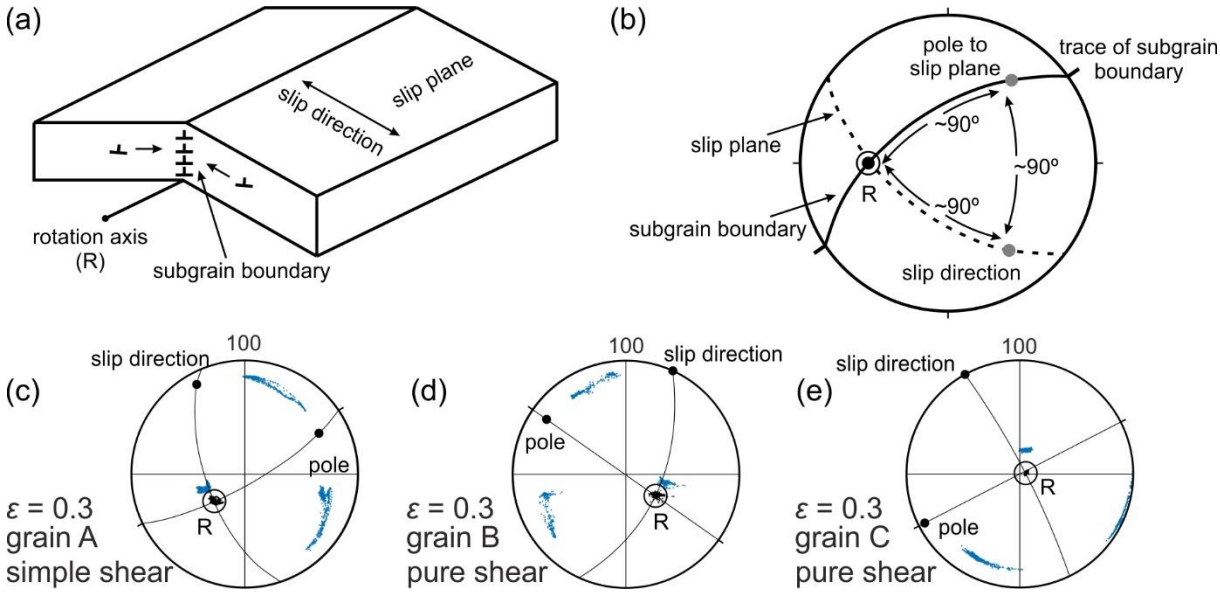

Figure 4.13. (a) Schematic of a subgrain boundary (low-angle tilt boundary) showing the rotation axis (R), slip plane, and slip direction (After Reddy et al. (2007) and Linckens et al. (2016)). (b) Stereographic projection of the subgrain boundary, slip plane, and rotation axis (After Reddy et al. (2007) and Linckens et al. (2016)). At low-angle tilt boundaries, the slip direction, slip plane, and rotation axis are mutually perpendicular. The rotation axis lies within the subgrain boundary plane. Using the subgrain boundary trace and the rotation axis orientation, the orientation of the subgrain boundary plane can be determined. The slip plane orientation can be determined as it is perpendicular to the subgrain boundary plane. The slip direction is in the slip plane and perpendicular to the rotation axis (R). (c-e) Boundary analysis results of the 100 pole figures from Fig. 4.6 to determine active slip systems during deformation. The traces of the subgrain boundaries are indicated on the periphery of the pole figures with thin lines. The subgrain boundary and the rotation axis lies in the same plane. The slip direction and the slip plane pole of grain A deformed in simple shear (c) have the same orientation as two of the <110> axes. The slip direction and slip plane pole of grain A deformed in simple shear (c) almost align with two of the <110> axes, indicating the activated slip system is $\{110\} < \bar{1}10 >$. The same conclusion applies to the 100 pole figures of grain B and grain C deformed in pure shear (d, e).

5 Influence of a second mineral phase on the shearing and recrystallization of halite polycrystalline aggregates

5.1 Summary

This chapter analyses the dynamic evolution of polycrystalline salt rock by means of a series of numerical simple shear simulations on a halite matrix containing a competent second-phase mineral. The primary aim is to examine how the presence of a second phase more competent than halite (representing carbonate of clastic minerals) influences the evolution of the microstructure and crystallographic preferred orientation (CPO). The content of the second phase ranges from 0% to 50% at simulated temperatures of 200°C and 300°C, representing moderate temperature settings. With the increase of the second phase content, the halite matrix exhibits a significantly smaller steady grain size, and its CPO intensity is weaker than that of pure halite aggregates. The pinning effect on grain boundaries by second-phase grains restricts grain boundary migration, obstructing grain growth, while simultaneously causing strain localization that enhances subgrain rotation recrystallization (SGR), leading to a more pronounced reduction in grain size. The content of a second-phase mineral alters the load transfer and strain partitioning within polymineralic aggregates, thereby affecting the intensity of the matrix CPO.

5.2 Model setup

All simulations start with a two-phase polycrystalline aggregate that exhibits a foam texture, and consists of halite and competent second-phase grains (Fig. 5.1 column I). Second-phase grains were placed at triple junctions among halite grains. Five initial microstructures, SP0, SP5, SP20, SP30, and SP50, corresponding to 0%, 5%, 20%, 30%, and 50% second-phase area fractions, respectively, were used. A "model mineral" with hexagonal symmetry was chosen to simulate the mechanical properties of the competent second phase (e.g., similar than in Finch et al., 2020 or Griera et al., 2011). The CRSS ratio between all slip systems of second phase was set to ten times stronger than the $\{110\} < \bar{1}10 >$ slip system of halite (Table 5.1). The stress exponents for slip systems were set at $n_H = 7$ for halite and $n_S = 5$ for the second phase (Table 5.1). All polymineralic aggregates were based on the same 6 × 6 cm² foam texture consisting of 1,020 grains (Fig. 5.1), where both halite and second-phase grains in all simulations originally had nearly identical initial sizes (Fig. 5.1; Table 5.2). All grains were assigned random initial Euler angles to define their crystallographic orientations, representing a bulk isotropic polycrystalline aggregate.

Dextral simple shear was applied to the initial polycrystalline aggregates at temperatures of 200°C and 300°C, with a shear increment $\Delta\gamma = 0.03$ per time step in the dynamic recrystallization (DRX) simulations. A constant time step of $\Delta t = 100$ s was used, yielding a shear strain rate of 3×10^{-4} s^{-1}. To examine the influence of second-phase minerals on grain growth in conditions without deformation, we also carried out static grain growth (SGG) simulations on the initial polycrystalline aggregates. In these simulations, only the boundary energy, controlled by the surface energy and boundary length, was used as the driving force to calculate the grain boundary displacement. All models progressed through 100 time steps,

equating to a finite shear strain of three at the end of the simulation time for DRX models and a total duration of 10,000 s in SGG simulations. Input parameters are detailed in Table 5.1.

Table 5.1. Input properties of numerical simulations.

Symbol	Explanation	Input value
L	Unit length	6 cm
Δt	Time step per simulation step	100 s
$\Delta\gamma$	Incremental shear strain per simulation step	0.03
n_H	Stress exponent of halite (Carter & Heard, 1970)	7
n_S	Stress exponent of second phase (e.g., calcite; Evans et al., 2001; Renner et al., 2002)	5
$\tau_{\{110\}}$-$\tau_{\{100\}}$-$\tau_{\{111\}}$	Critical resolved shear stress of $\{110\}<\bar{1}10>$, $\{100\}<011>$ and $\{111\}<\bar{1}10>$ slip systems of halite (Carter & Heard, 1970)	1-3-2
$\tau_S/\tau_{\{110\}}$	The CRSS ratio between all slip systems of second phase and $\{110\}<\bar{1}10>$ slip system of halite at 200℃ and 300℃ (De Bresser & Spiers, 1997)	10
$M_{0(HH)}$	Intrinsic mobility of halite–halite boundaries (Piazolo et al., 2006)	1.5×10^{-7} m^4 J^{-1} s^{-1}
$M_{0(SS)}$	Intrinsic mobility of second phase–second phase boundaries	3.0×10^{-8} m^4 J^{-1} s^{-1}
$M_{0(HS)}$	Intrinsic mobility of halite–second phase boundaries	3.0×10^{-9} m^4 J^{-1} s^{-1}
J_{HH}	Halite–halite interface boundary energy (Piazolo et al., 2006)	0.36 J m^{-2}
J_{HS}	Halite–second phase interface boundary energy	0.36 J m^{-2}
Q	Grain boundary migration activation energy (Piazolo et al., 2006)	4.7×10^4 J mol^{-1}
c	Compressibility factor (Steinbach et al., 2016)	0.1
α_{hagb}	Critical minimum misorientation for high-angle boundaries (Pennock et al., 2005)	10°
Velocity gradient tensor	Static grain growth (SGG simulations)	$\begin{bmatrix}0 & 0 & 0\\ 0 & 0 & 0\\ 0 & 0 & 0\end{bmatrix}$
	Dextral simple shear (DRX simulations)	$\begin{bmatrix}0 & 0.03 & 0\\ 0 & 0 & 0\\ 0 & 0 & 0\end{bmatrix}$

Table 5.2. Numerical simulation setup. Simulation names include a prefix denoting the temperature.

Simulation name	Area fraction of second phase (%)	Temperature (℃)	Initial grain size of halite/second phase (μm)	DRX: final grain size of halite/second phase (μm)	SGG: final grain size of halite/second phase (μm)	Final M index of halite CPO
200_SP0	0	200	212/	145/	222/	0.0754
200_SP5	5	200	212/212	145/209	221/212	0.0636
200_SP20	20	200	212/214	127/210	218/215	0.0392
200_SP30	30	200	215/205	125/193	219/206	0.0306
200_SP50	50	200	211/213	110/182	214/214	0.0309
300_SP0	0	300	212/	280/	285/	0.0698
300_SP5	5	300	212/212	254/210	279/212	0.0530
300_SP20	20	300	212/214	192/212	251/216	0.0434
300_SP30	30	300	215/205	164/200	240/207	0.0269
300_SP50	50	300	211/213	133/191	219/217	0.0507

5.3 Results

5.3.1 Microstructure characteristics

The SP0 experiment corresponds to a simulation of a pure halite polycrystalline aggregate. At 200°C, synthetic shear bands aligning subparallel to the shear direction are visible in the pure halite simulations, characterized by strongly elongated grains and clusters of small grains (Fig. 5.1(a)(iii)). At 300°C, GBM reduces grain elongation, resulting in larger and more equidimensional halite grains (Figs. 5.1(a)(v) & 5.2). Consequently, synthetic shear bands are not easily recognizable from the microstructure (Fig. 5.1(a)(v)).

In experiments SP5, SP20, SP30 and SP50, despite the presence of a second phase, halite grains get elongated subparallel to the shear direction, and a SPO is clearly seen at high strain (Figs. 5.1 & 5.2). At 200°C and a shear strain of 3, the aspect ratio of halite grains decreases from 2.8 to 2.2 as second phase content increases from 5% to 30%. It then rises from 2.2 to 2.8 as second phase content increases from 30% to 50% (Fig. 5.2(a)). At 300°C, the final aspect ratios of

halite grains are similar (Fig. 5.2(c)). In models with less than 50% second phase content, the second-phase grains show only slight elongation with increasing shear strain (Figs. 5.1 & 5.2). The angle between the major axis of the second-phase SPO and the shear direction is smaller than that of the halite SPO and the shear direction, suggesting that the second-phase grains rotate relative to the halite matrix. When the second-phase content increases to 50%, the grains elongate significantly with progressive deformation, with the major axis of their SPO becoming subparallel to the shear direction (Figs. 5.1 & 5.2). In the two-phase models, three distinct microstructures emerge as the content of the second phase increases: (1) second-phase minerals and surrounding distorted halite grains forming δ-porphyroclast systems (Fig. 5.1(c)(iii) & (c)(iii), in yellow frame); (2) antithetic ductile shear bands resulting from the rotation of adjacent competent second-phase minerals (Fig. 5.1(d)(ii) & (d)(iii), in white frame); (3) layer banding structure with alternating halite and second phase. These structures are not clearly visible at 300°C due to the effect of GBM.

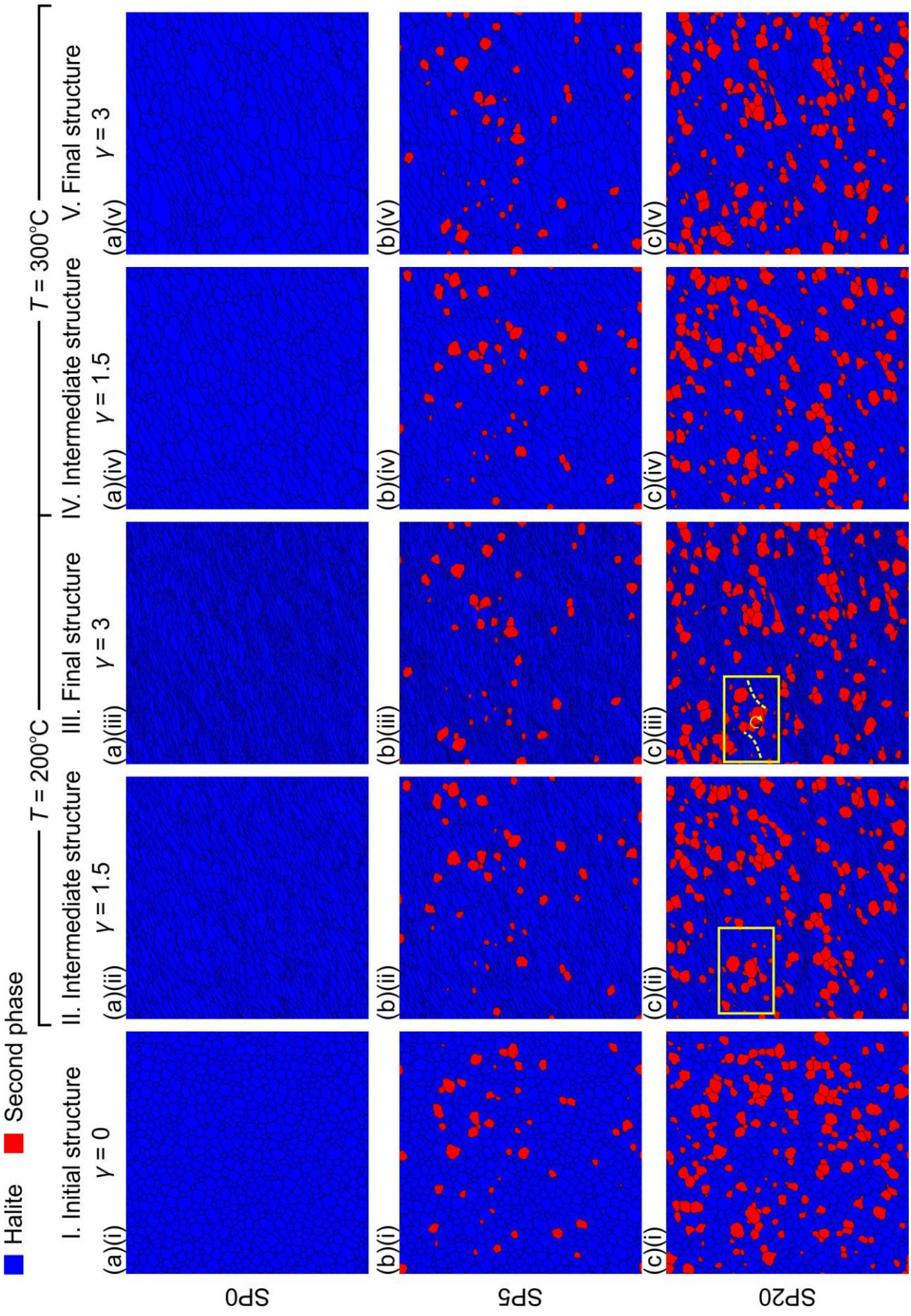
Halite
Second phase
T = 200°C
T = 300°C
I. Initial structure
γ = 0
II. Intermediate structure
γ = 1.5
III. Final structure
γ = 3
IV. Intermediate structure
γ = 1.5
V. Final structure
γ = 3
(a)(i)
(b)(i)
(c)(i)
(a)(ii)
(b)(ii)
(c)(ii)
(a)(iii)
(b)(iii)
(c)(iii)
(a)(iv)
(b)(iv)
(c)(iv)
(a)(v)
(b)(v)
(c)(v)
C
SP0
SP5
SP20

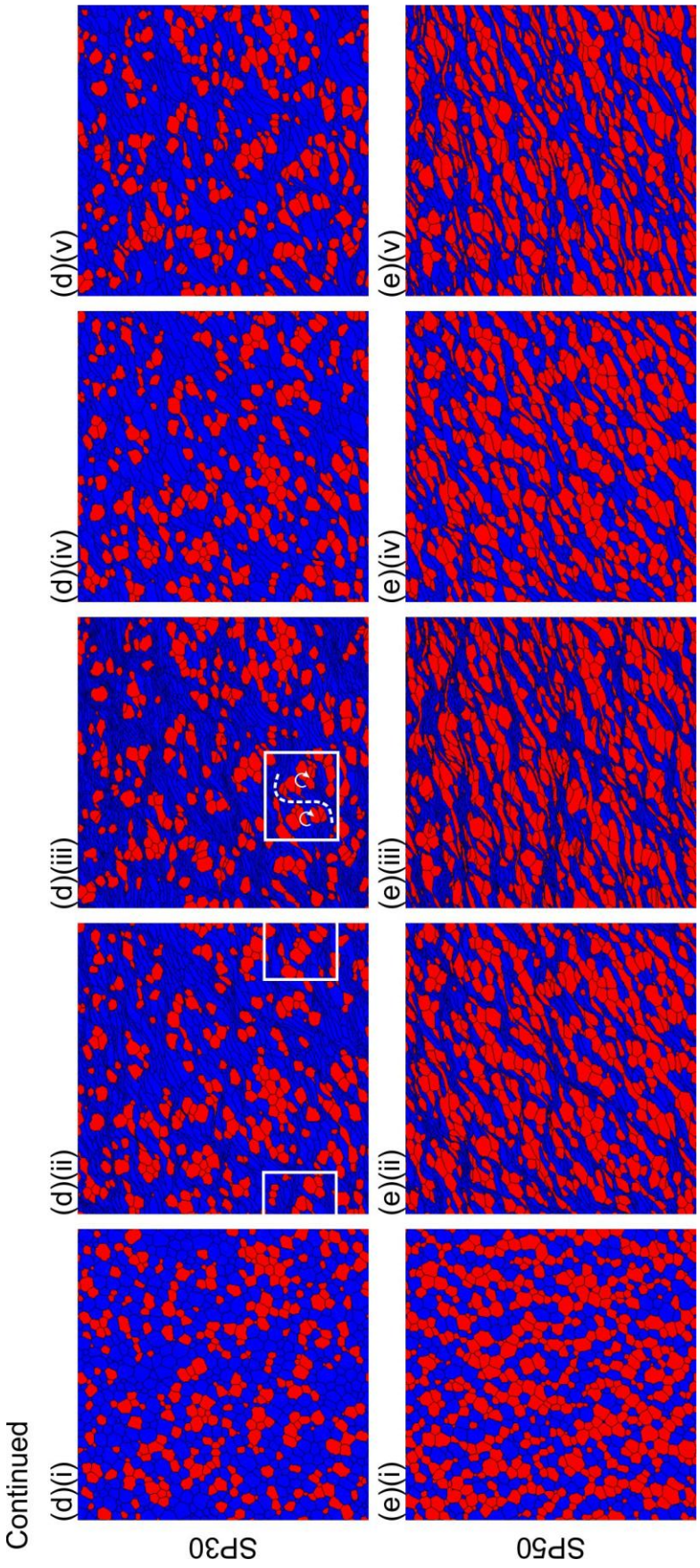

Figure 5.1. Microstructure maps under dextral simple shear. Column (I) shows the microstructure at shear strains of $\gamma = 0$; columns (II) & (IV) at $\gamma = 1.5$; columns (III) & (V) at $\gamma = 3$. Each row represents simulations with different second phase fractions: (a) 0%, (b) 5%, (c) 20%, (d) 30%, (e) 50%. Maps color halite grains blue and second-phase grains red, with boundaries in black. The simulations use a square model with side length of $L = 6$ cm.

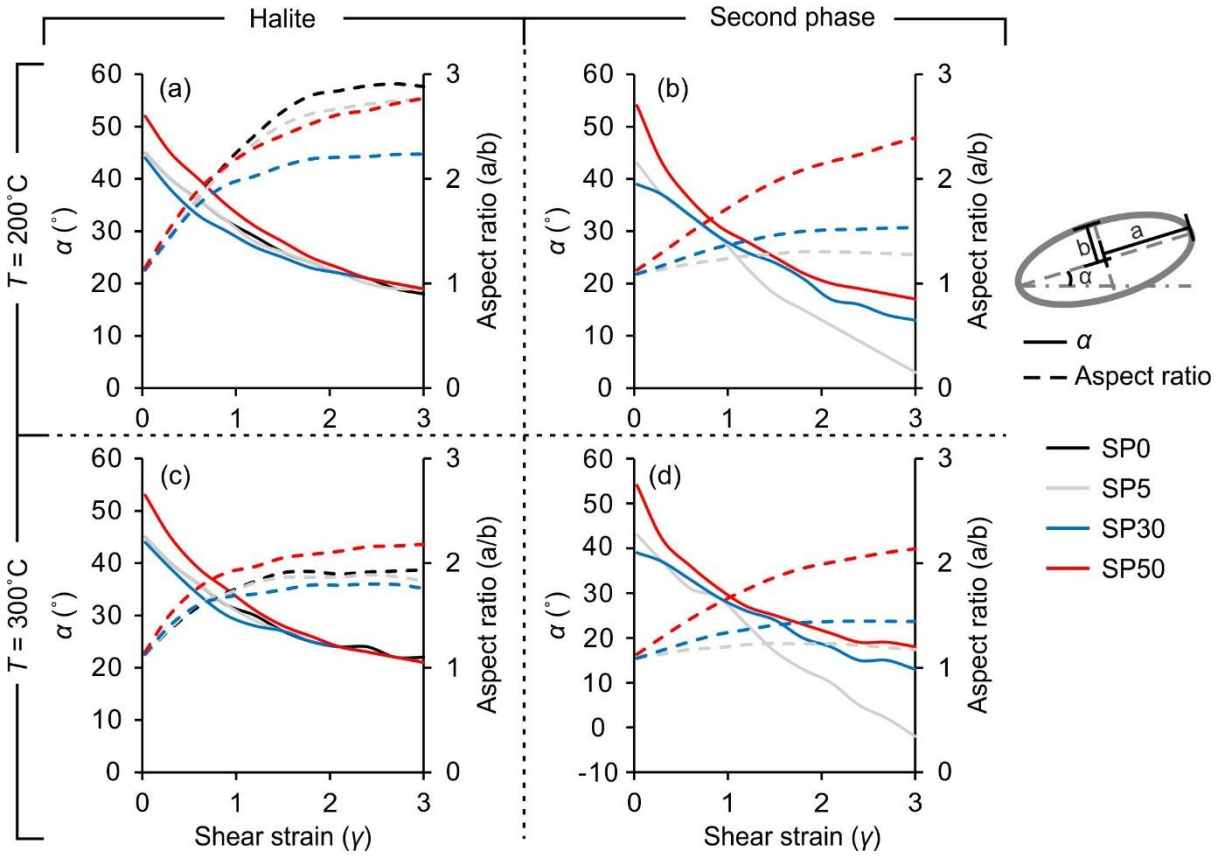

Figure 5.2. Evolution with shear strain of the average SPO angle (α) and aspect ratio (a/b) for halite (a, c) and the second phase (b, d) at 200°C and 300°C. Solid lines indicate the angle (α) between the major axis and the shear direction, while dashed lines indicate the aspect ratio (a/b). The black, grey, blue and red lines correspond to SP0, SP5, SP30 and SP50 simulations, respectively. The theoretical aspect ratio for a passive marker is 11 at shear strain of 3.

5.3.2 Grain size

The final grain size distribution of halite for static grain growth and DRX simulations is shown in Fig. 5.3, and average grain sizes are summarized in Table 5.2. To illustrate the effects of GBM during DRX, grain size distribution graphs are compared with observed trends from static grain growth (SGG) simulations. All SGG simulations show a normal distribution with an increase in the average grain size compared to the initial one, particularly for the 300°C case (Fig. 5.3 & Table 5.2). As the content of the second phase increases, the growth rate of halite grain size decreases (Table 5.2). Compared to SGG simulations, DRX simulations yield a grain size distribution skewed towards smaller grains (Fig. 5.3). The proportion of small grains in

the halite matrix significantly increases with higher contents of second-phase minerals (Fig. 5.3).

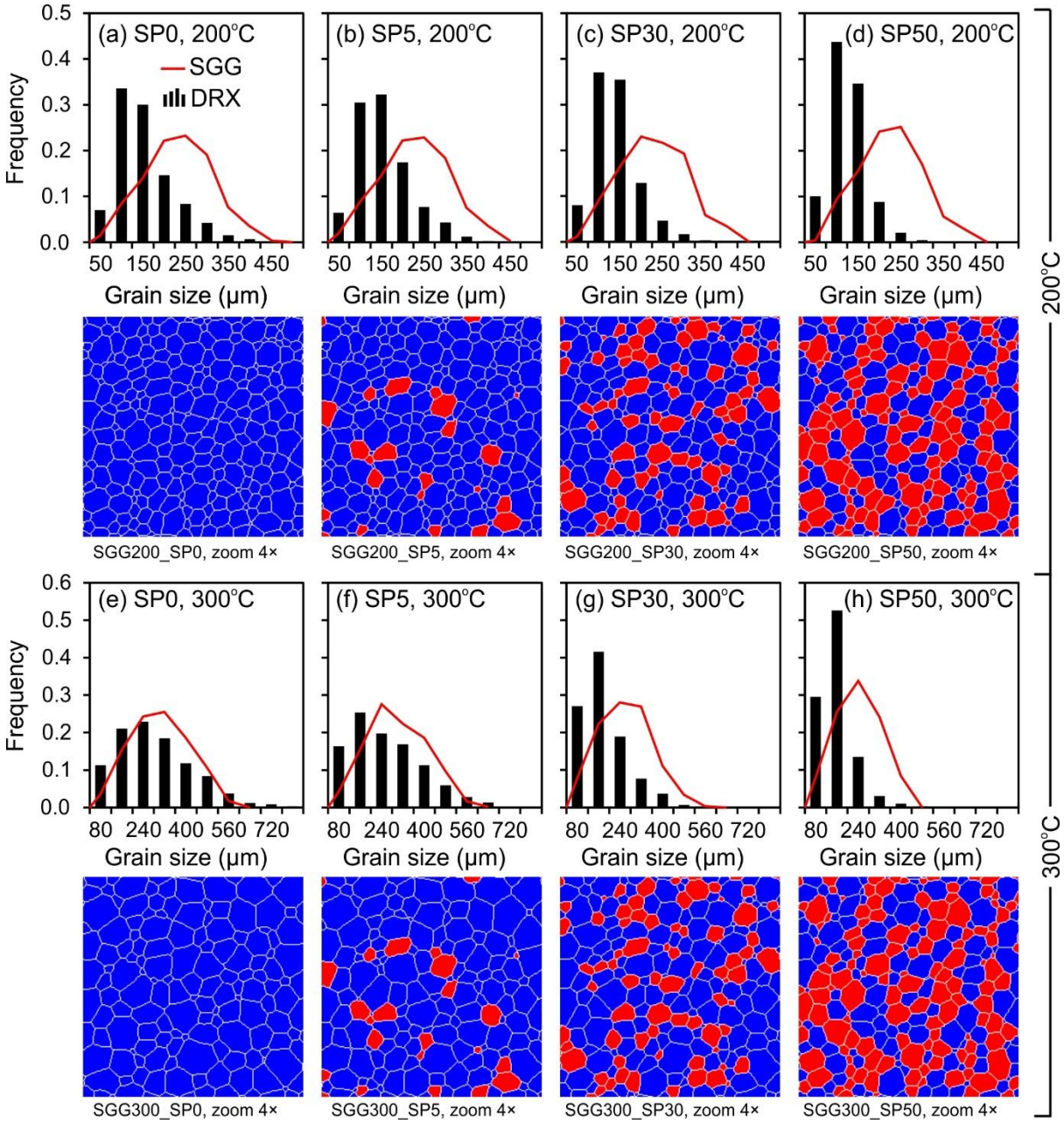

Figure 5.3. Comparison of halite grain size distribution at 200°C (a-d) and 300°C (e-h) at the final simulation step, with different second phase fractions (SP0 0%, SP5 5%, SP30 30% and SP50 50%). The results from SGG simulations at the equivalent time of t = 10,000s are compared with those from DRX simulations at a shear strain of γ = 3. Note that, for reference, microstructures from only the SGG simulations displayed beneath the histograms. They are magnified to allow easier visualization.

5.3.3 Strain rate, finite strain and stress fields

The spatial distribution of the instantaneous deformation in the halite matrix is illustrated through strain-rate maps (Fig. 5.4). To quantify the heterogeneity of deformation the localization factor (*F*) was used (see section 2.4 for definition). High strain-rate bands are heterogeneously distributed in the halite matrix. However, with increasing second-phase mineral content, the strain rate within the model shows higher values and a more localised distribution (Fig. 5.4). During progressive deformation, all simulations show *F* values larger than 0.2, indicating strain localization in all cases. Strain localization within the halite matrix intensifies as the second-phase mineral content increases. The localization factor for simulations with 50% second-phase minerals ($F \approx$ 0.42-0.56) is approximately 1.8 times higher than that in pure halite simulations ($F \approx$ 0.24-0.32).

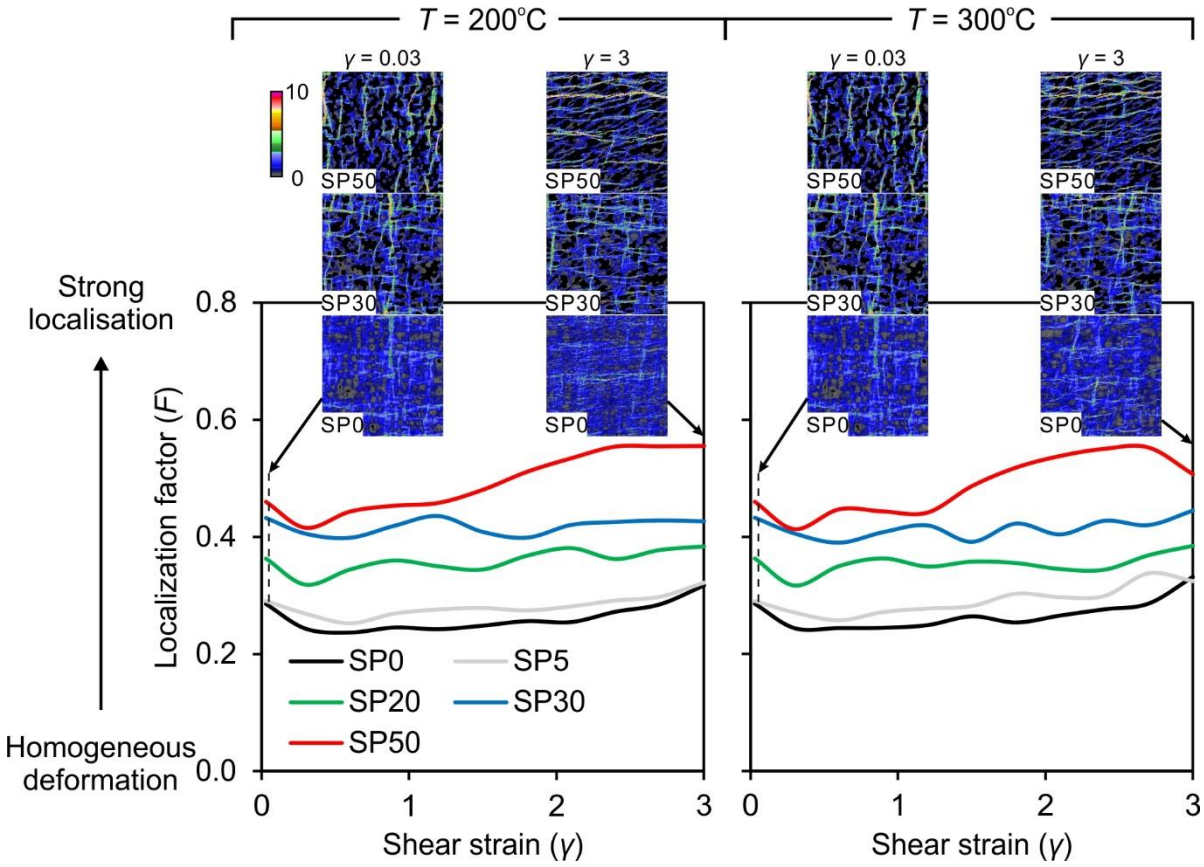

Figure 5.4. Evolution of the localization factor (*F*) in halite matrix at 200°C and 300°C. The normalized von Mises strain-rate maps at a shear strain of γ = 0.03 and 3 are shown for reference. The maps are

subdivided to show the results of simulation SP50 in the upper third, SP30 in the middle and SP0 in the lower third part of the model box. They illustrate strain rate localization at different stages of the simulation.

In order to investigate the effect of the second phase on the microstructure, the contribution of rotation and flattening, as well as the stress and strain distribution. Fig. 5.5 shows maps of the finite kinematic vorticity number (W_k, see section 2.4 for definition), normalized equivalent stress, and finite strain at a finite shear strain of $\gamma = 3$ for simulations deformed at 200°C. In pure halite simulations, the finite strain distribution is largely oblique and highly heterogeneous (Fig. 5.5(a)(iv)). In the two-phase simulations, finite strain is primarily concentrated in the halite matrix surrounding the second phase, forming a bridge-like structure (Fig. 5.5(b)(iv) & (c)(iv)). The remaining halite surrounding the second phase exhibits lower finite strain (Fig. 5.5(b)(iv)) and larger grain sizes (Fig. 5.5(b)(i)). The calculated high W_k values suggest that most of the second phase undergoes rigid rotation in the SP30 simulations, consistent with the low α and aspect ratio values of the second-phase SPO (Fig. 5.2(b)). From SP30 to SP50 simulations, as the second-phase content increases, the flattening effect intensifies and the contribution from rigid rotation decreases, showing the smaller regions with high W_k values (Fig. 5.5(c)(ii)). Regarding equivalent stresses, the second phase experiences higher stresses than the halite matrix. As the second-phase content increases, equivalent stresses rise in both phases, but particularly in the competent one (Fig. 5.5 row III).

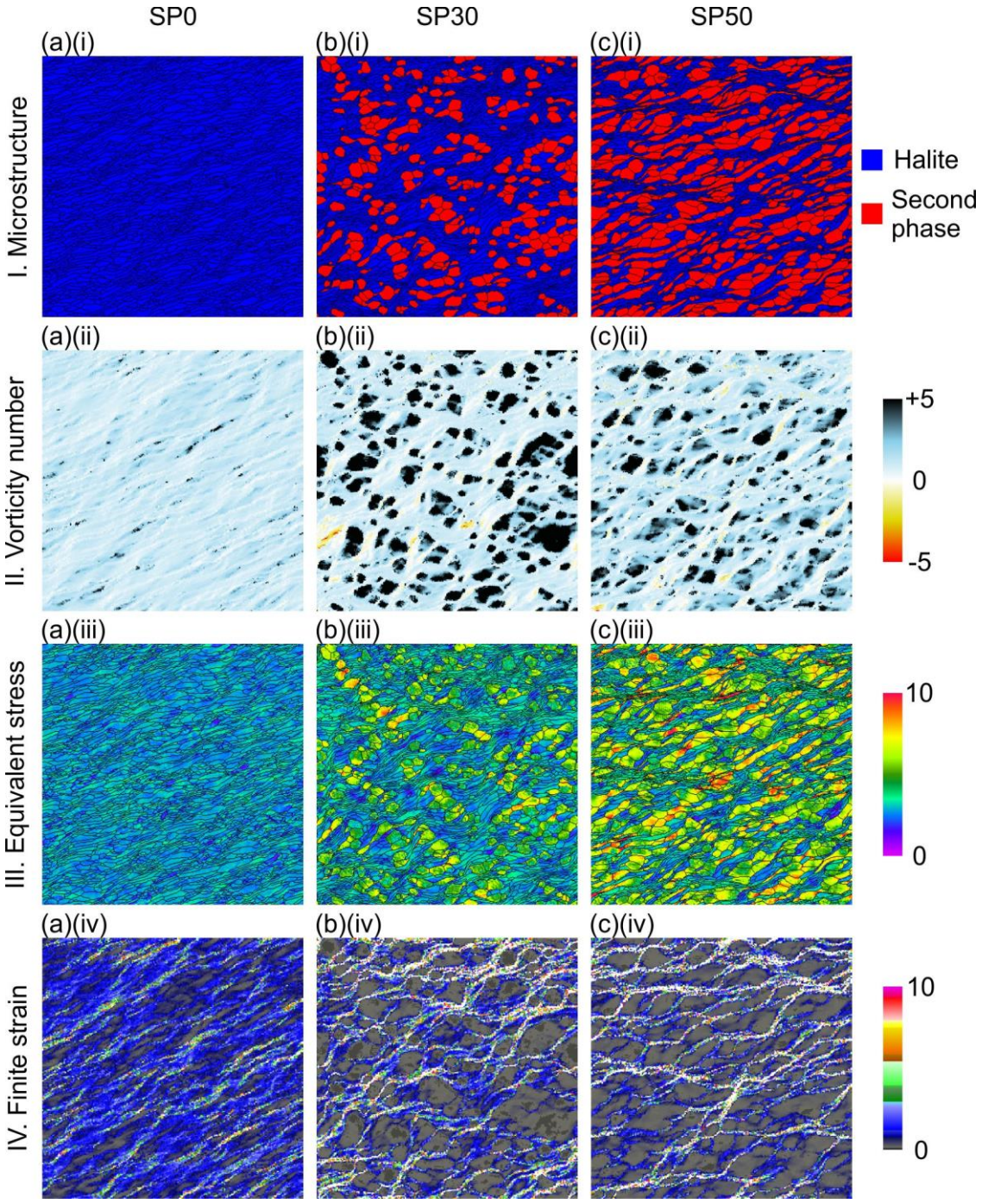

Figure 5.5. Microstructure maps (row I), finite kinematic vorticity number (row II), normalized equivalent stress (row III) and finite strain (row IV) at a shear strain of γ = 3 at 200°C. Each column represents simulations with different content of second phase: (a) 0%, (b) 30%, (c) 50%. The simulations use a square model with side length of L = 6 cm.

5.3.4 Crystallographic preferred orientation (CPO)

CPOs for halite crystals in simulations with DRX are shown in Fig. 5.6. The CPO intensity is quantified using the *M* index, a misorientation index derived from the orientation distribution

function (ODF; Skemer et al., 2005). The *M* index varies from zero, which indicates a random distribution of misorientation angles, to one, which represents a single crystal. The final CPO patterns are similar across all simulations but vary in intensity, as shown in columns II and III of Fig. 5.6. At the final shear strain of $\gamma = 3$, the CPO shows a {100} maximum nearly parallel to the *y*-axis and two maxima in the *XZ* plane about 45° to the *x*-axis (Fig. 5.6). Both the {110} and {111} pole figures exhibit mild hexagonal symmetry (Fig. 5.6). The *M* index reveals that pure halite has the highest CPO intensity, which diminishes when second-phase minerals are present (Fig. 5.6). Halite CPO intensity decreases steadily as second-phase grain content rises from 0% to 30%, then slightly increases as the content goes from 30% to 50% (Fig. 5.6).

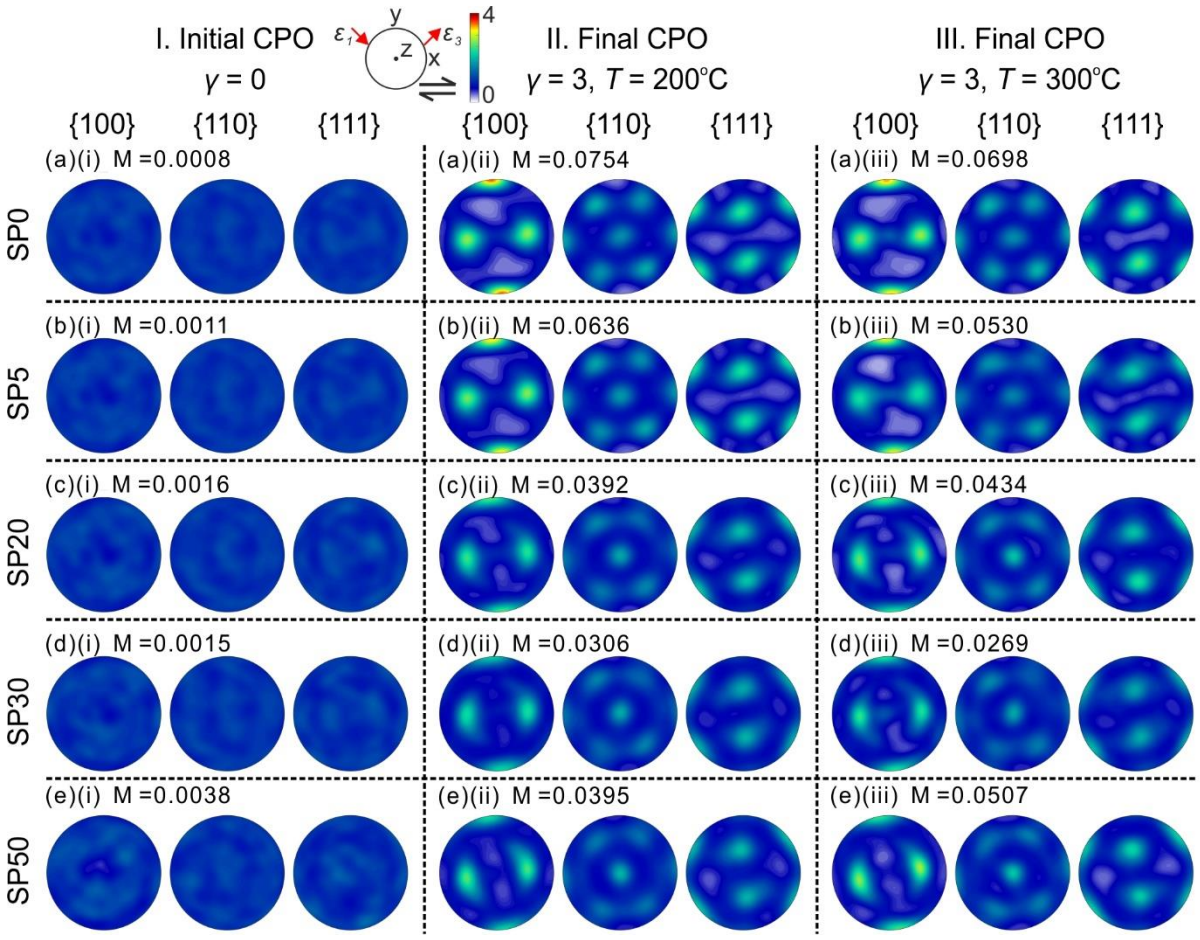

Figure 5.6. Crystallographic preferred orientation of halite grains under simple shear. Column (I) shows CPO at a shear strain of $\gamma = 0$; column (II) at $\gamma = 3$ and 200°C; column (iii) at $\gamma = 3$ and 300°C. Each row represents pole figures with varying second phase fractions: (a) 0%, (b) 5%, (c) 20%, (d) 30%, (e)

50%. CPO intensity is quantified as the *M* index (misorientation index) derived from the ODF (Philip Skemer et al., 2005).

5.4 Discussion

5.4.1 Microstructure development and strain localization

Simulations show significant strain localization in both pure (single-phase) and polymineralic (two-phase) halite aggregates. The strain rate remains heterogeneously distributed within the simulation (Fig. 5.4). This is consistent with numerous studies (Cyprych et al., 2016; Finch et al., 2020; Ran et al., 2018; Steinbach et al., 2016; Llorens et al., 2019). In pure halite (SP0 simulations), the isotropic starting polycrystalline aggregate evolves showing a highly heterogeneous strain rate and finite strain distribution (Figs. 5.4 & 5.5). This is due to Single-crystal anisotropy is transferred to the polycrystalline scale (de Riese et al., 2019b). The presence of competent second-phase minerals results in distinct regions of strain localization in the halite matrix. Such regions, characterized by a strain rate higher than the bulk one, typically form at bridges between second-phase grains (Fig. 5.4). As the content of the second phase increases, the spacing between these grains decreases, which enhances the intensity and heterogeneity of high strain-rate bands in the matrix (Fig. 5.4). The stress and strain partitioning in polymineralic rocks depend on the relative mineral content, viscous strength contrast and phase distribution (Handy, 1990, 1994; Takeda & Griera, 2006). As shown in Fig. 5.5, higher competent phase content leads to increased equivalent stresses in both halite and the second phase, particularly in the second phase. Moreover, with the second phase content increase, it becomes a weak rotation but strong flattening (Fig. 5.5 row II), suggesting a transition from a weak phase supported type to a strong phase supported type of the two-phase system (Takeda & Griera, 2006).

5.4.2 Effect of the second phase on grain size evolution

Static grain growth (SGG), driven by a reduction in grain boundary energy, typically results in a foam texture with straight grain boundaries (Bestmann et al., 2005; Weaire & Rivier, 1984). At 200°C, the GBM process minimally affects the microstructure, showing only a slight increase in grain size across all simulations (Fig. 5.3 & Table 5.2). At 300°C, SGG simulations reveal a notable increase in grain size due to the rapid rise of the GBM rate with temperature (Fig. 5.3 & Table 5.2), due to the exponential increase of the effective mobility. With the increase of the second-phase content, spacing between these grains decreases, slowing the growth of halite grains (Fig. 5.3 & Table 5.2).

Compared to SGG simulations, DRX simulations show a trend towards smaller halite grain size distributions (Fig. 5.3). This reflects the microstructural heterogeneity induced by DRX and strain localization (quantified by the localization factor, Fig. 5.4), especially from grain refinement by SGR. At 200°C, DRX simulations consistently show a reduction in halite grain size dominated by SGR, with the rate of grain-size reduction intensifying as second-phase content increases (Fig. 5.7), and more heterogeneous deformation occurs in the halite matrix (Fig. 5.5) leading to higher dislocation density. Dislocation migration and their rearrangement transform some low-angle grain boundaries (LAGBs) into high-angle ones (HAGBs), forming new grains thus reducing grain size. With increasing temperature, SP0 simulations reveal a transition of the halite matrix from an SGR-dominated grain size reduction regime (at 200°C) to a GBM-dominated grain growth regime (300°C) (Fig. 5.7). This transition, influenced primarily by temperature, is evident in both laboratory and simulated experiments of pure halite (Armann, 2008; Hao et al., 2023) and in natural microstructures of other minerals like quartz (Stipp et al., 2002). As the second phase content increases, two-phase simulations highlight a transition in the halite matrix from a GBM-dominated grain growth regime to a SGR-dominated grain size reduction regime (Fig. 5.7). The second phase content significantly

influences the balance between grain size reduction and growth. The content of a competent second mineral phase impacts the grain size evolution by: (1) pinning of matrix grain boundaries, which hinders grain coarsening (Fig. 5.3 and Table 5.2), and (2) causing more heterogeneous deformation, enhancing SGR and facilitating grain refinement (Fig. 5.4).

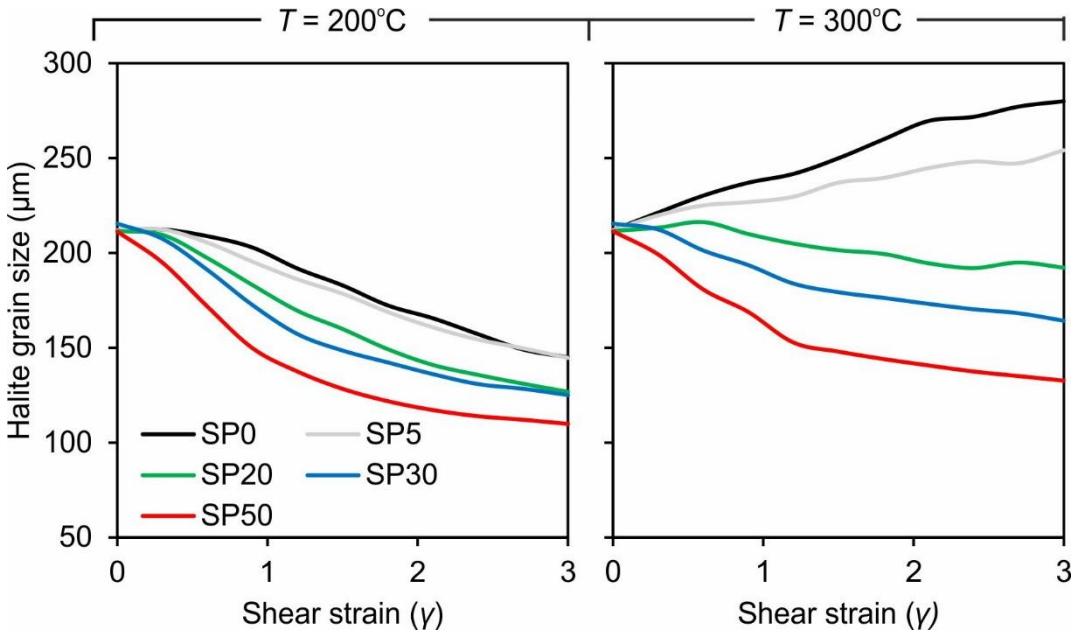

Figure 5.7. Evolution of the average grain size with shear strain at 200°C and 300°C. The lines with different color represent simulations with different second phase fractions in 0% (black), 5% (grey), 20% (green), 30% (blue) and 50% (red).

Our second-phase simulations display a microstructure qualitatively akin to natural two-phase rocks, such as the calcite-dolomite system (Fig. 5.8; Caldera, 2022). For example, in natural calcite-rich rocks subjected to moderate temperature shearing, calcite grain size often varies with the concentration of a second-phase mineral such as dolomite. Our results show similar trends, with halite grain size increasing from SP50 (high second-phase content) to SP0 (no second phase), reflecting patterns seen in natural settings. Závada et al. (2015) studied how solid second-phase minerals affect the microstructure and deformation mechanisms in rock salt diapirs. While our simulations, both with low and high second-phase contents, show microstructures that are qualitatively similar to what Závada et al. (2015) categorize as “clean” and “dirty” rock salts, a direct comparison of halite grain sizes was not feasible. For natural

conditions, various deformation mechanisms are activated in natural rock salt, including dislocation creep, pressure-dissolution creep, grain boundary sliding, or transgranular microcracking, among others. These mechanisms significantly influence the grain size and morphology of rock salt.

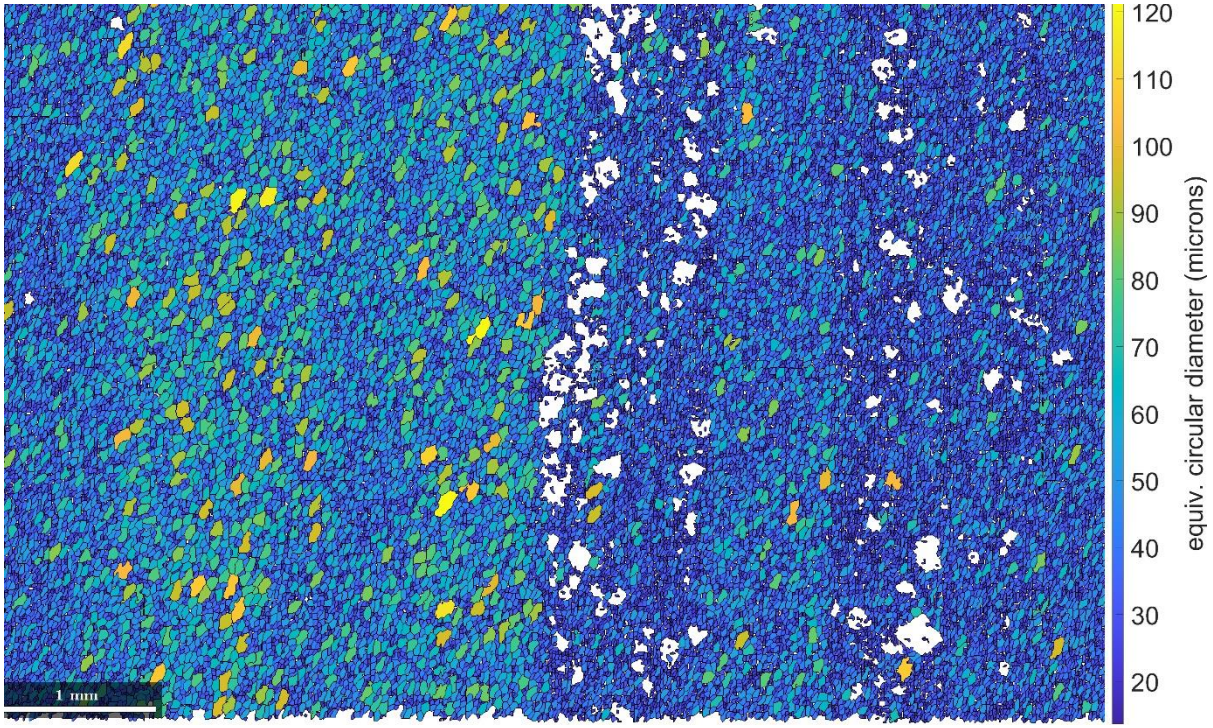

Figure 5.8. Grain size map of calcite grains from a natural calcite-dolomite polymineralic rock (from Caldera, 2022). Dolomite crystals are indicated by white colors. Larger grain sizes are observed in pure calcite regions (e.g. left side of the sample) while smaller in regions with dolomite content (e.g. central and right side).

Steady-state recrystallized grain size is achieved when grain size reduction and growth reach a dynamic equilibrium. The piezometric relationship links differential stress to steady-state recrystallized grain size (ter Heege et al., 2005a; Kohlstedt & Weathers, 1980; Stipp et al., 2010; Twiss, 1977). The influence of second-phase minerals is expected to result in a smaller steady-state recrystallized grain size compared to pure mineral cases (Herwegh & Berger, 2004). Caution is advised when using steady-state recrystallized grain size to predict differential stresses in polymineralic rocks, as smaller grain sizes may lead to overestimated stresses (Herwegh et al., 2005, 2011).

5.4.3 Effect of the second phase on CPO development

Second-phase mineral content considerably influences the matrix CPO intensity (Fig. 5.6), corroborated by prior laboratory experiments (Austin et al., 2014; Cyprych et al., 2016; Tullis & Wenk, 1994). In laboratory experiments, pure halite exhibits strong CPOs (e.g., Armann, 2008; Wenk et al., 2009), whereas natural halite often displays weaker or random patterns (e.g., Mansouri et al., 2019; Vargas-Meleza et al., 2015). The weaker CPO is often attributed to dissolution-precipitation creep (DP) and grain boundary sliding (GBS) (Desbois et al., 2010; Schléder & Urai, 2007; Prokop Závada et al., 2012). DP creep is typically associated with regions of high water content, featuring small grain sizes and fluid inclusions at grain boundaries (Urai et al., 2008; Urai, Spiers, et al., 1986). However, the minimal water content in diapiric rock salt, due to its low permeability and self-sealing potential (e.g., Bornemann et al., 2008; Mertineit et al., 2023), provides limited evidence for DP creep activation, such as pressure shadows, opaque seams or stylolites (Kneuker et al., 2014; Mertineit et al., 2023; Thiemeyer et al., 2016). Therefore, the DP creep alone does not fully explain the weak CPO observed in impure polycrystalline halite samples. In our simulations, dislocation creep, accompanied by SGR and GBM processes, is the sole deformation mechanism. The mere presence of additional mineral phases notably reduces the CPO intensity of the halite matrix dominated by dislocation creep (Fig. 5.6), without invoking any other process.

The stress exponent *n*, indicating the sensitivity of strain rate to stress variations, allows unravelling the deformation mechanisms that operate. For halite, when DP creep dominates, *n* approximates 1 (Spiers et al., 1990; Urai et al., 2008), whereas for dislocation creep, *n* exceeds 4 (Armann, 2008; Carter et al., 1993; Franssen, 1994; Marques et al., 2013; Wawersik & Zeuch, 1986). Experiments on halite with second-phase mixtures show *n* values well over 1, arguing against DP creep and GBS as dominant processes (Marques et al., 2010, 2011b, 2011a). This aligns with studies on ice-calcite (Cyprych et al., 2016) and calcite-amorphous carbon (Austin

et al., 2014). Hence, adding second-phase minerals does not change the primary deformation mechanism of halite matrix, as evidenced by consistent CPO across pure two-phase halite simulations (Fig. 5.6).

The final CPO intensity of the halite matrix consistently decreases as the second phase content increases from 0% to 30% (Fig. 5.6). This decrease is likely due to enhanced strain rate localization within the halite matrix (Fig. 5.4), where fewer crystals accommodate most of the imposed strain, resulting in less deformation overall and thus a reduced bulk CPO intensity. In addition, some areas of the halite matrix near the second phase grains are located in strain shadows, showing less finite deformation and lower CPO intensity (Fig. 5.5 row IV). As the second phase content increases, these strain shadow zones become more prevalent, further contributing to the reduction in the bulk CPO intensity. The final CPO intensity of the halite matrix rises as the second phase content grows from 30% to 50% (Fig. 5.6). This increase correlates with a shift from a weak-phase supported system to a competent-phase supported system, accompanied by a reduction in the proportion of strain-shaded areas (Fig. 5.5 row IV). Consequently, the overall CPO intensity increases as finite strain in the halite matrix does. Furthermore, as the second-phase content increases, these competent minerals bear more stress, consequently increasing locally the load on the halite matrix (Fig. 5.5 row III). In summary, an increase in second phase content modifies the strain-rate distribution, strain partitioning, and load transfer, significantly influencing the CPO intensity of the halite matrix (Fig. 5.6).

6 Discussion

This study aims to investigate the effects of factors such as temperature, kinematics of deformation and second-phase content on the evolution of halite-rich rocks microstructures (*i.e.*, grain size, SPO, etc.) and texture (CPO) of polycrystalline aggregates under viscoplastic deformation. In Chapter 3, we calibrated and confirmed that full-field simulations can successfully reproduce experimental results, based on the halite torsion experiments of Armann (2008) and Marques et al. (2013). Particularly, the microstructure (Figures 3.2 and 3.3), grain size statistics (Figures 3.4 and 3.7), and CPOs (Figures 3.2 and 3.5) of the numerical models can be directly compared to those of Armann (2008) and Marques et al. (2013) results from pure halite torsion experiments in the same range of temperatures (Figures 3.6 and 3.8). These temperatures correspond to different dynamic recrystallization regimes during dislocation creep, from subgrain rotation (SGR) to grain boundary migration recrystallization (GBM). Moreover, the simulations also agree with the numerical results of the VPSC simulations of Wenk et al. (2009) and the full-field simulations of Gomez-Rivas et al. (2017). The arithmetic mean of subgrain misorientation is quantitatively similar to the results obtained by Pennock et al. (2005) calculate from EBSD data of halite deformed under coaxial conditions (Fig. 6.2). All the above qualitative comparisons verify the correctness and validity of the proposed numerical method. On this basis, the influence of the kinematics of deformation (Chapter 4) and the role of a second competent phase (Chapter 5) on the dynamic evolution of halite was further studied.

6.1 Microstructure and CPO of halite: effects of temperature, deformation kinetics and presence of a second mineral phase

The results suggest that the grain size of pure polycrystalline halite depends on the competition between (i) grain size reduction due to dislocation gliding and subgrain rotation recrystallization (SGR) and (ii) grain growth associated with grain boundary migration recrystallization (GBM). With increasing temperature, microstructural development is dominated by GBM, which reduces grain elongation and even reshapes the grain morphology, thus masking the instantaneous and finite strain fields. The influence of GBM on the dynamic response of microstructures in naturally deformed salt rocks has been evident in various borehole samples (Henneberg et al., 2020; Schléder & Urai, 2005; Thiemeyer et al., 2016). Water present within the fluid film at grain boundaries reduces the threshold temperature required for initiating grain boundary migration (ter Heege et al., 2005a), expanding the potential occurrence of GBM under a broader range of natural conditions (e.g., top of the salt fountain; Mansouri et al., 2019). Therefore, our simulations highlight that GBM significantly controls grain morphology, emphasizing that grain morphology does not directly correlate with the amount of finite strain. Subgrain misorientation deviation is useful as a strain gauge for dislocation creep in polycrystalline halite, but the effect of dynamic recrystallization has not yet been considered. In Section 6.2 we discuss in detail the applicability of subgrain misorientation deviation as a strain gauge in systems with different degrees of dynamic recrystallization.

Deformation kinematics has a small effect on halite grain size evolution, but significantly affects the microstructure. Simple shear produces small grain bands subparallel to the grain SPO, whereas in pure shear simulations such bands are symmetrical conjugate and oriented oblique to the grain SPO. Thus, quantitative statistics of the microstructure can help to infer

the deformation kinematic of polycrystalline aggregates. In Section 6.3 we systematically summarise some indicators used to distinguish between simple shear deformation and pure shear deformation. The second mineral phase affects the grain size of the halite matrix by influencing the dynamic recrystallization processes. On the one hand, the second phase inhibits grain coarsening by impeding grain boundary migration through the pinning of grain boundaries. On the other hand, the second phase leads to more heterogeneous deformation of the matrix, enhancing the SGR process and facilitating grain refinement. As a result, the grain size of the matrix enriched with the second phase is smaller than that of the matrix lacking the second phase. This is qualitatively similar to the microstructure observed in natural two-phase rocks such as the calcite-dolomite system. The steady-state grain size of the matrix can be expressed by the Zener parameter ($Z = d_s/f_s$; Herwegh et al., 2011; Smith, 1948), which will be discussed further in Section 6.4.

Increasing GBM, linked to a higher temperature, minimally affects halite CPOs. Pronounced CPO maxima are observed during simple shear deformation at 300°C, like in studies on polar ice (e.g., Llorens et al., 2016a, 2016b, 2017). At this temperature, we were unable to replicate the distinct CPO with two {100} maxima at a 45° angle between the *x*-axis and *y*-axis, as observed at low strain in pure rock salt torsion experiments conducted under analogous deformation and temperature conditions (Armann, 2008). Hence, additional mechanisms likely influence CPO evolution during high-temperature rock salt deformation. Potential mechanisms include annealing-induced crystal axis rotation (Borthwick and Piazolo, 2010; Boneh et al, 2017) and discontinuous grain growth driven by anisotropic grain boundary energy (Piazolo et al, 2006). At low strain, the kinematics of deformation exerts little influence on the CPO, with CPOs in both simple and pure shear displaying six {100} maxima symmetric to the bulk maximum shortening strain-rate axis ($\dot{\varepsilon}_3$). As deformation progresses, the {100} CPO intensity

under pure shear gradually increases without altering the pattern (Fig. 7). With increasing strain, pure shear intensifies the {100} CPO without altering its pattern; while in simple shear, the {100} CPO rotates in accordance with the shear sense, producing a {100} maximum subperpendicular to the shear plane and two {100} maxima oblique to the shear direction**.** The evolution of the {100} CPO correlates with a dispersion of crystallographic orientations around the <100> misorientation axis within grains. Dextral simple shear deformation results in clockwise spreading of the crystallographic orientations around <100> misorientation axis, whereas pure shear deformation leads to clockwise and counterclockwise spreading directions. For the case of two-phase halite aggregates, the presence of a second phase weakens the CPO compared to monocrystalline halite. This is due to differences in the initial spatial distribution of the second phase, which alters the strain distribution and load transfer in the halite matrix. Considering halite mixtures as analogue materials for deformed polymineralic silicate rocks, we show that diffusion creep and GBS do not fully account for the weaker CPO observed in two-phase polycrystalline aggregates. This conclusion aligns with recent studies on ice mixtures (Cyprych et al., 2016) and natural quartzites (Little et al., 2015), in which the authors associated variations in the CPO intensity with changes in the content, shape, and strength of the second phase.

6.2 Effect of temperature on the misorientation frequency distribution: a strain gauge for recrystallized rocks

The frequency distributions of geometric mean subgrain misorientations at temperatures of 100°C, 200°C and 300°C for pure halite simulations are shown in Fig. 6.1. The results demonstrate that the frequency distribution of mean subgrain misorientations depends on the temperature at which the rock was deformed. At low temperatures (100°C and 200°C) the peak of the misorientation frequency distribution moves positively along the *x*-axis with progressive deformation, accompanied by an increase of the misorientation mean with increasing shear strain. Meanwhile, the skewness of the misorientation distribution decreases with increasing shear strain, and the proportion of low-angle subgrain misorientation diminishes, while the frequency of high-angle subgrain misorientation increases (Fig. 6.1a-j). However, at high temperature (300°C) the mean subgrain misorientation distribution initially raises and then stabilizes with increasing shear strain ($\gamma > 1.0$), while the relative abundance of high-angle subgrain misorientation values is low (Fig. 6.1k-o). Additionally, the frequency distribution of the geometric mean subgrain misorientation subgrains consistently conforms to a positive skew distribution, with the skewness remaining relatively constant at around 1.5 as shear strain increases. Although local boundary and strain stored energies are taken into account for the grain boundary migration calculation, the main driving force is the difference in stored strain energy of a grain with respect to its neighbours, during which grains enriched in subgrain boundaries are consumed by grains with no or few LAGBs (Fig. 3.2d-f). As GBM is enhanced by temperature, this process prevents the formation of 5°–10° subgrain boundaries (Fig. 6.2k-o), thus explaining the absence of high-angle subgrain boundaries in cases of deformed halite during dynamic recrystallization dominated by GBM (Trimby et al., 2000). At moderate shear

strain, there is a remarkable variation of the frequency distributions attending temperatures (Fig. 6.1e, j, o), with lower skewness values for lower temperature simulations.

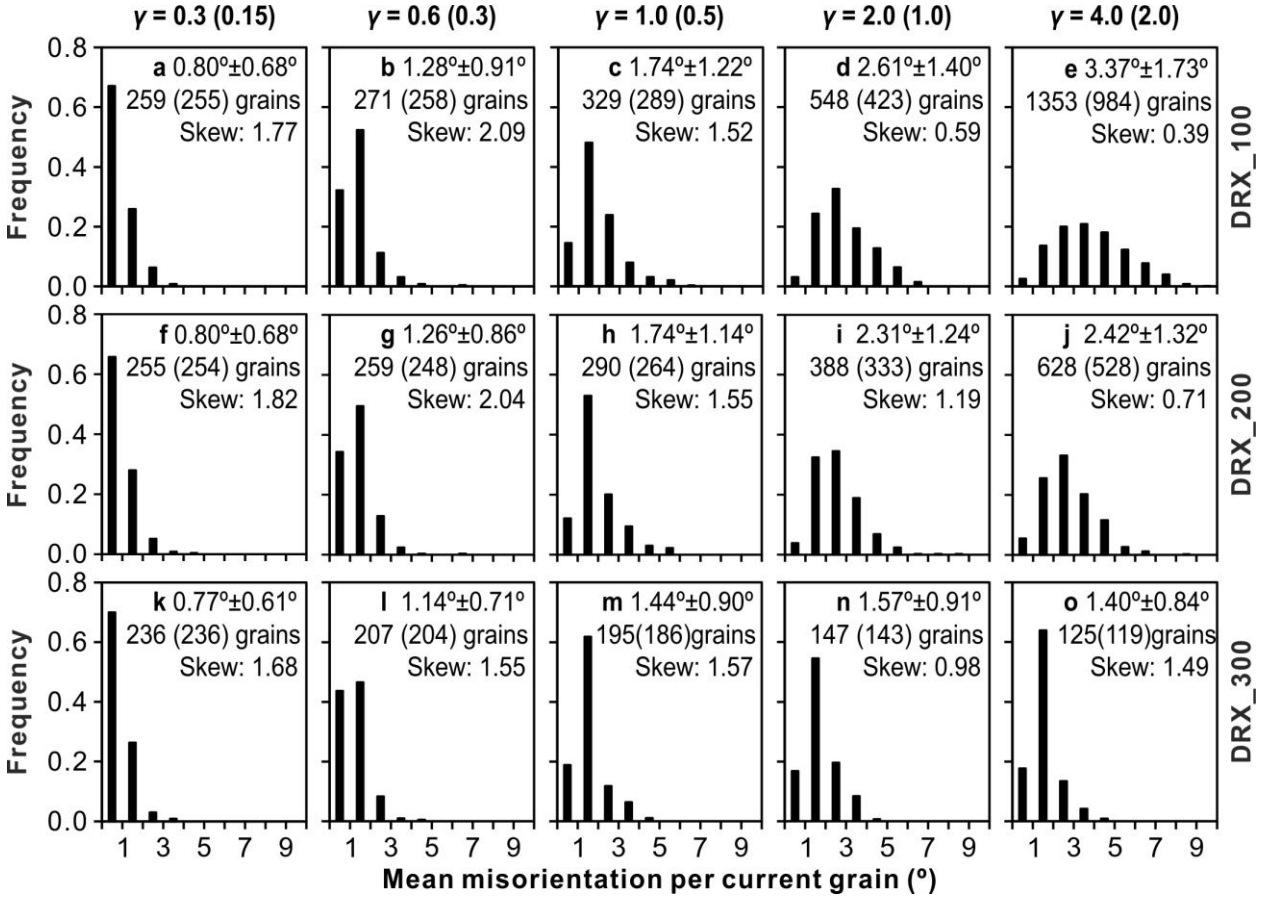

Figure 6.1. Frequency distribution of grain geometric mean misorientations at the temperature of 100°C, 200°C and 300°C at different shear strain γ (the value in parentheses is expressed as the natural strain). The geometric means of the misorientation distribution θ mean-grains are given along with the standard deviation of the mean. Misorientations were calculated with relevance the grains that form once the misorientation is above 10°. The value in parentheses corresponds to the number of grains that contain a minimum of 10 crystallites and are considered for use in the strain gauges discussed below. Skewness measures the distribution asymmetry.

The average subgrain misorientation across a sample (θ_{av}) displays a power law relationship with natural strain (ε), according to previous studies (Hughes et al., 1997, 1998, 2003; Pantleon, 1997, 1998, 2001; Sethna et al., 2003). These studies suggest that a $\theta_{av} \sim \varepsilon^n = 2/3$ relationship exists. Pennock & Drury (2005) obtained an exponent of n = 0.41 for halite pure shear

experiments, while Pennock et al. (2005) estimated an exponent of n = 0.42 in similar experiments but measuring misorientations by grain ($\theta_{\text{mean-grains}}$) instead of for the whole sample:

$$\theta_{\text{mean}-\text{grains}} = k_1 \varepsilon^n \quad (14)$$

where k_1 is a constant related to the material and deformation conditions (Hughes et al., 1997, 1998). The setting of the minimum misorientation angle threshold (0.5°, Pennock et al., 2005) in the experimental measurements may lead to an overestimation of the average misorientation angle for low-strain samples due to the limitation of the angular resolution of EBSD (Fig. 6.2), resulting in a lower value of the predicted exponent than the suggested universal exponent of n = 2/3. This is confirmed by the strong agreement between the arithmetic mean of misorientation (>0.5º) of DRX_100 simulation and experimental values (Pennock et al., 2005) shown in Fig. 6.2c. Considering the prevalent non-Gaussian misorientation distributions (Fig. 6.1), the employment of the geometric mean as opposed to the arithmetic mean is considered a better fitting metric (Fig. 6.2). Furthermore, it is assumed in our simulations that the recovery process is temperature-independent, that is, the recovery step remains constant for DRX subloops (see Table 3.2). This assumption is made to allow for a systematic investigation into the impact of GBM on misorientation. We find that, as strain increases, there is a deviation between the geometric mean of misorientation and the corresponding theoretical value (Fig. 6.2a-b). As temperature increases, a deviation emerges at lower strain thresholds, specifically from ε = 0.81 at 100°C to ε = 0.21 at 300°C, as illustrated in Fig. 6.2b. Accordingly, the k_1 constant also exhibits dependence on strain and, accordingly, lacks a tangible physical significance. Our simulations show three stages of increasing intracrystalline inhomogeneity, quantified by subgrain boundary misorientation (Fig. 6.2). In the first stage, the geometric mean of misorientation follows a theoretical power-law relationship with natural strain for models deformed at the whole range of temperatures considered (100-300°C) (Fig. 6.2), as predicted

in previous studies of metals (Hughes et al., 1997, 1998, 2003; Pantleon, 1997, 1998, 2001; Sethna et al., 2003). At this stage, lattice distortion and rotation associated with dislocation accumulation dominate, thus causing a misorientation increase following the aforementioned power-law relationship. In the second stage, as strain increases, the increase of the geometric mean misorientation slows down significantly and gradually deviates from the theoretical value, with a higher intensity of deviation in models deformed at higher temperatures (Fig. 6.2a-b). The third stage is characterized by stable misorientation mean values (Fig. 6.2a-b), indicating that the generation and annihilation of dislocations within grains are in dynamic equilibrium. As shown in Fig. 6.2b, the misorientation deviation is temperature-dependent, *i.e.*, related to the intensity of dynamic recrystallization in the system. At 100°C GBM plays almost no role (Fig. 3.1), so that the deviation of the mean misorientation at natural strain higher than 0.81 is due to SGR recrystallization. As temperature increases the mean misorientation deviation from the theoretical model takes place at lower strains compared to the 100°C case (Fig. 6.2a-b). This is associated with an increase in the GBM intensity that causes a strong reduction of the grain local misorientation by resetting misorientation in zones swept by moving grain boundaries.

In summary, the deviation from the theoretical power law correlates well with the occurrence of two dynamic recrystallization processes: subgrain rotation and grain boundary migration. This correlation can be attributed to variations in the rates of DRX processes, which in turn are influenced by changes in temperature. The power-law relationship between the geometric mean of subgrain misorientation and strain exhibits a close conformity with the universal exponent of 2/3, as demonstrated in prior studies. However, it is important to note that this correlation only holds true during the initial deformation stage. In subsequent stages, characterized by pronounced dynamic recrystallization and marked changes in the microstructure, reliance on this relationship may lead to a significant devaluation of natural strain estimations. Hence, the

accurate determination of strain gauge necessitates three calibrations for each of the three stages, or the construction of a theoretical model that incorporates factors such as temperature. The study conducted by Stipp et al. (2010) on quartz paleopiezometry demonstrated the requirement for distinct piezometer calibrations for diverse recrystallization regimes. For situations in which extensive recrystallization is inferred from natural samples (or experiments), in addition to the geometric mean misorientation as marker to estimate the strain, probably the strain gauge has more potential if is combined with the analysis of the skewness of the misorientation distribution (Fig. 6.3). In this way, the analysis of the discrepancy between measured geometric mean misorientation and skewness of the distribution with respect the to the theoretical trend could be used for the prediction of temperature and strain. A reduction of the skewness is expected for low temperature simulations, with limited recrystallization of the polycrystalline aggregate and a higher probability for the conservation of grains with higher misorientation angles. For high temperature cases, there are observed cycles of accumulation and swept of misorientations produced by larger mobility of grain boundaries and thus higher skewness of the misorientation distribution. However, more systematic analyses would be required to verify these observations.

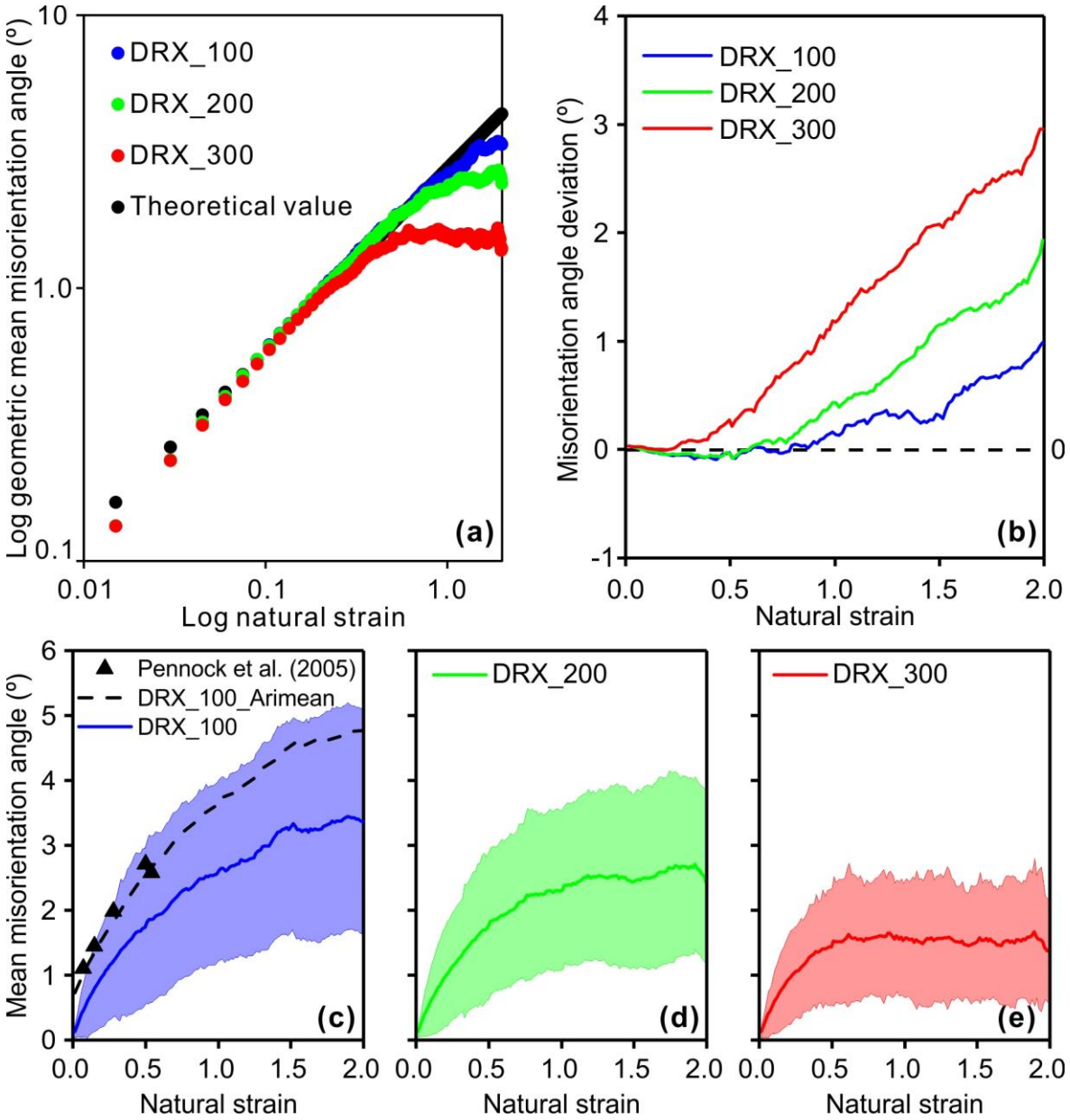

Figure 6.2. Evolution of the geometric mean of subgrain misorientation with natural strain at temperatures of 100°C (blue), 200°C (green) and 300°C (red), compared with the theoretical power law relationship following equation (13) (k_1 = 2.74, n = 2/3; black point). Only grains with at least 10 crystallites are considered for this the calculation. (a) Data plotted in logarithmic scale (log10). (b) Evolution of the misorientation deviation from the theoretical power law relationship. (c-d-e) Evolution of the geometric mean of subgrain misorientation and its standard deviation with natural strain (black dashed line: arithmetic mean of subgrain misorientation, which is higher than 0.5º; black triangle: experimental data from Pennock et al. (2005)).

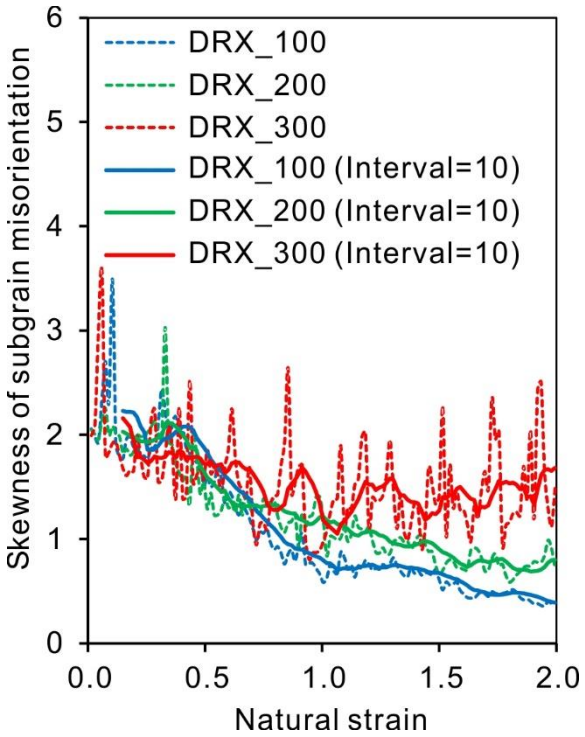

Figure 6.3. Evolution of the skewness of subgrain misorientation with natural strain at 100°C (blue dashed line), 200°C (green dashed line) and 300°C (red dashed line), and estimation of its evolution considering an average of 10 intervals (solid lines). After moderate shear strain, the skewness of the frequency distribution shows a temperature dependence.

6.3 Distinguishing simple shear and pure shear deformation patterns

An important question is whether the kinematics of deformation can be inferred from the resulting microstructure and CPOs of halite rocks. Table 6.1 summarizes our results on the characteristics of grain and subgrain boundaries, CPOs, SPOs, and grain size, categorized by temperature and deformation kinematics. A conjugate distribution of subgrain boundary orientations is observed in both simple shear and pure shear deformations (Fig. 4.2c-f). In cases where the sample reference system is oriented parallel to the grain SPO, the asymmetry of the distribution of subgrain boundaries can help distinguish between simple shear and pure shear. Under simple shear conditions, the conjugate distribution of orientation of subgrain boundaries is asymmetrically oriented about the grain SPO or stretching direction (Fig. 4.2c, e), while under pure shear tends to be symmetrically oriented about the grain SPO (Fig. 4.2d, f). As strain increases, SGR becomes dominant at low temperatures (100°C and 200°C). Simple shear deformation produces that most bands of small grains are subparallel to the grain SPO, while pure shear deformation results in the formation of conjugate bands of small grains that are symmetric around the grain SPO (Fig. 4.1). At high temperatures (300°C), increased GBM results in larger recrystallized grains, complicating the inference of the deformation kinematics from the grain boundary network, though it remains feasible through the orientation of the subgrain boundary network (Fig. 4.1). Regardless the temperature, when natural strain is higher than 1.0, three monoclinical symmetric {100} maxima form under simple shear. The orientation of these maxima relative to the grain SPO can be used to infer the shear sense (Fig. 4.12). Six {100} maxima with orthogonal symmetry develop in pure shear cases (Fig. 4.12). Additionally, the orientation of {111} CPO serves as a key indicator to differentiate between pure and simple shear cases (Fig. 4.12). Finally, simple shear is marked by brief stages of high strain-rate band evolution and periodic variation of strain localization (Fig. 4.11a). In contrast, pure shear shows steady strain-rate bands and decreasing strain localization (Fig. 4.11a),

leading to continuous elongation of some grains parallel to the stretching direction and resulting in longer SPOs compared to those in simple shear at high strain (Fig. 4.2a).

Table 6.1. Criteria to distinguish between simple shear and pure shear.

Criteria	Diagnostic	Explanation
Subgrain boundary orientation	Yes	Under simple shear, the conjugate subgrain boundary orientation distribution is asymmetric about the grain SPO (Fig. 4.2c, e), while under pure shear, it is always symmetric about the grain SPO (Fig. 4.2d, f).
Grain boundary network	Yes	Bands of small grains subparallel to the grain SPO in simple shear. Conjugate bands of small grains are symmetric about the grain SPO in pure shear (e.g., Fig. 4.1).
CPO	Yes	At high strains (ε > 1.0), three {100} maxima with monoclinic symmetry in simple shear, and six {100} maxima with orthotropic symmetry in pure shear (e.g., Fig. 4.12).
Crystallographic orientation dispersion direction	Possible	In simple shear, for most grains, the direction of spread of crystallographic orientations around <100> axis is clockwise, consistent with applied shear sense. While in pure shear, there are both clockwise and counterclockwise spread directions (e.g., Fig. 4.6). Practical application is challenging because of the difficulty of consistently tracking grain deformation in natural specimens.
Aspect ratio	Possible	Simple shear produces grains with higher aspect than pure shear at natural strain higher than 1.0 (e.g., Fig. 4.2a). Practical application is challenging.
Grain size	No	The evolution of the average grain size and its standard deviation during progressive deformation in simple shear is similar to that of pure shear (e.g., Fig. 4.4).

6.4 Effect of a second competent mineral phase on the halite matrix grain size: Zener parameters

In order to investigate the effect of a second competent mineral phase on the halite grain size under DRX, additional dextral shear deformation was applied to the polymineralic model (halite plus a second mineral) up to a shear strain of 6 (Figure 6.4). The grain size of halite remained almost consistent from a shear strain of 3 to 6, indicating that the model achieved a steady-state microstructure. The Zener parameter ($Z = d_s/f_s$, Herwegh et al., 2011) was used to explore how the second-phase content (f_s) and grain size (d_s) influence halite grain sizes, demonstrating its utility in distinguishing between second phase and dynamic recrystallization-controlled microstructures (Figure 6.4). At high Z values (*i.e.*, low second-phase content), DRX governs the matrix microstructure, affecting grain size based on temperature (De Bresser et al., 2001; Herwegh and Berger, 2004; Austin and Evans, 2007; Austin et al., 2008). High temperature (300°C) results in a significant increase of grain boundary migration, resulting in larger grains. Conversely, lower temperatures (100°C and 200°C) cause a reduction of the grain size. At low Z values (*i.e.*, high second-phase content), the second phase controls the microstructure and influences the matrix grain size (Fig. 6.4). This is qualitatively similar to many studies (Herwegh and Berger, 2004; Herwegh et al., 2007, 2008). Geometrically, a lower Z-value correlates with closer spacing between second-phase grains, thereby impeding the growth of matrix grains (Smith, 1948; Evans et al., 2001; Herwegh and Berger, 2004; Ebert et al., 2008). As migrating halite grain boundaries encounter second-phase grains, these exert a drag force, slowing or halting halite grain growth (Drury and Urai, 1990). This second-phase influence is pronounced in the 300°C simulations, increasing second-phase content from 5% to 20% and shifting the halite microstructural evolution from DRX-controlled grain growth to second-phase-controlled grain size reduction (Figures 5.1 & 6.4). As far as we know, this study is the first to explicitly model the effect of the Zener parameter under dynamic recrystallization

conditions, confirming the transition between the DRX-controlled and second phase-controlled regimes proposed by Herwegh et al. (2011).

Our simulations show that the Zener parameter also is applicable to polymineralic rock salt aggregates, at least in the case of dislocation creep and dynamic recrystallization. In this study we refrain from pursuing additional quantification of the scaling relationship between the Zener parameter and halite grains due to the need for precise calibration with comprehensive experimental data. Moreover, this scaling relationship could vary with the activation of other mechanisms, such as dissolution-precipitation and grain boundary sliding.

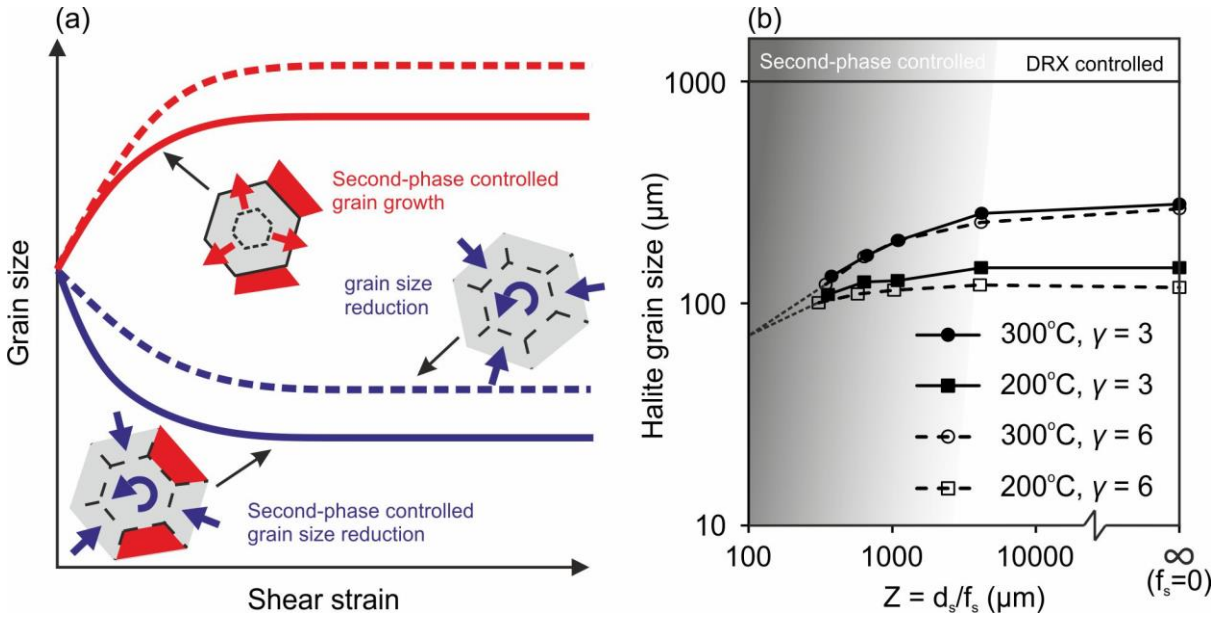

Figure 6.4. (a) Schematic diagram illustrating the evolution of matrix grain size during deformation in polymineralic aggregates. Dashed lines indicate grain size evolution controlled by dynamic recrystallization, while solid lines are controlled by the second phase. (b) Halite grain size versus the Zener parameter for $\gamma = 3$ and $\gamma = 6$ at 200°C and 300°C. The dotted lines indicate the interpolated trend for smaller Zener values from Herwergh et al (2011).

The full-field models discussed in this thesis accurately simulate the behaviour of monomineralic and polymineralic rock salt under various temperature and deformation kinematics. These simulations are crucial for advancing our understanding of the dynamic evolution of polymineralic rock salt aggregates and may also enhance our knowledge of the

behaviour of other minerals with similar crystal symmetries and slip systems (e.g., magnesiowüstite, Bystricky et al., 2006; Girard et al., 2016). The full-field simulations presented provide valuable insights into the interactions between different deformation mechanisms and the resulting microsturcture and texture in both crustal or mantle rocks, thereby enhancing our understanding of Earth's internal dynamics (e.g., Yu et al., 2024). However, to further improve these models, integration of additional deformation processes, such as grain boundary sliding, diffusion creep, dissolution precipitation creep, and slip system hardening, is essential. Moreover, calibration of these numerical models with experimental data is necessary for more accurate simulations.

7 Conclusions

This doctoral thesis investigates dynamic recrystallization (DRX) of rock salt under varied geological conditions, exploring how factors like temperature, kinematics of deformation, and second-phase mineral content influence the evolution of the microstructure and crystallographic preferred orientation (CPO) in polycrystalline halite. Using the state-of-the-art ELLE/VPFFT numerical approach, a series of full-field simulations are carried out under various conditions, yielding the following main conclusions:

1. The proposed VPFFT/ELLE approach successfully reproduces the evolution of halite microstructures, CPOs and grain size of laboratory torsion experiments at temperatures ranging between 100ºC and 300°C, providing new insights into the competition between grain size reduction by subgrain rotation (SGR) and grain size growth by grain boundary migration (GBM) recrystallization.

2. Temperature significantly impacts the microstructure development. Increasing temperatures intensify GBM, which weakens the grain size reduction process and leads to larger and more equidimensional grains. GBM reshapes the grain morphology, thus masking the heterogeneous distribution of strain (rate). When GBM is active in natural halite, it is difficult to detect the signs of strain localization. While temperature shapes grain morphology by modulating the interplay between SGR and GBM, it minimally affects the development of CPOs, only slightly altering its strength without changing the pattern.

3. The anisotropy of the single crystal is transferred to the polycrystalline scale, resulting in a heterogeneous distribution of strain rate and finite strain. The kinematics of deformation significantly influence the stability of high strain-rate bands during progressive deformation, which define grain and subgrain boundary orientations. The kinematics of deformation can be

deduced from the resulting microstructure. On the one hand, simple shear deformation features discontinuous evolution of high strain-rate bands and periodic variation of strain localization, resulting in asymmetric subgrain boundary orientations relative to the grain shape preferred orientation. On the other hand, pure shear deformation results in steady strain-rate bands and decreasing strain localization, producing symmetric conjugate subgrain boundaries and small grain bands relative to the grain shape preferred orientation (SPO), resulting in a higher grain aspect ratio at high strain than in simple shear.

4. The kinematics of deformation influence the rotation sense of the crystal dispersion axis within each grain, which determines the symmetry of the crystallographic preferred orientation of the polycrystalline aggregate. At low strain, six {100} maxima develop with orthotropic symmetry relative to the maximum shortening axis, regardless of temperature and deformation kinematics. With increasing strain, the {100} crystallographic preferred orientation for simple shear rotates consistently with the applied sense of shear and eventually forms three maxima with monoclinic symmetry. In contrast, the pure shear crystallographic preferred orientation of {100} axis gradually strengthens and maintains orthotropic symmetry through deformation. At high strains ($\varepsilon > 1.0$), the crystallographic preferred orientation can be used as a proxy to distinguish between coaxial and non-coaxial deformation and to determine the sense of shear.

5. The presence of a strong second-phase mineral forces strain to localize in the soft (halite) matrix. Increasing the second-phase content amplifies strain localization in the matrix matrix, thereby enhancing SGR and promoting more pronounced grain size reduction. Pinning of matrix grains by the second phase restricts GBM, leading to weaker grain growth. This study is the first to explicitly model the effect of the Zener parameter under dynamic recrystallization conditions, confirming the transition between the DRX-controlled and second phase-controlled regimes.

6. Changes in the content of the second phase modifies the strain-rate distribution, strain partitioning, and load transfer. This results in a weaker halite CPO in the two-phase material compared to pure halite cases. This offers an alternative explanation to pressure solution creep (SP) and grain boundary sliding (GBS) for the typically observed weak CPO in natural rock salt. Therefore, the difference in CPO strength between monomineralic and polymineralic rocks does not conclusively indicate the presence of diffusion creep, GBS or pressure solution creep.

7. At low strain, the relationship between finite natural strain and the geometric mean subgrain misorientation follows a power law and thus can be used as a strain gauge. However, at high strain the intensity of DRX, including SGR and GBM, causes a deviation from this universal scaling law (*i.e.*, independent of the material). The skewness of the frequency distribution of the geometrical mean misorientation can also be used as a proxy for a better prediction of strain and deformation temperature from the subgrain misorientation data, but more studies are required to define a more systematic quantitative tool.

References

Amelirad, O., & Assempour, A. (2022). Coupled continuum damage mechanics and crystal plasticity model and its application in damage evolution in polycrystalline aggregates. *Engineering with Computers*, *38*(S3), 2121–2135. https://doi.org/10.1007/s00366-021-01346-2

Armann, M. (2008). *Microstructural and textural development in synthetic rocksalt deformed in torsion.* (Doctoral dissertation). ETH-Zurich, Switzerland. Retrieved from https://doi.org/10.3929/ethz-a-005666840

Austin, N., Evans, B., Rybacki, E., & Dresen, G. (2014). Strength evolution and the development of crystallographic preferred orientation during deformation of two-phase marbles. *Tectonophysics*, *631*(C), 14–28. https://doi.org/10.1016/j.tecto.2014.04.018

Bachmann, F., Hielscher, R., & Schaeben, H. (2010). Texture Analysis with MTEX – Free and Open Source Software Toolbox. *Solid State Phenomena*, *160*, 63–68. https://doi.org/10.4028/www.scientific.net/SSP.160.63

Barabasch, J., Schmatz, J., Klaver, J., Schwedt, A., & Urai, J. L. (2023). Large grain-size-dependent rheology contrasts of halite at low differential stress: evidence from microstructural study of naturally deformed gneissic Zechstein 2 rock salt (Kristallbrockensalz) from the northern Netherlands. *Solid Earth*, *14*(3), 271–291. https://doi.org/10.5194/se-14-271-2023

Barrie, C. D., Boyle, A. P., Cox, S. F., & Prior, D. J. (2008). Slip systems and critical resolved shear stress in pyrite: an electron backscatter diffraction (EBSD) investigation.

Mineralogical Magazine, *72*(6), 1181–1199. https://doi.org/10.1180/minmag.2008.072.6.1181

Becker, J. K., Bons, P. D., & Jessell, M. W. (2008). A new front-tracking method to model anisotropic grain and phase boundary motion in rocks. *Computers & Geosciences*, *34*(3), 201–212. https://doi.org/10.1016/j.cageo.2007.03.013

Bestmann, M., & Prior, D. J. (2003). Intragranular dynamic recrystallization in naturally deformed calcite marble: diffusion accommodated grain boundary sliding as a result of subgrain rotation recrystallization. *Journal of Structural Geology*, *25*(10), 1597–1613. https://doi.org/10.1016/S0191-8141(03)00006-3

Bestmann, M., Piazolo, S., Spiers, C. J., & Prior, D. J. (2005). Microstructural evolution during initial stages of static recovery and recrystallization: new insights from in-situ heating experiments combined with electron backscatter diffraction analysis. *Journal of Structural Geology*, *27*(3), 447–457. https://doi.org/10.1016/j.jsg.2004.10.006

Boneh, Y., & Skemer, P. (2014a). The effect of deformation history on the evolution of olivine CPO. *Earth and Planetary Science Letters*, *406*, 213–222. https://doi.org/10.1016/j.epsl.2014.09.018

Boneh, Y., & Skemer, P. (2014b). The effect of deformation history on the evolution of olivine CPO. *Earth and Planetary Science Letters*, *406*, 213–222. https://doi.org/10.1016/j.epsl.2014.09.018

Boneh, Y., Wallis, D., Hansen, L. N., Krawczynski, M. J., & Skemer, P. (2017). Oriented grain growth and modification of 'frozen anisotropy' in the lithospheric mantle. *Earth and Planetary Science Letters*, *474*, 368–374. https://doi.org/10.1016/j.epsl.2017.06.050

Bons, P. D., & Urai, J. L. (1992). Syndeformational grain growth: microstructures and kinetics. *Journal of Structural Geology*, *14*(8–9), 1101–1109. https://doi.org/10.1016/0191-8141(92)90038-X

Bons, P. D., Koehn, D., & Jessell, M. W. (2008). *Microdynamics Simulation*. (P. D. Bons, D. Koehn, & M. W. Jessell, Eds.) (Vol. 106). Berlin: Springer. https://doi.org/10.1007/978-3-540-44793-1

Bornemann, O., Behlau, J., Fischbeck, R., Hammer, J., Jaritz, W., Keller, S., et al. (2008). Description of the Gorleben Site Part 3: Results of the geological surface and underground exploration of the salt formation. *Bundesanstalt Für Geowissenschaften Und Rohstoffe: Hannover, Germany*, 223.

Borthwick, V. E., & Piazolo, S. (2010). Post-deformational annealing at the subgrain scale: Temperature dependent behaviour revealed by in-situ heating experiments on deformed single crystal halite. *Journal of Structural Geology*, *32*(7), 982–996. https://doi.org/10.1016/j.jsg.2010.06.006

Borthwick, V. E., Piazolo, S., Evans, L., Griera, A., & Bons, P. D. (2014). What happens to deformed rocks after deformation? A refined model for recovery based on numerical simulations. *Geological Society, London, Special Publications*, *394*(1), 215–234. https://doi.org/10.1144/SP394.11

Bourcier, M., Bornert, M., Dimanov, A., Héripré, E., & Raphanel, J. L. (2013). Multiscale experimental investigation of crystal plasticity and grain boundary sliding in synthetic halite using digital image correlation. *Journal of Geophysical Research: Solid Earth*, *118*(2), 511–526. https://doi.org/10.1002/jgrb.50065

De Bresser, J. H. P., & Spiers, C. J. (1997). Strength characteristics of the r, f, and c slip systems in calcite. *Tectonophysics*, *272*(1), 1–23. https://doi.org/10.1016/S0040-1951(96)00273-9

Brodhag, S. H., & Herwegh, M. (2010). The effect of different second-phase particle regimes on grain growth in two-phase aggregates: insights from in situ rock analogue experiments. *Contributions to Mineralogy and Petrology*, *160*(2), 219–238. https://doi.org/10.1007/s00410-009-0474-6

Bystricky, M., Heidelbach, F., & Mackwell, S. (2006). Large-strain deformation and strain partitioning in polyphase rocks: Dislocation creep of olivine–magnesiowüstite aggregates. *Tectonophysics*, *427*(1–4), 115–132. https://doi.org/10.1016/j.tecto.2006.05.025

Caldera, G. N. (2022, November 21). *Ductile deformation of the Pyrenean hinterland during the Alpine collision: The case of the proximal Iberian margin in the Eaux-Chaudes massif (west-central Pyrenees)* (Doctoral dissertation). Universitat Autònoma de Barcelona, Barcelone. Retrieved from https://hdl.handle.net/10803/688310

Canérot, J., Hudec, M. R., & Rockenbauch, K. (2005). Mesozoic diapirism in the Pyrenean orogen: Salt tectonics on a transform plate boundary. *AAPG Bulletin*, *89*(2), 211–229. https://doi.org/10.1306/09170404007

Cao, Y., Ni, S., Liao, X., Song, M., & Zhu, Y. (2018). Structural evolutions of metallic materials processed by severe plastic deformation. *Materials Science and Engineering: R: Reports*, *133*, 1–59. https://doi.org/10.1016/j.mser.2018.06.001

Carter, N. L., & Heard, H. C. (1970). Temperature and rate dependent deformation of halite. *American Journal of Science*, *269*(3), 193–249. https://doi.org/10.2475/ajs.269.3.193

Carter, N. L., Horseman, S. T., Russell, J. E., & Handin, J. (1993). Rheology of rocksalt. *Journal of Structural Geology*, *15*(9–10), 1257–1271. https://doi.org/10.1016/0191-8141(93)90168-A

Cyprych, D., Brune, S., Piazolo, S., & Quinteros, J. (2016). Strain localization in polycrystalline material with second phase particles: Numerical modeling with application to ice mixtures. *Geochemistry, Geophysics, Geosystems*, *17*(9), 3608–3628. https://doi.org/10.1002/2016GC006471

Cyprych, Daria, Piazolo, S., Wilson, C. J. L., Luzin, V., & Prior, D. J. (2016). Rheology, microstructure and crystallographic preferred orientation of matrix containing a dispersed second phase: Insight from experimentally deformed ice. *Earth and Planetary Science Letters*, *449*, 272–281. https://doi.org/10.1016/j.epsl.2016.06.010

Desbois, G., Závada, P., Schléder, Z., & Urai, J. L. (2010). Deformation and recrystallization mechanisms in actively extruding salt fountain: Microstructural evidence for a switch in deformation mechanisms with increased availability of meteoric water and decreased grain size (Qum Kuh, central Iran). *Journal of Structural Geology*, *32*(4), 580–594. https://doi.org/10.1016/j.jsg.2010.03.005

Dillon, S. J., & Rohrer, G. S. (2009). Mechanism for the development of anisotropic grain boundary character distributions during normal grain growth. *Acta Materialia*, *57*(1), 1–7. https://doi.org/10.1016/j.actamat.2008.08.062

Drury, M. R., & Urai, J. L. (1990). Deformation-related recrystallization processes. *Tectonophysics*, *172*(3–4), 235–253. https://doi.org/10.1016/0040-1951(90)90033-5

Duffy, O. B., Dooley, T. P., Hudec, M. R., Jackson, M. P. A., Fernandez, N., Jackson, C. A.-L., & Soto, J. I. (2018). Structural evolution of salt-influenced fold-and-thrust belts: A

synthesis and new insights from basins containing isolated salt diapirs. *Journal of Structural Geology*, *114*, 206–221. https://doi.org/10.1016/j.jsg.2018.06.024

Eisenlohr, P., Diehl, M., Lebensohn, R. A., & Roters, F. (2013). A spectral method solution to crystal elasto-viscoplasticity at finite strains. *International Journal of Plasticity*, *46*, 37–53. https://doi.org/10.1016/j.ijplas.2012.09.012

Evans, B., Renner, J., & Hirth, G. (2001). A few remarks on the kinetics of static grain growth in rocks. *International Journal of Earth Sciences*, *90*(1), 88–103. https://doi.org/10.1007/s005310000150

Fei, H., Ballmer, M. D., Faul, U., Walte, N., Cao, W., & Katsura, T. (2023). Variation in bridgmanite grain size accounts for the mid-mantle viscosity jump. *Nature*, *620*(7975), 794–799. https://doi.org/10.1038/s41586-023-06215-0

Finch, M. A., Bons, P. D., Steinbach, F., Griera, A., Llorens, M.-G., Gomez-Rivas, E., et al. (2020). The ephemeral development of C′ shear bands: A numerical modelling approach. *Journal of Structural Geology*, *139*, 104091. https://doi.org/10.1016/j.jsg.2020.104091

Finch, M. A., Bons, P. D., Weinberg, R. F., Llorens, M.-G., Griera, A., & Gomez-Rivas, E. (2022). A dynamic atlas of interference patterns in superimposed, opposite sense ductile shear zones. *Journal of Structural Geology*, 104739. https://doi.org/10.1016/j.jsg.2022.104739

Fossen, H. (2010). Deformation bands formed during soft-sediment deformation: Observations from SE Utah. *Marine and Petroleum Geology*, *27*(1), 215–222. https://doi.org/10.1016/j.marpetgeo.2009.06.005

Franssen, R. C. M. W. (1994). The rheology of synthetic rocksalt in uniaxial compression. *Tectonophysics*, *233*(1–2), 1–40. https://doi.org/10.1016/0040-1951(94)90218-6

Franssen, R. C. M. W., & Spiers, C. J. (1990). Deformation of polycrystalline salt in compression and in shear at 250–350°C. *Geological Society, London, Special Publications*, *54*(1), 201–213. https://doi.org/10.1144/GSL.SP.1990.054.01.20

Frost, H. J., & Ashby, M. F. (1982). *Deformation-mechanism maps: The plasticity and creep of metals and ceramics*. *Oxford, Pergamon Press, 1982, 175 p*. Oxford: Pergamon.

Ghosh, B., Misra, S., & Morishita, T. (2017). Plastic deformation and post-deformation annealing in chromite: Mechanisms and implications. *American Mineralogist*, *102*(1), 216–226. https://doi.org/10.2138/am-2017-5709

Girard, J., Amulele, G., Farla, R., Mohiuddin, A., & Karato, S. (2016). Shear deformation of bridgmanite and magnesiowüstite aggregates at lower mantle conditions. *Science*, *351*(6269), 144–147. https://doi.org/10.1126/science.aad3113

Godin, L., Grujic, D., Law, R. D., & Searle, M. P. (2006). Channel flow, ductile extrusion and exhumation in continental collision zones: an introduction. *Geological Society, London, Special Publications*, *268*(1), 1–23. https://doi.org/10.1144/GSL.SP.2006.268.01.01

Gomez-Rivas, E., Griera, A., Llorens, M.-G., Bons, P. D., Lebensohn, R. A., & Piazolo, S. (2017). Subgrain Rotation Recrystallization During Shearing: Insights From Full-Field Numerical Simulations of Halite Polycrystals. *Journal of Geophysical Research: Solid Earth*, *122*(11), 8810–8827. https://doi.org/10.1002/2017JB014508

Gomez-Rivas, Enrique, Butler, R. W. H., Healy, D., & Alsop, I. (2020). From hot to cold - The temperature dependence on rock deformation processes: An introduction. *Journal of Structural Geology*, *132*, 103977. https://doi.org/10.1016/j.jsg.2020.103977

Griera, A., Bons, P. D., Jessell, M. W., Lebensohn, R. A., Evans, L., & Gomez-Rivas, E. (2011). Strain localization and porphyroclast rotation. *Geology*, *39*(3), 275–278. https://doi.org/10.1130/G31549.1

Griera, A., Llorens, M.-G., Gomez-Rivas, E., Bons, P. D., Jessell, M. W., Evans, L. A., & Lebensohn, R. (2013). Numerical modelling of porphyroclast and porphyroblast rotation in anisotropic rocks. *Tectonophysics*, *587*, 4–29. https://doi.org/10.1016/j.tecto.2012.10.008

Grujic, D. (2006). Channel flow and continental collision tectonics: an overview. *Geological Society, London, Special Publications*, *268*(1), 25–37. https://doi.org/10.1144/GSL.SP.2006.268.01.02

Guillope, M., & Poirier, J. P. (1979). Dynamic recrystallization during creep of single-crystalline halite: An experimental study. *Journal of Geophysical Research*, *84*(B10), 5557. https://doi.org/10.1029/JB084iB10p05557

Handy, M. R. (1990). The solid-state flow of polymineralic rocks. *Journal of Geophysical Research: Solid Earth*, *95*(B6), 8647–8661. https://doi.org/10.1029/JB095iB06p08647

Handy, M. R. (1994). Flow laws for rocks containing two non-linear viscous phases: A phenomenological approach. *Journal of Structural Geology*, *16*(3), 287–301. https://doi.org/10.1016/0191-8141(94)90035-3

Hao, B., Llorens, M. -G., Griera, A., Bons, P. D., Lebensohn, R. A., Yu, Y., & Gomez-Rivas, E. (2023). Full-Field Numerical Simulation of Halite Dynamic Recrystallization From Subgrain Rotation to Grain Boundary Migration. *Journal of Geophysical Research: Solid Earth*, *128*(12). https://doi.org/10.1029/2023JB027590

ter Heege, J. H., de Bresser, J. H. P., & Spiers, C. J. (2004). Dynamic Recrystallization of Dense Polycrystalline NaCl: Dependence of Grain Size Distribution on Stress and Temperature. *Materials Science Forum*, *467–470*, 1187–1192. https://doi.org/10.4028/www.scientific.net/MSF.467-470.1187

ter Heege, J. H., de Bresser, J. H. P., & Spiers, C. J. (2005a). Dynamic recrystallization of wet synthetic polycrystalline halite: dependence of grain size distribution on flow stress, temperature and strain. *Tectonophysics*, *396*(1–2), 35–57. https://doi.org/10.1016/j.tecto.2004.10.002

ter Heege, J. H., de Bresser, J. H. P., & Spiers, C. J. (2005b). Rheological behaviour of synthetic rocksalt: the interplay between water, dynamic recrystallization and deformation mechanisms. *Journal of Structural Geology*, *27*(6), 948–963. https://doi.org/10.1016/j.jsg.2005.04.008

Henneberg, M., Linckens, J., Schramm, M., Hammer, J., Gerdes, A., & Zulauf, G. (2020). Structural evolution of continental and marine Permian rock salt of the North German Basin: constraints from microfabrics, geochemistry and U–Pb ages. *International Journal of Earth Sciences*, *109*(7), 2369–2387. https://doi.org/10.1007/s00531-020-01905-w

Herwegh, M., de Bresser, J. H. P., & ter Heege, J. H. (2005). Combining natural microstructures with composite flow laws: an improved approach for the extrapolation of lab data to nature. *Journal of Structural Geology*, *27*(3), 503–521. https://doi.org/10.1016/j.jsg.2004.10.010

Herwegh, M., Linckens, J., Ebert, A., Berger, A., & Brodhag, S. H. (2011). The role of second phases for controlling microstructural evolution in polymineralic rocks: A review. *Journal of Structural Geology*, *33*(12), 1728–1750. https://doi.org/10.1016/j.jsg.2011.08.011

Herwegh, Marco, & Berger, A. (2004). Deformation mechanisms in second-phase affected microstructures and their energy balance. *Journal of Structural Geology*, *26*(8), 1483–1498. https://doi.org/10.1016/j.jsg.2003.10.006

Hirth, G., & Tullis, J. (1992). Dislocation creep regimes in quartz aggregates. *Journal of Structural Geology*, *14*(2), 145–159. https://doi.org/10.1016/0191-8141(92)90053-Y

Hu, Y., Bons, P. D., de Riese, T., Liu, S., Llorens, M.-G., González-Esvertit, E., et al. (2024). Folding of a single layer in an anisotropic viscous matrix under layer-parallel shortening. *Journal of Structural Geology*, *188*, 105246. https://doi.org/10.1016/j.jsg.2024.105246

Hudec, M. R., & Jackson, M. P. A. (2007). Terra infirma: Understanding salt tectonics. *Earth-Science Reviews*, *82*(1–2), 1–28. https://doi.org/10.1016/j.earscirev.2007.01.001

Hughes, D. A., & Hansen, N. (2018). The microstructural origin of work hardening stages. *Acta Materialia*, *148*, 374–383. https://doi.org/10.1016/j.actamat.2018.02.002

Hughes, D. A., Liu, Q., Chrzan, D. C., & Hansen, N. (1997). Scaling of microstructural parameters: Misorientations of deformation induced boundaries. *Acta Materialia*, *45*(1), 105–112. https://doi.org/10.1016/S1359-6454(96)00153-X

Hughes, D. A., Chrzan, D. C., Liu, Q., & Hansen, N. (1998). Scaling of Misorientation Angle Distributions. *Physical Review Letters*, *81*(21), 4664–4667. https://doi.org/10.1103/PhysRevLett.81.4664

Hughes, D. A., Hansen, N., & Bammann, D. J. (2003). Geometrically necessary boundaries, incidental dislocation boundaries and geometrically necessary dislocations. *Scripta Materialia*, *48*(2), 147–153. https://doi.org/10.1016/S1359-6462(02)00358-5

Hunsche, U., & Hampel, A. (1999). Rock salt — the mechanical properties of the host rock material for a radioactive waste repository. *Engineering Geology*, *52*(3–4), 271–291. https://doi.org/10.1016/S0013-7952(99)00011-3

Jackson, C. A.-L., Jackson, M. P. A., Hudec, M. R., & Rodriguez, C. R. (2015). Enigmatic structures within salt walls of the Santos Basin—Part 1: Geometry and kinematics from 3D seismic reflection and well data. *Journal of Structural Geology*, *75*, 135–162. https://doi.org/10.1016/j.jsg.2015.01.010

Jackson, M. P., & Hudec, M. R. (2017). *Salt tectonics: Principles and Practice*. *Salt tectonics*.

Jackson, M. P. A., & Talbot, C. J. (1986). External shapes, strain rates, and dynamics of salt structures. *Geological Society of America Bulletin*, *97*(3), 305. https://doi.org/10.1130/0016-7606(1986)97<305:ESSRAD>2.0.CO;2

Jessell, M. W., Bons, P. D., Evans, L., Barr, T., & Stüwe, K. (2001). Elle: the numerical simulation of metamorphic and deformation microstructures. *Computers & Geosciences*, *27*(1), 17–30. https://doi.org/10.1016/S0098-3004(00)00061-3

Jessell, M. W., Kostenko, O., & Jamtveit, B. (2003). The preservation potential of microstructures during static grain growth. *Journal of Metamorphic Geology*, *21*(5), 481–491. https://doi.org/10.1046/j.1525-1314.2003.00455.x

Jessell, M. W., Bons, P. D., Griera, A., Evans, L. A., & Wilson, C. J. L. (2009). A tale of two viscosities. *Journal of Structural Geology*, *31*(7), 719–736. https://doi.org/10.1016/j.jsg.2009.04.010

Kaminski, É., & Ribe, N. M. (2001). A kinematic model for recrystallization and texture development in olivine polycrystals. *Earth and Planetary Science Letters*, *189*(3–4), 253–267. https://doi.org/10.1016/S0012-821X(01)00356-9

Kaminski, É., Ribe, N. M., & Browaeys, J. T. (2004). D-Rex, a program for calculation of seismic anisotropy due to crystal lattice preferred orientation in the convective upper mantle. *Geophysical Journal International*, *158*(2), 744–752. https://doi.org/10.1111/j.1365-246X.2004.02308.x

Karato, S. (2008). *Deformation of earth materials*. *An introduction to the rheology of Solid Earth* (Vol. 463). Cambridge Press Cambridge.

Kern, H. (1977). Preferred orientation of experimentally deformed limestone marble, quartzite and rock salt at different temperatures and states of stress. *Tectonophysics*, *39*(1–3), 103–120. https://doi.org/10.1016/0040-1951(77)90091-9

Kilian, R., Heilbronner, R., & Stünitz, H. (2011). Quartz grain size reduction in a granitoid rock and the transition from dislocation to diffusion creep. *Journal of Structural Geology*, *33*(8), 1265–1284. https://doi.org/10.1016/j.jsg.2011.05.004

Kneuker, T., Zulauf, G., Mertineit, M., Behlau, J., & Hammer, J. (2014). Deformationsverhalten von permischem Staßfurt-Steinsalz aus Morsleben (Deutschland) bei unterschiedlichem finitem Strain: Abschätzungen aus Mikrogefüge-Studien und EBSD-Analysen. *Zeitschrift Der Deutschen Gesellschaft Für Geowissenschaften*, *165*(1), 91–106. https://doi.org/10.1127/1860-1804/2013/0041

Kohlstedt, D. L., & Weathers, M. S. (1980). Deformation-induced microstructures, paleopiezometers, and differential stresses in deeply eroded fault zones. *Journal of Geophysical Research: Solid Earth*, *85*(B11), 6269–6285. https://doi.org/10.1029/JB085iB11p06269

Langille, J., Lee, J., Hacker, B., & Seward, G. (2010). Middle crustal ductile deformation patterns in southern Tibet: Insights from vorticity studies in Mabja Dome. *Journal of Structural Geology*, *32*(1), 70–85. https://doi.org/10.1016/j.jsg.2009.08.009

Lebensohn, R. A. (2001). N-site modeling of a 3D viscoplastic polycrystal using Fast Fourier Transform. *Acta Materialia*, *49*(14), 2723–2737. https://doi.org/10.1016/S1359-6454(01)00172-0

Lebensohn, R. A., & Rollett, A. D. (2020). Spectral methods for full-field micromechanical modelling of polycrystalline materials. *Computational Materials Science*, *173*, 109336. https://doi.org/10.1016/j.commatsci.2019.109336

Lebensohn, R. A., & Tomé, C. N. (1993). A self-consistent anisotropic approach for the simulation of plastic deformation and texture development of polycrystals: Application to zirconium alloys. *Acta Metallurgica et Materialia*, *41*(9), 2611–2624. https://doi.org/10.1016/0956-7151(93)90130-K

Lebensohn, R. A., Dawson, P. R., Kern, H. M., & Wenk, H.-R. (2003). Heterogeneous deformation and texture development in halite polycrystals: comparison of different modeling approaches and experimental data. *Tectonophysics*, *370*(1–4), 287–311. https://doi.org/10.1016/S0040-1951(03)00192-6

Lebensohn, R. A., Brenner, R., Castelnau, O., & Rollett, A. D. (2008). Orientation image-based micromechanical modelling of subgrain texture evolution in polycrystalline copper. *Acta Materialia*, *56*(15), 3914–3926. https://doi.org/10.1016/j.actamat.2008.04.016

Leitner, C., Neubauer, F., Urai, J. L., & Schoenherr, J. (2011). Structure and evolution of a rocksalt-mudrock-tectonite: The haselgebirge in the Northern Calcareous Alps. *Journal of Structural Geology*, *33*(5), 970–984. https://doi.org/10.1016/j.jsg.2011.02.008

Linckens, J, Zulauf, G., & Hammer, J. (2016). Experimental deformation of coarse-grained rock salt to high strain. *Journal of Geophysical Research: Solid Earth*, *121*(8), 6150–6171. https://doi.org/10.1002/2016JB012890

Linckens, Jolien, Herwegh, M., Müntener, O., & Mercolli, I. (2011). Evolution of a polymineralic mantle shear zone and the role of second phases in the localization of deformation. *Journal of Geophysical Research*, *116*(B6), B06210. https://doi.org/10.1029/2010JB008119

Little, T. A., Prior, D. J., Toy, V. G., & Lindroos, Z. R. (2015). The link between strength of lattice preferred orientation, second phase content and grain boundary migration: A case study from the Alpine Fault zone, New Zealand. *Journal of Structural Geology*, *81*, 59–77. https://doi.org/10.1016/j.jsg.2015.09.004

Liu, Y., Gilormini, P., & Castañeda, P. P. (2005). Homogenization estimates for texture evolution in halite. *Tectonophysics*, *406*(3–4), 179–195. https://doi.org/10.1016/j.tecto.2005.06.007

Llorens, M.-G., Griera, A., Bons, P. D., Roessiger, J., Lebensohn, R., Evans, L., & Weikusat, I. (2016). Dynamic recrystallisation of ice aggregates during co-axial viscoplastic deformation: a numerical approach. *Journal of Glaciology*, *62*(232), 359–377. https://doi.org/10.1017/jog.2016.28

Llorens, M.-G., Griera, A., Bons, P. D., Lebensohn, R. A., Evans, L. A., Jansen, D., & Weikusat, I. (2016). Full-field predictions of ice dynamic recrystallisation under simple shear conditions. *Earth and Planetary Science Letters*, *450*, 233–242. https://doi.org/10.1016/j.epsl.2016.06.045

Llorens, M.-G., Griera, A., Steinbach, F., Bons, P. D., Gomez-Rivas, E., Jansen, D., et al. (2017). Dynamic recrystallization during deformation of polycrystalline ice: insights from numerical simulations. *Philosophical Transactions of the Royal Society A: Mathematical, Physical and Engineering Sciences*, *375*(2086), 20150346. https://doi.org/10.1098/rsta.2015.0346

Llorens, M.-G., Gomez-Rivas, E., Ganzhorn, A.-C., Griera, A., Steinbach, F., Roessiger, J., et al. (2019). The effect of dynamic recrystallisation on the rheology and microstructures of partially molten rocks. *Journal of Structural Geology*, *118*, 224–235. https://doi.org/10.1016/j.jsg.2018.10.013

Llorens, M.-G., Griera, A., Bons, P. D., Weikusat, I., Prior, D. J., Gomez-Rivas, E., et al. (2022). Can changes in deformation regimes be inferred from crystallographic preferred orientations in polar ice? *The Cryosphere*, *16*(5), 2009–2024. https://doi.org/10.5194/tc-16-2009-2022

Lücke, K., & Stüwe, H. P. (1971). On the theory of impurity controlled grain boundary motion. *Acta Metallurgica*, *19*(10), 1087–1099. https://doi.org/10.1016/0001-6160(71)90041-1

Mainprice, D., Hielscher, R., & Schaeben, H. (2011). Calculating anisotropic physical properties from texture data using the MTEX open-source package. *Geological Society, London, Special Publications*, *360*(1), 175–192. https://doi.org/10.1144/SP360.10

Mainprice, D., Bachmann, F., Hielscher, R., & Schaeben, H. (2015). Descriptive tools for the analysis of texture projects with large datasets using MTEX : strength, symmetry and components. *Geological Society, London, Special Publications*, *409*(1), 251–271. https://doi.org/10.1144/SP409.8

Mansouri, H., Prior, D. J., Ajalloeian, R., & Elyaszadeh, R. (2019). Deformation and recrystallization mechanisms inferred from microstructures of naturally deformed rock salt from the diapiric stem and surface glaciers of a salt diapir in Southern Iran. *Journal of Structural Geology*, *121*, 10–24. https://doi.org/10.1016/j.jsg.2019.01.005

Marques, F. O., Burlini, L., & Burg, J.-P. (2010). Rheology and microstructure of synthetic halite/calcite porphyritic aggregates in torsion. *Journal of Structural Geology*, *32*(3), 342–349. https://doi.org/10.1016/j.jsg.2010.01.001

Marques, F. O., Burlini, L., & Burg, J.-P. (2011a). Microstructural and mechanical effects of strong fine-grained muscovite in soft halite matrix: Shear strain localization in torsion. *Journal of Geophysical Research*, *116*(B8), B08213. https://doi.org/10.1029/2010JB008080

Marques, F. O., Burlini, L., & Burg, J.-P. (2011b). Microstructure and mechanical properties of halite/coarse muscovite synthetic aggregates deformed in torsion. *Journal of Structural Geology*, *33*(4), 624–632. https://doi.org/10.1016/j.jsg.2011.01.003

Marques, F. O., Burg, J.-P., Armann, M., & Martinho, E. (2013). Rheology of synthetic polycrystalline halite in torsion. *Tectonophysics*, *583*, 124–130. https://doi.org/10.1016/j.tecto.2012.10.024

McClay, K., Muñoz, J.-A., & García-Senz, J. (2004). Extensional salt tectonics in a contractional orogen: A newly identified tectonic event in the Spanish Pyrenees. *Geology*, *32*(9), 737. https://doi.org/10.1130/G20565.1

Means, W. D., Hobbs, B. E., Lister, G. S., & Williams, P. F. (1980). Vorticity and non-coaxiality in progressive deformations. *Journal of Structural Geology*, *2*(3), 371–378. https://doi.org/10.1016/0191-8141(80)90024-3

Mertineit, M., Schramm, M., Thiemeyer, N., Blanke, H., Patzschke, M., & Zulauf, G. (2023). Paleostress, deformation mechanisms and finite strain related to chocolate-tablet boudinage and folding of a Permian rock salt/anhydrite sequence (Morsleben site, Germany). *Tectonophysics*, *847*, 229703. https://doi.org/10.1016/j.tecto.2023.229703

Michels, Z. D., Kruckenberg, S. C., Davis, J. R., & Tikoff, B. (2015). Determining vorticity axes from grain-scale dispersion of crystallographic orientations. *Geology*, *43*(9), 803–806. https://doi.org/10.1130/G36868.1

Mika, D. P., & Dawson, P. R. (1999). Polycrystal plasticity modeling of intracrystalline boundary textures. *Acta Materialia*, *47*(4), 1355–1369. https://doi.org/10.1016/S1359-6454(98)00386-3

Miralles, L., Sans, M., Pueyo, J. J., & Santanach, P. (2000). Recrystallization salt fabric in a shear zone (Cardona diapir, southern Pyrenees, Spain). *Geological Society, London, Special Publications*, *174*(1), 149–167. https://doi.org/10.1144/GSL.SP.1999.174.01.09

Miranda, E. A., Hirth, G., & John, B. E. (2016). Microstructural evidence for the transition from dislocation creep to dislocation-accommodated grain boundary sliding in naturally deformed plagioclase. *Journal of Structural Geology*, *92*, 30–45. https://doi.org/10.1016/j.jsg.2016.09.002

Mises, R. V. (1928). Mechanik der plastischen Formänderung von Kristallen. *ZAMM - Journal of Applied Mathematics and Mechanics / Zeitschrift Für Angewandte Mathematik Und Mechanik*, *8*(3), 161–185. https://doi.org/10.1002/zamm.19280080302

Mohr, M., Kukla, P. A., Urai, J. L., & Bresser, G. (2005). Multiphase salt tectonic evolution in NW Germany: seismic interpretation and retro-deformation. *International Journal of Earth Sciences*, *94*(5–6), 917–940. https://doi.org/10.1007/s00531-005-0039-5

Morales, L. F. G., Lloyd, G. E., & Mainprice, D. (2014). Fabric transitions in quartz via viscoplastic self-consistent modeling part I: Axial compression and simple shear under constant strain. *Tectonophysics*, *636*, 52–69. https://doi.org/10.1016/j.tecto.2014.08.011

Moulinec, H., & Suquet, P. (1994). A fast numerical method for computing the linear and nonlinear mechanical properties of composites. *Comptes Rendus de l'Académie Des Sciences. Série II. Mécanique, Physique, Chimie, Astronomie*, 1417–1423. Retrieved from https://hal.science/hal-03019226/document

Moulinec, H., & Suquet, P. (1998). A numerical method for computing the overall response of nonlinear composites with complex microstructure. *Computer Methods in Applied Mechanics and Engineering*, *157*(1–2), 69–94. https://doi.org/10.1016/S0045-7825(97)00218-1

Olgaard, D. L., & Evans, B. (1988). Grain growth in synthetic marbles with added mica and water. *Contributions to Mineralogy and Petrology*, *100*(2), 246–260. https://doi.org/10.1007/BF00373591

Otsuka, T., Brenner, R., & Bacroix, B. (2018). FFT-based modelling of transformation plasticity in polycrystalline materials during diffusive phase transformation. *International Journal of Engineering Science*, *127*, 92–113. https://doi.org/10.1016/j.ijengsci.2018.02.008

Pantleon, W. (1997). On the evolution of disorientations in dislocation cell structures during plastic deformation. *Materials Science and Engineering: A*, *234–236*, 567–570. https://doi.org/10.1016/S0921-5093(97)00227-X

Pantleon, W. (1998). On the statistical origin of disorientations in dislocation structures. *Acta Materialia*, *46*(2), 451–456. https://doi.org/10.1016/S1359-6454(97)00286-3

Pantleon, W. (2001). The evolution of disorientations for several types of boundaries. *Materials Science and Engineering: A*, *319–321*, 211–215. https://doi.org/10.1016/S0921-5093(01)00947-9

Paterson, M. S., & Olgaard, D. L. (2000). Rock deformation tests to large shear strains in torsion. *Journal of Structural Geology*, *22*(9), 1341–1358. https://doi.org/10.1016/S0191-8141(00)00042-0

Peach, C. J., & Spiers, C. J. (1996). Influence of crystal plastic deformation on dilatancy and permeability development in synthetic salt rock. *Tectonophysics*, *256*(1–4), 101–128. https://doi.org/10.1016/0040-1951(95)00170-0

Peach, C. J., Spiers, C. J., & Trimby, P. W. (2001). Effect of confining pressure on dilatation, recrystallization, and flow of rock salt at 150°C. *Journal of Geophysical Research: Solid Earth*, *106*(B7), 13315–13328. https://doi.org/10.1029/2000JB900300

Pennacchioni, G., Menegon, L., Leiss, B., Nestola, F., & Bromiley, G. (2010). Development of crystallographic preferred orientation and microstructure during plastic deformation of natural coarse-grained quartz veins. *Journal of Geophysical Research: Solid Earth*, *115*(B12). https://doi.org/10.1029/2010JB007674

Pennock, G. M., & Drury, M. R. (2005). Low-angle subgrain misorientations in deformed NaCl. *Journal of Microscopy*, *217*(2), 130–137. https://doi.org/10.1111/j.1365-2818.2005.01410.x

Pennock, G. M., Drury, M. R., Trimby, P. W., & Spiers, C. J. (2002). Misorientation distributions in hot deformed NaCl using electron backscattered diffraction. *Journal of Microscopy*, *208*(1), 75–75. https://doi.org/10.1046/j.1365-2818.2002.00993.x

Pennock, G. M., Drury, M. R., & Spiers, C. J. (2005). The development of subgrain misorientations with strain in dry synthetic NaCl measured using EBSD. *Journal of Structural Geology*, *27*(12), 2159–2170. https://doi.org/10.1016/j.jsg.2005.06.013

Pennock, G. M., Coleman, M., Drury, M. R., & Randle, V. (2009). Grain boundary plane populations in minerals: the example of wet NaCl after low strain deformation. *Contributions to Mineralogy and Petrology*, *158*(1), 53–67. https://doi.org/10.1007/s00410-008-0370-5

Piazolo, S., Bestmann, M., Prior, D. J., & Spiers, C. J. (2006). Temperature dependent grain boundary migration in deformed-then-annealed material: Observations from experimentally deformed synthetic rocksalt. *Tectonophysics*, *427*(1–4), 55–71. https://doi.org/10.1016/j.tecto.2006.06.007

Piazolo, S., Bons, P. D., Griera, A., Llorens, M.-G., Gomez-Rivas, E., Koehn, D., et al. (2019). A review of numerical modelling of the dynamics of microstructural development in rocks and ice: Past, present and future. *Journal of Structural Geology*, *125*, 111–123. https://doi.org/10.1016/j.jsg.2018.05.025

Picard, D., Dimanov, A., & Raphanel, J. L. (2018). Plastic behavior of halite single-crystals at different temperatures and strain rates: New insights from in-situ experiments and full field measures. *Materials Science and Engineering: A*, *732*, 284–297. https://doi.org/10.1016/j.msea.2018.07.009

Poirier, J. P. (1976). On the symmetrical role of cross-slip of screw dislocations and climb of edge dislocations as recovery processes controlling high-temperature creep. *Revue de Physique Appliquée*, *11*(6), 731–738. https://doi.org/10.1051/rphysap:01976001106073100

Poirier, J.-P. (1985). *Creep of Crystals*. *Cambridge Earth Science Series*. Cambridge University Press. https://doi.org/10.1017/CBO9780511564451

Pokharel, R., Lind, J., Kanjarla, A. K., Lebensohn, R. A., Li, S. F., Kenesei, P., et al. (2014). Polycrystal Plasticity: Comparison Between Grain - Scale Observations of Deformation

and Simulations. *Annual Review of Condensed Matter Physics*, *5*(1), 317–346. https://doi.org/10.1146/annurev-conmatphys-031113-133846

Prior, D. J., Wheeler, J., Peruzzo, L., Spiess, R., & Storey, C. (2002). Some garnet microstructures: an illustration of the potential of orientation maps and misorientation analysis in microstructural studies. *Journal of Structural Geology*, *24*(6–7), 999–1011. https://doi.org/10.1016/S0191-8141(01)00087-6

Radhakrishnan, B., & Sarma, G. B. (2008). Coupled simulations of texture evolution during deformation and recrystallization of fcc and bcc metals. *Materials Science and Engineering: A*, *494*(1–2), 73–79. https://doi.org/10.1016/j.msea.2007.10.094

Ran, H., Bons, P. D., Wang, G., Steinbach, F., Finch, M. A., Griera, A., et al. (2018). High-strain deformation of conglomerates: Numerical modelling, strain analysis, and an example from the Wutai Mountains, North China Craton. *Journal of Structural Geology*, *114*, 222–234. https://doi.org/10.1016/j.jsg.2018.06.018

Ran, H., de Riese, T., Llorens, M.-G., Finch, M. A., Evans, L. A., Gomez-Rivas, E., et al. (2019). Time for anisotropy: The significance of mechanical anisotropy for the development of deformation structures. *Journal of Structural Geology*, *125*, 41–47. https://doi.org/10.1016/j.jsg.2018.04.019

Ran, H., Bons, P. D., Wang, G., Griera, A., de Riese, T., Gomez-Rivas, E., et al. (2022). Folds inside pebbles: When do they form during conglomerate deformation? Numerical modelling and comparison with the Hutuo Group conglomerates, North China Craton. *Journal of Structural Geology*, *160*, 104620. https://doi.org/10.1016/j.jsg.2022.104620

Randle, V. (1993). Microtexture investigation of the relationship between strain and anomalous grain growth. *Philosophical Magazine A*, *67*(6), 1301–1313. https://doi.org/10.1080/01418619308225356

Read, W. T., & Shockley, W. (1950). Dislocation Models of Crystal Grain Boundaries. *Physical Review*, *78*(3), 275–289. https://doi.org/10.1103/PhysRev.78.275

Reddy, S. M., Timms, N. E., Pantleon, W., & Trimby, P. (2007). Quantitative characterization of plastic deformation of zircon and geological implications. *Contributions to Mineralogy and Petrology*, *153*(6), 625–645. https://doi.org/10.1007/s00410-006-0174-4

Renner, J., Evans, B., & Siddiqi, G. (2002). Dislocation creep of calcite. *Journal of Geophysical Research: Solid Earth*, *107*(B12). https://doi.org/10.1029/2001JB001680

de Riese, T., Evans, L., Gomez-Rivas, E., Griera, A., Lebensohn, R. A., Llorens, M.-G., et al. (2019a). Shear localisation in anisotropic, non-linear viscous materials that develop a CPO: A numerical study. *Journal of Structural Geology*, *124*, 81–90. https://doi.org/10.1016/j.jsg.2019.03.006

de Riese, T., Evans, L., Gomez-Rivas, E., Griera, A., Lebensohn, R. A., Llorens, M.-G., et al. (2019b). Shear localisation in anisotropic, non-linear viscous materials that develop a CPO: A numerical study. *Journal of Structural Geology*, *124*, 81–90. https://doi.org/10.1016/j.jsg.2019.03.006

Roessiger, J., Bons, P. D., Griera, A., Jessell, M. W., Evans, L., Montagnat, M., et al. (2011). Competition between grain growth and grain-size reduction in polar ice. *Journal of Glaciology*, *57*(205), 942–948. https://doi.org/10.3189/002214311798043690

Roessiger, J., Bons, P. D., & Faria, S. H. (2014). Influence of bubbles on grain growth in ice. *Journal of Structural Geology*, *61*, 123–132. https://doi.org/10.1016/j.jsg.2012.11.003

Rohrer, G. S. (2011). Grain boundary energy anisotropy: a review. *Journal of Materials Science*, *46*(18), 5881–5895. https://doi.org/10.1007/s10853-011-5677-3

Roters, F., Eisenlohr, P., Hantcherli, L., Tjahjanto, D. D., Bieler, T. R., & Raabe, D. (2010). Overview of constitutive laws, kinematics, homogenization and multiscale methods in crystal plasticity finite-element modeling: Theory, experiments, applications. *Acta Materialia*, *58*(4), 1152–1211. https://doi.org/10.1016/j.actamat.2009.10.058

Rowan, M. G., Urai, J. L., Fiduk, J. C., & Kukla, P. A. (2019). Deformation of intrasalt competent layers in different modes of salt tectonics. *Solid Earth*, *10*(3), 987–1013. https://doi.org/10.5194/se-10-987-2019

Sarkarinejad, K., Sarshar, M. A., & Adineh, S. (2018). Structural, micro-structural and kinematic analyses of channel flow in the Karmostaj salt diapir in the Zagros foreland folded belt, Fars province, Iran. *Journal of Structural Geology*, *107*, 109–131. https://doi.org/10.1016/j.jsg.2017.12.005

Schléder, Z., & Urai, J. L. (2005). Microstructural evolution of deformation-modified primary halite from the Middle Triassic Röt Formation at Hengelo, The Netherlands. *International Journal of Earth Sciences*, *94*(5–6), 941–955. https://doi.org/10.1007/s00531-005-0503-2

Schléder, Z., & Urai, J. L. (2007). Deformation and recrystallization mechanisms in mylonitic shear zones in naturally deformed extrusive Eocene–Oligocene rocksalt from Eyvanekey plateau and Garmsar hills (central Iran). *Journal of Structural Geology*, *29*(2), 241–255. https://doi.org/10.1016/j.jsg.2006.08.014

Schmid, E., & Boas, W. (1950). *Plasticity of crystals*. London: F. A. Hughes & CO. LIMITED. Retrieved from

https://citeseerx.ist.psu.edu/document?repid=rep1&type=pdf&doi=d1e2e7febcb03f66d7ab79c7bda5bdfb34966ff4

Segal, V. M. (2002). Severe plastic deformation: simple shear versus pure shear. *Materials Science and Engineering: A*, *338*(1–2), 331–344. https://doi.org/10.1016/S0921-5093(02)00066-7

Sethna, J. P., Coffman, V. R., & Demler, E. (2003). Scaling in plasticity-induced cell-boundary microstructure: Fragmentation and rotational diffusion. *Physical Review B*, *67*(18), 184107. https://doi.org/10.1103/PhysRevB.67.184107

Signorelli, J., & Tommasi, A. (2015). Modeling the effect of subgrain rotation recrystallization on the evolution of olivine crystal preferred orientations in simple shear. *Earth and Planetary Science Letters*, *430*, 356–366. https://doi.org/10.1016/j.epsl.2015.08.018

Skemer, P., Warren, J. M., Kelemen, P. B., & hirth, G. (2010). Microstructural and Rheological Evolution of a Mantle Shear Zone. *Journal of Petrology*, *51*(1–2), 43–53. https://doi.org/10.1093/petrology/egp057

Skemer, Philip, Katayama, I., Jiang, Z., & Karato, S. (2005). The misorientation index: Development of a new method for calculating the strength of lattice-preferred orientation. *Tectonophysics*, *411*(1–4), 157–167. https://doi.org/10.1016/j.tecto.2005.08.023

Skrotzki, W., Helming, K., Brokmeier, H.-G., Dornbusch, H.-J., & Welch, P. (1995). Textures in Pure Shear Deformed Rock Salt. *Textures and Microstructures*, *24*(1–3), 133–141. https://doi.org/10.1155/TSM.24.133

Smith, C. S. (1948). Grains, phases, and interfaces: an interpretation of microstructure. *Transactions of the American Institute of Mining and Metallurgical Engineers*, *175*, 15–51.

Spiers, C. J., Peach, C. J., Brzesowsky, R. H., Schutjens, P. M. T. M., Liezenberg, J. L., & Zwart, H. J. (1988). *Long-term rheological and transport properties of dry and wet salt rocks*. Luxembourg: Office for Official Publications of the European Communities.

Spiers, C. J., Schutjens, P. M. T. M., Brzesowsky, R. H., Peach, C. J., Liezenberg, J. L., & Zwart, H. J. (1990). Experimental determination of constitutive parameters governing creep of rocksalt by pressure solution. *Geological Society, London, Special Publications*, *54*(1), 215–227. https://doi.org/10.1144/GSL.SP.1990.054.01.21

Steinbach, F., Bons, P. D., Griera, A., Jansen, D., Llorens, M.-G., Roessiger, J., & Weikusat, I. (2016). Strain localization and dynamic recrystallization in the ice–air aggregate: a numerical study. *The Cryosphere*, *10*(6), 3071–3089. https://doi.org/10.5194/tc-10-3071-2016

Steinbach, F., Kuiper, E.-J. N., Eichler, J., Bons, P. D., Drury, M. R., Griera, A., et al. (2017). The Relevance of Grain Dissection for Grain Size Reduction in Polar Ice: Insights from Numerical Models and Ice Core Microstructure Analysis. *Frontiers in Earth Science*, *5*. https://doi.org/10.3389/feart.2017.00066

Stipp, M., Stünitz, H., Heilbronner, R., & Schmid, S. M. (2002). The eastern Tonale fault zone: a 'natural laboratory' for crystal plastic deformation of quartz over a temperature range from 250 to 700°C. *Journal of Structural Geology*, *24*(12), 1861–1884. https://doi.org/10.1016/S0191-8141(02)00035-4

Stipp, M., Tullis, J., Scherwath, M., & Behrmann, J. H. (2010). A new perspective on paleopiezometry: Dynamically recrystallized grain size distributions indicate mechanism changes. *Geology*, *38*(8), 759–762. https://doi.org/10.1130/G31162.1

Stöckhert, B., & Duyster, J. (1999). Discontinuous grain growth in recrystallised vein quartz — implications for grain boundary structure, grain boundary mobility, crystallographic preferred orientation, and stress history. *Journal of Structural Geology*, *21*(10), 1477–1490. https://doi.org/10.1016/S0191-8141(99)00084-X

Sun, R. C., & Bauer, C. L. (1970). Tilt boundary migration in NaCl bicrystals. *Acta Metallurgica*, *18*(6), 639–647. https://doi.org/10.1016/0001-6160(70)90093-3

Sundberg, M., & Cooper, R. F. (2008). Crystallographic preferred orientation produced by diffusional creep of harzburgite: Effects of chemical interactions among phases during plastic flow. *Journal of Geophysical Research: Solid Earth*, *113*(B12). https://doi.org/10.1029/2008JB005618

Takeda, Y.-T., & Griera, A. (2006). Rheological and kinematical responses to flow of two-phase rocks. *Tectonophysics*, *427*(1–4), 95–113. https://doi.org/10.1016/j.tecto.2006.03.050

Talbot, C. J., & Jackson, M. P. A. (1987). Internal Kinematics of Salt Diapirs. *AAPG Bulletin*, *71*(9), 1068–1093. https://doi.org/10.1306/703C7DF9-1707-11D7-8645000102C1865D

Talbot, Christopher J., & Pohjola, V. (2009). Subaerial salt extrusions in Iran as analogues of ice sheets, streams and glaciers. *Earth-Science Reviews*, *97*(1–4), 155–183. https://doi.org/10.1016/j.earscirev.2009.09.004

Thiemeyer, N., Zulauf, G., Mertineit, M., Linckens, J., Pusch, M., & Hammer, J. (2016). Microfabrics and 3D grain shape of Gorleben rock salt: Constraints on deformation mechanisms and paleodifferential stress. *Tectonophysics*, *676*, 1–19. https://doi.org/10.1016/j.tecto.2016.02.046

Tikoff, B., & Fossen, H. (1995). The limitations of three-dimensional kinematic vorticity analysis. *Journal of Structural Geology*, *17*(12), 1771–1784. https://doi.org/10.1016/0191-8141(95)00069-P

Trimby, P. W., Drury, M. R., & Spiers, C. J. (2000). Recognising the crystallographic signature of recrystallisation processes in deformed rocks: a study of experimentally deformed rocksalt. *Journal of Structural Geology*, *22*(11–12), 1609–1620. https://doi.org/10.1016/S0191-8141(00)00059-6

Truesdell, C. (1953). Two Measures of Vorticity. *Journal of Rational Mechanics and Analysis*, *2*, 173–217. Retrieved from http://www.jstor.org/stable/24900328

Tullis, J., & Wenk, H.-R. (1994). Effect of muscovite on the strength and lattice preferred orientations of experimentally deformed quartz aggregates. *Materials Science and Engineering: A*, *175*(1–2), 209–220. https://doi.org/10.1016/0921-5093(94)91060-X

Twiss, R. J. (1977). Theory and Applicability of a Recrystallized Grain Size Paleopiezometer. In *Stress in the Earth* (Vol. 115, pp. 227–244). Basel: Birkhäuser Basel. https://doi.org/10.1007/978-3-0348-5745-1_13

Urai, J. L., Means, W. D., & Lister, G. S. (1986). Dynamic recrystallization of minerals. In B. E. Hobbs & H. C. Heard (Eds.), *Mineral and rock deformation: laboratory studies: The Paterson Volume* (Vol. 36, pp. 161–199). Washington, D. C.: American Geophysical Union. https://doi.org/https://doi.org/10.1029/GM036p0161

Urai, J. L., Spiers, C. J., Zwart, H. J., & Lister, G. S. (1986). Weakening of rock salt by water during long-term creep. *Nature*, *324*(6097), 554–557. https://doi.org/10.1038/324554a0

Urai, J. L., Schléder, Z., Spiers, C. J., & Kukla, P. A. (2008). Flow and transport properties of salt rocks. In R. Littke, U. Bayer, D. Gajewski, & S. Nelskamp (Eds.), *Dynamics of*

complex intracontinental basins: The central European basin system (pp. 277–290). Berlin: Springer.

Vargas-Meleza, L., Healy, D., Alsop, G. I., & Timms, N. E. (2015). Exploring the relative contribution of mineralogy and CPO to the seismic velocity anisotropy of evaporites. *Journal of Structural Geology*, *70*, 39–55. https://doi.org/10.1016/j.jsg.2014.11.001

Wawersik, W. R., & Zeuch, D. H. (1986). Modeling and mechanistic interpretation of creep of rock salt below 200°C. *Tectonophysics*, *121*(2–4), 125–152. https://doi.org/10.1016/0040-1951(86)90040-5

Weaire, D., & Rivier, N. (1984). Soap, cells and statistics—random patterns in two dimensions. *Contemporary Physics*, *25*(1), 59–99. https://doi.org/10.1080/00107518408210979

Weijermars, R., Jackson, M. P. A., & Vendeville, B. (1993). Rheological and tectonic modeling of salt provinces. *Tectonophysics*, *217*(1–2). https://doi.org/10.1016/0040-1951(93)90208-2

Wenk, H. R., Takeshita, T., Bechler, E., Erskine, B. G., & Matthies, S. (1987). Pure shear and simple shear calcite textures. Comparison of experimental, theoretical and natural data. *Journal of Structural Geology*, *9*(5–6), 731–745. https://doi.org/10.1016/0191-8141(87)90156-8

Wenk, H. R., Canova, G., Molinari, A., & Mecking, H. (1989). Texture development in halite: Comparison of Taylor model and self-consistent theory. *Acta Metallurgica*, *37*(7), 2017–2029. https://doi.org/10.1016/0001-6160(89)90086-2

Wenk, H.-R., Bennett, K., Canova, G. R., & Molinari, A. (1991). Modelling plastic deformation of peridotite with the self-consistent theory. *Journal of Geophysical Research*, *96*(B5), 8337. https://doi.org/10.1029/91JB00117

Wenk, H.-R., Armann, M., Burlini, L., Kunze, K., & Bortolotti, M. (2009). Large strain shearing of halite: Experimental and theoretical evidence for dynamic texture changes. *Earth and Planetary Science Letters*, *280*(1–4), 205–210. https://doi.org/10.1016/j.epsl.2009.01.036

Xypolias, P. (2010). Vorticity analysis in shear zones: A review of methods and applications. *Journal of Structural Geology*, *32*(12), 2072–2092. https://doi.org/10.1016/j.jsg.2010.08.009

Yu, Y., Griera, A., Gomez-Rivas, E., Bons, P. D., García-Castellanos, D., Hao, B., et al. (2024). Dynamic Recrystallization of Olivine During Simple Shear: Evolution of Microstructure and Crystallographic Preferred Orientation From Full-Field Numerical Simulations. *Geochemistry, Geophysics, Geosystems*, *25*(9). https://doi.org/10.1029/2023GC011212

Závada, P., Desbois, G., Urai, J. L., Schulmann, K., Rahmati, M., Lexa, O., & Wollenberg, U. (2015). Impact of solid second phases on deformation mechanisms of naturally deformed salt rocks (Kuh-e-Namak, Dashti, Iran) and rheological stratification of the Hormuz Salt Formation. *Journal of Structural Geology*, *74*, 117–144. https://doi.org/10.1016/j.jsg.2015.02.009

Závada, Prokop, Desbois, G., Schwedt, A., Lexa, O., & Urai, J. L. (2012). Extreme ductile deformation of fine-grained salt by coupled solution-precipitation creep and microcracking: Microstructural evidence from perennial Zechstein sequence (Neuhof salt mine, Germany). *Journal of Structural Geology*, *37*, 89–104. https://doi.org/10.1016/j.jsg.2012.01.024

Appendix 1. Article1

Hao, B., Llorens, M. -G., Griera, A., Bons, P. D., Lebensohn, R. A., Yu, Y., & Gomez-Rivas, E. (2023). Full-Field Numerical Simulation of Halite Dynamic Recrystallization From Subgrain Rotation to Grain Boundary Migration. *Journal of Geophysical Research: Solid Earth*, *128*(12). https://doi.org/10.1029/2023JB027590

JGR Solid Earth

RESEARCH ARTICLE
10.1029/2023JB027590

Full-Field Numerical Simulation of Halite Dynamic Recrystallization From Subgrain Rotation to Grain Boundary Migration

B. Hao[1], M.-G. Llorens[2], A. Griera[3], P. D. Bons[4], R. A. Lebensohn[5], Y. Yu[2], and E. Gomez-Rivas[1]

[1]Departament de Mineralogia, Petrologia i Geologia Aplicada, Universitat de Barcelona, Barcelona, Spain, [2]Geosciences Barcelona, CSIC, Barcelona, Spain, [3]Departament de Geologia, Universitat Autònoma de Barcelona, Barcelona, Spain, [4]Department of Geosciences, Eberhard Karls University of Tübingen, Tübingen, Germany, [5]Materials Science and Technology Division, Los Alamos National Laboratory, Los Alamos, NM, USA

Key Points:

- The temperature-dependent transition from subgrain rotation to grain boundary migration (GBM) is simulated, reproducing torsion experiments
- Isotropic GBM changes grain size and shape but only slightly affects crystallographic preferred orientation
- The relationship between subgrain misorientation and strain is influenced by dynamic recrystallization and thus by temperature

Supporting Information:

Supporting Information may be found in the online version of this article.

Correspondence to:

E. Gomez-Rivas,
e.gomez-rivas@ub.edu

Citation:

Hao, B., Llorens, M.-G., Griera, A., Bons, P. D., Lebensohn, R. A., Yu, Y., & Gomez-Rivas, E. (2023). Full-field numerical simulation of halite dynamic recrystallization from subgrain rotation to grain boundary migration. *Journal of Geophysical Research: Solid Earth*, *128*, e2023JB027590. https://doi.org/10.1029/2023JB027590

Received 3 AUG 2023
Accepted 20 NOV 2023

Author Contributions:

Conceptualization: B. Hao, M.-G. Llorens, A. Griera, E. Gomez-Rivas
Data curation: B. Hao, M.-G. Llorens, A. Griera, E. Gomez-Rivas
Formal analysis: B. Hao, M.-G. Llorens, A. Griera, P. D. Bons, E. Gomez-Rivas
Funding acquisition: M.-G. Llorens, A. Griera, E. Gomez-Rivas
Investigation: B. Hao, M.-G. Llorens, A. Griera, E. Gomez-Rivas

Abstract Full-field numerical modeling is a useful method to gain understanding of rock salt deformation at multiple scales, but it is quite challenging due to the anisotropic and complex plastic behavior of halite, together with dynamic recrystallization processes. This contribution presents novel results of full-field numerical simulations of coupled dislocation glide and dynamic recrystallization of halite polycrystalline aggregates during simple shear deformation, including both subgrain rotation and grain boundary migration (GBM) recrystallization. The results demonstrate that the numerical approach successfully replicates the evolution of pure halite microstructures from laboratory torsion deformation experiments at 100–300°C. Temperature determines the competition between (a) grain size reduction controlled by dislocation glide and subgrain rotation recrystallization (at low temperature) and (b) grain growth associated with GBM (at higher temperature), while the resulting crystallographic preferred orientations are similar for all cases. The relationship between subgrain misorientation and strain follows a power law relationship with a universal exponent of 2/3 at low strain. However, dynamic recrystallization causes a progressive deviation from this relationship when strain increases, as revealed by the skewness of the subgrain misorientation distribution. A systematic investigation of the subgrain misorientation evolution shows that strain or temperature prediction from microstructures requires careful calibration.

Plain Language Summary Rock salt, which is dominantly composed of halite, has unique physical properties and plays a key role controlling the evolution of sedimentary basins and mountain chains. Such rocks are also important in petroleum systems, and are used for the geological storage of Geo-Energy products. However, understanding rock salt behavior is challenging because multiple deformation and recrystallization processes often operate simultaneously when halite is subjected to stress. This contribution presents microdynamic numerical simulations that replicate the main processes that take place during halite deformation at different temperatures. These include glide of dislocations, which are crystallographic defects, and temperature-controlled recrystallization processes including rotation of subgrains, nucleation of new grains, and migration of existing grain boundaries. The simulations are compared with laboratory experiments, and successfully reproduce them. Subgrain rotation is active at low temperatures, leading to the splitting of grains into smaller ones. As temperature increases, grain boundaries become mobile and grains grow to reduce the energy produced by dislocation glide. Although these processes strongly influence the resulting microstructure, the crystallographic axes are oriented similarly in all cases. We discuss how the effects of multiple microdynamic processes can be evaluated together to accurately estimate strain and the deformation conditions of rock salt.

1. Introduction

Evaporites, including rock salt, are common components of sedimentary successions and have unique physical properties such as low permeability, low density, low strength, and high ductility. Owing to these properties, salt deposits play a key role in the dynamic evolution of sedimentary basins and orogens (e.g., Canérot et al., 2005; Fossen, 2010). Their ability to flow in a viscous manner in the solid state results in the formation of structures such as salt diapirs, which cause faulting and folding of their surrounding rocks and thus often control traps in oil

Methodology: B. Hao, M.-G. Llorens, A. Griera, P. D. Bons, R. A. Lebensohn, Y. Yu, E. Gomez-Rivas
Project Administration: M.-G. Llorens, A. Griera, E. Gomez-Rivas
Resources: M.-G. Llorens, A. Griera, E. Gomez-Rivas
Software: B. Hao, M.-G. Llorens, A. Griera, P. D. Bons, R. A. Lebensohn, E. Gomez-Rivas
Supervision: M.-G. Llorens, A. Griera, E. Gomez-Rivas
Validation: B. Hao, M.-G. Llorens, A. Griera, P. D. Bons, Y. Yu, E. Gomez-Rivas
Visualization: B. Hao, M.-G. Llorens, A. Griera, P. D. Bons, E. Gomez-Rivas
Writing – original draft: B. Hao
Writing – review & editing: M.-G. Llorens, A. Griera, P. D. Bons, R. A. Lebensohn, Y. Yu, E. Gomez-Rivas

and natural gas reservoirs (Hudec & Jackson, 2007). Moreover, rock salt typically acts as detachment levels for thrusts, and determines the lateral displacement of overlying rock units and, accordingly, the dynamic evolution of orogens (McClay et al., 2004). Moreover, the dominant salt mineral halite has been extensively used as an analogue material in deformation experiments for silicate rocks and metals. This is due to its mechanical properties, which facilitate the study of deformation mechanisms at laboratory spatial and temporal scales. Specifically, halite exhibits deformation behavior that is akin to that of crustal rocks, but at substantially lower confining pressures and temperatures (Drury & Urai, 1990). Halite is also a key mineral for the energy transition, since subsurface salt bodies are targets for the storage of geo-energy products, such as hydrogen or compressed air in salt caverns. Therefore, improving our understanding of how halite deforms and recrystallizes under different conditions is essential both in terms of fundamental science, and also to meet societal challenges.

The microdynamic evolution of rock salt is controlled by the interaction between different deformation mechanisms that mostly depend on the temperature, stress/strain rate, confining pressure and water content, among others (Bourcier et al., 2013; Carter & Heard, 1970; Franssen, 1994; Franssen & Spiers, 1990; Hunsche & Hampel, 1999; Linckens et al., 2016; ter Heege et al., 2005a, 2005b; Wenk et al., 2009). At low temperature and high deviatoric stress, (semi-) brittle failure occurs in rock salt, mainly resulting in microcrack formation and propagation, and intergranular sliding (Peach & Spiers, 1996; Peach et al., 2001). As confining pressure and temperature increase cracking is suppressed, and halite deformation is dominated by dislocation creep (e.g., Urai et al., 2008). When brine is present, dislocation creep can be accompanied by dissolution-precipitation creep (Spiers et al., 1988, 1990). Dynamic recrystallization (DRX) processes accompany dislocation creep and affect the rock salt microstructure by causing changes in grain size, grain boundary network, and influencing shape-preferred orientations (SPO) (Desbois et al., 2010; Franssen, 1994; Guillope & Poirier, 1979; Mansouri et al., 2019; Schléder & Urai, 2007; ter Heege et al., 2004). DRX can result in grain size reduction or grain growth depending on the balance of driving forces involved. Grain size reduction takes place by subgrain rotation recrystallization (SGR), where the movement and reorganization of dislocations leads to the gradual increase of the local misorientation between the crystal lattices forming subgrain boundaries (low-angle grain boundaries, LAGBs), which may finally evolve to form high-angle grain boundaries (HAGBs) and the formation of new grains (Urai et al., 1986). Grain size increase is the result of grain boundary migration (GBM), a recrystallization process characterized by the migration of grain boundaries by diffusion of atoms across the boundary between grains. There are several driving forces for GBM in rocks (e.g., Bons et al., 2008). When GBM is driven by the reduction of the difference in stored strain energy (i.e., associated with dislocation densities) across the boundaries is called strain-induced GBM. During strain-induced GBM, grain boundaries migrate from grains with low dislocation density to neighboring grains with high dislocation density due to the difference in strain energy. When GBM is driven by the reduction of grain-boundary surface energy it is called surface energy-induced or boundary-energy induced GBM (Karato, 2008; Weaire & Rivier, 1984). During boundary energy-induced GBM, grain boundaries from large grains tend to overgrow small grains driven by the reduction of grain curvature, which results in grain growth (Karato, 2008). The final microstructure and grain size will depend on the competition of the interacting processes between grain size growth and reduction (Franssen, 1994; Gomez-Rivas et al., 2020; Leitner et al., 2011 and references therein).

The amount of plastic strain correlates with the probability density of subgrain misorientation angles in polycrystalline aggregates in which dislocation creep is the dominant deformation mechanism (Hughes et al., 1998, 2003, 1997; Hughes & Hansen, 2018; Pennock & Drury, 2005; Pennock et al., 2002). A scaling behavior between the mean subgrain misorientation and finite strain was proposed based on metal deformation experiments (Hughes et al., 1997), and its physical origin was established by Pantleon (1997, 1998, 2001). Pennock et al. (2005, 2002) observed that this also applies to halite and found a power-law relationship between the mean subgrain misorientation and natural strain for relatively low finite strain (up $\varepsilon = 0.54$). Their results are in agreement with numerical simulations of Mika and Dawson (1999) and Gomez-Rivas et al. (2017). This strain gauge can be a useful tool for structural analysis if it can be further tested and generalized for materials deformed under a variety of dynamic recrystallization processes, and thus at different temperatures. However, the effect of GBM on the probability density of subgrain misorientation angles has not yet been evaluated, although this recrystallization process dominates the mechanical behavior of wet rock salt in a wide range of conditions, and also of dry rock salt at relatively high temperature (Leitner et al., 2011; Trimby et al., 2000). GBM produces a reduction of intragranular heterogeneities and a significant change in the microstructure of polycrystalline aggregates (Urai et al., 1986), in a way that subgrain misorientation and the grain boundary network may not clearly reflect the strain a volume of rock has experienced (Llorens, Griera, Bons, Lebensohn, et al., 2016).

New insights into halite deformation mechanisms and rheology can be gained from laboratory experiments of natural or synthetic rock salt, and from the careful observation of samples deformed in natural settings. However, natural samples only show a "frozen" stage of the deformation history, while rock deformation experiments are inherently limited by the grain size and strain rate that can be achieved in the laboratory (e.g., Franssen, 1994; Picard et al., 2018; ter Heege et al., 2005b). Numerical simulations can overcome these barriers and are considered a key complement to these techniques. Compared to experiments, simulations allow polycrystalline aggregates to achieve significantly higher finite strains at lower strain rates, and can be used to explore a wide range of deformation conditions by varying parameters such as the sample size, strain rate, and temperature. Moreover, numerical simulations allow studying the influence of deformation mechanisms in isolation and also how they interact when they are coupled (Amelirad & Assempour, 2022; Bons et al., 2008; Eisenlohr et al., 2013; Lebensohn, 2001; Otsuka et al., 2018; Pokharel et al., 2014). Several numerical approaches have been developed to simulate dynamic recrystallization of polycrystalline materials. For example, Signorelli and Tommasi (2015) combined the viscoplastic self-consistent approach (VPSC, Lebensohn & Tomé, 1993; Liu et al., 2005; Wenk et al., 1991) with a subgrain formation probability model so as to account for SGR effects in the evolution of crystallographic preferred orientations (CPOs). In this approach, each grain is regarded as an inhomogeneity in a viscoplastic homogeneous effective medium, and therefore it does not take into account the intragranular heterogeneities for the simulation of DRX processes. Radhakrishnan and Sarma (2008) simulated DRX and the resulting CPOs in metals by coupling finite element (FEM) and Monte-Carlo (MC) approaches. However, FEM requires a high-resolution mesh to reproduce the details of heterogeneous deformation of the microstructure, which limits the use of models at larger scales due to the limitations of computational time (Roters et al., 2010). Additionally, since the changes of the microstructure in MC models occur randomly, the final texture components are highly dependent on the nucleation criterion. Another approach is the D-Rex method, which employs a kinematic constraint model to simulate dynamic recrystallization by introducing two dimensionless parameters of nucleation and GBM, but without considering mechanical interactions between grains (D-Rex, Kaminski & Ribe, 2001; Kaminski et al., 2004). All the methods mentioned above have limitations for the simulation of the evolution of the rock texture, grain boundary network and grain size.

The full-field formulation based on Fast Fourier Transforms (FFT, Moulinec & Suquet, 1994) allows overcoming the aforementioned limitations. It was initially designed to predict the mechanical properties of composite materials (Moulinec & Suquet, 1998), and was later applied to polycrystalline single-phase aggregates by Lebensohn (2001), which provided an efficient solution to model the spatial evolution of viscoplastic deformation. The Viscoplastic Full-Field Transform code (VPFFT, Lebensohn et al., 2003; Lebensohn & Rollett, 2020) and the numerical software platform ELLE (Bons et al., 2008; Jessell et al., 2001; Piazolo et al., 2019; Ran et al., 2018) were integrated for the large-strain full-field simulation of dislocation creep (Griera et al., 2011, 2013). The numerical scheme comprises a variety of dynamic recrystallization processes, including intracrystalline recovery, grain nucleation, and GBM, by mapping misorientations between local lattice orientations on a regular grid. This full-field numerical modeling approach has been widely used to model the evolution of microstructure of polycrystals such as 1-h ice and halite, as well as multiphase anisotropic rocks (Finch et al., 2022; Gomez-Rivas et al., 2017; Llorens, Griera, Bons, Lebensohn, et al., 2016; Ran et al., 2022; Steinbach et al., 2016).

This contribution presents VPFFT-ELLE simulations of the deformation of halite polycrystalline aggregates at 100°C, 200°C, and 300°C including SGR and GBM recrystallization processes, up to a finite shear strain (γ) of four. The simulations are calibrated by comparing them with torsion experiments of synthetic pure rock salt by Armann (2008). Moreover, we investigate how the interplay between SGR and GBM processes influences grain size and grain morphology at different temperatures. In addition, we estimate the subgrain misorientation of whole grains and evaluate the use of the geometric mean of subgrain misorientation as a strain gauge for systems deformed at different temperatures and, therefore, under different recrystallization processes (i.e., SGR vs. GBM-dominated). This approach allows to systematically visualize and quantify the influence of temperature on rock deformation, test how different recrystallization processes affect strain gauges, and analyze whether subgrain misorientations can be utilized to reveal the environmental conditions under which rocks deform.

2. Methods

2.1. ELLE Numerical Platform

ELLE is an open-source multi-scale software used to simulate the evolution of microstructures during deformation and metamorphic processes (http://www.elle.ws). So far, it has been widely used to simulate a variety

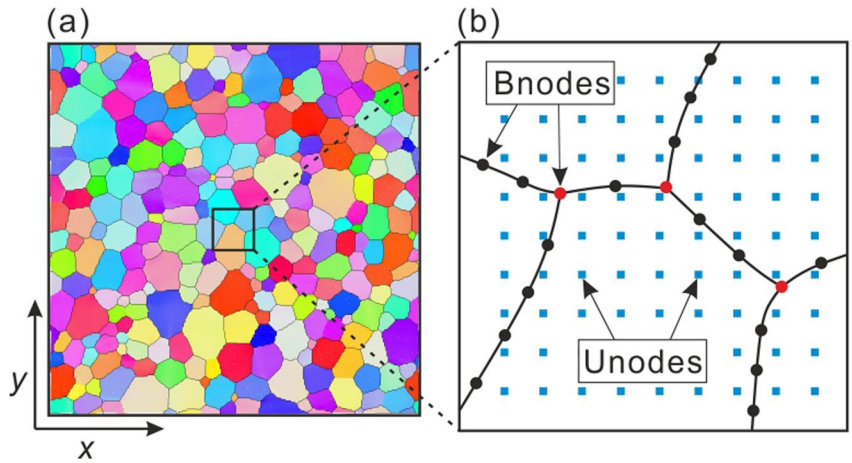

Figure 1. (a) Initial microstructure used in this study, and (b) maximization showing the discretization in two layers of unconnected nodes (*unodes*) and boundary nodes (*bnodes*) used in the numerical approach. Each color in (a) represents a different crystallographic orientation.

of microstructural processes, such as static grain growth (Jessell et al., 2003; Roessiger et al., 2011), dynamic recrystallization (Gomez-Rivas et al., 2017; Llorens, Griera, Bons, Roessiger, et al., 2016, 2017; Steinbach et al., 2016, 2017), strain localization (de Riese et al., 2019; Griera et al., 2011), rotation of rigid objects in anisotropic rocks (Griera et al., 2013; Ran et al., 2019), or deformation of multiple phase materials (Finch et al., 2020, 2022; Jessell et al., 2009; Llorens et al., 2019; Ran et al., 2018; Steinbach et al., 2017) among many other studies. A comprehensive introduction to the ELLE principles and modeling approach can be found in Bons et al. (2008) and more recent developments in the review by Piazolo et al. (2019).

Here the data structure of ELLE is only briefly introduced, and the reader is referred to the aforementioned reviews for more details. In ELLE, a 2D polycrystalline aggregate (Figure 1a) is discretized in two data layers as shown in Figure 1b: (a) a periodic grid formed by unconnected nodes (*unodes*) or Fourier points, which are regarded as crystallites (i.e., the smallest unit with homogeneous properties) and used to store physical properties such as dislocation density, local stress, or local lattice orientation, among other parameters, and (b) a set of continuous polygons that are here defined as grains, defined by boundary nodes (*bnodes*) and straight line segments linking them. These boundary nodes can move to simulate GBM.

ELLE uses an operator-splitting approach (Becker et al., 2008; Bons et al., 2008), whereby the initial data file goes through a loop of sequential processes at each time step of the simulation (Figure 2). This loop includes deformation by dislocation glide, using the VPFFT approach, and all DRX processes organized in a subloop. On top of these main processes, other routines are used for data management, data conversion, and topology checks. The next section provides an overview of the processes used in this study. ELLE and VPFFT use periodic boundaries, where the left and right parts of the model unit cell, as well as the upper and lower ones, are connected and continuous (Jessell et al., 2001). After each deformation step, the areas that fall out of the square unit cell are repositioned back into the unit cell (Reposition, Figure 2). This approach allows visualizing the microstructure even at very high shear strains.

2.2. VPFFT—Viscoplastic Deformation by Dislocation Glide

The VPFFT (Lebensohn, 2001) is a suitable and widely used method for solving problems in the field of micromechanics. The approach is based on the application of Green functions to transform and solve the mechanical problem by means of the fast Fourier transform algorithm. The approach minimizes the average local work rate under the constraints of compatibility and equilibrium by finding an admissible stress and strain rate field. A detailed explanation of the VPFFT method can be found in Lebensohn (2001) and Lebensohn and Rollett (2020), and its implementation in ELLE is described by Griera et al. (2013). The VPFFT is a spectral method that discretizes the polycrystalline aggregate into a periodic rectangular grid composed of Fourier points. This approach assumes that the crystalline deformation of the polycrystalline aggregate is only achieved by dislocation slip

Table 1
Input Properties of Numerical Simulations

Symbol	Explanation	Input value
	Unit length	3×10^{-3} m
	Minimum *bnode* separation	3.96×10^{-5} m
	Maximum *bnode* separation	1.8×10^{-5} m
	Time step per simulation step	100 s
	Incremental strain per simulation step	0.03
n	Stress exponent (Carter & Heard, 1970)	7
$\tau_{\{110\}}$	Critical resolved shear stress of $\{110\} < \bar{1}10 >$ slip system (Carter & Heard, 1970)	1
$\tau_{\{111\}}$	Critical resolved shear stress of $\{111\} < \bar{1}10 >$ slip system (Carter & Heard, 1970)	2
$\tau_{\{100\}}$	Critical resolved shear stress of $\{100\} < 011 >$ slip system (Carter & Heard, 1970)	3
b	Burgers vector (Frost & Ashby, 1982)	3.9×10^{-10} m
G	Shear modulus	7.1×10^{9} Pa
M_0	Intrinsic mobility (Piazolo et al., 2006; Sun & Bauer, 1970)	1.5×10^{-7} m^4 J^{-1} s^{-1}
Q	Grain boundary migration activation energy (Piazolo et al., 2006)	4.7×10^{4} J mol^{-1}
J	Boundary energy (Bruno et al., 2008) (average value)	0.36 J m^{-2}
α_{hagb}	Critical minimum misorientation for halite high-angle boundaries (Pennock et al., 2005)	10°

along predefined slip systems of the crystal. The calculation of stress $\sigma'(\mathbf{x})$ and strain rate $\dot{\varepsilon}_{ij}(\mathbf{x})$ at each Fourier point obeys a nonlinear viscous rate-dependent power law based on the strength of the different slip systems. The constitutive equation is given by:

$$\dot{\varepsilon}_{ij}(\mathbf{x}) = \sum_{s=1}^{N_s} m_{ij}^{s}(\mathbf{x})\dot{\gamma}^{s}(\mathbf{x}) = \dot{\gamma}_0 \sum_{s=1}^{N_s} m_{ij}^{s}(\mathbf{x}) \left| \frac{m^{s}(\mathbf{x}) : \sigma'(\mathbf{x})}{\tau^{s}(\mathbf{x})} \right|^{n} \mathrm{sgn}\left(m^{s}(\mathbf{x}) : \sigma'(\mathbf{x})\right), \quad (1)$$

where N_s is the number of all slip systems in the crystal, m_{ij}^{s} is the symmetric Schmid tensor, $\dot{\gamma}^{s}$ is the shear strain rate, $\dot{\gamma}_0$ is a reference strain rate, τ^{s} is critical resolved shear stress for the slip system s, and n is the stress exponent. Here we use an exponent of $n = 7$ for all the slip systems (Table 1). The actual stress exponent (n) obtained from torsion experiments ranges from 4.5 to 5.4 (Armann, 2008), which is consistent with the n values (4.1–13.2) obtained from other experiments (Carter et al., 1993; Franssen, 1994; Marques et al., 2013; Wawersik & Zeuch, 1986). In order to be consistent with previous halite viscoplastic simulations (e.g., Gomez-Rivas et al., 2017) all simulations presented here are carried out with $n = 7$.

2.3. ELLE—Recrystallization Processes

The simulation of recrystallization processes is applied in a subloop with three main numerical modules that simulate polygonization, GBM, and intracrystalline recovery. The polygonization module determines whether to generate new HAGBs if the misorientation angle of a cluster of *unodes* (i.e., subgrain) is higher than a predefined threshold. The movement of HAGBs is applied by the GBM code (Becker et al., 2008; Llorens, Griera, Bons, Roessiger, et al., 2016), which calculates their displacement based on the grain boundary energy and the intragranular strain stored energy as driving forces. The intracrystalline recovery process is driven by the reduction of the local misorientation and associated energy of dislocation densities, and reproduces the annihilation of dislocations and their rearrangement into LAGBs (Borthwick et al., 2014; Gomez-Rivas et al., 2017). It is worth noting that the *unodes* in ELLE code and the Fourier points in VPFFT have a one-to-one mapping relationship, where the physical properties stored in *unodes* and Fourier points can be directly transferred between the ELLE and VPFFT code (Griera et al., 2013).

2.3.1. Polygonization

In the polygonization process, new grains are defined as clusters of *unodes*, in a way that the misorientation between them and that of adjacent clusters is greater than the predefined misorientation threshold (HAGB),

which is set to 10° following Pennock et al. (2005). The polygonization routine detects clusters with misorientation higher than the predefined threshold and inserts new boundary nodes between them to segment the preexisting grain. Specifically, the approach uses Voronoi tessellations of the *unode* layer clipped to the preexistent grain boundaries to define new positions of *bnodes* from a cluster of critical *unodes*. The new grain is therefore defined as a small part of a preexistent grain and, therefore, preserves the topology of the grain network. Two main restrictions are imposed in this approach: (a) island grains (i.e., new grains within old grains) are not allowed to prevent topology misfits and (b) a minimum of four *unodes* are required to create a new grain in order to prevent numerical instabilities due to lack of information inside the new grain. The reader is referred to Steinbach et al. (2016) for a more detailed description of this numerical process.

2.3.2. Grain Boundary Migration (GBM)

The GBM code used in this contribution is the same as the one described in Llorens, Griera, Bons, Lebensohn, et al. (2016) and Steinbach et al. (2016). This subsection provides an overview of the process, but a more detailed explanation of the approach and its implementation can be found in Becker et al. (2008) and Llorens, Griera, Bons, Roessiger, et al. (2016). The driving forces used to move HAGBs are the reduction of grain boundary energy and intragranular strain energy. The driving stress (ΔF) can be expressed as:

$$\Delta F = \Delta H - \frac{2J}{r}, \tag{2}$$

where J is the boundary energy and r is the local radius of curvature of the grain boundary. ΔH is the differential strain stored energy across a grain boundary, which is calculated from the shear modulus (G, assumed to be isotropic), the Burgers vector (b), and the difference in dislocation density ($\Delta\rho$):

$$\Delta H = \Delta\rho G|b|^2. \tag{3}$$

The velocity of a grain boundary (v) is calculated from the grain boundary mobility (M) and driving stress (ΔF):

$$v = M\Delta F\vec{n}, \tag{4}$$

where $\vec{n}$ is the unit vector perpendicular to the boundary. M has an exponential relationship with temperature (T), which is calculated from the GBM activation energy (Q), the intrinsic mobility (M_0), and the universal gas constant (R):

$$M = M_0 \exp^{(-Q/RT)}. \tag{5}$$

The GBM code is based on the front-tracking method of Becker et al. (2008), which moves the boundary nodes (*bnodes*) to achieve a reduction of Gibb's free energy. This direction is determined using four orthogonal trial positions close to the current *bnode* position and determining the gradient of energy reduction in x and y directions. In the area swept by the grain boundary movement, the dislocation density ρ is set to 0. All parameters involved in GBM are listed in Table 1.

2.3.3. Intracrystalline Recovery

This module simulates intracrystalline recovery, reproducing the annihilation of dislocations and their rearrangement into LAGBs. This approach assumes that intracrystalline heterogeneities in the lattice orientation produce a local increase of the effective interface energy of low angle boundaries. The reduction of local misorientation produces a reduction of the free energy of the system. The approach assumes that the rotation rate of the *unode* or crystallite is proportional to the torque (Randle, 1993), and follows a linear viscous rate law (i.e., linear relationship between shear stress and strain rate) (Gomez-Rivas et al., 2017). For a random *unode* chosen, the module only considers the first-neighbor *unodes* belonging in the same grain (i.e., *unodes* with a local misorientation angle lower than HAGB). The routine calculates for each *unode* the local misorientation and boundary energy with respect to the neighbor *unodes* following the Read-Schockley equation (Read & Shockley, 1950). Then, a small increment of the lattice orientation (in our simulations 0.02°) of the reference *unode* is applied using sample directions as rotation axis. The reference *unode* crystal orientation is changed toward the value that accounts for the maximum energy reduction. For a detailed description of the recovery module, the reader is referred to Borthwick et al. (2014) and Gomez-Rivas et al. (2017) (including the supplementary material of the latter publication).

Table 2
Numerical Simulation Setup

Simulation name	Temperature (°C)	Recovery/polygonization/ GBM/VPFFT steps*	Initial average grain size (μm)	Final average grain size (μm)	Equivalent final time (s)/Shear strain	Strain rate (s^{-1})
G10_100	100	0/0/10/0	212	212	13,300/0	0
G10_200	200	0/0/10/0	212	223	13,300/0	0
G10_300	300	0/0/10/0	212	299	13,300/0	0
DRX_100	100	5/20/10/1	212	92	13,300/4	3×10^{-4}
DRX_200	200	5/20/10/1	212	135	13,300/4	3×10^{-4}
DRX_300	300	5/20/10/1	212	303	13,300/4	3×10^{-4}

Note. * indicates the number of subloops of the different processes during one simulation step. The suffix of the simulation name indicates the temperature.

2.4. Validation of the Numerical Setup With Experimental Results

In order to calibrate our modeling approach, torsion experiments of synthetic rock salt by Armann (2008) have been compared with the results of our simulations. The parameters analyzed include, but are not limited to, grain size statistics, crystallographic orientation maps, and pole figures. The halite polycrystalline aggregate used in the experiments of Armann (2008) (with a water content of 35 ppm, determined by Fourier transform infrared spectroscopy—FTIR) consisted of isotropic polygonal crystals with an initial average grain size of 216 μm. Cylindrical samples with a diameter of 15 mm were cored from the starting material and dried at atmospheric pressure and 110°C for at least 24 hr before testing (following the protocol by Marques et al., 2013). The torsion experiments were conducted in a temperature-controlled triaxial deformation Paterson rig (Paterson & Olgaard, 2000). Shear strain rate and shear strain increase linearly in the torsion experiments from the sample's central axis to the outer circumference, and any position of the sample can be regarded as undergoing approximate simple shear deformation. The experiments of Armann (2008) were carried out at three sets of constant twist rates, corresponding to nominal strain rates of 3×10^{-3}, 3×10^{-4}, and 3×10^{-5} s^{-1}, respectively. The samples were deformed up to a shear strain of eight at 100°C, 200°C, and 300°C, with a constant confining pressure of 250 MPa. The reader is referred to Armann (2008) and Marques et al. (2013) for a more detailed description of their experimental setup.

The setup of our simulations is similar to those of these laboratory experiments, including the initial grain size, boundary conditions, temperature ranges, and strain rates, in order to allow a direct comparison. Specifically, a 3×3 cm^2 initial foam structure consisting of 255 grains was discretized into a grid of 256×256 *unodes* (Fourier points or crystallites), resulting in a unit cell defined by 65,536 *unodes* (Figures 1a and 1b). The initial average grain diameter of our model is 212 μm (Table 2). The starting material is considered isotropic, as the initial distribution of lattice grain orientations is random (Figure 1a). A detailed summary of all the input parameters for the simulations is presented in Table 1. For parameters not listed there, the input parameters used by Llorens, Griera, Bons, Roessiger, et al. (2016) were adopted (see their Table 1).

In this study we simulated the microstructure evolution of pure halite at different temperatures (100°C, 200°C, and 300°C) under dextral simple-shear deformation up to a finite shear strain of $\gamma = 4$, by the application of shear strain increments of $\Delta\gamma = 0.03$ in each time step, followed by a subloop of recrystallization processes (Figure 2) where different recrystallization modules were called (Table 2). Initially, a set of simulations that activate the DRX subloop with 5 times recovery, 20 polygonization, and 10 times GBM per deformation time step (see DRX simulations in Table 2) were done for comparison with the experiments. In order to check the equivalent time and influence of GBM (details are in Section 3.1), a set of simulations without deformation and with only GBM (static grain growth) were carried out (see G10 simulations in Table 2). In these simulations only the boundary energy was used as a driving force to calculate grain boundary displacement. By activating each module in turn, the microstructure undergoes a loop of deformation processes within a constant time step ($\Delta t = 100$ s). The simulations go through a total of 133 loops up to shear strain of 4, so the equivalent total time is 13,300 s and the shear strain rate is $\dot{\gamma} = 3 \times 10^{-4}$ s^{-1} for all simulations.

Lattice orientation and other data generated after each of the simulation steps were post-processed using the texture analysis software MTEX (http://mtex.googlecode.com; Bachmann et al., 2010; Mainprice et al., 2011) to

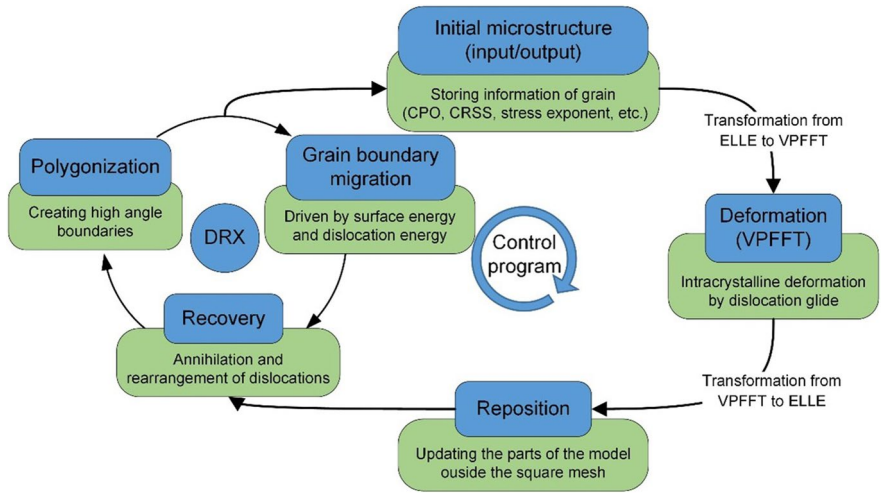

Figure 2. Loop showing the process workflow for one simulation time step. The initial microstructure is first subjected to viscoplastic deformation (VPFFT), followed by reposition, and a subloop of dynamic recrystallization processes (DRX). The DRX subloop includes polygonization, grain boundary migration (GBM), and intracrystalline recovery.

map the crystallographic textures (i.e., crystallographic preferred orientation maps, pole figures), analyze grain boundary misorientations, and the grain size network.

3. Results

3.1. Static Grain Growth

Static grain growth is simulated as GBM driven exclusively by grain boundary energy reduction (without considering GBM induced by dislocation stored strain energy; Karato, 2008; Weaire & Rivier, 1984). The kinetics of this process can be defined by the average area A from an initial area A_0 (Bons & Urai, 1992; Olgaard & Evans, 1988):

$$A - A_0 = MJt, \tag{6}$$

where M is the grain boundary mobility according to Equation 4, J is the grain boundary energy, and t is time. The total time is equivalent to the duration of the experiments of Armann (2008) (approx. 13,300 s). The input parameters are presented in Tables 1 and 2. We assume surface and grain boundary energies to be equal. This implies a strong binding energy between surfaces (e.g., Rohrer, 2011). The simulations only including static grain growth (G10_100, G10_200, and G10_300 simulations) are used to test the validity of the setup of the GBM model, by comparing it with the theoretical calculation following Equation 6. As shown in Figure 3, and taking G10_300 as an example, the average grain diameter (as a proxy of grain size) in the simulation increases from 212 to 299 μm after 13,300s, while that following the theoretical calculation raised to 303 μm for the same time (Table 2 and Figure 3, red lines). The diameter-time curves of G10_100 and G10_200 are also in agreement with the theoretical curves (Figure 3, blue and green lines). Compared with the significant grain growth of the G10_200 and G10_300 simulations, those of the G10_100 simulation do not change during the limited equivalent time. This reveals that the ratio GBM/VPFFT of 10 steps is correct, and validates the selected GBM parameters for our simulations (Table 2).

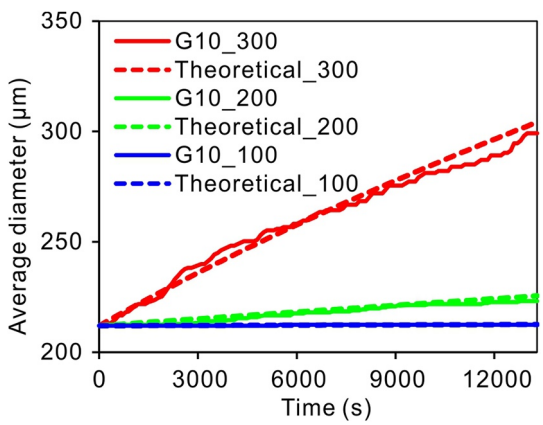

Figure 3. Evolution of the average grain size for simulations with only GBM (G10 simulations, solid lines) compared with the theoretical calculation (dashed lines) at temperatures of 100°C (blue), 200°C (green) and 300°C (red).

Analysis of the grain boundary orientation distribution of slightly deformed polycrystalline aggregates of synthetic rock salt using EBSD reveals that grain boundaries show a preference for {110} planes, which may be related to the anisotropy of the grain boundary energy (Pennock et al., 2009). Our

study assumes that all planes per unit length have the same grain boundary energy (i.e., isotropic) and, therefore, we refer to GBM driven by isotropic grain boundary energy (and dislocation energy) as isotropic GBM to distinguish it from natural and synthetic rock experiments. Figures 4l–4n show the microstructure of the simulations with static grain growth driven by grain boundary energy at equivalent time of 10,000 s (G10_100, G10_200, and G10_300 simulations). All static grain growth simulations produce classical foam texture patterns, similar to the starting mineral aggregate (Figure 3a), which is coherent with the isotropic boundary energy setup considered in this initial set of simulations.

3.2. Microstructure Evolution

Simulations DRX_100, DRX_200, and DRX_300 represent systems in which dislocation creep and dynamic recrystallization processes (i.e., intracrystalline recovery, polygonization and GBM) are coupled at various temperatures (100°C, 200°C, and 300°C). At low temperatures (100°C and 200°C) grain boundaries tend to be elongated and parallel to the stretching direction, showing a SPO oblique to the shear plane (Figures 4f, 4g and 4b). As expected, the angle between the SPO and the shear plane gradually decreases with progressive deformation, and at shear strain of three the foliation already lies at a low angle with respect to the shear plane (approximately 17°, Figures 4i, 4j and 4b). At high temperatures (300°C), elongated grains parallel to the stretching direction and SPO are still visible, but their aspect ratio is lower, and grains are larger and more equidimensional than those of the low-temperature models at a similar shear strain (100°C and 200°C) (Figures 4k and 4b). At low temperatures, the initial grain size (Figure 4a) decreases significantly with increasing strain due to polygonization of new (recrystallized) grains (Figures 4i and 4j, Table 2), and an intense network of LAGBs can be recognized within relict grains, as shown in Figures 4i and 4j. The density of the LAGB network gradually increases with progressive strain, revealing a general trend of increasing intergranular heterogeneities with deformation (Figures 4i and 4j). However, increasing GBM weakens this trend, resulting in a lower density of LAGBs (e.g., Figure 4k).

A close look at the evolution of the grain boundary network more clearly reveals the effect of temperature on DRX. A detail of the grain boundary map of a small area of the simulations is shown in Figure 5 for the 100°C (DRX_100) and 300°C (DRX_300) cases. Increasing temperature accelerates GBM and reduces the number of LAGBs. At low shear strain ($\gamma = 0.3$) the microstructures show similar grain boundary and subgrain boundary networks regardless of the temperature (Figures 5a and 5d, red circle). With progressive strain grains split into multiple new grains at 100°C, as a consequence of the increase in local misorientation of the LAGBs (Figures 5b and 5c). However, at 300°C, and for an equivalent region of grains to that of the 100°C case, there is a tendency of the grains with stronger substructure heterogeneities to disappear before they accumulate enough misorientation to split and produce new grains. The effect of GBM at high temperature is observed in Figures 5d–5f, where the boundaries of grains containing no or few low-angle grain boundaries move toward grains with higher subgrain heterogeneities, so that the substructures rich of grains are consumed and eventually disappear (Figure 5f, red arrow). A similar process is visible in the blue circles of Figure 5.

The evolution of grain size distribution during progressive deformation is shown in Figure 6, where the frequencies of grain size fractions are represented by different colors. The statistical results show that the grain size distribution in logarithmic scale is always unimodal at different temperatures. At 100°C and 200°C (Figures 6a and 6b) the grain size distribution shifts toward smaller grain sizes. Specifically, the proportion of small grains gradually increases with progressive deformation (Figure 6, log grain size ranges between 1.4 and 2.0), while the proportion of large grains gradually decreases (Figure 6, log grain size ranges between 2.0 and 2.6), revealing that the grain refinement process dominated by SGR induces grain size reduction. The situation at 300°C is different because the grain size distribution reveals larger grain sizes, and is basically stable for the logarithmic grain-size range of 2.4–2.6, remaining constant at around 30% with increasing shearing (Figure 6c). The grain size distribution of the 200°C model is more uniform than that of the 100°C case at high strain ($\gamma > 2$), possibly due to the large effective mobility of GBM at higher temperatures. The population of small grains remains essentially unchanged with increasing shear strain at 300°C (Figure 6c, log grain size ranges between 1.2 and 1.6), which is different from that of the low-temperature models (100 and 200°C), whose proportions gradually increase.

3.3. CPO Evolution

The crystallographic preferred orientation maps of DRX simulations (Table 2) at different shear strains ($\gamma = 1$, 2, 3) and different temperatures ($T = 100$°C, 200°C, 300°C) are shown in Figure 4, while the pole figures of the CPOs are plotted in Figure 7. As shown in Figures 4 and 7, the CPO evolution with progressive strain

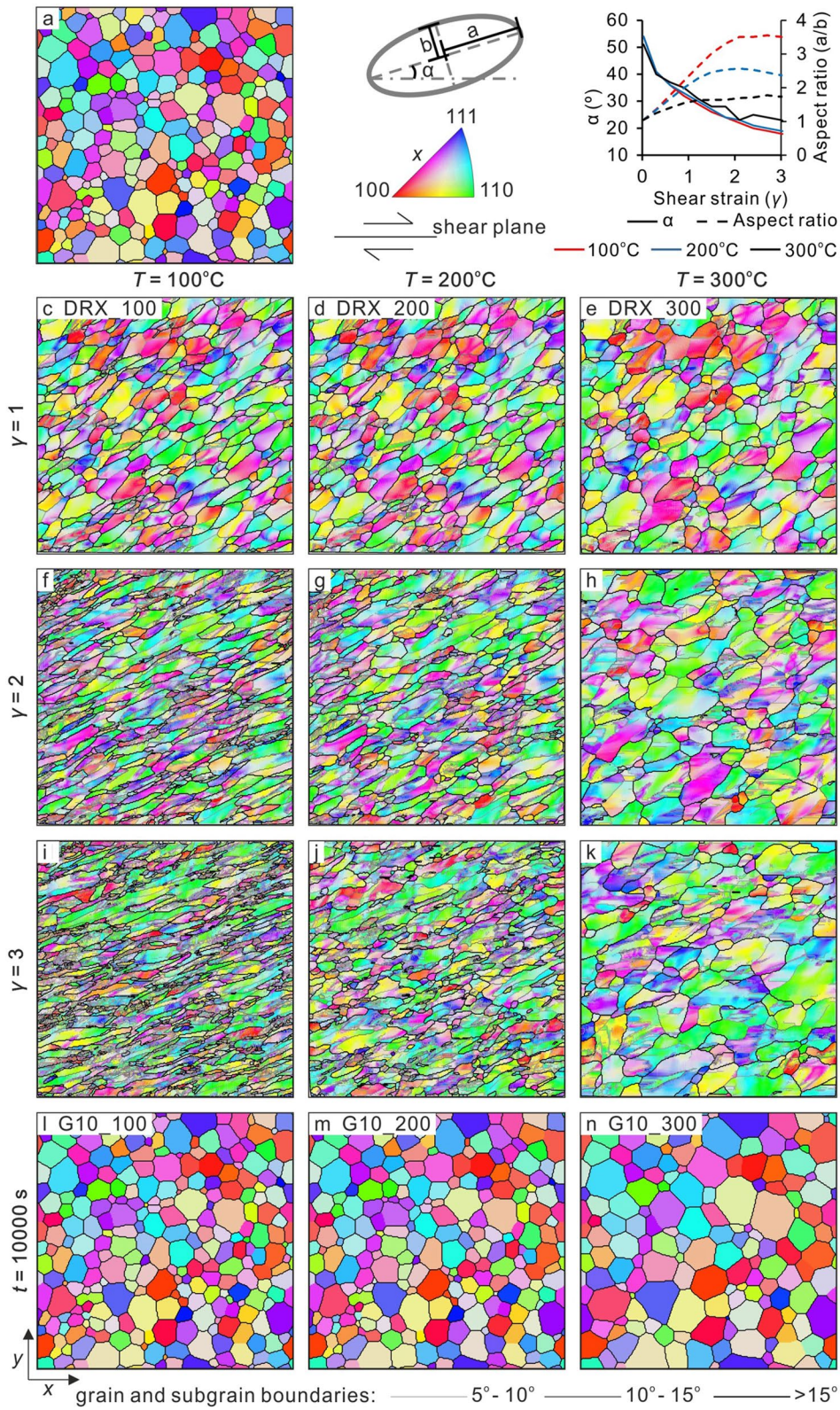

Figure 4.

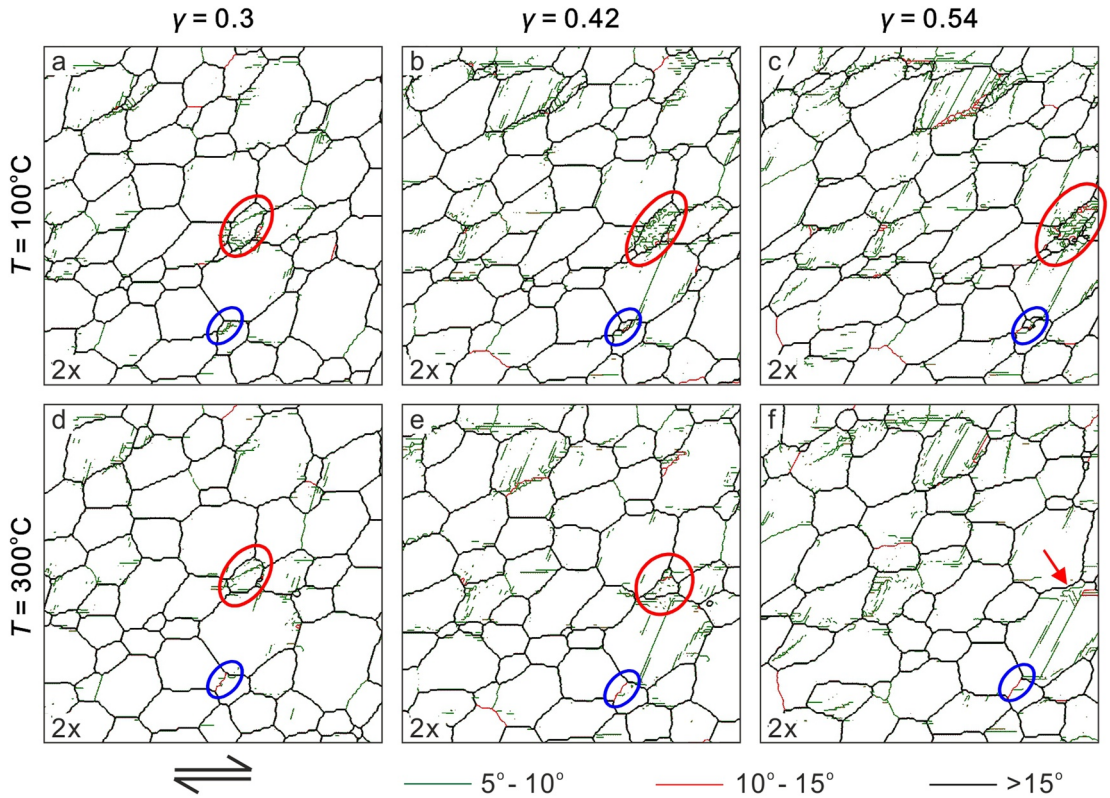

Figure 5. Comparison of the details of the grain boundary evolution of a selected grain with fully activated dynamic recrystallization processes (DRX) at shear strains of $\gamma = 0.3$, 0.42, and 0.54 at 100°C (a–c) and 300°C (d–f), respectively.

is very similar regardless of the temperature. Pole figures show the progressive evolution and intensity of the initial random distribution of crystallographic orientations (Figure 7a), which in all cases evolve to form a {100} maximum CPO approximately perpendicular to the shear plane and two maxima at approximately 45° to it (Figures 7d, 7g and 7j). At low strain ($\gamma = 1$), the {100} pole figure shows two maxima. One of these maxima is obliquely oriented to the shear plane with the opposite sense of shear, and the other one is approximately perpendicular to it ($\gamma = 1$, Figures 7b, 7e and 7h). For the same shear strain, the {110} and {111} pole figures show a weak hexagonal symmetry (Figures 7b, 7e and 7h). The {110} CPO evolves with shear strain to form two maxima parallel to the shear plane and other four maxima oriented at 45° from it (Figures 7d, 7g and 7j). The {111} CPO evolves toward a pattern with four maxima at 45° to the shear direction. The {110} and {111} CPO intensity increases when temperature raises (compare Figures 7d, 7g and 7j). However, the intensity of the final {100} CPO oriented perpendicular to the shear plane is reduced while the intensity of the two maxima oblique to the shear plane increases (Figures 7d, 7g and 7j). Dynamic recrystallization does not change the CPOs, but shows a reduction of dispersion of crystallographic axes and strengthening of the maxima (Figure 7).

4. Discussion

The objective of this study is to investigate the microstructural evolution of halite aggregates in simple shear viscoplastic deformation including DRX at different temperatures, and compare numerical predictions with torsion experiments. We calibrate and corroborate that full-field DRX simulations are able to reproduce results from the experiments of Armann (2008). Specifically, the grain size statistics (Figures 6 and 8), microstructures,

Figure 4. Crystallographic orientation and grain and subgrain boundary network maps of simulations with fully activated dynamic recrystallization processes (DRX) at different shear strains ($\gamma = 1$, 2, 3) at (c, f, i) 100°C, (d, g, j) 200°C, and (e, h, k) 300°C, and simulations with only GBM at a time $t = 10{,}000$s and at (l) 100°C, (m) 200°C, and (n) 300°C, respectively. The initial microstructure is shown in (a). Crystal lattice orientations are plotted as inverse pole figure colors with respect to the horizontal x axis (the shear direction). (b) Evolution of average shape-preferred orientation (solid lines indicate the angle between the major axis and the shear direction, while dashed lines the aspect ratio) with shear strain from $\gamma = 0.03$ to $\gamma = 3$ at 100°C (red lines), 200°C (blue lines), and 300°C (black lines).

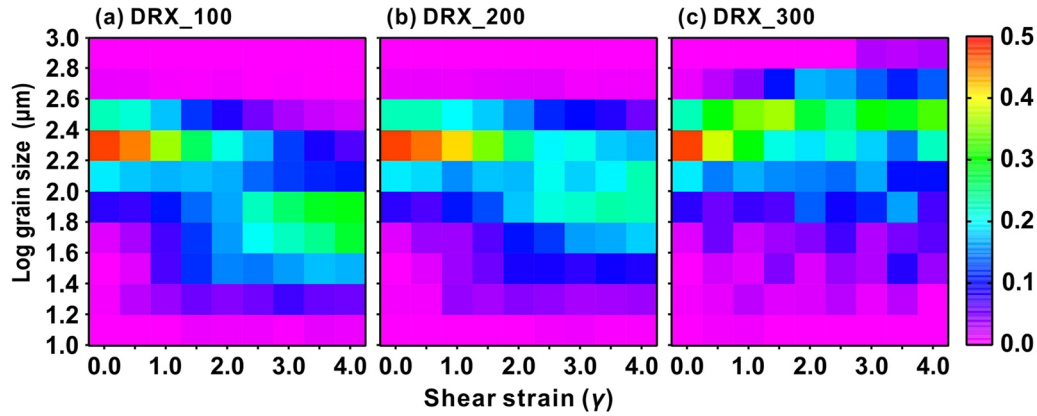

Figure 6. Evolution of grain size distribution with progressive strain for the simulations with fully activated dynamic recrystallization processes (DRX) (DRX_100/200/300). The grain size corresponds to the equivalent grain size (in logarithmic form, $\log_{10}$).

and crystallographic orientation maps (Figures 4 and 7) of our numerical models can be directly compared with those from the pure halite torsion experiments of Armann (2008) and Marques et al. (2013) at the same temperature range (Figure S1 in Supporting Information S1). The simulations presented here also match the numerical results from VPSC simulations of Wenk et al. (2009) and full-field simulations of Gomez-Rivas et al. (2017), expanding the range of simulation conditions to include GBM recrystallization during halite deformation.

4.1. Effect of Temperature on the Evolution of Microstructures

Under static conditions, when grain growth is purely driven by isotropic grain boundary energy reduction (Equation 6) (G10 simulations), the resulting microstructure is a typical foam texture (e.g., Weaire & Rivier, 1984) similar to those reported for undeformed rock salt after heating experiments by Bestmann et al. (2005). Under dynamic recrystallization conditions (DRX simulations), we can observe how temperature determines the balance between grain size reduction/growth, significantly affecting the microstructure evolution of halite polycrystalline aggregates at a constant shear strain rate. When the microstructure is deformed at high-temperature

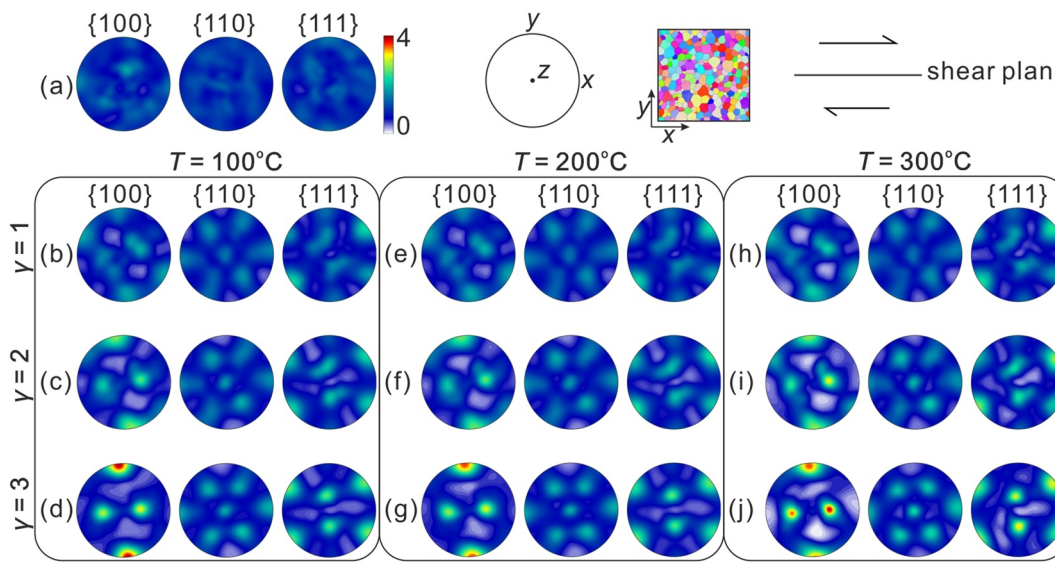

Figure 7. Pole figures of the crystallographic preferred orientations (CPOs) during deformation, where the shear sense is dextral and the shear plane is horizontal. The stereoplots of (a) correspond to the initial stage. Stereograms of the three groups of columns show the CPO evolution for the simulations with fully activated dynamic recrystallization processes (DRX) (DRX_100/200/300) at different shear strains (γ = 1, 2, 3) at (b–d) 100°C, (e–g) 200°C, and (h–j) 300°C, respectively.

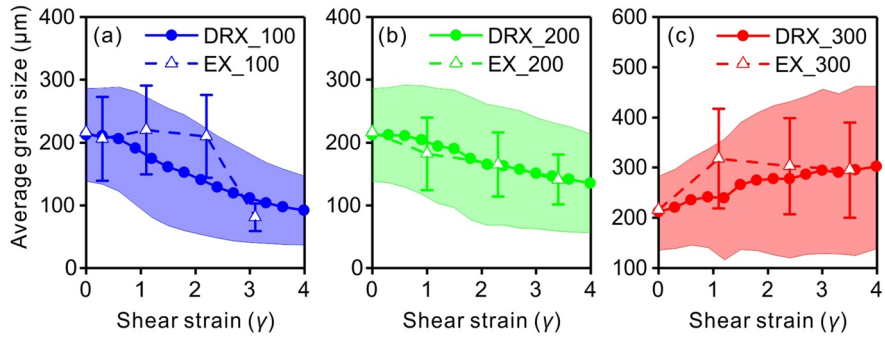

Figure 8. Comparison of evolution of the average grain size (solid lines) with its standard deviation (shaded areas) for simulations (DRX_100/200/300) run in this study at (a) 100°C, (b) 200°C, and (c) 300°C with laboratory experiments of Armann (2008) (dashed lines with error bars, EX_100/200/300) at the same temperatures. All the models and experiments were run at shear strain rate of 3×10^{-4} s^{-1}.

conditions (300°C), GBM produces a larger average grain size than that of the initial microstructure, while when the models are run at lower temperatures (100°C and 200°C) (Table 2, Figures 8a and 8b) grain size reduction is clearly observable (Armann, 2008). Moreover, there are more equidimensional grains at 200°C than at 100°C (Figure 4b), showing that temperature-dependent GBM strongly affects the grain shapes. The transition from low (100°C and 200°C) to high temperature (300°C) in our numerical microstructures is comparable with that taking place in quartz deformation experiments from the regime II to regime III of Stipp et al. (2002). Regime II is dominated by SGR, in which a portion of LAGBs eventually evolve to HAGBs, and with the formation of new grains due to the gradual increase of dislocations within grains as a result of dislocation movement and reorganization (Hirth & Tullis, 1992; Urai et al., 1986). Regime III is characterized by a significant increase in grain boundary mobility at higher temperature and large recrystallized grains (Stipp et al., 2010).

The grain size evolution of the laboratory experiments of Armann (2008) versus our simulations at 100°C, 200°C, and 300°C at a shear strain rate of 3×10^{-4} s^{-1} is shown in Figure 8 (grain size mean and standard deviation). The numerical simulation average grain size at different temperatures is basically consistent with that of the torsion experiments. It gradually decreases with increasing shear strain for the low-temperature systems (100°C and 200°C) (Figures 8a and 8b), while it increases when temperature is higher (300°C) (black line in Figure 8c). The reduction rate of the grain diameter standard deviation of simulations is significantly lower than the estimated value of the experiments (Armann, 2008). This reveals that the grain size distribution in our simulations during progressive strain is more inhomogeneous than that in experiments (Armann, 2008). One of the reasons may be that the discontinuous GBM processes affected by grain boundary pinning may limit the growth of large grains in laboratory experiments (Guillope & Poirier, 1979; Lücke & Stüwe, 1971), while impurity pinning processes are not included in our simulations. Deformation annealing experiments of rock salt (Piazolo et al., 2006) convincingly show that GBM is sensitive to changes in solute impurities or the substructure when the temperature is lower than 400°C.

Our results reveal that grains with a large number of subgrain boundaries are consumed by grains with no or few low-angle grain boundaries (Figure 5). This is a phenomenon similar to that described from halite laboratory experiments (Armann, 2008; ter Heege et al., 2005b) and borehole sample observations (Henneberg et al., 2020; Schléder & Urai, 2005; Thiemeyer et al., 2016). Our simulations assume that the rate of GBM has an exponential relationship with temperature. As expected, the GBM rate increases rapidly with increasing temperature and dominates rock salt deformation, potentially resulting in a microstructure reset (Franssen, 1994; Leitner et al., 2011).

4.2. Effect of Temperature on the Crystallographic Preferred Orientation (CPO) Evolution

The numerical CPO evolution (Figures 7b–7g) at low temperature is similar to those of the rock deformation experiments at 100°C and 200°C of Armann (2008) (Figure 9), and to numerical simulations by Wenk et al. (2009). However, the models at higher temperature (300°C) (Figure 7h) differ from the experimental results of Armann (2008) (see discussion in the next paragraph below). Strong CPOs develop rapidly with progressive

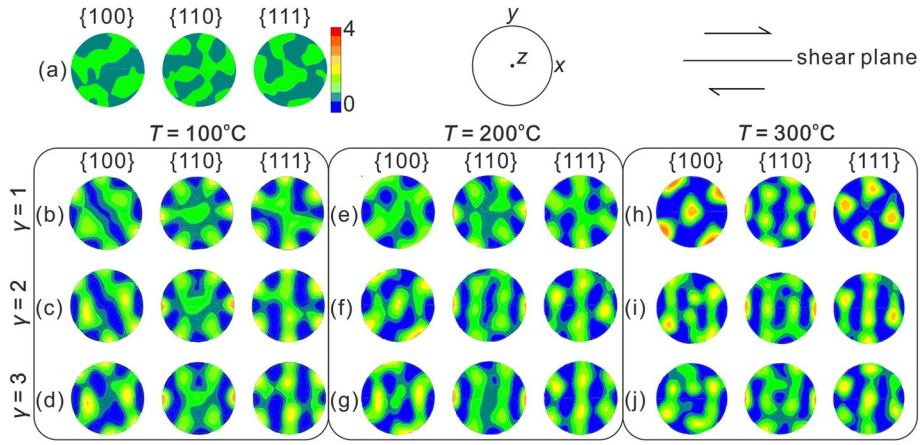

Figure 9. Pole figures of the crystallographic preferred orientations (CPOs) from torsion experiments (Armann, 2008). The stereoplots of (a) correspond to the initial stage. Stereograms of the three groups of columns show the CPO evolution for the torsion experiments at different shear strains ($\gamma = 1, 2, 3$) at (b–d) 100°C, (e–g) 200°C, and (h–j) 300°C, respectively.

deformation for the whole series of experiments, regardless of whether GBM was active or not (Figure 7). The initial randomly distributed CPOs quickly evolve into a pole to {100} sub-perpendicular to the shear plane at lower strain of 2 (Figures 7c, 7f and 7i). The {100} maximum then gets rotated according to the sense of shear up to becoming perpendicular to the shear plane at high shear strain ($\gamma = 3$) (Figures 7d, 7g and 7j). The results of our simulations show that isotropic GBM has a very limited effect on the CPOs, with the only effect that there is less scattering and more intense pole of lattice orientation in higher temperature systems (Figure 7). This is in agreement with many other studies on 1-hr polar ice (e.g., Llorens, Griera, Bons, Lebensohn, et al., 2016; Llorens, Griera, Bons, Roessiger, et al., 2016; Llorens et al., 2017).

When the temperature is high (300°C) a particular CPO (Figure 9h) that is accompanied by two {100} maxima at 45° between the shear plane and the shear plane normal was observed in torsion experiments (Armann, 2008) at low strain, which our simulations do not reproduce. Armann (2008) refers to it as grain growth CPO and suggests that it is produced by static annealing after deformation ceased in the experiments. Borthwick and Piazolo (2010) carried out thermal annealing experiments (>300°C) on a pre-deformed single crystal halite and found that annealing resulted in a change of the rotation axis of some part of LAGBs and an increase of the LAGBs. Static annealing experiments of olivine aggregates by Boneh et al. (2017) revealed that [100] poles rotate 10°–15° from the original direction during annealing by discontinuous grain growth, in a sample almost composed of porphyroblasts that distinctly have a different CPO from that of the matrix of small grains. The CPO difference between large strain-free grains and surrounding matrix grains was also observed in recrystallized vein quartz (Stöckhert & Duyster, 1999) and chromite (Ghosh et al., 2017). Large free grains are visible in the reflected light micrograph of the experimental microstructure corresponding to the grain growth CPO of Armann (2008) (see Figure 6a of Armann, 2008), which means that discontinuous grain growth took place at high temperature. Therefore, the formation of such CPOs may be influenced by the discontinuous grain growth with anisotropic grain boundary energy (Piazolo et al., 2006) or by the preferred elimination of high-energy grain boundaries during grain growth (Dillon & Rohrer, 2009; Pennock et al., 2009).

4.3. Effect of Temperature on the Misorientation Frequency Distribution of Misorientation: A Strain Gauge?

Figure 10 demonstrates that the frequency distribution of mean subgrain misorientations depends on temperature. At low temperatures (100°C and 200°C) the peak of the misorientation frequency distribution moves positively along the *x*-axis with progressive deformation, accompanied by an increase of the misorientation mean with increasing shear strain. Meanwhile, the skewness of the distribution decreases with increasing shear strain, and the proportion of low-angle subgrain misorientation diminishes, while the frequency of high-angle subgrain misorientation increases (Figures 10a–10j). However, at high temperature (300°C) the mean subgrain misorientation distribution initially raises and then stabilizes with increasing shear strain ($\gamma > 1.0$), while the relative

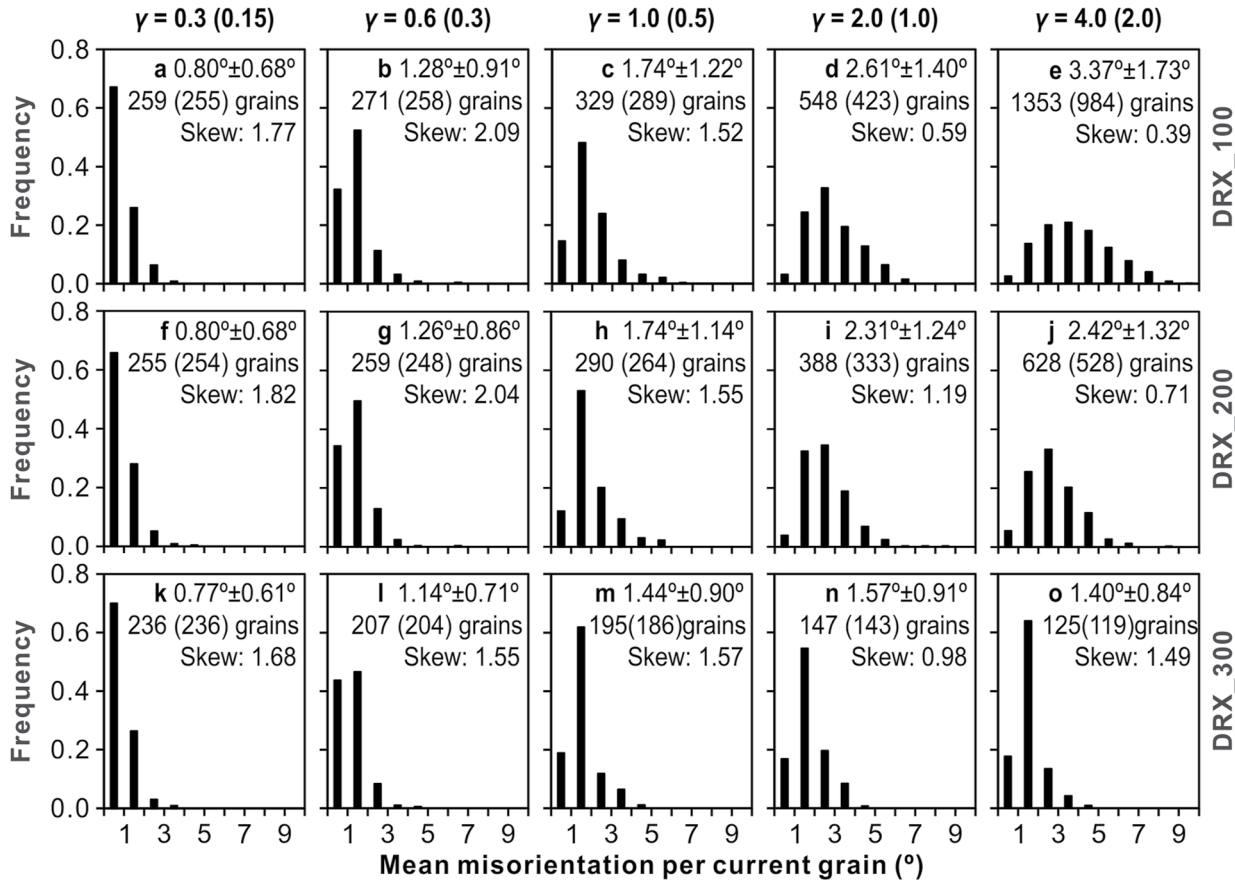

Figure 10. Frequency distribution of grain geometric mean misorientations at the temperature of 100°C, 200°C, and 300°C at different shear strain γ (the value in parentheses is expressed as the natural strain). The geometric means of the misorientation distribution $\theta_{\text{mean-grains}}$ are given along with the standard deviation of the mean. Misorientations were calculated with relevance of the grains that form once the misorientation is above 10°. The value in parentheses corresponds to the number of grains that contain a minimum of 10 crystallites and are considered for use in the strain gauges discussed below. Skewness measures the distribution asymmetry.

abundance of high-angle subgrain misorientation values is low (Figures 10k–10o). Additionally, the frequency distribution of the geometric mean subgrain misorientation subgrains consistently conforms to a positive skew distribution, with the skewness remaining relatively constant at around 1.5 as shear strain increases. Although local boundary and strain stored energies are taken into account for the GBM calculation, the main driving force is the difference in stored strain energy of a grain with respect to its neighbors, during which grains enriched in subgrain boundaries are consumed by grains with no or few LAGBs (Figures 4d–4f). As GBM is enhanced by temperature, this process prevents the formation of 5°–10° subgrain boundaries (Figures 10k–10o), thus explaining the absence of high-angle subgrain boundaries in cases of deformed halite during dynamic recrystallization dominated by GBM (Trimby et al., 2000). At moderate shear strain, there is a remarkable variation of the frequency distributions attending temperatures (Figures 10e, 10j and 10o), with lower values of skewness for lower temperature simulations.

The average subgrain misorientaion across a sample (θ_{av}) displays a power law relationship with natural strain (ε), according to previous studies (Hughes et al., 1998, 2003, 1997; Pantleon, 1997, 1998, 2001; Sethna et al., 2003). These studies suggest that a $\theta_{\text{av}} \sim \varepsilon^n = 2/3$ relationship exists. Pennock and Drury (2005) obtained an exponent of $n = 0.41$ for halite pure shear experiments, while Pennock et al. (2005) estimated an exponent of $n = 0.42$ in similar experiments but measuring misorientations by grain ($\theta_{\text{mean-grains}}$) instead of for the whole sample:

$$\theta_{\text{mean-grains}} = k_1 \varepsilon^n, \tag{7}$$

where k_1 is a constant related to the material and deformation conditions (Hughes et al., 1998, 1997). The setting of the minimum misorientation angle threshold (0.5°, Pennock et al., 2005) in the experimental measurements

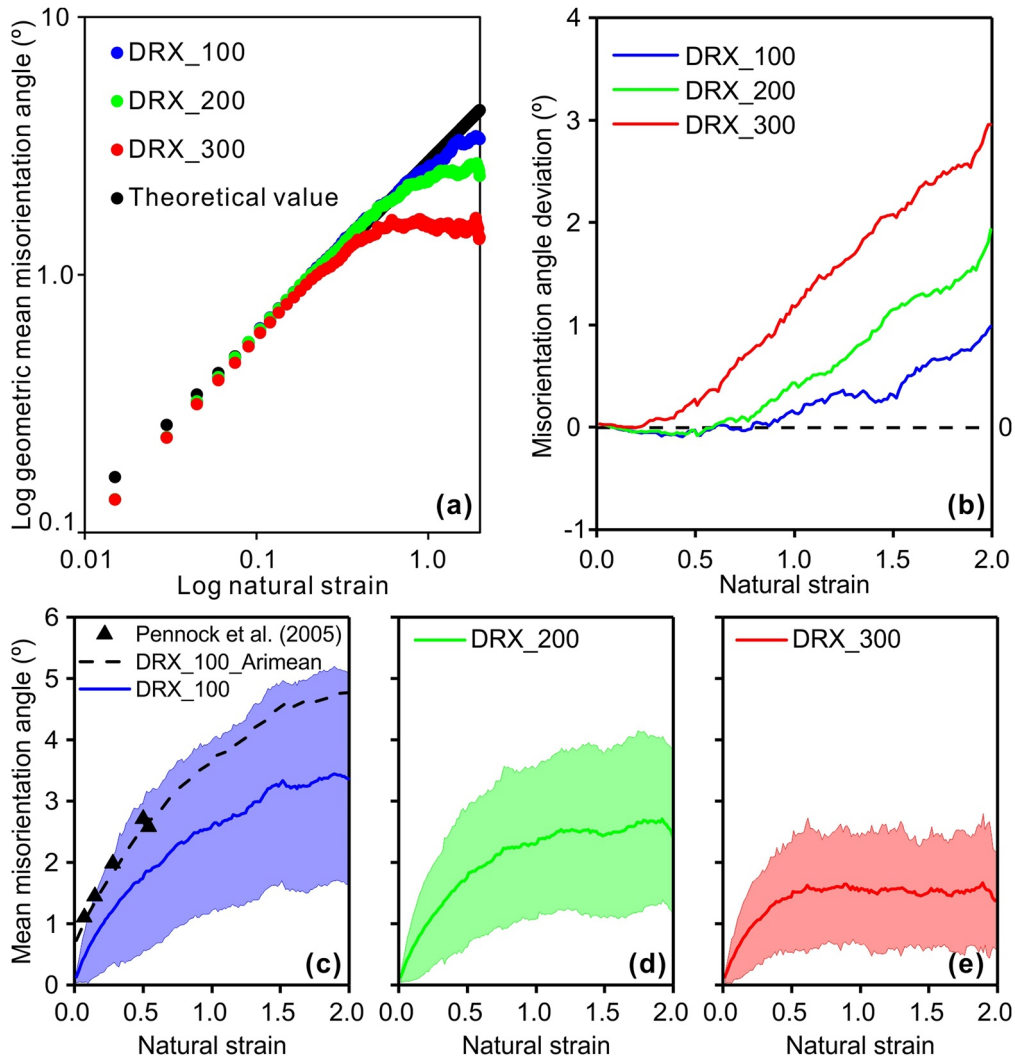

Figure 11. Evolution of the geometric mean of subgrain misorientation with natural strain at temperatures of 100°C (blue), 200°C (green), and 300°C (red), compared with the theoretical power law relationship following Equation 7 ($k_1 = 2.74$, $n = 2/3$; black point). Only grains with at least 10 crystallites are considered in the calculation. (a) Plotted in logarithmic form, log10. (b) Evolution of misorientation deviation from the theoretical power law relationship. (c–e) Evolution of the geometric mean of subgrain misorientation and its standard deviation with natural strain (black dashed line: arithmetic mean of subgrain misorientation, which is higher than 0.5°; black triangle: experimental data from Pennock et al. (2005)).

may lead to an overestimation of the average misorientation angle for low-strain samples due to the limitation of the angular resolution of EBSD (Figure 11), resulting in a lower value of the predicted exponent than the suggested universal exponent of $n = 2/3$. This is confirmed by the strong agreement between the arithmetic mean of misorientation (>0.5°) of DRX_100 simulation and experimental values (Pennock et al., 2005) shown in Figure 11c. In light of the prevalent non-Gaussian misorientation distributions (Figure 10), the employment of the geometric mean as opposed to the arithmetic mean is considered a better fitting metric (Figure 11). Furthermore, it is assumed in our simulations that the recovery process is temperature-independent, that is, the recovery step remains constant for DRX subloops (see Table 2). This assumption is made to allow for a systematic investigation into the impact of GBM on misorientation. We find that, as the level of strain increases, there is a deviation between the geometric mean of misorientation and the corresponding theoretical value (Figures 11a and 11b). As temperature increases, a deviation emerges at lower strain thresholds, specifically from $\varepsilon = 0.81$ at 100°C to $\varepsilon = 0.21$ at 300°C, as illustrated in Figure 11b. Accordingly, the k_1 constant also exhibits dependence on strain and, accordingly, lacks a tangible physical significance. Our simulations show three stages of increasing intracrystalline inhomogeneity, quantified by subgrain boundary misorientation (Figure 11). In the first stage,

the geometric mean of misorientation follows a theoretical power-law relationship with natural strain for models deformed at the whole range of temperatures considered (100–300°C) (Figure 11), as predicted in previous studies of metals (Hughes et al., 1998, 2003, 1997; Pantleon, 1997, 1998, 2001; Sethna et al., 2003). At this stage, lattice distortion and rotation associated with dislocation accumulation dominate, thus causing a misorientation increase following the aforementioned power-law relationship. In the second stage, as strain increases, the increase of geometric mean misorientation slows down significantly and gradually deviates from the theoretical value, with a higher intensity for models deformed at higher temperatures (Figures 11a and 11b). The third stage is characterized by stable misorientation mean values (Figures 11a and 11b), indicating that the generation and annihilation of dislocations within grains are in dynamic equilibrium. As shown in Figure 11b, the misorientation deviation is temperature-dependent, that is, related to the intensity of the dynamic recrystallization in the system. At 100°C GBM plays almost no role (Figure 3), so that the deviation of the mean misorientation at natural strain higher than 0.81 is due to SGR recrystallization. As temperature increases the mean misorientation deviation from the theoretical model takes place at lower strains compared to the 100°C case (Figures 11a and 11b). This is associated with an increase in the GBM intensity that cause a strong reduction of the grain local misorientation by resetting misorientation in zones swept by moving grain boundaries.

In summary, the deviation from the theoretical power law correlates well with the occurrence of two dynamic recrystallization processes: subgrain rotation and GBM. This correlation can be attributed to variations in the rates of DRX processes, which in turn are influenced by changes in temperature. The power-law relationship between the geometric mean of subgrain misorientation and strain exhibits a close conformity with the universal exponent of 2/3, as demonstrated in prior studies. However, it is important to note that this correlation only holds true during the initial deformation stage. In subsequent stages, characterized by pronounced dynamic recrystallization and marked changes in the microstructure, reliance on this relationship may lead to a significant devaluation of natural strain estimations. Hence, the accurate determination of strain gauge necessitates three calibrations of its three stages, or the construction of a theoretical model incorporating factors such as temperature. The study conducted by Stipp et al. (2010) on quartz paleopiezometry demonstrated the requirement for distinct piezometer calibrations for diverse recrystallization processes. For situations in which extensive recrystallization is inferred from natural samples (or experiments), in addition to the geometric mean misorientation as marker to estimate the strain, probably the strain gauge has more potential if it is combined with the skewness of the misorientation distribution (Figure 10 and Figure S2 in Supporting Information S1). In this way, the analysis of the discrepancy between the measured geometric mean misorientation and the skewness of the distribution with respect to the theoretical trend could be used for the prediction of temperature and strain. A reduction of the skewness is expected for low temperature simulations, with limited recrystallization of the polycrystalline aggregate and a higher probability to conserve grains with higher misorientation angles. For the high temperature case, there are observed cycles of accumulation and swept of misorientations produced by larger mobility of grain boundaries, resulting in a higher skewness of the misorientation distribution. However, more systematic analyses would be required to verify these observations.

5. Conclusions

This study presents a novel method to simulate dislocation creep including dynamic recrystallization processes in halite polycrystalline aggregates subjected to simple shear deformation. The VPFFT/ELLE numerical simulation results of simulations run at different temperatures lead to the following conclusions:

1. The proposed full-field approach successfully reproduces the evolution of halite microstructures from laboratory torsion experiments at temperatures of 100–300°C, providing new insights into the competition between grain size reduction by SGR and grain size growth by GBM recrystallization.
2. The intensity of GBM recrystallization, related to temperature, strongly affects the grain morphology and texture, resulting in weaker grain size reduction, more dispersed grain size distributions and more equidimensional grains.
3. Isotropic GBM has little effect on the crystallographic preferred orientation, and it only results in a slightly more intense pole of lattice orientation with respect to cases with no GBM.
4. At low strain the relationship between finite natural strain and the geometric mean subgrain misorientation follows a power law and thus can be used as a strain gauge. However, at high strain the intensity of dynamic recrystallization, including subgrain rotation and GBM, causes a deviation from this the universal scaling law.

The skewness of the frequency distribution of the geometrical mean misorientation can also be used for a better prediction of strain and deformation temperature from the misorientation data.

Data Availability Statement

The software used in this work is open access and can be found in the references cited in the main text and figure captions, as well as in the repository published in Hao et al. (2023a). The data files used in this article are available in Hao et al. (2023b).

Acknowledgments

This study has been funded by DGICYT Spanish Projects PID-2020-118999GB-I00 (Ministerio de Ciencia e Innovación/Agencia Estatal de Investigación/10.13039/501100011033) and PID-2021-122467NB-C21 (Ministerio de Ciencia e Innovación/Agencia Estatal de Investigación/10.13039/501100011033/FEDER), and 2021 SGR 00349 "Geologia Sedimentària" and 2021 SGR 00410 "Modelització Geodinàmica de la Litosfera" (Agència de Gestió d'Ajuts Universitaris i de Recerca). MG-L acknowledges the "Consolidación Investigadora" Grant CNS2022-135819 funded by Ministerio de Ciencia e Innovación/Agencia Estatal de Investigación/10.13039/501100011033 and EU NextGenerationEU/PRTR. Baoqin Hao acknowledges funding by the China Scholarship Council for a PhD scholarship (CSC-202006930010). EG-R acknowledges the "Ramón y Cajal" Fellowship RyC-2018-026335-I, funded by the Ministerio de Ciencia e Innovación/Agencia Estatal de Investigación/10.13039/501100011033. We are grateful to Marina Armann for communication regarding her PhD thesis, and to Till Sachau for helping to create ELLE software containers.

References

Amelirad, O., & Assempour, A. (2022). Coupled continuum damage mechanics and crystal plasticity model and its application in damage evolution in polycrystalline aggregates. *Engineering with Computers*, *38*(S3), 2121–2135. https://doi.org/10.1007/s00366-021-01346-2

Armann, M. (2008). *Microstructural and textural development in synthetic rocksalt deformed in torsion* (Doctoral dissertation). ETH-Zurich. https://doi.org/10.3929/ethz-a-005666840

Bachmann, F., Hielscher, R., & Schaeben, H. (2010). Texture analysis with MTEX – Free and open source software toolbox. *Solid State Phenomena*, *160*, 63–68. https://doi.org/10.4028/www.scientific.net/SSP.160.63

Becker, J. K., Bons, P. D., & Jessell, M. W. (2008). A new front-tracking method to model anisotropic grain and phase boundary motion in rocks. *Computers & Geosciences*, *34*(3), 201–212. https://doi.org/10.1016/j.cageo.2007.03.013

Bestmann, M., Piazolo, S., Spiers, C. J., & Prior, D. J. (2005). Microstructural evolution during initial stages of static recovery and recrystallization: New insights from in-situ heating experiments combined with electron backscatter diffraction analysis. *Journal of Structural Geology*, *27*(3), 447–457. https://doi.org/10.1016/j.jsg.2004.10.006

Boneh, Y., Wallis, D., Hansen, L. N., Krawczynski, M. J., & Skemer, P. (2017). Oriented grain growth and modification of 'frozen anisotropy' in the lithospheric mantle. *Earth and Planetary Science Letters*, *474*, 368–374. https://doi.org/10.1016/j.epsl.2017.06.050

Bons, P. D., Koehn, D., & Jessell, M. W. (Eds.). (2008). *Microdynamics simulation* (Vol. 106). Springer. https://doi.org/10.1007/978-3-540-44793-1

Bons, P. D., & Urai, J. L. (1992). Syndeformational grain growth: Microstructures and kinetics. *Journal of Structural Geology*, *14*(8–9), 1101–1109. https://doi.org/10.1016/0191-8141(92)90038-X

Borthwick, V. E., & Piazolo, S. (2010). Post-deformational annealing at the subgrain scale: Temperature dependent behaviour revealed by in-situ heating experiments on deformed single crystal halite. *Journal of Structural Geology*, *32*(7), 982–996. https://doi.org/10.1016/j.jsg.2010.06.006

Borthwick, V. E., Piazolo, S., Evans, L., Griera, A., & Bons, P. D. (2014). What happens to deformed rocks after deformation? A refined model for recovery based on numerical simulations. *Geological Society, London, Special Publications*, *394*(1), 215–234. https://doi.org/10.1144/SP394.11

Bourcier, M., Bornert, M., Dimanov, A., Héripré, E., & Raphanel, J. L. (2013). Multiscale experimental investigation of crystal plasticity and grain boundary sliding in synthetic halite using digital image correlation. *Journal of Geophysical Research: Solid Earth*, *118*(2), 511–526. https://doi.org/10.1002/jgrb.50065

Bruno, M., Aquilano, D., Pastero, L., & Prencipe, M. (2008). Structures and surface energies of (100) and octopolar (111) faces of halite (NaCl): An ab initio quantum-mechanical and thermodynamical study. *Crystal Growth & Design*, *8*(7), 2163–2170. https://doi.org/10.1021/cg8000027

Canérot, J., Hudec, M. R., & Rockenbauch, K. (2005). Mesozoic diapirism in the Pyrenean orogen: Salt tectonics on a transform plate boundary. *AAPG Bulletin*, *89*(2), 211–229. https://doi.org/10.1306/09170404007

Carter, N. L., & Heard, H. C. (1970). Temperature and rate dependent deformation of halite. *American Journal of Science*, *269*(3), 193–249. https://doi.org/10.2475/ajs.269.3.193

Carter, N. L., Horseman, S. T., Russell, J. E., & Handin, J. (1993). Rheology of rocksalt. *Journal of Structural Geology*, *15*(9–10), 1257–1271. https://doi.org/10.1016/0191-8141(93)90168-A

de Riese, T., Evans, L., Gomez-Rivas, E., Griera, A., Lebensohn, R. A., Llorens, M.-G., et al. (2019). Shear localisation in anisotropic, non-linear viscous materials that develop a CPO: A numerical study. *Journal of Structural Geology*, *124*, 81–90. https://doi.org/10.1016/j.jsg.2019.03.006

Desbois, G., Závada, P., Schléder, Z., & Urai, J. L. (2010). Deformation and recrystallization mechanisms in actively extruding salt fountain: Microstructural evidence for a switch in deformation mechanisms with increased availability of meteoric water and decreased grain size (Qum Kuh, central Iran). *Journal of Structural Geology*, *32*(4), 580–594. https://doi.org/10.1016/j.jsg.2010.03.005

Dillon, S. J., & Rohrer, G. S. (2009). Mechanism for the development of anisotropic grain boundary character distributions during normal grain growth. *Acta Materialia*, *57*(1), 1–7. https://doi.org/10.1016/j.actamat.2008.08.062

Drury, M. R., & Urai, J. L. (1990). Deformation-related recrystallization processes. *Tectonophysics*, *172*(3–4), 235–253. https://doi.org/10.1016/0040-1951(90)90033-5

Eisenlohr, P., Diehl, M., Lebensohn, R. A., & Roters, F. (2013). A spectral method solution to crystal elasto-viscoplasticity at finite strains. *International Journal of Plasticity*, *46*, 37–53. https://doi.org/10.1016/j.ijplas.2012.09.012

Finch, M. A., Bons, P. D., Steinbach, F., Griera, A., Llorens, M.-G., Gomez-Rivas, E., et al. (2020). The ephemeral development of C′ shear bands: A numerical modelling approach. *Journal of Structural Geology*, *139*, 104091. https://doi.org/10.1016/j.jsg.2020.104091

Finch, M. A., Bons, P. D., Weinberg, R. F., Llorens, M.-G., Griera, A., & Gomez-Rivas, E. (2022). A dynamic atlas of interference patterns in superimposed, opposite sense ductile shear zones. *Journal of Structural Geology*, *165*, 104739. https://doi.org/10.1016/j.jsg.2022.104739

Fossen, H. (2010). Deformation bands formed during soft-sediment deformation: Observations from SE Utah. *Marine and Petroleum Geology*, *27*(1), 215–222. https://doi.org/10.1016/j.marpetgeo.2009.06.005

Franssen, R. C. M. W. (1994). The rheology of synthetic rocksalt in uniaxial compression. *Tectonophysics*, *233*(1–2), 1–40. https://doi.org/10.1016/0040-1951(94)90218-6

Franssen, R. C. M. W., & Spiers, C. J. (1990). Deformation of polycrystalline salt in compression and in shear at 250–350°C. *Geological Society, London, Special Publications*, *54*(1), 201–213. https://doi.org/10.1144/GSL.SP.1990.054.01.20

Frost, H. J., & Ashby, M. F. (1982). *Deformation-mechanism maps: The plasticity and creep of metals and ceramics* (175 pp.). Pergamon Press.

Ghosh, B., Misra, S., & Morishita, T. (2017). Plastic deformation and post-deformation annealing in chromite: Mechanisms and implications. *American Mineralogist*, *102*(1), 216–226. https://doi.org/10.2138/am-2017-5709

Gomez-Rivas, E., Butler, R. W. H., Healy, D., & Alsop, I. (2020). From hot to cold – The temperature dependence on rock deformation processes: An introduction. *Journal of Structural Geology*, *132*, 103977. https://doi.org/10.1016/j.jsg.2020.103977

Gomez-Rivas, E., Griera, A., Llorens, M.-G., Bons, P. D., Lebensohn, R. A., & Piazolo, S. (2017). Subgrain rotation recrystallization during shearing: Insights from full-field numerical simulations of halite polycrystals. *Journal of Geophysical Research: Solid Earth*, *122*(11), 8810–8827. https://doi.org/10.1002/2017JB014508

Griera, A., Bons, P. D., Jessell, M. W., Lebensohn, R. A., Evans, L., & Gomez-Rivas, E. (2011). Strain localization and porphyroclast rotation. *Geology*, *39*(3), 275–278. https://doi.org/10.1130/G31549.1

Griera, A., Llorens, M.-G., Gomez-Rivas, E., Bons, P. D., Jessell, M. W., Evans, L. A., & Lebensohn, R. (2013). Numerical modelling of porphyroclast and porphyroblast rotation in anisotropic rocks. *Tectonophysics*, *587*, 4–29. https://doi.org/10.1016/j.tecto.2012.10.008

Guillope, M., & Poirier, J. P. (1979). Dynamic recrystallization during creep of single-crystalline halite: An experimental study. *Journal of Geophysical Research*, *84*(B10), 5557–5567. https://doi.org/10.1029/JB084iB10p05557

Hao, B., Llorens, M.-G., Griera Artigas, A., Bons, P. D., Lebensohn, R., Yu, Y., & Gomez-Rivas, E. (2023a). Full-field numerical simulation of halite dynamic recrystallization from subgrain rotation to grain boundary migration [Software]. Journal of Geophysical Research Solid Earth (1.0). Zenodo. https://doi.org/10.5281/zenodo.10259841

Hao, B., Llorens, M.-G., Griera, A., Bons, P. D., Lebensohn, R. A., Yu, Y., & Gómez-Rivas, E. (2023b). Full-field numerical simulations of sub grain rotation and grain boundary migration in halite during viscoplastic deformation [Dataset]. DIGITAL.CSIC. https://doi.org/10.20350/digitalCSIC/15474

Henneberg, M., Linckens, J., Schramm, M., Hammer, J., Gerdes, A., & Zulauf, G. (2020). Structural evolution of continental and marine Permian rock salt of the North German basin: Constraints from microfabrics, geochemistry and U–Pb ages. *International Journal of Earth Sciences*, *109*(7), 2369–2387. https://doi.org/10.1007/s00531-020-01905-w

Hirth, G., & Tullis, J. (1992). Dislocation creep regimes in quartz aggregates. *Journal of Structural Geology*, *14*(2), 145–159. https://doi.org/10.1016/0191-8141(92)90053-Y

Hudec, M. R., & Jackson, M. P. A. (2007). Terra infirma: Understanding salt tectonics. *Earth-Science Reviews*, *82*(1–2), 1–28. https://doi.org/10.1016/j.earscirev.2007.01.001

Hughes, D. A., Chrzan, D. C., Liu, Q., & Hansen, N. (1998). Scaling of misorientation angle distributions. *Physical Review Letters*, *81*(21), 4664–4667. https://doi.org/10.1103/PhysRevLett.81.4664

Hughes, D. A., & Hansen, N. (2018). The microstructural origin of work hardening stages. *Acta Materialia*, *148*, 374–383. https://doi.org/10.1016/j.actamat.2018.02.002

Hughes, D. A., Hansen, N., & Bammann, D. J. (2003). Geometrically necessary boundaries, incidental dislocation boundaries and geometrically necessary dislocations. *Scripta Materialia*, *48*(2), 147–153. https://doi.org/10.1016/S1359-6462(02)00358-5

Hughes, D. A., Liu, Q., Chrzan, D. C., & Hansen, N. (1997). Scaling of microstructural parameters: Misorientations of deformation induced boundaries. *Acta Materialia*, *45*(1), 105–112. https://doi.org/10.1016/S1359-6454(96)00153-X

Hunsche, U., & Hampel, A. (1999). Rock salt — The mechanical properties of the host rock material for a radioactive waste repository. *Engineering Geology*, *52*(3–4), 271–291. https://doi.org/10.1016/S0013-7952(99)00011-3

Jessell, M. W., Bons, P. D., Evans, L., Barr, T., & Stüwe, K. (2001). Elle: The numerical simulation of metamorphic and deformation microstructures. *Computers & Geosciences*, *27*(1), 17–30. https://doi.org/10.1016/S0098-3004(00)00061-3

Jessell, M. W., Bons, P. D., Griera, A., Evans, L. A., & Wilson, C. J. L. (2009). A tale of two viscosities. *Journal of Structural Geology*, *31*(7), 719–736. https://doi.org/10.1016/j.jsg.2009.04.010

Jessell, M. W., Kostenko, O., & Jamtveit, B. (2003). The preservation potential of microstructures during static grain growth. *Journal of Metamorphic Geology*, *21*(5), 481–491. https://doi.org/10.1046/j.1525-1314.2003.00455.x

Kaminski, É., & Ribe, N. M. (2001). A kinematic model for recrystallization and texture development in olivine polycrystals. *Earth and Planetary Science Letters*, *189*(3–4), 253–267. https://doi.org/10.1016/S0012-821X(01)00356-9

Kaminski, É., Ribe, N. M., & Browaeys, J. T. (2004). D-Rex, a program for calculation of seismic anisotropy due to crystal lattice preferred orientation in the convective upper mantle. *Geophysical Journal International*, *158*(2), 744–752. https://doi.org/10.1111/j.1365-246X.2004.02308.x

Karato, S. (2008). *Deformation of earth materials. An introduction to the rheology of Solid Earth* (Vol. 463). Cambridge Press.

Lebensohn, R. A. (2001). N-site modeling of a 3D viscoplastic polycrystal using Fast Fourier Transform. *Acta Materialia*, *49*(14), 2723–2737. https://doi.org/10.1016/S1359-6454(01)00172-0

Lebensohn, R. A., Dawson, P. R., Kern, H. M., & Wenk, H.-R. (2003). Heterogeneous deformation and texture development in halite polycrystals: Comparison of different modeling approaches and experimental data. *Tectonophysics*, *370*(1–4), 287–311. https://doi.org/10.1016/S0040-1951(03)00192-6

Lebensohn, R. A., & Rollett, A. D. (2020). Spectral methods for full-field micromechanical modelling of polycrystalline materials. *Computational Materials Science*, *173*, 109336. https://doi.org/10.1016/j.commatsci.2019.109336

Lebensohn, R. A., & Tomé, C. N. (1993). A self-consistent anisotropic approach for the simulation of plastic deformation and texture development of polycrystals: Application to zirconium alloys. *Acta Metallurgica et Materialia*, *41*(9), 2611–2624. https://doi.org/10.1016/0956-7151(93)90130-K

Leitner, C., Neubauer, F., Urai, J. L., & Schoenherr, J. (2011). Structure and evolution of a rocksalt-mudrock-tectonite: The haselgebirge in the Northern Calcareous Alps. *Journal of Structural Geology*, *33*(5), 970–984. https://doi.org/10.1016/j.jsg.2011.02.008

Linckens, J., Zulauf, G., & Hammer, J. (2016). Experimental deformation of coarse-grained rock salt to high strain. *Journal of Geophysical Research: Solid Earth*, *121*(8), 6150–6171. https://doi.org/10.1002/2016JB012890

Liu, Y., Gilormini, P., & Castañeda, P. P. (2005). Homogenization estimates for texture evolution in halite. *Tectonophysics*, *406*(3–4), 179–195. https://doi.org/10.1016/j.tecto.2005.06.007

Llorens, M.-G., Gomez-Rivas, E., Ganzhorn, A.-C., Griera, A., Steinbach, F., Roessiger, J., et al. (2019). The effect of dynamic recrystallisation on the rheology and microstructures of partially molten rocks. *Journal of Structural Geology*, *118*, 224–235. https://doi.org/10.1016/j.jsg.2018.10.013

Llorens, M.-G., Griera, A., Bons, P. D., Lebensohn, R. A., Evans, L. A., Jansen, D., & Weikusat, I. (2016). Full-field predictions of ice dynamic recrystallisation under simple shear conditions. *Earth and Planetary Science Letters*, *450*, 233–242. https://doi.org/10.1016/j.epsl.2016.06.045

Llorens, M.-G., Griera, A., Bons, P. D., Roessiger, J., Lebensohn, R., Evans, L., & Weikusat, I. (2016). Dynamic recrystallisation of ice aggregates during co-axial viscoplastic deformation: A numerical approach. *Journal of Glaciology*, *62*(232), 359–377. https://doi.org/10.1017/jog.2016.28

Llorens, M.-G., Griera, A., Steinbach, F., Bons, P. D., Gomez-Rivas, E., Jansen, D., et al. (2017). Dynamic recrystallization during deformation of polycrystalline ice: Insights from numerical simulations. *Philosophical Transactions of the Royal Society A: Mathematical, Physical & Engineering Sciences*, *375*(2086), 20150346. https://doi.org/10.1098/rsta.2015.0346

Lücke, K., & Stüwe, H. P. (1971). On the theory of impurity controlled grain boundary motion. *Acta Metallurgica*, *19*(10), 1087–1099. https://doi.org/10.1016/0001-6160(71)90041-1

Mainprice, D., Hielscher, R., & Schaeben, H. (2011). Calculating anisotropic physical properties from texture data using the MTEX open-source package. *Geological Society, London, Special Publications*, *360*(1), 175–192. https://doi.org/10.1144/SP360.10

Mansouri, H., Prior, D. J., Ajalloeian, R., & Elyaszadeh, R. (2019). Deformation and recrystallization mechanisms inferred from microstructures of naturally deformed rock salt from the diapiric stem and surface glaciers of a salt diapir in Southern Iran. *Journal of Structural Geology*, *121*, 10–24. https://doi.org/10.1016/j.jsg.2019.01.005

Marques, F. O., Burg, J.-P., Armann, M., & Martinho, E. (2013). Rheology of synthetic polycrystalline halite in torsion. *Tectonophysics*, *583*, 124–130. https://doi.org/10.1016/j.tecto.2012.10.024

McClay, K., Muñoz, J.-A., & García-Senz, J. (2004). Extensional salt tectonics in a contractional orogen: A newly identified tectonic event in the Spanish Pyrenees. *Geology*, *32*(9), 737. https://doi.org/10.1130/G20565.1

Mika, D. P., & Dawson, P. R. (1999). Polycrystal plasticity modeling of intracrystalline boundary textures. *Acta Materialia*, *47*(4), 1355–1369. https://doi.org/10.1016/S1359-6454(98)00386-3

Moulinec, H., & Suquet, P. (1994). A fast numerical method for computing the linear and nonlinear mechanical properties of composites. *Comptes Rendus de l'Académie Des Sciences. Série II. Mécanique, Physique, Chimie, Astronomie*, 1417–1423. Retrieved from https://hal.science/hal-03019226/document

Moulinec, H., & Suquet, P. (1998). A numerical method for computing the overall response of nonlinear composites with complex microstructure. *Computer Methods in Applied Mechanics and Engineering*, *157*(1–2), 69–94. https://doi.org/10.1016/S0045-7825(97)00218-1

Olgaard, D. L., & Evans, B. (1988). Grain growth in synthetic marbles with added mica and water. *Contributions to Mineralogy and Petrology*, *100*(2), 246–260. https://doi.org/10.1007/BF00373591

Otsuka, T., Brenner, R., & Bacroix, B. (2018). FFT-based modelling of transformation plasticity in polycrystalline materials during diffusive phase transformation. *International Journal of Engineering Science*, *127*, 92–113. https://doi.org/10.1016/j.ijengsci.2018.02.008

Pantleon, W. (1997). On the evolution of disorientations in dislocation cell structures during plastic deformation. *Materials Science and Engineering: A*, *234–236*, 567–570. https://doi.org/10.1016/S0921-5093(97)00227-X

Pantleon, W. (1998). On the statistical origin of disorientations in dislocation structures. *Acta Materialia*, *46*(2), 451–456. https://doi.org/10.1016/S1359-6454(97)00286-3

Pantleon, W. (2001). The evolution of disorientations for several types of boundaries. *Materials Science and Engineering: A*, *319–321*, 211–215. https://doi.org/10.1016/S0921-5093(01)00947-9

Paterson, M. S., & Olgaard, D. L. (2000). Rock deformation tests to large shear strains in torsion. *Journal of Structural Geology*, *22*(9), 1341–1358. https://doi.org/10.1016/S0191-8141(00)00042-0

Peach, C. J., & Spiers, C. J. (1996). Influence of crystal plastic deformation on dilatancy and permeability development in synthetic salt rock. *Tectonophysics*, *256*(1–4), 101–128. https://doi.org/10.1016/0040-1951(95)00170-0

Peach, C. J., Spiers, C. J., & Trimby, P. W. (2001). Effect of confining pressure on dilatation, recrystallization, and flow of rock salt at 150°C. *Journal of Geophysical Research*, *106*(B7), 13315–13328. https://doi.org/10.1029/2000JB900300

Pennock, G. M., Coleman, M., Drury, M. R., & Randle, V. (2009). Grain boundary plane populations in minerals: The example of wet NaCl after low strain deformation. *Contributions to Mineralogy and Petrology*, *158*(1), 53–67. https://doi.org/10.1007/s00410-008-0370-5

Pennock, G. M., & Drury, M. R. (2005). Low-angle subgrain misorientations in deformed NaCl. *Journal of Microscopy*, *217*(2), 130–137. https://doi.org/10.1111/j.1365-2818.2005.01410.x

Pennock, G. M., Drury, M. R., & Spiers, C. J. (2005). The development of subgrain misorientations with strain in dry synthetic NaCl measured using EBSD. *Journal of Structural Geology*, *27*(12), 2159–2170. https://doi.org/10.1016/j.jsg.2005.06.013

Pennock, G. M., Drury, M. R., Trimby, P. W., & Spiers, C. J. (2002). Misorientation distributions in hot deformed NaCl using electron backscattered diffraction. *Journal of Microscopy*, *208*(1), 75. https://doi.org/10.1046/j.1365-2818.2002.00993.x

Piazolo, S., Bestmann, M., Prior, D. J., & Spiers, C. J. (2006). Temperature dependent grain boundary migration in deformed-then-annealed material: Observations from experimentally deformed synthetic rocksalt. *Tectonophysics*, *427*(1–4), 55–71. https://doi.org/10.1016/j.tecto.2006.06.007

Piazolo, S., Bons, P. D., Griera, A., Llorens, M.-G., Gomez-Rivas, E., Koehn, D., et al. (2019). A review of numerical modelling of the dynamics of microstructural development in rocks and ice: Past, present and future. *Journal of Structural Geology*, *125*, 111–123. https://doi.org/10.1016/j.jsg.2018.05.025

Picard, D., Dimanov, A., & Raphanel, J. L. (2018). Plastic behavior of halite single-crystals at different temperatures and strain rates: New insights from in-situ experiments and full field measures. *Materials Science and Engineering: A*, *732*, 284–297. https://doi.org/10.1016/j.msea.2018.07.009

Pokharel, R., Lind, J., Kanjarla, A. K., Lebensohn, R. A., Li, S. F., Kenesei, P., et al. (2014). Polycrystal plasticity: Comparison between grain-scale observations of deformation and simulations. *Annual Review of Condensed Matter Physics*, *5*(1), 317–346. https://doi.org/10.1146/annurev-conmatphys-031113-133846

Radhakrishnan, B., & Sarma, G. B. (2008). Coupled simulations of texture evolution during deformation and recrystallization of fcc and bcc metals. *Materials Science and Engineering: A*, *494*(1–2), 73–79. https://doi.org/10.1016/j.msea.2007.10.094

Ran, H., Bons, P. D., Wang, G., Griera, A., de Riese, T., Gomez-Rivas, E., et al. (2022). Folds inside pebbles: When do they form during conglomerate deformation? Numerical modelling and comparison with the Hutuo group conglomerates, North China Craton. *Journal of Structural Geology*, *160*, 104620. https://doi.org/10.1016/j.jsg.2022.104620

Ran, H., Bons, P. D., Wang, G., Steinbach, F., Finch, M. A., Griera, A., et al. (2018). High-strain deformation of conglomerates: Numerical modelling, strain analysis, and an example from the Wutai Mountains, North China Craton. *Journal of Structural Geology*, *114*, 222–234. https://doi.org/10.1016/j.jsg.2018.06.018

Ran, H., de Riese, T., Llorens, M.-G., Finch, M. A., Evans, L. A., Gomez-Rivas, E., et al. (2019). Time for anisotropy: The significance of mechanical anisotropy for the development of deformation structures. *Journal of Structural Geology*, *125*, 41–47. https://doi.org/10.1016/j.jsg.2018.04.019

Randle, V. (1993). Microtexture investigation of the relationship between strain and anomalous grain growth. *Philosophical Magazine A*, *67*(6), 1301–1313. https://doi.org/10.1080/01418619308225356

Read, W. T., & Shockley, W. (1950). Dislocation models of crystal grain boundaries. *Physical Review*, *78*(3), 275–289. https://doi.org/10.1103/PhysRev.78.275

Roessiger, J., Bons, P. D., Griera, A., Jessell, M. W., Evans, L., Montagnat, M., et al. (2011). Competition between grain growth and grain-size reduction in polar ice. *Journal of Glaciology*, *57*(205), 942–948. https://doi.org/10.3189/002214311798043690

Rohrer, G. S. (2011). Grain boundary energy anisotropy: A review. *Journal of Materials Science*, *46*(18), 5881–5895. https://doi.org/10.1007/s10853-011-5677-3

Roters, F., Eisenlohr, P., Hantcherli, L., Tjahjanto, D. D., Bieler, T. R., & Raabe, D. (2010). Overview of constitutive laws, kinematics, homogenization and multiscale methods in crystal plasticity finite-element modeling: Theory, experiments, applications. *Acta Materialia*, *58*(4), 1152–1211. https://doi.org/10.1016/j.actamat.2009.10.058

Schléder, Z., & Urai, J. L. (2005). Microstructural evolution of deformation-modified primary halite from the Middle Triassic Röt formation at Hengelo, The Netherlands. *International Journal of Earth Sciences*, *94*(5–6), 941–955. https://doi.org/10.1007/s00531-005-0503-2

Schléder, Z., & Urai, J. L. (2007). Deformation and recrystallization mechanisms in mylonitic shear zones in naturally deformed extrusive Eocene–Oligocene rocksalt from Eyvanekey plateau and Garmsar hills (central Iran). *Journal of Structural Geology*, *29*(2), 241–255. https://doi.org/10.1016/j.jsg.2006.08.014

Sethna, J. P., Coffman, V. R., & Demler, E. (2003). Scaling in plasticity-induced cell-boundary microstructure: Fragmentation and rotational diffusion. *Physical Review B*, *67*(18), 184107. https://doi.org/10.1103/PhysRevB.67.184107

Signorelli, J., & Tommasi, A. (2015). Modeling the effect of subgrain rotation recrystallization on the evolution of olivine crystal preferred orientations in simple shear. *Earth and Planetary Science Letters*, *430*, 356–366. https://doi.org/10.1016/j.epsl.2015.08.018

Spiers, C. J., Peach, C. J., Brzesowsky, R. H., Schutjens, P. M. T. M., Liezenberg, J. L., & Zwart, H. J. (1988). *Long-term rheological and transport properties of dry and wet salt rocks*. Office for Official Publications of the European Communities.

Spiers, C. J., Schutjens, P. M. T. M., Brzesowsky, R. H., Peach, C. J., Liezenberg, J. L., & Zwart, H. J. (1990). Experimental determination of constitutive parameters governing creep of rocksalt by pressure solution. *Geological Society, London, Special Publications*, *54*(1), 215–227. https://doi.org/10.1144/GSL.SP.1990.054.01.21

Steinbach, F., Bons, P. D., Griera, A., Jansen, D., Llorens, M.-G., Roessiger, J., & Weikusat, I. (2016). Strain localization and dynamic recrystallization in the ice–air aggregate: A numerical study. *The Cryosphere*, *10*(6), 3071–3089. https://doi.org/10.5194/tc-10-3071-2016

Steinbach, F., Kuiper, E.-J. N., Eichler, J., Bons, P. D., Drury, M. R., Griera, A., et al. (2017). The relevance of grain dissection for grain size reduction in polar ice: Insights from numerical models and ice core microstructure analysis. *Frontiers in Earth Science*, *5*. https://doi.org/10.3389/feart.2017.00066

Stipp, M., Stünitz, H., Heilbronner, R., & Schmid, S. M. (2002). The eastern Tonale fault zone: A 'natural laboratory' for crystal plastic deformation of quartz over a temperature range from 250 to 700°C. *Journal of Structural Geology*, *24*(12), 1861–1884. https://doi.org/10.1016/S0191-8141(02)00035-4

Stipp, M., Tullis, J., Scherwath, M., & Behrmann, J. H. (2010). A new perspective on paleopiezometry: Dynamically recrystallized grain size distributions indicate mechanism changes. *Geology*, *38*(8), 759–762. https://doi.org/10.1130/G31162.1

Stöckhert, B., & Duyster, J. (1999). Discontinuous grain growth in recrystallised vein quartz — Implications for grain boundary structure, grain boundary mobility, crystallographic preferred orientation, and stress history. *Journal of Structural Geology*, *21*(10), 1477–1490. https://doi.org/10.1016/S0191-8141(99)00084-X

Sun, R. C., & Bauer, C. L. (1970). Tilt boundary migration in NaCl bicrystals. *Acta Metallurgica*, *18*(6), 639–647. https://doi.org/10.1016/0001-6160(70)90093-3

ter Heege, J. H., de Bresser, J. H. P., & Spiers, C. J. (2004). Dynamic recrystallization of dense polycrystalline NaCl: Dependence of grain size distribution on stress and temperature. *Materials Science Forum*, *467–470*, 1187–1192. https://doi.org/10.4028/www.scientific.net/MSF.467-470.1187

ter Heege, J. H., de Bresser, J. H. P., & Spiers, C. J. (2005a). Dynamic recrystallization of wet synthetic polycrystalline halite: Dependence of grain size distribution on flow stress, temperature and strain. *Tectonophysics*, *396*(1–2), 35–57. https://doi.org/10.1016/j.tecto.2004.10.002

ter Heege, J. H., de Bresser, J. H. P., & Spiers, C. J. (2005b). Rheological behaviour of synthetic rocksalt: The interplay between water, dynamic recrystallization and deformation mechanisms. Journal of Structural Geology, *27*, 948–963. https://doi.org/10.1016/j.jsg.2005.04.008

Thiemeyer, N., Zulauf, G., Mertineit, M., Linckens, J., Pusch, M., & Hammer, J. (2016). Microfabrics and 3D grain shape of Gorleben rock salt: Constraints on deformation mechanisms and paleodifferential stress. *Tectonophysics*, *676*, 1–19. https://doi.org/10.1016/j.tecto.2016.02.046

Trimby, P. W., Drury, M. R., & Spiers, C. J. (2000). Recognising the crystallographic signature of recrystallisation processes in deformed rocks: A study of experimentally deformed rocksalt. *Journal of Structural Geology*, *22*(11–12), 1609–1620. https://doi.org/10.1016/S0191-8141(00)00059-6

Urai, J. L., Means, W. D., & Lister, G. S. (1986). Dynamic recrystallization of minerals. In B. E. Hobbs & H. C. Heard (Eds.), *Mineral and rock deformation: Laboratory studies: The Paterson Volume* (Vol. 36, pp. 161–199). American Geophysical Union. https://doi.org/10.1029/GM036p0161

Urai, J. L., Schléder, Z., Spiers, C. J., & Kukla, P. A. (2008). Flow and transport properties of salt rocks. In R. Littke, U. Bayer, D. Gajewski, & S. Nelskamp (Eds.), *Dynamics of complex intracontinental basins: The central European basin system* (pp. 277–290). Springer.

Wawersik, W. R., & Zeuch, D. H. (1986). Modeling and mechanistic interpretation of creep of rock salt below 200°C. *Tectonophysics*, *121*(2–4), 125–152. https://doi.org/10.1016/0040-1951(86)90040-5

Weaire, D., & Rivier, N. (1984). Soap, cells and statistics—Random patterns in two dimensions. *Contemporary Physics*, *25*(1), 59–99. https://doi.org/10.1080/00107518408210979

Wenk, H.-R., Armann, M., Burlini, L., Kunze, K., & Bortolotti, M. (2009). Large strain shearing of halite: Experimental and theoretical evidence for dynamic texture changes. *Earth and Planetary Science Letters*, *280*(1–4), 205–210. https://doi.org/10.1016/j.epsl.2009.01.036

Wenk, H.-R., Bennett, K., Canova, G. R., & Molinari, A. (1991). Modelling plastic deformation of peridotite with the self-consistent theory. *Journal of Geophysical Research*, *96*(B5), 8337–8349. https://doi.org/10.1029/91JB00117

Journal of Geophysical Research Solid Earth

Supporting Information for

Full-field numerical simulation of halite dynamic recrystallization from subgrain rotation to grain boundary migration

B. Hao[1], M.-G. Llorens[2], A. Griera[3], P.D. Bons[4], R. A. Lebensohn[5], Y. Yu[2] and E. Gomez-Rivas[1]

[1]Departament de Mineralogia, Petrologia i Geologia Aplicada, Universitat de Barcelona, Spain

[2]Geosciences Barcelona, CSIC, Spain

[3]Departament de Geologia, Universitat Autònoma de Barcelona, Spain

[4]Department of Geosciences, Eberhard Karls University of Tübingen, Germany

[5]Materials Science and Technology Division, Los Alamos National Laboratory, Los Alamos, NM, USA

Contents of this file

Additional Supporting Information (Files uploaded separately)

Introduction

This supporting information provides (i) crystallographic orientation maps of the laboratory experiments of Armann (2008) (**Figure S1**; modified from Armann, 2008) for qualitative comparison with the numerical results presented in this study (see Figure 4 of section 3.2), (ii) a figure to demonstrate the evolution of the skewness of subgrain misorientaiton (**Figure S2**), and (iii) movies of three numerical experiments **(Movie ms01**, **Movie ms02** and **Movie ms03**).

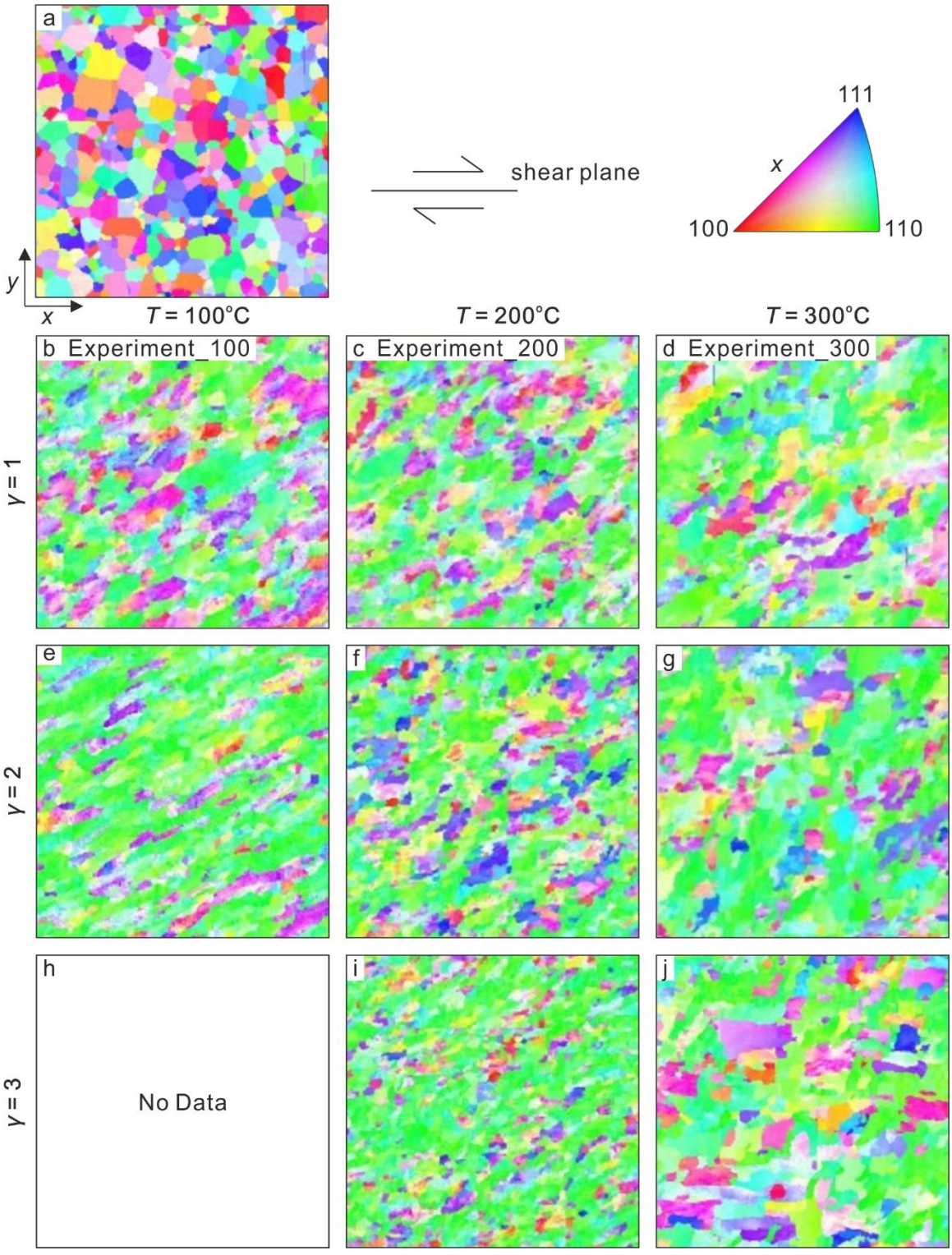

Figure S1. Crystallographic orientation maps of the experiments of Armann (2008) at different shear strains (γ = 1, 2, 3) at 100℃ (b, e, h), 200℃ (c, f, i) and 300℃ (d, g, j), respectively. The initial orientation is shown in (a). Crystal lattice orientations are plotted

as inverse pole figure colors with respect to the horizontal x axis (i.e., shear direction). Figure modified from Armann (2008).

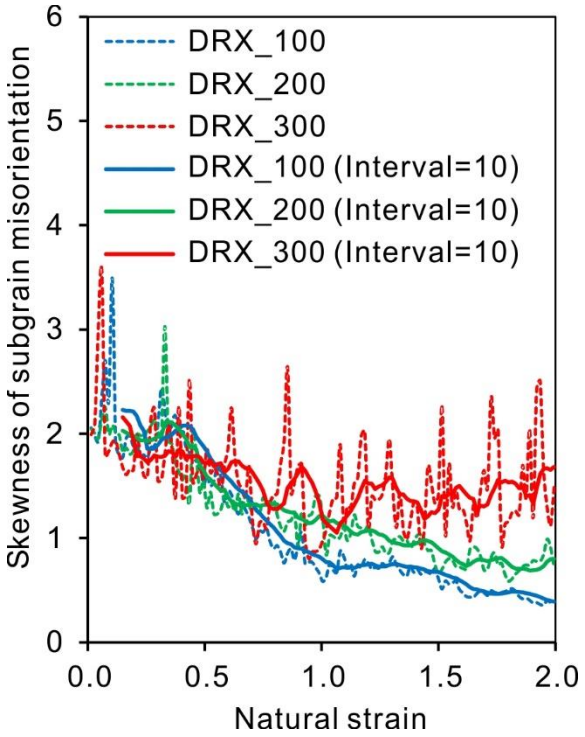

Figure S2. Evolution of skewness of subgrain misorientation with the natural strain at the temperature of 100℃ (blue dashed line), 200℃ (green dashed line) and 300℃ (red dashed line) and estimation of its evolution considering average of 10 intervals (solid lines). After moderate shear strain, the skewness of frequency distribution shows a dependence on temperature.

Movie ms01. Movie of the DRX_100 (simulation with fully activated dynamic recrystallization at 100℃) up to a shear strain of γ=4. The main window shows the evolution of the crystallographic orientation and grain boundary network map with progressive deformation. Stereograms display pole figures of the CPO evolution, using equal angle projection.
https://agupubs.onlinelibrary.wiley.com/action/downloadSupplement?doi=10.1029%2F2023JB027590&file=2023JB027590-sup-0002-Movie+SI-S01.m4v

Movie ms02. Movie of the DRX_200 (simulation with fully activated dynamic recrystallization at 200℃) up to a shear strain of γ=4. The main window shows the evolution of the crystallographic orientation and grain boundary network map with progressive deformation. Stereograms display pole figures of the CPO evolution, using equal angle projection.

https://agupubs.onlinelibrary.wiley.com/action/downloadSupplement?doi=10.1029%2F2023JB027590&file=2023JB027590-sup-0003-Movie+SI-S02.m4v

Movie ms03. Movie of the DRX_300 (simulation with fully activated dynamic recrystallization at 300℃) up to a shear strain of γ=4. The main window shows the evolution of the crystallographic orientation and grain boundary network map with progressive deformation. Stereograms display pole figures of the CPO evolution, using equal angle projection.
https://agupubs.onlinelibrary.wiley.com/action/downloadSupplement?doi=10.1029%2F2023JB027590&file=2023JB027590-sup-0004-Movie+SI-S03.m4v

Appendix 2. Article2

Hao, B., Griera, A., Llorens, M. -G., Bons, P. D., Lebensohn, R. A., Yu, Y., & Gomez-Rivas, E. (2024). The influence of kinematics of deformation on polycrystalline halite dynamic recrystallization: full-field simulation of simple shear versus pure shear. *Journal of Structural Geology, in review.*

Journal of Structural Geology

The influence of kinematics of deformation on polycrystalline halite dynamic recrystallization: full-field simulation of simple shear versus pure shear

--Manuscript Draft--

Manuscript Number:	SG-D-24-00235
Article Type:	VSI: Janos L. Urai
Keywords:	dynamic recrystallization, halite microstructure, viscoplastic anisotropy, crystallographic preferred orientation
Corresponding Author:	Baoqin Hao University of Barcelona SPAIN
First Author:	Baoqin Hao
Order of Authors:	Baoqin Hao
	Albert Griera
	Maria-Gema Llorens
	Paul Bons
	Ricardo Lebensohn
	Yuanchao Yu
	Enrique Gomez-Rivas
Abstract:	Rock salt, composed mainly of halite, flows plastically over a wide range of geological conditions, strongly impacting the dynamic evolution of sedimentary basins and orogens. Understanding how dislocation creep, which involves dislocation glide, intracrystalline recovery and dynamic recrystallization, influences the microstructure and rheology of halite under various deformation kinematics and temperatures is crucial for enhancing knowledge of salt flow dynamics. This study employs a full-field numerical simulation method to compare the viscoplastic deformation of polycrystalline halite under simple shear and pure shear conditions up to a natural strain of $\varepsilon = 1.5$ at temperatures ranging from 100℃ to 300℃. The results are presented in terms of crystallographic preferred orientation (CPO), grain shape preferred orientation (SPO), subgrain boundary orientation, grain size and strain rate distribution. The results indicate that the anisotropy of individual halite crystals is transferred to the polycrystalline scale, resulting in strain localization, particularly in simple shear simulations. The kinematics of deformation affect the evolution and distribution of strain-rate bands, determining the orientation of intragranular substructures and the morphology of strain-induced grain boundaries, with minimal impact on grain size. The intensity of grain boundary migration increases with temperature, significantly influencing grain morphology and size, thereby obscuring strain localization, while having little effect on CPOs. At low strain ($\varepsilon < 1.0$), CPOs relative to the maximum shortening direction are similar regardless of the deformation kinematics. At high strain ($\varepsilon > 1.0$), simple shear CPOs exhibit three stronger {100} maxima with a monoclinic symmetry compared to the six {100} maxima with an orthotropic symmetry generated under pure shear, due to the rotation of CPOs observed in the former simulations. Therefore, microstructures and CPOs can serve as indicators of the strain path in polycrystalline halite under various conditions, aiding in determining the shear sense and elucidating the deformation kinematics of salt structures.

The influence of kinematics of deformation on polycrystalline halite dynamic recrystallization: full-field simulation of simple shear versus pure shear

Baoqin Hao[1,2], Albert Griera[3], Maria-Gema Llorens[4], Paul D. Bons[5], Ricardo. A. Lebensohn[6], Yuanchao Yu[1,4] and Enrique Gomez-Rivas[1]

[1] Departament de Mineralogia, Petrologia i Geologia Aplicada, Universitat de Barcelona, Spain

[2] Institut de Recerca Geomodels, Universitat de Barcelona, Spain

[3] Departament de Geologia, Universitat Autònoma de Barcelona, Spain

[4] Geosciences Barcelona, GEO3BCN-CSIC, Spain

[5] Department of Geosciences, Eberhard Karls University of Tübingen, Germany

[6] Materials Science and Technology Division, Los Alamos National Laboratory, Los Alamos, NM, USA

Corresponding author: Baoqin Hao (baoqin.hao@ub.edu, haobaoqin@hotmail.com)

Abstract

Rock salt, composed mainly of halite, flows plastically over a wide range of geological conditions, strongly impacting the dynamic evolution of sedimentary basins and orogens. Understanding how dislocation creep, which involves dislocation glide, intracrystalline recovery and dynamic recrystallization, influences the microstructure and rheology of halite under various deformation kinematics and temperatures is crucial for enhancing knowledge of salt flow dynamics. This study employs a full-field numerical simulation method to compare the viscoplastic deformation of polycrystalline halite under simple shear and pure shear conditions up to a natural strain of $\varepsilon = 1.5$ at temperatures ranging from 100°C to 300°C. The results are presented in terms of crystallographic preferred orientation (CPO), grain shape preferred orientation (SPO), subgrain boundary orientation, grain size and strain rate distribution. The results indicate that the anisotropy of individual halite crystals is transferred to the polycrystalline scale, resulting in strain localization, particularly in simple shear simulations. The kinematics of deformation affect the evolution and distribution of strain-rate bands, determining the orientation of intragranular substructures and the morphology of strain-induced grain boundaries, with minimal impact on grain size. The intensity of grain boundary migration increases with temperature, significantly influencing grain morphology and size, thereby obscuring strain localization, while having little effect on CPOs. At low strain ($\varepsilon < 1.0$), CPOs relative to the maximum shortening direction are similar regardless of the deformation kinematics. At high strain ($\varepsilon > 1.0$), simple shear CPOs exhibit three stronger {100} maxima with a monoclinic symmetry compared to the six {100} maxima with an orthotropic symmetry generated under pure shear, due to the rotation of CPOs observed in the former simulations. Therefore, microstructures and CPOs can serve as indicators of the strain path in polycrystalline halite under various conditions, aiding in determining the shear sense and elucidating the deformation kinematics of salt structures.

Keywords:

dynamic recrystallization, halite microstructure, viscoplastic anisotropy, crystallographic preferred orientation

1. Introduction

With their seminal paper "Dynamic recrystallization of minerals" (Urai et al., 1986a), Janos Urai and co-authors showed the geosciences community that dynamic recrystallization (*DRX*) is a common process in ductile deforming minerals. This study was particularly convincing as it showed *DRX* in progressive time steps using in-situ deformation experiments with the "Urai-Means deformation apparatus" (Means, 1977, 1989; Urai et al., 1980; Means and Xia, 1981). In these experiments, a thin sample could be deformed between glass plates to allow continuous observation with a microscope, producing a revolution for the structural community. This technique required the use of very soft minerals, such as bischofite and carnallite (Urai, 1985, 1987), ice (Wilson, 1984), or soft crystalline organic compounds, such as octachloropropane (OCP; McCrone and Cheng, 1949; Means, 1983; Jessell, 1986; Bons and Jessell, 1999) and camphor (Urai et al., 1980; Urai and Humphreys, 1981). These experiments made it possible to watch and record the evolving microstructure, including migrating boundaries, lattice rotation and the formation of subgrain and new grain boundaries. At the time that these in-situ experiments revealed how dynamic recrystallization works and how it affects the microstructure, numerical simulations were still in their infancy. Jessell and Lister (1990) were the first to publish a numerical simulation of quartz deformation that included both rotation and migration recrystallization and their effects on the developing crystallographic preferred orientation. The in-situ experiments inspired the development of the ELLE-platform for the numerical simulation of the deformation of polycrystalline aggregates with a focus on visualizing the evolving microstructure (Jessell et al., 2001; Bons et al., 2008). In this paper we continue to follow the path set by Janos Urai and colleagues decades ago to elucidate how the kinematic of deformation affects dynamic recrystallization of microstructures and influences in the crystallographic

preferred orientations (CPO). In this study, we focus on the mineral halite, which was subject of Janos Urai's research throughout his career (Urai et al., 1986b, 1987, 2008; Van Gent et al., 2011).

Rock salt, chiefly composed of halite, has characteristic physical properties, including low density, incompressibility, low permeability, and a rheology that allows it flowing in a viscous manner under low stresses (Carter et al., 1993; Weijermars et al., 1993). Consequently, the deformational behaviour of rock salt with respect to their surrounding rocks results in the formation (e.g., Jackson and Talbot, 1986; Canérot et al., 2005) of complex tectonic structures, such as salt diapirs and salt walls, and causes folding and faulting of their encasing rocks. Salt serves as detachment levels for thrust systems, accommodating significant horizontal shortening in orogenic belts. This interaction significantly influences he overall deformation style and structural evolution of the orogen (Jackson and Hudec, 2017). Moreover, salt flow controls the deposition and distribution of other sedimentary rocks in sedimentary basins (e.g., Canérot et al., 2005; Mohr et al., 2005; Rowan et al., 2019). Understanding and predicting rock salt flow is also important from the economic point of view, because these rocks typically act as seals for fluid migration and produce structural traps in oil and gas reservoirs (Hudec and Jackson, 2007). Besides, artificially made caverns in rock salt are used for the storage of Geo-Energy products, such as hydrogen and compressed air (Duffy et al., 2018). Such storage sites undergo cycles of loading and unloading, also affecting the host rock properties. Accordingly, it is essential to understand the rheology of salt rocks, which controls their flow behaviour and resulting microstructures, under a range of scenarios.

The viscous flow of rock salt in collisional settings, and its interaction with deformation zones, can result in a diverse array of salt structures. The channel flow model assumes a blend of Couette (simple shear) and Poiseuille (pipe-type) flow (Godin et al., 2006; Sarkarinejad et al., 2018). As shown in Fig. 1a, Couette flow occurs between moving rigid plates, generating uniform induced simple shear in the channel (Godin et al., 2006; Grujic, 2006). This flow type is characteristic of salt layers serving as detachments for thrusts (Fig. 1b) (McClay et al., 2004). In case of Poiseuille flow, the velocity of the flowing salt is highest inside the channel center which results in opposing shear sense at the top and bottom (Fig. 1a) (Godin et al., 2006; Sarkarinejad et al., 2018). Poiseuille flow is also expected during salt flow into growing salt diapirs or anticlines (Fig. 1c) (Fossen, 2010). The central part of the Poiseuille flow channel

(e.g., central diapir stem) (Hudec and Jackson, 2007) is anticipated to be dominated by pure shear deformation, while rocks within the channel flow boundary (e.g., edge of the salt body) (Fossen, 2010) are expected to mainly deform by simple shear. Generally, deformation paths in most salt body regions incorporate both simple and pure shear components, described by a parameter of kinematic vorticity number (i.e., the curl of flow velocity normalized respect to the stretching; Truesdell, 1953; Means et al., 1980). Recent studies based on samples (Langille et al., 2010; Skemer et al., 2010; Michels et al., 2015), experiments (Boneh and Skemer, 2014), and numerical models (Llorens et al., 2017, 2022) indicate that the spatial and temporal evolution of deformation kinematics governs the deformation of polycrystalline aggregates and their resulting structures and textures. However, accurately quantifying kinematic vorticity and finite strain using microstructures is challenging due to the complex natural deformation. Analytical methods rely on homogeneous steady-state flow models, subject to necessary assumptions whose practical application is not always straightforward (Xypolias, 2010). Additionally, factors like dynamic recrystallization in viscoplastic deformation of polycrystalline aggregates can significantly impact the use of strain gauges (Hao et al., 2023) and paleopiezometers (Stipp et al., 2010).

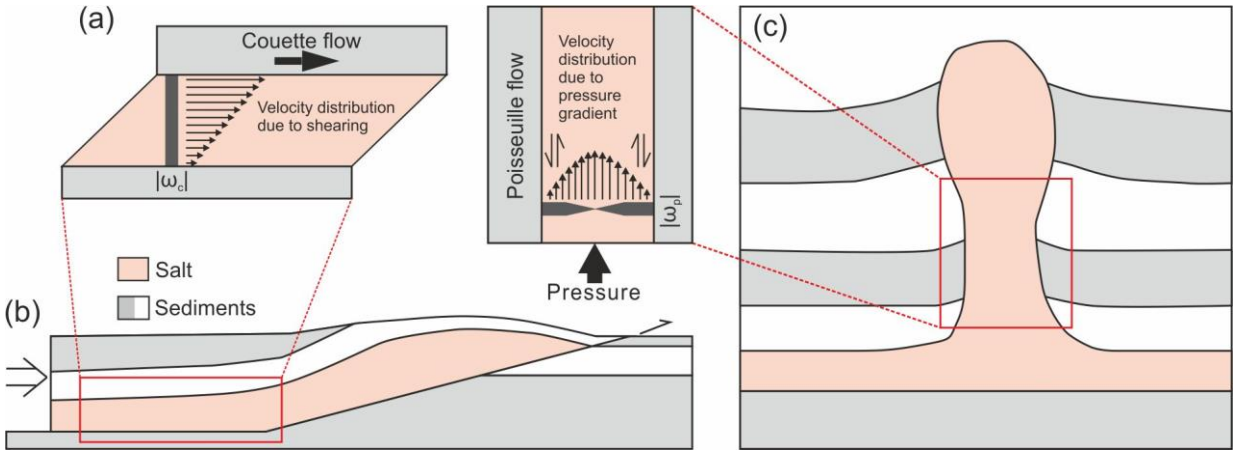

Fig. 1. Sketch of the flow pattern in a salt channel flow. (a) Couette flow (left) with velocity profile (arrows) and kinematic vorticity (dark bar, ω_c) caused by shearing; Poiseuille flow (right) with velocity profile (arrows) and kinematic vorticity (dark bar, ω_p) caused by pressure gradient within the channel (After Godin et al. (2006) and Sarkarinejad et al. (2018)). The kinematic vorticity numbers are visually indicated by the width of a black bar. A wider segment of the bar indicates a higher component of simple shear, whereas a narrower segment indicates a greater component of pure shear. The diagrams display

only the absolute magnitude of the kinematic vorticity, without distinguishing between positive (sinistral simple shear) and negative (dextral simple shear) directions. (b) Couette flow can occur in a salt layer beneath the sliding overburden (After Hudec and Jackson (2007)). (c) In stem of salt diapir, a Poiseuille flow can occur as salt moves into a salt structure. The central salt within the diapir stem flows faster than the salt along the boundary due to boundary drag restrictions. Poiseuille flow results in a predominant pure shear component at the centre of the channel and a significant simple shear component at its margins (Sarkarinejad et al., 2018).

Halite exhibits viscoplastic anisotropy at the single crystal level because it primarily deforms by dislocation glide along specific crystallographic slip systems (Carter and Heard, 1970; Guillope and Poirier, 1979). The viscoplastic deformation induced by dislocation creep in halite polycrystalline aggregates results in the development of CPO (also known as texture) and microstructure, including grain shape preferred orientation (SPO). These evolve in response to temperature, applied stress, and deformation kinematics (e.g., Urai et al., 2008). Two dynamic recrystallization (*DRX*) processes, subgrain-rotation recrystallization (*SGR*) and grain boundary migration recrystallization (*GBM*), can accompany dislocation creep in halite (Urai et al., 1986a; Schléder and Urai, 2007; Desbois et al., 2010; Mansouri et al., 2019). With increasing temperature and/or water content, the dominant dynamic recrystallization process in deformed synthetic rock salt shifts from *SGR* to *GBM*, resulting in changes of grain size and shape, influencing the resulting microstructure (Franssen, 1994; ter Heege et al., 2004; Armann, 2008). Solution-precipitation creep occurs along halite grain boundaries in the presence of brine (Spiers et al., 1988, 1990; Urai et al., 2008). This process involves mass transfer around grain boundaries and has not been included in this study. As far as we know, the internal structure development of rock salt, including grain SPO and strain localization, is not fully understood for the full range of deformation conditions. Franssen and Spiers (1990) noted from deformation experiments of dry synthetic rock salt at different temperatures that the flow strength of rock salt undergoing uniaxial compressive deformation was greater than that of simple shear deformation, suggesting a potential link to anisotropy due to CPO evolution. However, there is a lack of further systematic quantification.

Numerical simulations can overcome limitations related to temperature, strain rate, and strain scale inherent in laboratory experiments, and allow visualization of the dynamic behaviour of the system. In contrast, the study of natural samples only allows analysis of the final stage of finite deformation. This study conducts a series of full-field numerical simulations of pure halite, integrating dislocation glide and various dynamic recrystallization processes (including *SGR* and *GBM*), over a temperature range of 100-300°C. The simulations apply two endmembers of deformation kinematics: pure shear and simple shear, representing coaxial and non-coaxial deformation paths, respectively. The primary goal is to quantify and evaluate the effect of deformation kinematics and temperature on the resulting microstructures and textures. We focus on the evolution of SPO and CPO in both pure shear and simple shear, and the associated development of strain localization. We specifically capture indicators for determining the deformation kinematics at the microscale.

2. Methods

We use the Viscoplastic Fast Fourier Transform algorithm (VPFFT; Lebensohn, 2001; Lebensohn et al., 2008; Lebensohn and Rollett, 2020) that simulates the viscoplastic deformation of polycrystalline aggregates coupled with the multi-scale numerical simulation platform ELLE (Bons et al., 2008; http://www.elle.ws), which allows incorporating several dynamic recrystallization processes, enabling quantification of intra- and inter-crystalline heterogeneity during deformation (Llorens et al., 2016a; Steinbach et al., 2016; Gomez-Rivas et al., 2017; Hao et al., 2023).

ELLE-VPFFT simulations have effectively modelled halite deformation microstructures in simple shear, including subgrain rotation recrystallization (*SGR*) and intracrystalline recovery processes, as well as grain boundary migration (*GBM*) (Hao et al., 2023). The latter study reproduces torsion experiments of pure halite deformed at different temperatures (100°C, 200°C and 300°C), achieving a satisfactory agreement between numerical and experimental results in terms of average grain size evolution and CPOs.

The VPFFT approach employs a spectral method based in the Green's functions and the fast Fourier transform algorithm for solving micromechanical problems for periodic unit cells. By satisfying the constitutive relation locally while adhering to the constraints of equilibrium and compatibility and the applied boundary conditions, this approach gives the stress field and strain rate field distributions. Lebensohn & Rollett (2020) give a detailed explanation of the VPFFT approach and Griera et al. (2013) describes its implementation in ELLE. VPFFT discretizes the polycrystalline aggregate into a periodic grid consisting of regularly-spaced elements, each with a certain crystallographic orientation. The approach assumes that deformation is achieved solely through dislocation slip along pre-defined slip systems. The calculation of the deviatoric stress $\sigma'(\mathbf{x})$ and strain rate $\dot{\varepsilon}(\mathbf{x})$ tensors at each material point follows a non-linear viscous rate-dependent equation, which considers the local crystallographic orientation and strength of different slip systems. The local constitutive equation is given by:

$$\dot{\varepsilon}_{ij}(\mathbf{x}) = \sum_{s=1}^{N_s} m_{ij}^{s}(\mathbf{x})\dot{\gamma}^{s}(\mathbf{x}) = \dot{\gamma}_0 \sum_{s=1}^{N_s} m_{ij}^{s}(\mathbf{x}) \left| \frac{m^{s}(\mathbf{x}) : \sigma'(\mathbf{x})}{\tau^{s}(\mathbf{x})} \right|^{n} \operatorname{sgn}\left(m^{s}(\mathbf{x}) : \sigma'(\mathbf{x})\right) \quad (1)$$

where N_s is the total number of slip systems within the crystal, m_{ij}^{s} is the symmetric Schmid tensor, which encodes the orientation of slip system (*s*), expressed in a sample reference frame, i.e. varying from material point to material point, depending on local euler angles. The scalars $\dot{\gamma}^{s}$ and τ^{s} are the shear strain rate, and the critical resolved shear stress (CRSS) of slip system (s). The constant $\dot{\gamma}_0$ is a reference strain rate, and *n* is the stress exponent. The symbol ":" indicates double contraction of second-order tensors. In our model, viscoplastic deformation of halite is accommodated by three sets of slip systems based on the cubic symmetry: $\{110\} < \bar{1}10 >, \{100\} < 011 >$ and $\{111\} < \bar{1}10 >$ (Carter and Heard, 1970). The critical resolved shear stress (CRSS) for these three slip systems is temperature-dependent (Table1; Carter and Heard, 1970). A stress exponent value of $n = 7$ was employed consistently across all temperatures (Table1; Gomez-Rivas et al., 2017). The abbreviation "FFT" in VPFFT stands for "Fast Fourier Transform" and refers to the spectral solver used by the code. This approach requires a rectangular grid of 2^m by 2^m elements, with *m* whole number greater than one. A further requirement is that the model is wrapping in both *x* and *y*-direction to maintain periodic boundary conditions. The model

that describes the polycrystalline aggregate with variations in lattice orientation resolved down to the scale of individual elements can thus be regarded as a unit cell that is infinitely repeated in all directions. For a given state of the microstructure and applied deformation (e.g. pure shear or simple shear), VPFFT calculates the stress field and all resulting kinematics fields (velocity, strain rate, rigid-body and lattice rotation-rate fields) that are applied to the model for small increments of strain, by updating the microstructure in ELLE.

ELLE uses an operator-splitting approach where each process is executed in a sequential loop, representing a small increment of time (Bons et al., 2008). Each loop commences with the application of viscoplastic deformation (VPFFT) for a given deformation kinematic given by a velocity gradient tensor (Table 1). Subsequently, the *DRX* subloop is performed, including intracrystalline recovery, polygonization and *GBM* processes (Fig. 2). Additionally, supplementary routines handle data management, data conversion, and topology checks (Fig. 2). The ELLE-VPFFT approach requires periodic boundaries, resulting in the continuous connection of the left-right and upper-lower parts of the model unit cell (Jessell et al., 2001). The reposition process repositions any areas that have moved out of the rectangular unit cell back into the cell after each VPFFT step. This process is only necessary in simple shear simulations as the initial square model here deforms into a parallelogram. An advantage is that it facilitates the visualization of microstructures even up to high strains (Fig. 2). The data structure in ELLE consisted of two layers: (i) a contiguous set of polygons referred to as *flynns*, defined by boundary nodes (*bnodes*) connected by straight boundary segments, and (ii) a set of unconnected nodes (*unodes*) that constitute the periodic grid for storing physical properties within grains. In our model, a resolution of 256 × 256 *unodes* was employed to map crystallographic orientations, resulting in a unit cell comprising 65,536 discrete *unodes*. Each *unode* represents a smallest unit with homogeneous lattice orientation, along with local parameters such as dislocation density or local stress. The information stored in these *unodes* is used to calculate viscoplastic deformation with the VPFFT module.

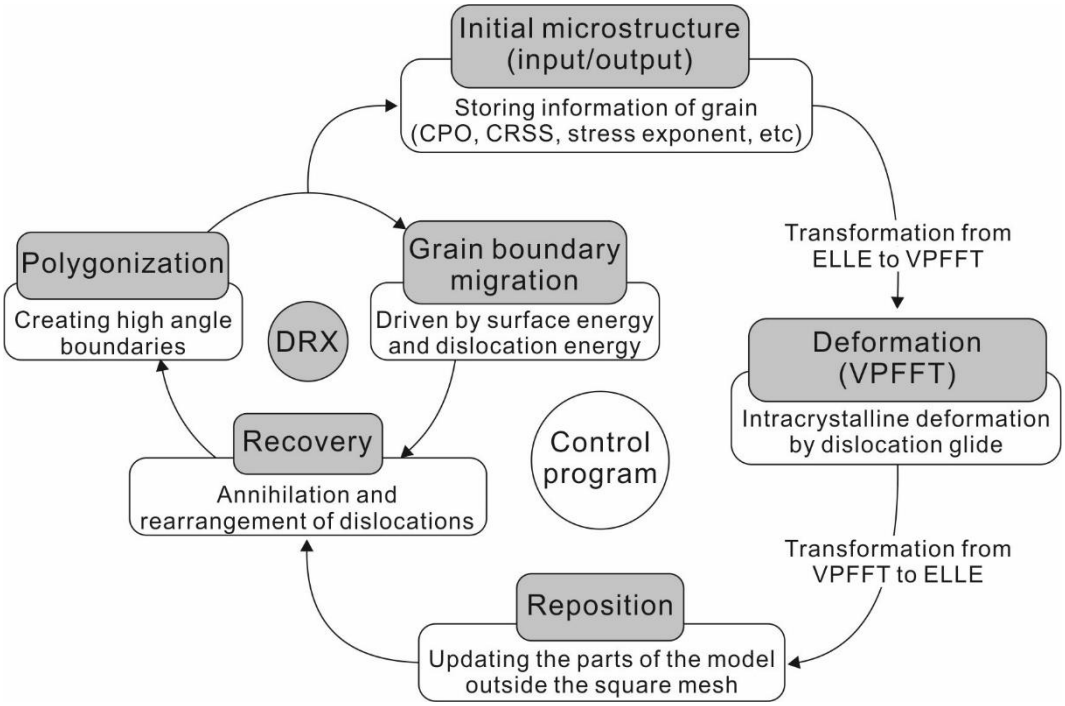

Fig. 2. Loop showing the process workflow for one simulation time step. The initial microstructure is first subjected to viscoplastic deformation (VPFFT), followed by reposition, and a subloop of dynamic recrystallization processes (*DRX*). The *DRX* subloop includes polygonization, grain boundary migration (*GBM*) and intracrystalline recovery.

The *DRX* subloop, called after each VPFFT step (Fig. 2), initiates intracrystalline recovery, polygonization (formation of new grains through lattice rotation), and *GBM* processes. For every deformation time step (i.e. VPFFT step), the recovery, polygonization and GBM modules are activated 5, 10 and 20 times, respectively. In the context of intracrystalline recovery, dislocation annihilation and rearrangement occur, leading to the formation of low-angle grain boundaries (LAGBs; also known as subgrain boundaries) and a reduction in stored strain energy (Urai et al., 1986a). Detailed formulations and implementation of intracrystalline recovery process can be found in the work by Borthwick et al. (2014) and Gomez-Rivas et al. (2017). The polygonization process involves the generation of additional high-angle grain boundaries (HAGBs) when a cluster of *unodes* (crystallites) within a grain exceeds a predefined threshold for misorientation within the cluster. In this study, a threshold angle of α_{hagb} =10° (Table 1) is adopted based on investigations of high-resolution misorientation measurements on halite (Pennock et al., 2005). To create new HAGBs, the parent grain is divided into smaller grains by

introducing new boundary nodes. This process entails identifying clusters with similar lattice orientations and inserts new boundary nodes at their interfaces utilizing Voronoi tessellation. This technique ensures that the new grain is a subset of the original grain, preserving the topology of the grain network. Two restrictions are imposed: (1) to prevent topological inconsistencies, new grains that are entirely within old grains (island grains) are not allowed, and (2) a minimum of four *unodes* is required to create a new grain, avoiding numerical instabilities due to insufficient information within the new grain. For a more detailed description of this numerical process, the reader is referred to Steinbach et al. (2016). The *GBM* process employs the front-tracking technique described in Becker et al. (2008) and further elaborated on by Roessiger et al. (2011) and Llorens et al. (2016b). The technique assumes that a reduction of Gibbs' free energy drives the movement of a grain boundary (Urai et al., 1986a). The movement direction of a *bnode* is determined by evaluating the direction with the maximum gradient in free energy as a function of a change in the position of that *bnode*. The distance the *bnode* is then moved is calculated by assuming that the work done to move the *bnode* equals the change in free energy resulting from that movement (Becker et al. 2008; Roessiger et al. 2011).

Table 1. Input properties of numerical simulations.

Symbol	Explanation	Input value
n	Stress exponent (Carter and Heard, 1970)	7
$\tau_{\{110\}}$-$\tau_{\{100\}}$-$\tau_{\{111\}}$ (100°C)	Critical resolved shear stress of $\{110\} < \bar{1}10 >, \{100\} < 011 >$ and $\{111\} < \bar{1}10 >$ slip systems at different temperatures (Carter and Heard, 1970)	4.2-18.0-12.2
$\tau_{\{110\}}$-$\tau_{\{100\}}$-$\tau_{\{111\}}$ (200°C)		3.1-8.2-7.6
$\tau_{\{110\}}$-$\tau_{\{100\}}$-$\tau_{\{111\}}$ (300°C)		2.0-4.0-4.0
α_{hagb}	Critical minimum misorientation for halite high-angle boundaries (Pennock et al., 2005)	10°
Velocity gradient tensor	Dextral simple shear (SSH_100/200/300)*	$\begin{bmatrix} 0 & 0.03 & 0 \\ 0 & 0 & 0 \\ 0 & 0 & 0 \end{bmatrix}$
	Pure shear (PSH_100/200/300)*	$\begin{bmatrix} 0.015 & 0 & 0 \\ 0 & -0.015 & 0 \\ 0 & 0 & 0 \end{bmatrix}$

Note. * indicates the simulation names. Suffixes in the simulation names denote the temperatures.

Crystallographic orientation maps, including grain and subgrain boundary network maps (Fig. 3), and pole figures (Figs. 5 and 6), were plotted using the texture calculation toolbox MTEX (Mainprice et al., 2011). This method is based on the orientation distribution function (ODF) calculated from the three Euler angles stored at each *unode* of the model. The Schmid factor (Fig. 5) was calculated using crystallographic orientation data and the applied stress tensor in MTEX. The misorientation axis of an individual grain is a pole to arcs that best fits the patterns of the dispersion of orientations within a grain (Fig. 5; black points and orange arcs) (Mainprice et al., 2015). Using these pole figures and subgrain boundary traces, a boundary trace analysis can be performed to determine the active slip systems (Fig. 11) (Prior et al., 2002; Reddy et al., 2007; Barrie et al., 2008; Mainprice et al., 2015; Linckens et al., 2016).

To assess the effect of deformation kinematics and temperature on rock salt deformation, two numerical series were implemented for simple shear (SSH_100, SSH_200 and SSH_300) and pure shear (PSH_100, PSH_200 and PSH_300), with numerical suffixes denoting different temperatures (100°C, 200°C and 300°C). We use a pure halite polycrystalline aggregate, with a cell size of 3×3 cm^2 for simple shear and a 3×6 cm^2 cell for pure shear. Both deformation kinematics with an initial average grain size of 212 μm, and are modelled in increments of $\Delta\varepsilon = 0.015$ up to natural strain of $\varepsilon = 1.5$ at temperatures of 100°C, 200°C and 300°C. A natural strain of $\varepsilon = 1.5$ corresponds to 78 % shortening in pure shear, or a shear strain of $g = 3$ in simple shear. All simulations employ a constant time step of 100 s, resulting in a natural strain rate of 1.5×10^{-4} s^{-1}. Implementation and input values for the numerical model are detailed in (Hao et al., 2023).

3. Results

3.1 Microstructure Evolution

Viscoplastic deformation leads to the development of a SPO due to grain elongation along the stretching direction (Figs. 3b-d). In simple shear simulations, the grain aspect ratio increases gradually with strain, reaching a maximum approximately at a natural strain of 1.0, then stabilizing (Fig. 4a). However, in pure

277 shear simulations it increases steadily with strain (Fig. 4a). Under simple shear, the angle between the
278 grain SPO and the horizontal shear plane gradually decreases as strain increases (Fig. 4b). Under pure
279 shear, the grain SPO aligns parallel to the *x*-axis or the direction of maximum stretching, as expected
280 (Figs. 3e-g and 4b). As temperature increases, the higher intensity of *GBM* reduces grain elongation,
281 resulting in larger and more equidimensional grains (Figs. 3 and 4a).

282 At low temperatures (100℃ and 200℃), qualitative variations in the grain boundary network between
283 two deformation kinematics are observed at a natural strain of ε = 1.0 (Fig. 3). The bands of
284 (recrystallized) small grains (also known as shear bands) are observed subparallel to the grain SPO. In
285 simple shear models, these bands appear at low angle to the shear direction (Figs 3b, c). In pure shear
286 models, these bands align diagonally relative to the maximum stretching direction (Figs. 3e, f). At high
287 temperature (300℃), subgrain boundaries are visible within some grains, although they are significantly
288 less numerous than in lower temperature models. The bands of small grains are barely visible at 300°C
289 (Figs. 3d, g).

290

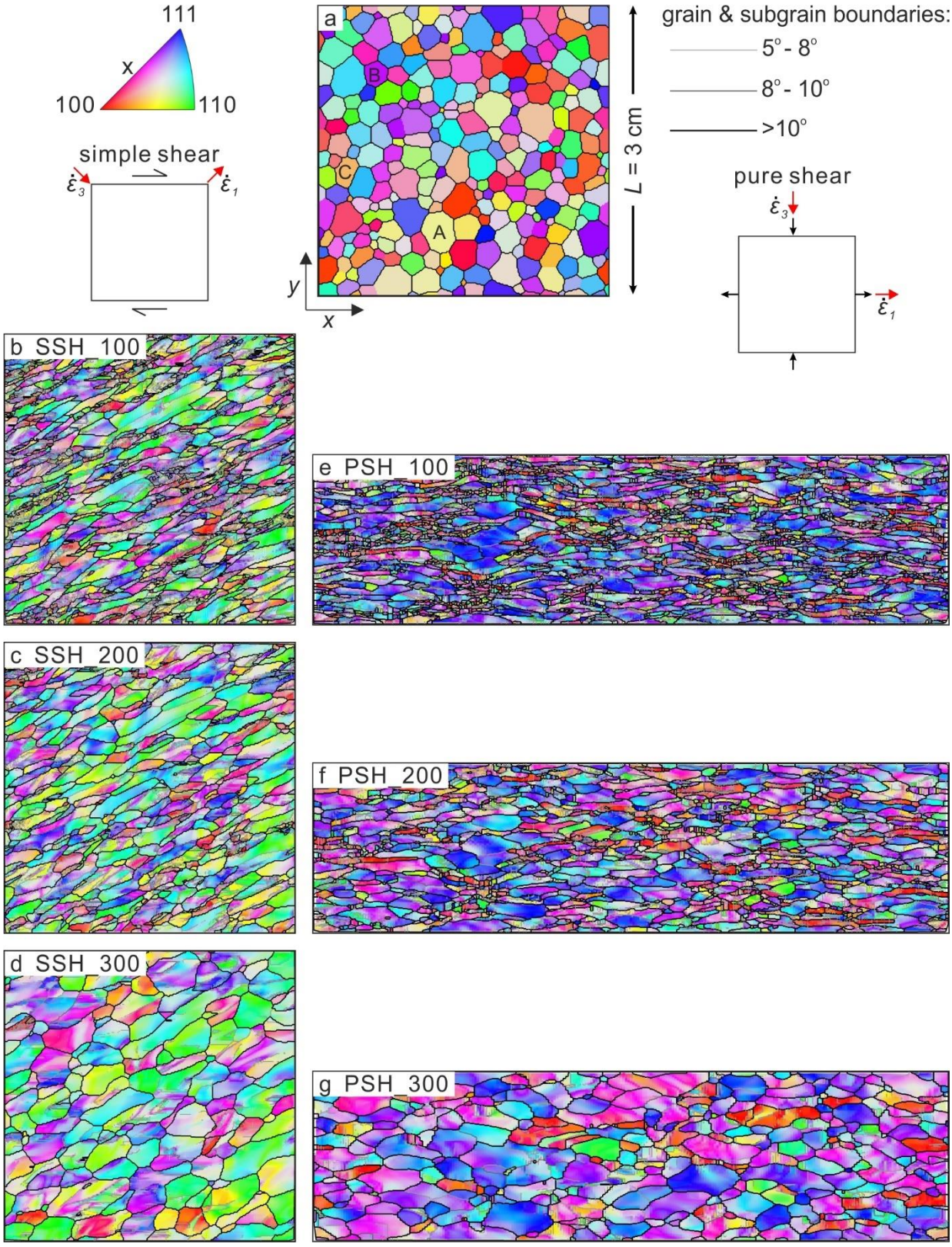

291

292 **Fig. 3.** Crystallographic orientation and grain and subgrain boundary network maps at a natural strain of
293 ε = 1.0 for simulations deformed in simple shear (b-d) and pure shear (e-g). Please note that the size of
294 images corresponding to pure shear simulations (e-g) is displayed as 0.8 times that of the original images.
295 The initial microstructure for simple shear simulations is a square model with a side length of one unit (L
296 = 3 cm) (a). The initial model size for pure shear simulations is doubled vertically ($2L$). Crystal lattice

orientations are plotted with inverse pole figure (IPF) colors with respect to the horizontal *x*-axis. Grains and subgrains are delimited by black and grey lines, respectively.

Rose diagrams displaying the orientation distribution of subgrain boundaries at natural strains of $\varepsilon = 0.3$ and 0.6 are shown in Figs. 4c-f. Conjugate preferred orientations are observed in both deformation kinematics, along with an additional maximum at a low angle to the grain SPO (red lines in Figs. 4c-f). In simple shear models, the frequencies of conjugate directions are asymmetric, with increased asymmetry at higher strain (Figs. 4c, e). In pure shear models, the frequencies of conjugate directions remain nearly symmetric throughout the deformation (Figs. 4 d, f). The orientation distribution normalized based on the subgrain boundary lengths is shown in Fig. S1. These figures are largely similar to orientation distribution, though some orientations slightly vary. Subgrain boundaries that are nearly perpendicular to the grain SPO appear more frequently in Fig. 4, yet are less prominent in Fig. S1, suggesting these subgrain boundaries are more numerous yet shorter.

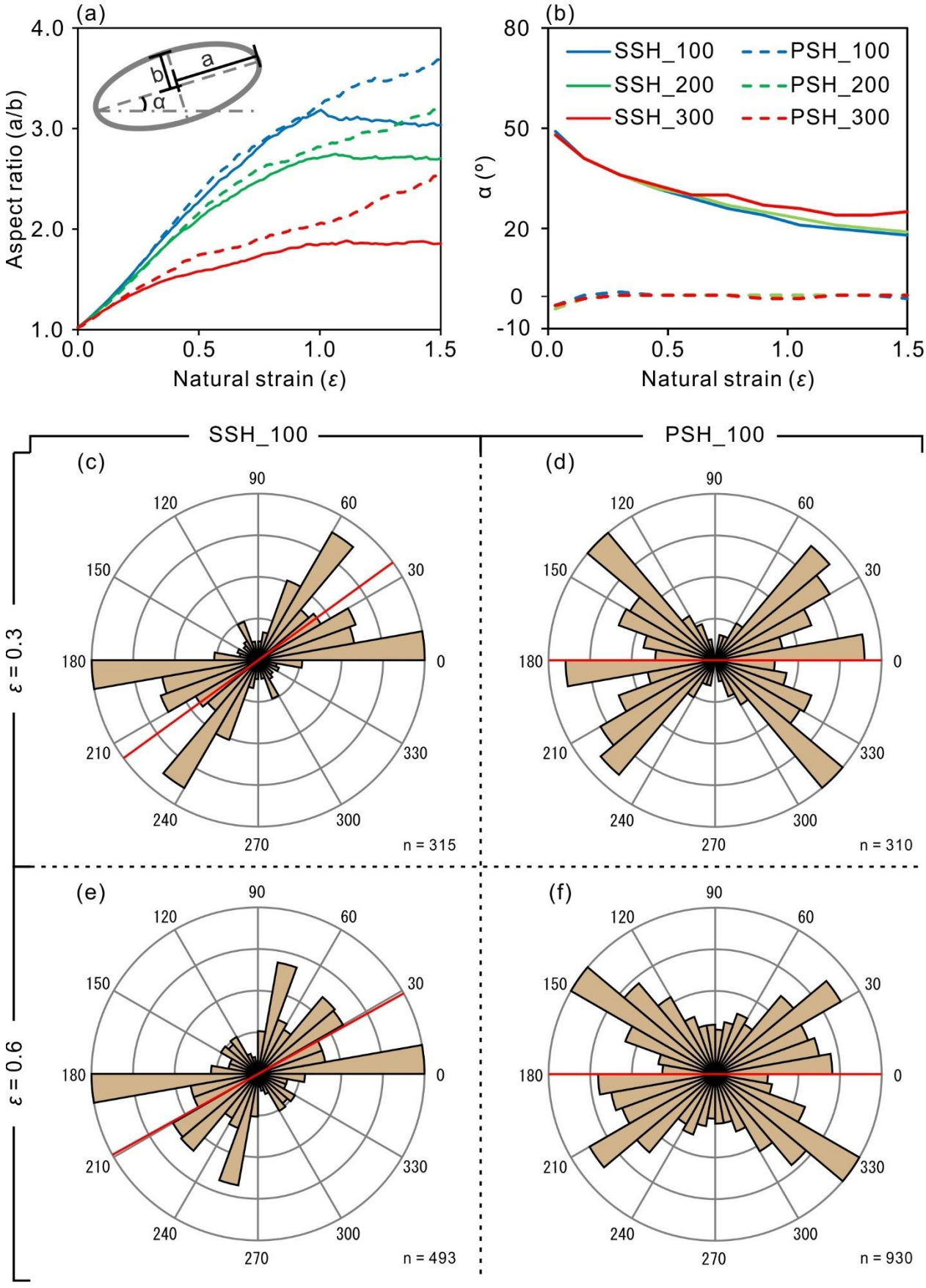

Fig. 4. Evolution of the average shape preferred orientation (a) and aspect ratio (b) of grains with natural strain. Simulations deformed in simple shear (SSH_100/200/300) are marked in solid lines, while pure shear simulations (PSH_100/200/300) are marked with dashed lines. Colour lines indicate temperature,

being 100°C, 200°C and 300°C shown in blue, green and red, respectively. (c-f) Rose diagrams displaying orientations of subgrain boundaries at natural strain of ε = 0.3 and 0.6 in simulations deformed under simple shear and pure shear at 100°C. Red lines in rose diagrams represent the grain SPO. Diagrams are normalised to the orientation with maximum frequency.

The evolution of the average grain size and its standard deviation during progressive deformation in simple shear simulations is similar to that of pure shear at the same temperature, with only slight variations at high strain (Fig. 5). For instance, the grain size and its standard deviation under simple shear is marginally larger than that under pure shear at a finite strain of 1.5 at 200°C and 300°C, whereas the reverse holds true at 100°C (Fig. 5). The proportion of small grains gradually increases with strain (Fig. S2, logarithmic grain size ranging between 1.2 and 2.0) while the proportion of large grains gradually decreases (Fig. S2, logarithmic grain size ranging between 2.0 and 2.6) at 100°C and 200°C. The evolution of the grain size distribution is characterized by a gradual increase in the proportion of large grains at 300°C (Fig. S2, logarithmic grain size ranging between 2.0 and 2.6). At 200°C and 300°C, simple shear produces a more dispersed grain distribution than that of pure shear deformation at high strain (ε > 1.0), with a higher proportion of both large and small grains (Fig. S2), leading to a larger standard deviation of the average grain size (Figs. 5b, c).

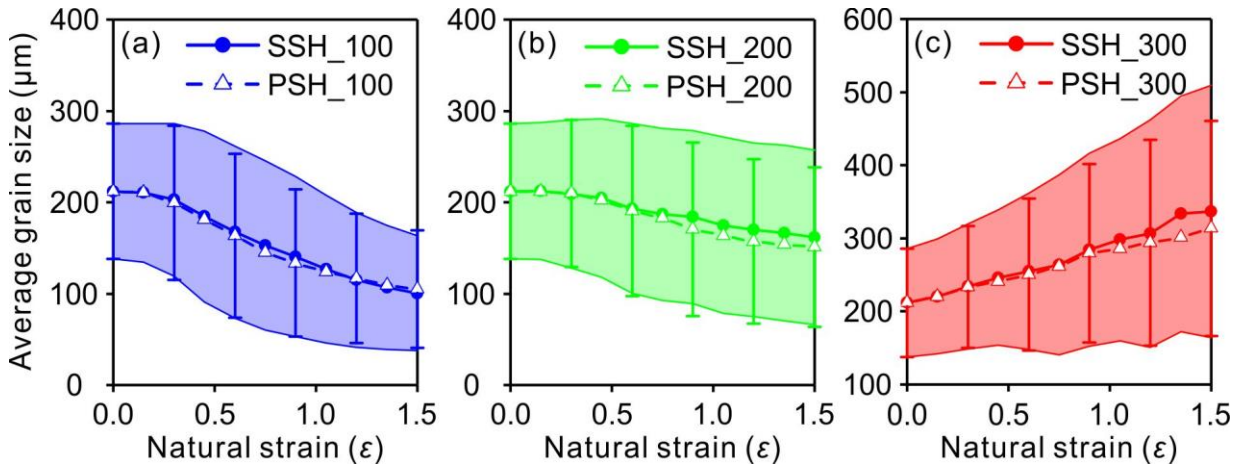

Fig. 5. Evolution of the average grain size with its standard deviation (a-c) with natural strain. Simulations deformed in simple shear (SSH_100/200/300) are marked in solid lines and shaded areas, while pure

shear simulations (PSH_100/200/300) are marked with dashed lines and error bars. Colour lines indicate temperature, being 100°C, 200°C and 300°C shown in blue, green and red, respectively.

Fig. 6 shows the details of the subgrain boundaries and crystal orientation of three selected grains (indicated as A, B and C in Fig. 3a) at low strain (ε = 0.3), comparing them under simple shear and pure shear deformation conditions. The kinematics of deformation affects the morphology of subgrain boundaries and the dispersion of crystallographic orientation. Under simple shear, grain A exhibits subgrain boundaries aligned subparallel to the maximum stretching direction ($\dot{\varepsilon}_1$ axis). Under pure shear, grain A instead develops two small subgrains with differing crystallographic orientations from the parent grain. Grain B develops subgrains oblique to the maximum stretching direction when is deformed under pure shear. Similar to Grain B, grain C also develops a subgrain boundary oblique to the direction of maximum stretching ($\dot{\varepsilon}_1$ axis), when is affected by pure shear.. Under simple shear deformation, grains B and C do not exhibit an evident substructure, but lattice bending occurs. The 100 pole figures of selected grains show the dispersion of crystallographic orientations around the <100> misorientation axis due to the deformation (Fig. 6). The dispersion of orientations increases as the natural strain increases from 0.15 to 0.3. The direction of spread of the crystallographic orientations around the <100> axis is correlated with the deformation kinematics. Simple shear deformation results in clockwise spreading of the crystallographic orientations along the best fitting fibre, whereas pure shear deformation leads to clockwise and/or counterclockwise spreading directions (Fig. 6, red arrows in pole figures).

Fig. 6 displays the initial Schmid factors for different slip systems in selected grains. The resolved shear stress (τ) is related to the applied stress (σ_a) by schmid factor (m):

$$\tau = \sigma_a m = \sigma_a(\cos(\lambda)\cos(\varphi)) \quad (2)$$

where λ is the angle between the stress direction and the slip direction, and φ is the angle between the stress direction and the normal to the slip plane (Schmid and Boas, 1950). The Schmid factor predicts the likelihood of slip systems in crystalline materials under applied stress. If m is zero, no resolved shear stress acts on the specific slip system. The maximum value of m is 0.5. As shown in Fig. 6, the initial

Schmid factors for the various slip systems within the grains at the onset of deformation (ε = 0) are calculated using the theoretical applied stress and the crystallographic orientations of the individual grains. Under simple shear, the initial Schmid factors for the $\{110\}<\bar{1}10>$, {100} <011> and $\{111\}<\bar{1}10>$ slip systems in grain A are 0.112, 0.449 and 0.318, respectively. Under pure shear, the initial Schmid factors for these three slip systems in grain A are 0.423, 0.254 and 0.492, respectively, distinctly different from those under simple shear. Similar deformation responses are observed in grains B and C, with comparable changes in their initial Schmid factors under both simple and pure shear conditions.

Additionally, Fig. 6 shows the distribution of slip system activity in selected grains at natural strain of ε = 0.3. The $\{110\}<\bar{1}10>$ (green tones), $\{111\}<\bar{1}10>$ (blue tones), and {100} <011> (red tones) slip systems all contribute to the deformation of the grains. Different deformation kinematics within the same grain produce varied slip system activity distributions. In simple shear the upper half of grain A shows activation of the $\{111\}<\bar{1}10>$ and {100} <011> slip systems, while the lower half shows activation of the $\{110\}<\bar{1}10>$ slip system. Under pure shear, the same grain is primarily dominated by the $\{110\}<\bar{1}10>$ slip system, with smaller regions dominated by the $\{111\}<\bar{1}10>$ and {100} <011> slip systems. Under simple shear, the distribution of the three slip systems in grain B appears random. Under pure shear, grain B displays a green band inclined toward the direction of maximum stretching, indicating dominated by the $\{110\}<\bar{1}10>$ slip system. Most of grain C shows activation of the $\{110\}<\bar{1}10>$ slip system under both simple shear and pure shear conditions.

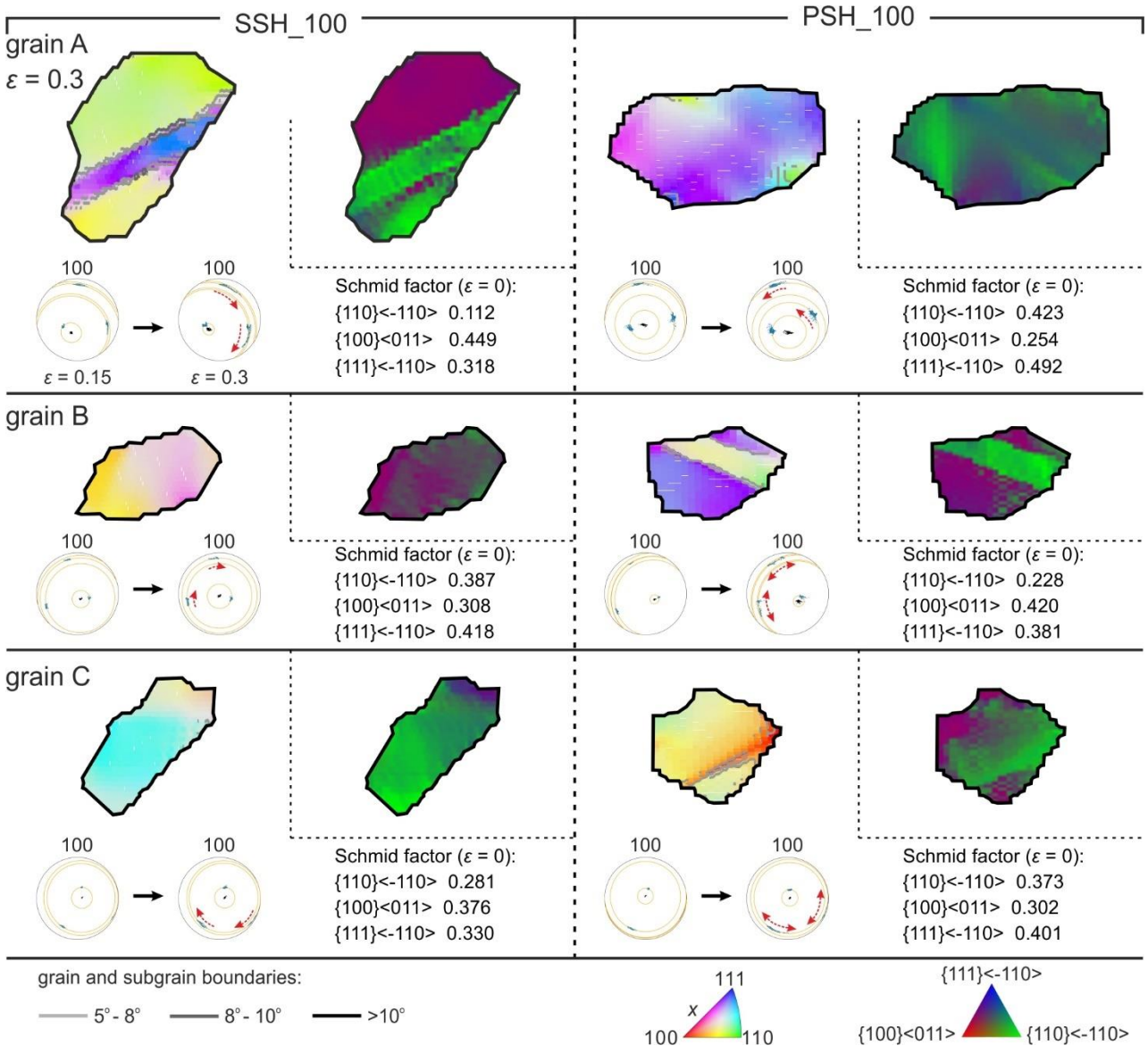

Fig. 6. Crystallographic orientation, subgrain boundary network, distribution of the slip system activity and calculated initial Schmid factor of selected grains (see grains A, B and C in Fig. 3a for their original orientation and geometry) at natural strain of $\varepsilon = 0.3$. Left-hand column shows the results for simulations deformed in simple shear (SSH_100) and right-hand column results under pure shear (PSH_100), both at 100°C. The crystallographic orientations are plotted in 100 pole figures, where every point represents the orientation of a crystallite inside the grain. The evolution of orientations dispersion with increasing strain (from 0.15 to 0.3) is marked in red arrows. Orange arcs and black points are the best fitting fibre with a specific misorientation axis for given orientations (Mainprice et al., 2015). Crystallographic orientations are plotted with inverse pole figure (IPF) colors with respect to the horizontal *x* axis. The initial Schmid factor was calculated using crystallographic orientation of selected grains and the applied stress tensor at the onset of deformation ($\varepsilon = 0$).

3.2 CPO evolution

The pole figures of Fig. 7 illustrate the evolution of the CPO throughout simple *versus* pure shear deformation at the different modelled temperatures (T = 100°C, 200°C and 300°C). At a natural strain ε = 0.5, {100} CPO features six maxima that are orthogonally symmetric with respect to the maximum shortening axis ($\dot{\varepsilon}_3$ axis) both in simple shear and pure shear simulations. Under simple shear, three {100} maxima slightly rotate synthetically, aligning with the applied shearing sense, while the other three maxima diminish and eventually disappear with progressive deformation (Figs. 7b-g). With increasing strain, simple shear tends to create a marginally stronger fabric compared to pure shear, attributed to a higher concentration of the maxima (see M index comparison between pure and simple shear in Fig. 7). At the final strain of 1.5, the simple shear CPO exhibits a {100} maximum that is nearly parallel to the *y* axis, with two additional maxima in the XZ plane approximately 45° to the *x*-axis. The evolution of {110} and {111} CPOs during incremental deformation is akin to that of {100} CPO, where simple shear CPOs rotate according to the synthetic shear direction, while the pure shear CPOs remain static. Although both the {110}and {111} pole figures show mild hexagonal symmetry, the dispersion of crystallographic axes in simple shear CPOs is less than that in pure shear CPOs. In simple shear, a higher temperature modestly increases the CPO strength without changing its orientation (Fig. 7). However, the CPO strength in pure shear simulations decreases with increasing temperature.

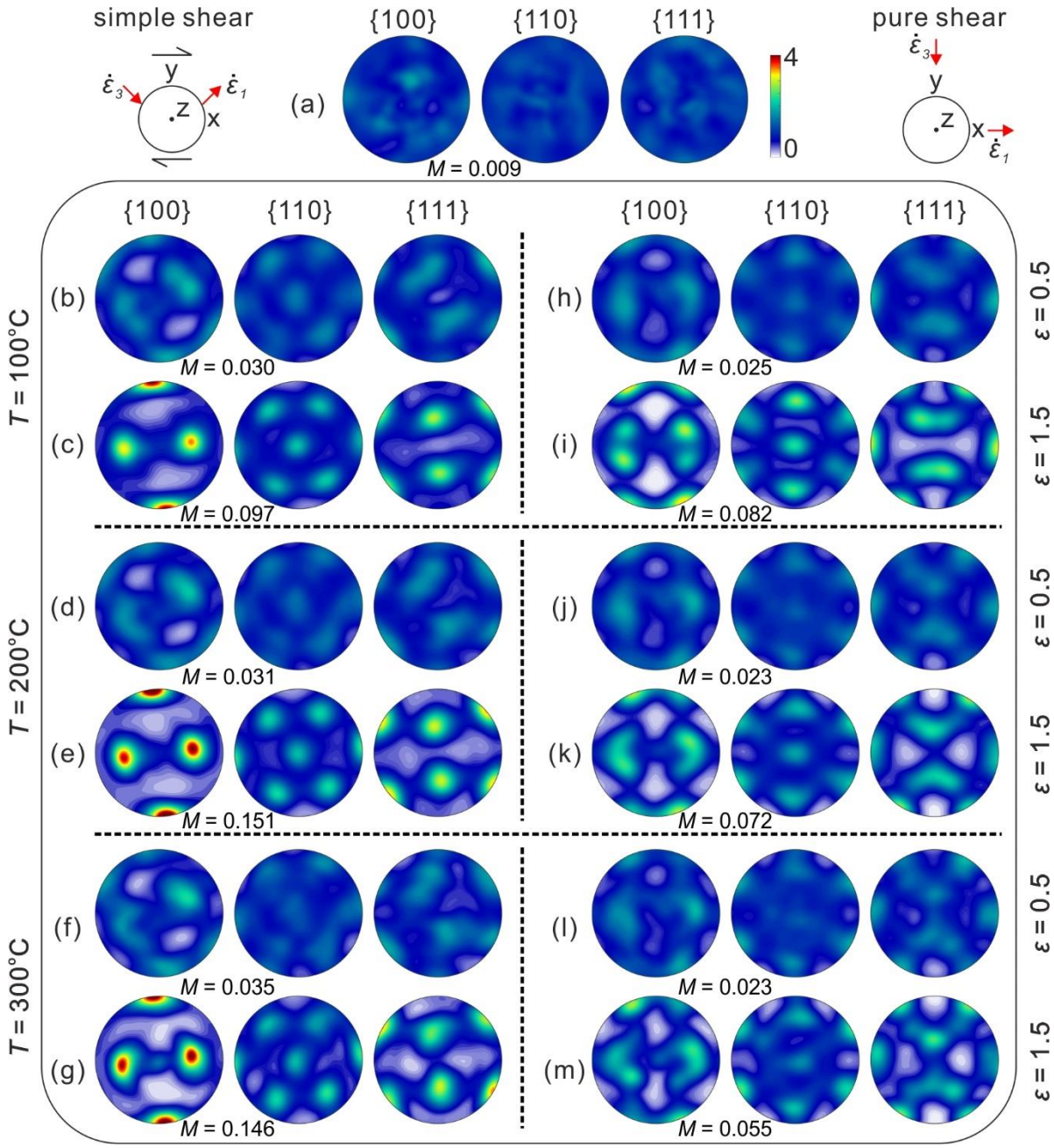

Fig. 7. Pole figures of crystallographic preferred orientations at natural strain of ε = 0.5 and 1.5, for simulations performed at temperatures of 100°C (b-c-h-i), 200°C (d-e-j-k) and 300°C (f-g-l-m). Left-hand column shows results under simple shear, and right-hand column under pure shear deformation. The initial CPO is shown in (a). The CPO intensity is quantified as the M index (misorientation index) from the ODF (Skemer et al., 2005).

3.3 Slip system evolution and distribution

Fig. 8 shows the evolution of the activity of the slip systems during deformation for all simulations presented. In all instances, the CRSS is defined as a temperature-dependent constant (Table 1). At 100°C,

roughly 50% of the deformation is accommodated by the softest $\{110\} < \bar{1}10 >$ system, 20% by the hardest {100} <011> system, and approximately 30% by the $\{111\} < \bar{1}10 >$system at the onset of deformation. However, at 200°C and 300°C, the $\{111\} < \bar{1}10 >$ slip system becomes less active and accommodates approximately only 14%-19% of strain, remaining almost constant throughout the simulation. The kinematics of deformation clearly influence this behaviour: for pure shear the $\{110\} < \bar{1}10 >$ system activity experiences a slight decrease with increasing strain at all temperatures, while that of the {100} <011> system slightly increases (see dashed lines in Fig. 8). However, in simple shear, the equilibrium of activity between the softest $\{110\} < \bar{1}10 >$ and hardest {100} <011> systems is disrupted at moderate strains, with the activity of the hardest system surpassing that of the softest system (Figs. 8b, c). Temperature clearly affects this dynamic, with the hardest system surpassing the softest earlier at higher temperatures (ε = 0.6; Fig. 8c) than at lower temperatures (ε = 1; Fig. 8b).

Maps illustrating the distribution of slip system activity at a natural strain of 1.0 reveal the dominance of the $\{110\} < \bar{1}10 >$ and $\{111\} < \bar{1}10 >$ slip systems, significantly influencing the entire sample at 100°C (green and blue tones in Figs. S3a, c) while at 300°C the dominant slip systems are $\{110\} < \bar{1}10 >$ and {100} <011> (green and red tones in Figs. S3b, d). This is consistent with the results shown in Fig. 8.

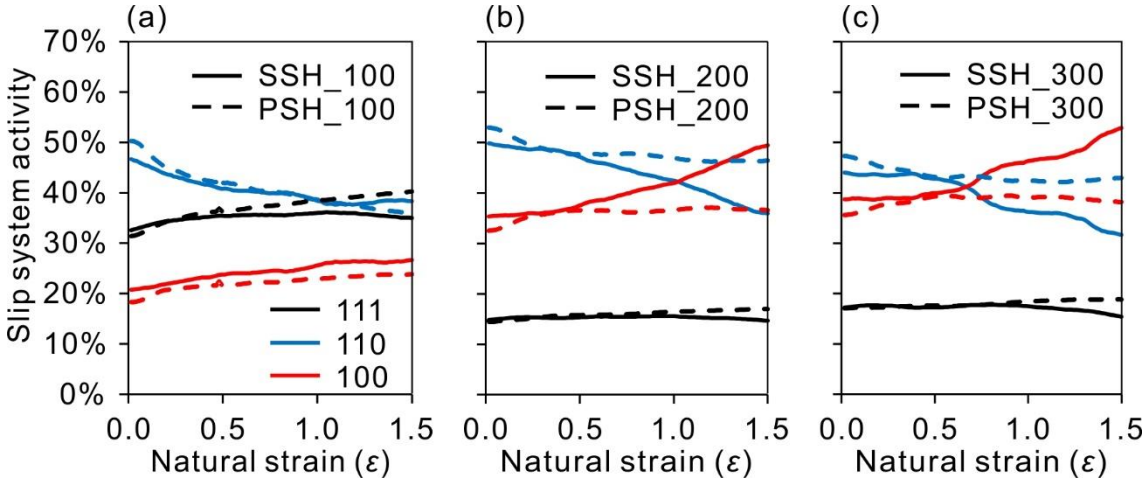

Fig. 8. Evolution of the average relative slip system activity ($\{110\} < \bar{1}10 >, \{100\} < 011 >$ and $\{111\} < \bar{1}10 >$ with natural strain for simulations at 100°C (a) and 200°C (b) and 300°C (c).

3.4 Strain localization

Regardless the temperature, for simple shear deformation most of the high strain-rate bands are almost parallel to the horizontal shear plane (*x*-axis), while a smaller portion of high strain-rate bands are nearly perpendicular to it (Figs. 9a, b). For pure shear deformation, conjugate high strain-rate bands are symmetrically orientated relative to the vertical *y*-axis (Figs. 9c, d). As expected, due high temperature *GBM* reduces the intensity and number of high strain-rate bands in both simple shear and pure shear simulations (Figs. 9b, d). At low temperature, the high strain-rate bands can be recognized by the regions rich in small grains. However, *GBM* produces large and equidimensional grains, masking the high-strain bands, even reaching a point where they cannot be identified from the microstructure.

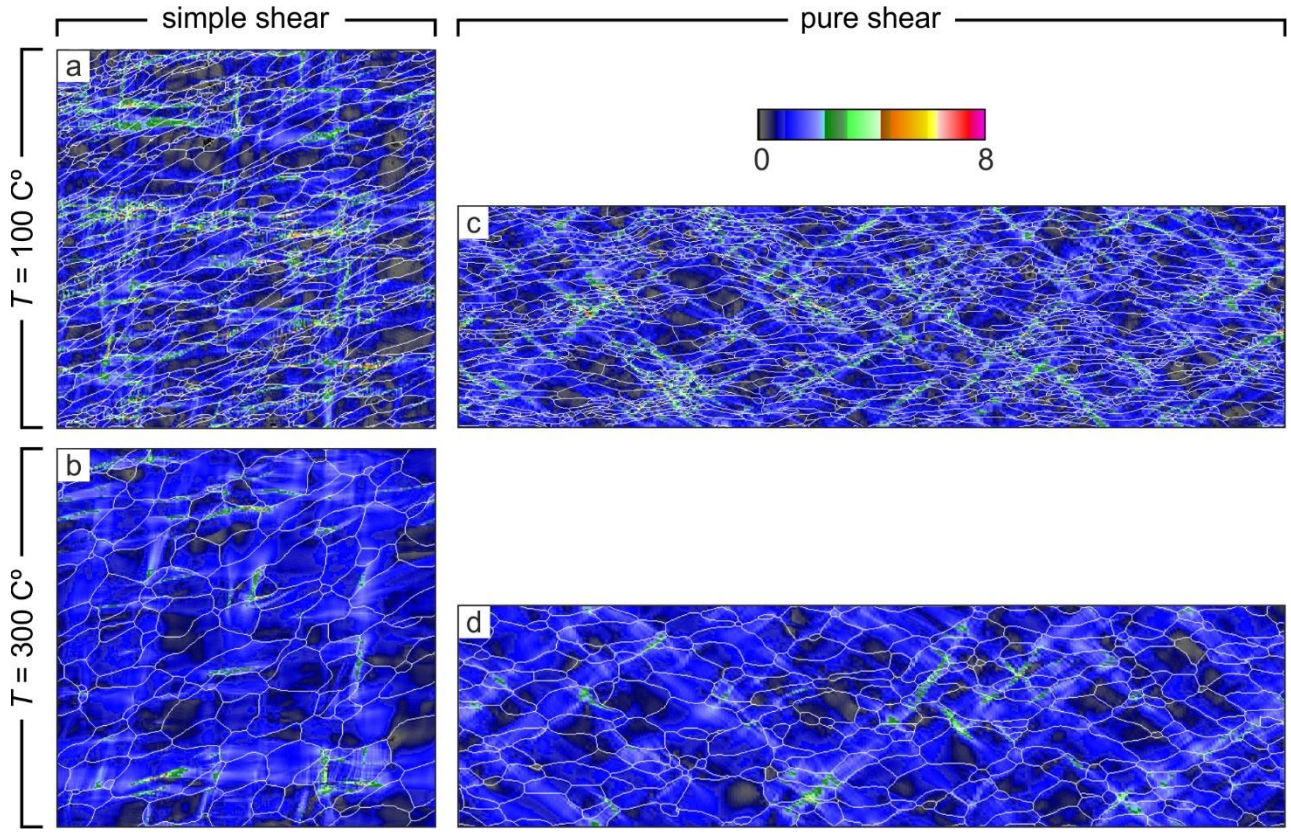

Fig. 9. Maps of the von Mises strain-rate field at natural strain of ε = 1.0 for simulations deformed in simple shear (a, b) and pure shear (c, d) at 100°C (a, c) and 300°C (b, d), respectively. Please note that the size of images corresponding to pure shear simulations (c, d) is displayed as 0.8 times that of the original images.

We quantify the strain heterogeneity using the localization factor (F) as originally defined by Sornette et al. (1993) and later implemented in ELLE by Gomez-Rivas (2008):

$$F = 1 - \frac{1}{N_u}\frac{(\sum \dot{\varepsilon}_{vM})^2}{\sum \dot{\varepsilon}_{vM}{}^2} \tag{3}$$

where N_u represents the total number of unodes, $\dot{\varepsilon}_{vM}$ is the von Mises strain rate, which is calculated as a function of the symmetric strain-rate tensor $\dot{\varepsilon}_{ij}$:

$$\dot{\varepsilon}_{vM} = \sqrt{\frac{2}{3}\dot{\varepsilon}_{ij}\dot{\varepsilon}_{ij}} \tag{4}$$

F varies from 0 to 1, representing the full spectrum between totally homogeneous deformation and maximum localization, respectively. As depicted in Fig. 10a, the localization factor in simple shear simulations exhibits a quasi-periodic evolution, with a trend remaining relatively stable or mildly intensified. However, the factor of the pure shear simulations displays a steadily decreasing trend with progressive deformation, resulting in more homogeneous deformation. As shown in Fig. 10b, the intragranular inhomogeneity can be quantified by the average dislocation density. At the same temperature, simple shear results in a higher dislocation density than pure shear as the strain increases.

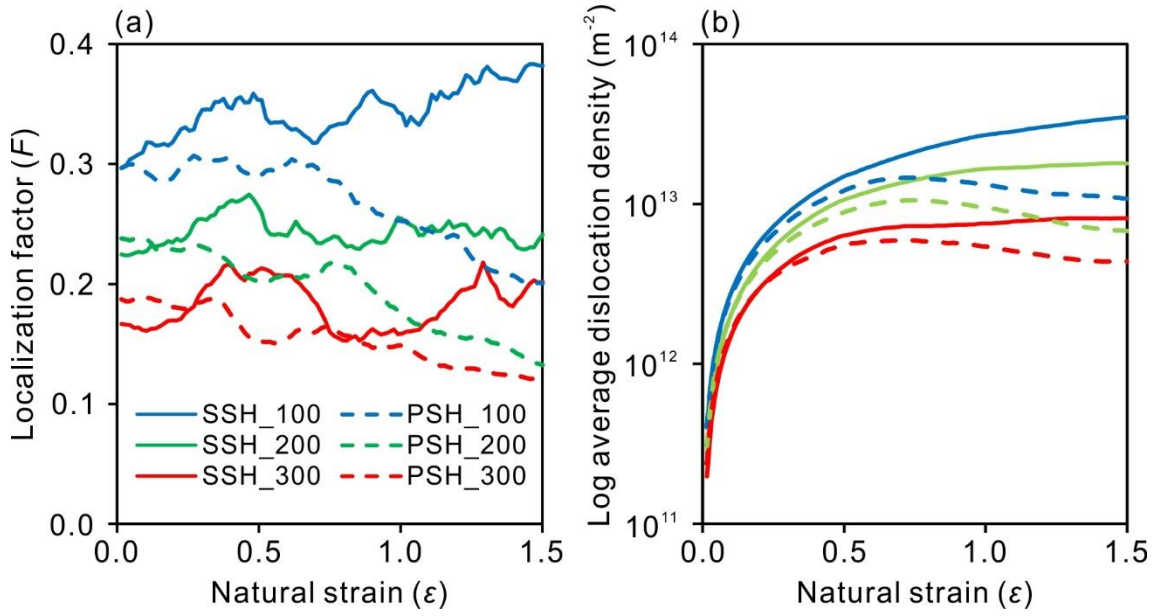

Fig. 10. Evolution of the localization factor *F* (a) and average dislocation density (b; plotted in logarithmic form, log10) with natural strain for simulations deformed in simple shear (solid lines) and pure shear (dashed lines) at 100°C (blue lines), 200°C (green lines) and 300°C (red lines).

4. Discussion

4.1 Effects of kinematics of salt flow on the evolution of microstructures and CPOs

The flow of salt and the resulting development of diverse tectonic structures are a complex phenomenon (Hudec and Jackson, 2007). Shear zones, dominated by non-coaxial deformation, have been observed within salt bodies and along their perimeter (Talbot and Jackson, 1987; Miralles et al., 2000; Fossen, 2010; Jackson et al., 2015). The central portion of a diapir stem is anticipated to experience pure shear deformation (Hudec and Jackson, 2007; Talbot and Pohjola, 2009). Hence, comprehending the distinct behaviour of halite under varying deformation kinematics is crucial.

The simulation results reveal that the boundary kinematics slightly affect the halite grain size evolution (Fig. 5), but they significantly influence the SPO (Fig. 4a) during viscoplastic deformation, primarily due to strain heterogeneity. Regardless of the temperature, simple shear deformation results in a higher degree of strain localization than pure shear deformation (Fig. 10a), leading to higher dislocation densities (Fig. 10b). Higher dislocation density contributes to the formation of new LAGBs and HAGBs, accelerating *SGR* and resulting in grain size reduction (Fig. S2). Additionally, it also enhances the driving force for grain boundary migration at high temperatures, accelerating *GBM* and eventually resulting in grain size increase (Fig. S2). The evolution pattern of the strain-rate field affects the microstructure. During progressive deformation, simple shear produces small grain bands subparallel to the grain SPO, whereas in pure shear simulations, such bands are conjugate and symmetric oblique to the grain SPO (Fig. 3). Simple shear results in highly variable strain-rate bands, creating distinct and dynamic deformation domains. Finch et al. (2020) also observed this phenomenon in their simulations of simple shear deformation of granitoid rocks. Given the high variability of strain-rate bands, in simple shear, a grain may initially elongate, subsequently move and rotate passively with progressive deformation, and then shorten. In contrast, pure shear simulations show a steady evolution of the strain-rate bands, resulting in

continuous deformation of grains. Consequently, pure shear deformation yields a larger average grain aspect ratio compared to simple shear deformation (Fig. 4a). The influence of salt deformation patterns on grain size and morphology is significant for understanding the kinematics of deformation and estimating finite strain in salt tectonics (e.g., in salt diapirs; Sarkarinejad et al., 2018). For instance, at a natural strain of ε = 1.5 flow pattern differences alone can cause grain aspect ratio variations of up to 20% (Fig. 4a). Experiments of high-strain plastic deformation of metals underscore the impact of the kinematics of deformation on the stability of shear band evolution (Cao et al., 2018). Simple shear is characterized by the discontinuous evolution of shear bands and early strain localization, while pure shear involves the continuous evolution of shear bands, resulting in variations in the grain boundary network (Segal, 2002).

One goal of this study is to provide systematic details of the evolution of halite CPOs with a view to deciphering deformation kinematics from the textures. Our study reveals that the CPOs evolve as anticipated under both simple shear and pure shear deformation conditions, and can be directly compared with halite torsion experiments, such as those carried out by Armann (2008) at temperatures of 100°C and 200°C, as well as pure shear experiments (e.g., Kern, 1977; Skrotzki et al., 1995). The CPOs resulting from simple shearing are generally associated with a monoclinic symmetry, whereas the CPOs from pure shear exhibit an orthotropic symmetry (Wenk et al., 1987). In our study, the {100} CPO pattern is similar for both the simple and pure shear cases at low strain (e.g., Fig. 7, ε = 0.5). In this scenario, the CPO displays six {100} maxima orthogonally symmetric to the maximum shortening axis ($\dot{\varepsilon}_3$), implying that the deformation kinematics have little impact on the CPO evolution of halite at low strains. As deformation progresses, the {100} CPO intensity under pure shear gradually increases without altering the pattern (Fig. 7). Meanwhile, in simple shear cases, the {100} CPO undergoes rotation following the sense of shear (clockwise here). Eventually, it culminates in a {100} maximum subperpendicular to the shear plane and two {100} maxima oblique to the shear direction (Fig. 7). The primary reason for this contrast is that once crystal lattices attain a stable orientation, for a specific dominant set of slip systems in alignment with the imposed pure shear deformation, further rotation is prevented. However, simple shear CPOs continuously rotate, leading to a stronger texture compared to pure shear (Fig. 7). Wenk et

al. (2009) similarly noted the continuous regeneration and rotation of CPOs in simple shear using the viscoplastic self-consistent (VPSC) simulations of halite, even at shear strains as high as 35. Therefore, our study illustrates that the CPOs may serve as a sensitive indicator of the strain path in rock salt. This enables differentiating between simple and pure shear, determining the sense of shear and identifying the non-coaxial deformation component. The same applies to minerals such as calcite (e.g., Wenk et al., 1987) and quartz (e.g., Morales et al., 2014).

4.2 Effect of temperature on the evolution of microstructures and CPOs

Regardless the kinematics of deformation, our study shows that temperature has a significant impact on the microstructural evolution of polycrystalline halite, influencing both grain size and SPO. At low temperatures (100°C and 200°C), the average grain size notably decreases with increasing natural strain. On the contrary, the average grain size gradually increases at high temperatures (300°C) with progressive deformation, resulting in the formation of more equidimensional grains than at lower temperatures (Figs. 3 and 4a). This trend is qualitatively similar to the size evolution measured in halite torsion experiments conducted at the same temperatures (Armann, 2008). These changes reveal a transition from a microstructure dominated by *SGR* to another one dominated by *GBM* in rock salt systems as the intensity of *GBM* increases (Hirth & Tullis, 1992; Urai et al., 1986). Additionally, *GBM* reduces the elongation of grains, which could mask signs of strain localization (Figs. 9b, d) (Franssen, 1994; Leitner et al., 2011; Llorens et al., 2016a). The influence of *GBM* on the dynamic response of microstructures in naturally deformed rock salt has been evident in various borehole samples (Schléder and Urai, 2005; Thiemeyer et al., 2016; Henneberg et al., 2020). Water present within the fluid film at grain boundaries reduces the threshold temperature required for initiating grain boundary migration (ter Heege et al., 2005), expanding the potential occurrence of *GBM* under a broader range of natural conditions (e.g., top of the salt fountain; Mansouri et al., 2019). Therefore, our simulations highlight that *GBM* significantly controls grain morphology, emphasizing that grain morphology does not directly correlate with the amount of finite strain.

Our results indicate that increasing *GBM* (i.e. increasing temperature) has a minimal impact on the CPOs. The only effect observed is the more pronounced maxima of CPOs during simple shear deformation at 300°C (Fig. 7). This aligns with many studies of 1h polar ice (*e.g.*, Llorens et al., 2016a, 2016b, 2017). When simulating simple shear deformation at 300°C, we are unable to replicate the distinct CPO with two {100} maxima at a 45° angle between the *x*-axis and *y*-axis, as observed at low strain in pure rock salt torsion experiments conducted under analogous deformation and temperature conditions (Armann, 2008). Hence, additional mechanisms likely influence CPO evolution during high-temperature rock salt deformation. These mechanisms could include annealing-induced rotation of the crystal axis (Borthwick and Piazolo, 2010; Boneh et al., 2017) or discontinuous grain growth driven by anisotropic grain boundary energy (Piazolo et al., 2006). A detailed discussion about this issue can be found in the previous study of halite deformation by Hao et al. (2023).

4.3 Slip systems

The ELLE-VPFFT method allows calculating the evolution of the average relative slip system activity with natural strain at different temperatures (Fig. 8), a parameter not directly quantifiable from rock deformation experiments. The results reveal the contributions of slip systems to strain, and whether these contributions increase or decrease as the CPOs develop. Our study indicates that variations in CRSS due to their temperature dependency result in notable differences in the relative contribution of slip systems to strain at the onset of the deformation. Specifically, the $\{111\} < \bar{1}10 >$ slip system accommodates 30% of strain at 100°C, decreasing to less than 20% at 200°C and 300°C. Despite the substantial alteration in slip system activity, its impact on the CPOs evolution remains minor. Previous studies on viscoplastic deformation of halite reported similar CPOs, despite varying CRSS and inconsistent contributions from slip systems at the onset of deformation (e.g., Wenk et al., 2009; Gomez-Rivas et al., 2017). These studies commonly observe a gradual decrease in the contribution of the softest $\{110\} < \bar{1}10 >$ slip system with increasing strain, while the contribution of the harder {100} <011> slip system increases during progressive deformation. In simple shear simulations at higher temperatures, the activity of the {100} <011> slip system increases significantly after moderate strains (Figs. 8b and c), enhancing the alignment of {100} lattice orientations (Fig. 7). Fig. S4 shows that the deformation of yellow grains primarily

involves the $\{110\} < \bar{1}10 >$slip system, showing high strain-rate shear bands with high dislocation densities. Conversely, deformation of orange grains is predominantly governed by the {100} <011> slip system, exhibiting lower dislocation density. With increasing strain, more intense *GBM* eliminates high strain-rate bands, attributable to high temperatures and differences in stored strain energy along grain boundaries. This prompts the deformation/growth of grains with unfavourably oriented lattices where the {100} <011> slip system is activated (Llorens et al., 2016a). Pure shear deformation results in lower strain localization and dislocation density (Fig. 10), causing the slip systems to change slower compared to simple shear cases (Fig. 8).

To identify active slip systems, boundary trace analysis was conducted using crystallographic orientation data (Prior et al., 2002; Reddy et al., 2007; Barrie et al., 2008; Linckens et al., 2016). For the analysis, it is assumed that subgrain boundaries are ideal tilt boundaries, formed by the accumulation of edge dislocations (Fig. 11a). The rotation axis and the pole to the slip plane are within the subgrain boundary plane and are perpendicular to the slip direction (Figs. 11a, b). From the crystallographic orientation data, the slip direction and the pole to the slip plane can be derived using the subgrain boundary trace and the rotation axis (misorientation axis). Figs. 11c-e shows the boundary trace analysis of several selected grains with distinct subgrain boundaries from Fig. 6. In simple shear simulations at the onset of deformation, the initial Schmid factors for the $\{110\} < \bar{1}10 >$, {100} <011> and $\{111\} < \bar{1}10 >$ slip systems in grain A are 0.112, 0.449 and 0.318, respectively, indicating potential activity for all of them. The boundary trace analysis reveals that both the pole to the slip plane and the slip direction align with the <110> axes, suggesting activation of the $\{110\} < \bar{1}10 >$ slip system. Maps of distribution of slip systems indicate that all three slip systems contribute to grain deformation, particularly $\{110\} < \bar{1}10 >$ and $\{111\} < \bar{1}10 >$ (Fig. 6). The slip system analysis of grains B and C deformed in pure shear is similar to that of the grain A. Although the initial Schmid factors suggest substantial stress acting on the {100} <011> and $\{111\} < \bar{1}10 >$ systems for all three grains, boundary trace analyses only confirm activation of the $\{110\} < \bar{1}10 >$ system. Linckens et al. (2016) found divergent results between the two approaches in their experiments of polycrystalline halite deformation. Our simulations confirm that all three slip systems are active in these grains (Fig. 6). The von Mises criterion requires five independent

slip systems for homogeneous deformation in polycrystals (Mises, 1928). Since only two of the six $\{110\} < \bar{1}10 >$ systems are independent, other systems must be activated to meet this criterion. Despite their lower Schmid factors, the $\{110\} < \bar{1}10 >$ systems activate significantly due to their lower critical resolved shear stress (CRSS, Carter and Heard, 1970). This underscores the importance of considering CRSS when using Schmid factors to predict slip system activity.

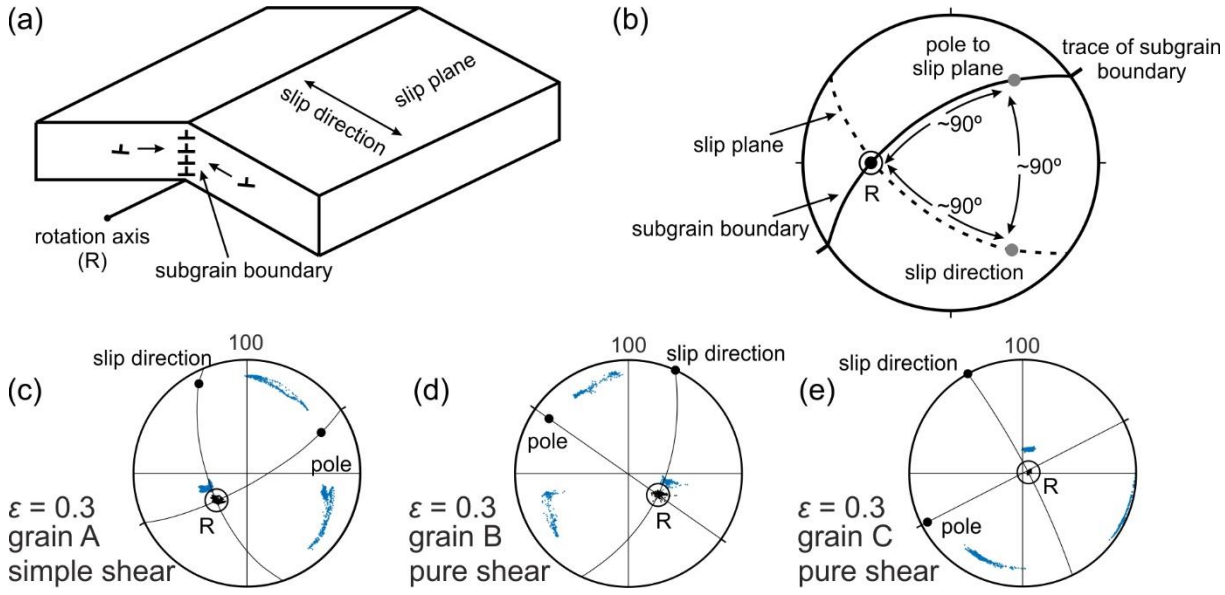

Fig. 11. (a) Schematic of a subgrain boundary (low-angle tilt boundary) showing the rotation axis (R), slip plane, and slip direction (After Reddy et al. (2007) and Linckens et al. (2016)). (b) Stereographic projection of the subgrain boundary, slip plane, and rotation axis (After Reddy et al. (2007) and Linckens et al. (2016)). At low-angle tilt boundaries, the slip direction, slip plane, and rotation axis are mutually perpendicular. The rotation axis lies within the subgrain boundary plane. Using the subgrain boundary trace and the rotation axis orientation, the orientation of the subgrain boundary plane can be determined. The slip plane orientation can be determined as it is perpendicular to the subgrain boundary plane. The slip direction is in the slip plane and perpendicular to the rotation axis (R). (c-e) Boundary analysis results of the 100 pole figures from Fig. 6 to determine active slip systems during deformation. The traces of the subgrain boundaries are indicated on the periphery of the pole figures with thin lines. The subgrain boundary and the rotation axis lies in the same plane. The slip direction and the slip plane pole of grain A deformed in simple shear (c) have the same orientation as two of the <110> axes. The slip direction and slip plane pole of grain A deformed in simple shear (c) almost align with two of the <110> axes, indicating the activated slip system is $\{110\} < \bar{1}10 >$. The same conclusion applies to the 100 pole figures of grain B and grain C deformed in pure shear (d, e).

628

629 **4.4 Distinguishing simple and pure shear deformation patterns**

630 An important question is whether the kinematics of deformation can be inferred from the resulting
631 microstructure and CPOs of halite specimens. Table 2 summarizes our results on the characteristics of
632 grain and subgrain boundaries, CPOs, SPOs, and grain size, categorized by temperature and deformation
633 kinematics. Conjugate subgrain boundary orientation distributions are observed in both simple shear and
634 pure shear deformations (Figs. 4c-f). In cases where samples are oriented parallel to the grain SPO, the
635 asymmetry in the distribution of subgrain boundaries can help distinguish between simple shear and pure
636 shear. Under simple shear, the conjugate orientation distribution is asymmetric about the grain SPO (Figs.
637 4c, e), while under pure shear, it tends to be symmetric about the grain SPO (Figs. 4d, f). As strain
638 increases, *SGR* becomes dominant at low temperatures (100°C and 200°C). Simple shear deformation
639 produces most of bands of small grains subparallel to the grain SPO, while pure shear deformation forms
640 conjugate bands of small grains that are symmetric around the grain SPO (Fig. 3). At high temperature
641 (300°C), increased *GBM* results in larger recrystallized grains, complicating the inference of deformation
642 kinematics from the grain boundary network, though it remains feasible through the orientation of
643 subgrain boundary (Fig. 3). Regardless of temperature, when natural strain is higher than 1.0 three
644 monoclinical symmetric {100} maxima form simple shear with rotational directions relative to the SPO
645 consistent with the shear sense (Fig. 7). Six {100} maxima with orthogonal anisotropic symmetry develop
646 in pure shear cases (Fig. 7). Additionally, the {111} CPO serves as a marker to differentiate between pure
647 and simple shear cases (Fig. 7). Simple shear is marked by brief stages of high strain-rate band evolution
648 and periodic variation of strain localization (Fig. 10a). In contrast, pure shear shows steady strain-rate
649 bands development and decreasing strain localization (Fig. 10a), leading to continuous elongation of some
650 grains along specific orientations, resulting in longer SPOs compared to those in simple shear at high
651 strain (Fig. 4a).

652

653 **Table 2.** Criteria to distinguish between simple shear and pure shear.

Criteria	Diagnostic	Explanation
Subgrain boundary orientation	Yes	Under simple shear, the conjugate subgrain boundary orientation distribution is asymmetric about the grain SPO (Figs. 4c, e), while under pure shear, it is always symmetric about the grain SPO (Figs. 4d, f).
Grain boundary network	Yes	Bands of small grains subparallel to the grain SPO in simple shear. Conjugate bands of small grains are symmetric about the grain SPO in pure shear (e.g., Fig. 3).
CPO	Yes	At high strains (ε > 1.0), three {100} maxima with monoclinic symmetry in simple shear, and six {100} maxima with orthotropic symmetry in pure shear (e.g., Fig. 7).
Crystallographic orientation dispersion direction	Possible	In simple shear, for most grains, the direction of spread of crystallographic orientations around <100> axis is clockwise, consistent with applied shear sense. While in pure shear, there are both clockwise and counterclockwise spread directions (e.g., Fig. 6). Practical application is challenging because of the difficulty of consistently tracking grain deformation in natural specimens.
Aspect ratio	Possible	Simple shear produces grains with higher aspect than pure shear at natural strain higher than 1.0 (e.g., Fig. 4a). Practical application is challenging.
Grain size	No	The evolution of the average grain size and its standard deviation during progressive deformation in simple shear is similar to that of pure shear (e.g., Fig. 5).

5. Conclusions

In this study, we show that kinematics of deformation can be deduced from the resulting microstructure and crystallographic preferred orientation of salt structures at the microscale. From the presented full-field numerical simulations of polycrystalline halite subjected to different deformation conditions and temperatures, we can conclude:

1. Deformation kinematics significantly influence the stability of high strain-rate bands during viscoplastic deformation, defining subgrain and grain boundary orientations. Simple shear deformation features discontinuous evolution of high strain-rate bands and periodic variation of strain localization, resulting in asymmetric subgrain boundary orientations relative to the grain shape preferred orientation. However, pure shear deformation results in steady strain-rate bands and decreasing strain localization,

producing symmetric conjugate subgrain boundaries and small grain bands relative to the to grain shape preferred orientation, resulting in a higher grain aspect ratio at high strain than in simple shear.

2. Deformation kinematics influence the rotation sense of the crystal dispersion axis within each grain, which determines the symmetry of the crystallographic preferred orientation of the polycrystalline aggregate. At low strain six {100} maxima develop with orthotropic symmetry relative to the maximum shortening axis, regardless of temperature and deformation kinematics. With increasing strain, the simple shear {100} crystallographic preferred orientation rotates consistently with the applied sense of shear and eventually forms three maxima with monoclinic symmetry. In contrast, the pure shear crystallographic preferred orientation gradually strengthens and maintains orthotropic symmetry through deformation. At high strains ($\varepsilon > 1.0$), the crystallographic preferred orientation can distinguish between coaxial and non-coaxial deformation and determine the sense of shear.

3. Temperature significantly affects the microstructure evolution in both pure and simple shear cases. Increasing temperatures intensify grain boundary migration, leading to a microstructure characterized by larger and more equidimensional grains, complicating the assessment of strain localization from grain morphology.

Acknowledgments

This paper is dedicated to the memory of Janos L. Urai, a pioneer of the study of rock deformation microstructures. This study has been funded by DGICYT Spanish Projects PID-2020-118999GB-I00 (Ministerio de Ciencia e Innovación/Agencia Estatal de Investigación/10.13039/501100011033), PID-2021-122467NB-C21 (Ministerio de Ciencia e Innovación/Agencia Estatal de Investigación/10.13039/501100011033/FEDER), the “Consolidación Investigadora” grants CNS2022-135819 (to MGL) and CNS2023-145382 (to EGR) (Ministerio de Ciencia e Innovación/Agencia Estatal de Investigación/10.13039/501100011033 and EU NextGenerationEU/PRTR), and the 2021 SGR 00349 “Geologia Sedimentària” and 2021 SGR 00410 “Modelització Geodinàmica de la Litosfera” consolidated research groups (Agència de Gestió d’Ajuts Universitaris i de Recerca). Baoqin Hao acknowledges

692 funding by the China Scholarship Council for a PhD scholarship (CSC-202006930010). EGR
693 acknowledges the “Ramón y Cajal” Fellowship RyC-2018-026335-I, funded by the Ministerio de Ciencia
694 e Innovación/Agencia Estatal de Investigación/10.13039/501100011033.

695

696 **References**

697 Armann, M., 2008. Microstructural and textural development in synthetic rocksalt deformed in torsion.
698 Doctoral dissertation. ETH-Zurich, Switzerland.

699 Barrie, C.D., Boyle, A.P., Cox, S.F., Prior, D.J., 2008. Slip systems and critical resolved shear stress in
700 pyrite: an electron backscatter diffraction (EBSD) investigation. Mineralogical Magazine 72, 1181–
701 1199. https://doi.org/10.1180/minmag.2008.072.6.1181

702 Becker, J.K., Bons, P.D., Jessell, M.W., 2008. A new front-tracking method to model anisotropic grain
703 and phase boundary motion in rocks. Computers & Geosciences 34, 201–212.
704 https://doi.org/10.1016/j.cageo.2007.03.013

705 Boneh, Y., Skemer, P., 2014. The effect of deformation history on the evolution of olivine CPO. Earth
706 and Planetary Science Letters 406, 213–222. https://doi.org/10.1016/j.epsl.2014.09.018

707 Boneh, Y., Wallis, D., Hansen, L.N., Krawczynski, M.J., Skemer, P., 2017. Oriented grain growth and
708 modification of ‘frozen anisotropy’ in the lithospheric mantle. Earth and Planetary Science Letters 474,
709 368–374. https://doi.org/10.1016/j.epsl.2017.06.050

710 Bons, P.D., Jessell, M.W., 1999. Micro-shear zones in experimentally deformed octachloropropane.
711 Journal of Structural Geology 21, 323–334. https://doi.org/10.1016/S0191-8141(98)90116-X

712 Bons, P.D., Koehn, D., Jessell, M.W., 2008. Microdynamics Simulation, Lecture Notes in Earth
713 Sciences. Springer, Berlin. https://doi.org/10.1007/978-3-540-44793-1

714 Borthwick, V.E., Piazolo, S., 2010. Post-deformational annealing at the subgrain scale: Temperature
715 dependent behaviour revealed by in-situ heating experiments on deformed single crystal halite. Journal
716 of Structural Geology 32, 982–996. https://doi.org/10.1016/j.jsg.2010.06.006

Borthwick, V.E., Piazolo, S., Evans, L., Griera, A., Bons, P.D., 2014. What happens to deformed rocks after deformation? A refined model for recovery based on numerical simulations. Geological Society, London, Special Publications 394, 215–234. https://doi.org/10.1144/SP394.11

Canérot, J., Hudec, M.R., Rockenbauch, K., 2005. Mesozoic diapirism in the Pyrenean orogen: Salt tectonics on a transform plate boundary. AAPG Bulletin 89, 211–229. https://doi.org/10.1306/09170404007

Cao, Y., Ni, S., Liao, X., Song, M., Zhu, Y., 2018. Structural evolutions of metallic materials processed by severe plastic deformation. Materials Science and Engineering: R: Reports 133, 1–59. https://doi.org/10.1016/j.mser.2018.06.001

Carter, N.L., Heard, H.C., 1970. Temperature and rate dependent deformation of halite. American Journal of Science 269, 193–249. https://doi.org/10.2475/ajs.269.3.193

Carter, N.L., Horseman, S.T., Russell, J.E., Handin, J., 1993. Rheology of rocksalt. Journal of Structural Geology 15, 1257–1271. https://doi.org/10.1016/0191-8141(93)90168-A

Desbois, G., Závada, P., Schléder, Z., Urai, J.L., 2010. Deformation and recrystallization mechanisms in actively extruding salt fountain: Microstructural evidence for a switch in deformation mechanisms with increased availability of meteoric water and decreased grain size (Qum Kuh, central Iran). Journal of Structural Geology 32, 580–594. https://doi.org/10.1016/j.jsg.2010.03.005

Duffy, O.B., Dooley, T.P., Hudec, M.R., Jackson, M.P.A., Fernandez, N., Jackson, C.A.-L., Soto, J.I., 2018. Structural evolution of salt-influenced fold-and-thrust belts: A synthesis and new insights from basins containing isolated salt diapirs. Journal of Structural Geology 114, 206–221. https://doi.org/10.1016/j.jsg.2018.06.024

Finch, M.A., Bons, P.D., Steinbach, F., Griera, A., Llorens, M.-G., Gomez-Rivas, E., Ran, H., de Riese, T., 2020. The ephemeral development of C′ shear bands: A numerical modelling approach. Journal of Structural Geology 139, 104091. https://doi.org/10.1016/j.jsg.2020.104091

Fossen, H., 2010. Deformation bands formed during soft-sediment deformation: Observations from SE Utah. Marine and Petroleum Geology 27, 215–222. https://doi.org/10.1016/j.marpetgeo.2009.06.005

743 Franssen, R.C.M.W., 1994. The rheology of synthetic rocksalt in uniaxial compression. Tectonophysics
744 233, 1–40. https://doi.org/10.1016/0040-1951(94)90218-6
745 Franssen, R.C.M.W., Spiers, C.J., 1990. Deformation of polycrystalline salt in compression and in shear
746 at 250–350°C. Geological Society, London, Special Publications 54, 201–213.
747 https://doi.org/10.1144/GSL.SP.1990.054.01.20
748 Godin, L., Grujic, D., Law, R.D., Searle, M.P., 2006. Channel flow, ductile extrusion and exhumation
749 in continental collision zones: an introduction. Geological Society, London, Special Publications 268,
750 1–23. https://doi.org/10.1144/GSL.SP.2006.268.01.01
751 Gomez-Rivas, E., 2008. Localización de deformación en medios dúctiles y anisótropos: estudio de
752 campo, experimental y numérico.
753 Gomez-Rivas, E., Griera, A., Llorens, M.-G., Bons, P.D., Lebensohn, R.A., Piazolo, S., 2017. Subgrain
754 Rotation Recrystallization During Shearing: Insights From Full-Field Numerical Simulations of Halite
755 Polycrystals. Journal of Geophysical Research: Solid Earth 122, 8810–8827.
756 https://doi.org/10.1002/2017JB014508
757 Griera, A., Llorens, M.-G., Gomez-Rivas, E., Bons, P.D., Jessell, M.W., Evans, L.A., Lebensohn, R.,
758 2013. Numerical modelling of porphyroclast and porphyroblast rotation in anisotropic rocks.
759 Tectonophysics 587, 4–29. https://doi.org/10.1016/j.tecto.2012.10.008
760 Grujic, D., 2006. Channel flow and continental collision tectonics: an overview. Geological Society,
761 London, Special Publications 268, 25–37. https://doi.org/10.1144/GSL.SP.2006.268.01.02
762 Guillope, M., Poirier, J.P., 1979. Dynamic recrystallization during creep of single-crystalline halite: An
763 experimental study. Journal of Geophysical Research 84, 5557.
764 https://doi.org/10.1029/JB084iB10p05557
765 Hao, B., Llorens, M. -G., Griera, A., Bons, P.D., Lebensohn, R.A., Yu, Y., Gomez-Rivas, E., 2023.
766 Full-Field Numerical Simulation of Halite Dynamic Recrystallization From Subgrain Rotation to Grain
767 Boundary Migration. Journal of Geophysical Research: Solid Earth 128.
768 https://doi.org/10.1029/2023JB027590

769 Henneberg, M., Linckens, J., Schramm, M., Hammer, J., Gerdes, A., Zulauf, G., 2020. Structural
770 evolution of continental and marine Permian rock salt of the North German Basin: constraints from
771 microfabrics, geochemistry and U–Pb ages. International Journal of Earth Sciences 109, 2369–2387.
772 https://doi.org/10.1007/s00531-020-01905-w
773 Hudec, M.R., Jackson, M.P.A., 2007. Terra infirma: Understanding salt tectonics. Earth-Science
774 Reviews 82, 1–28. https://doi.org/10.1016/j.earscirev.2007.01.001
775 Jackson, C.A.-L., Jackson, M.P.A., Hudec, M.R., Rodriguez, C.R., 2015. Enigmatic structures within
776 salt walls of the Santos Basin—Part 1: Geometry and kinematics from 3D seismic reflection and well
777 data. Journal of Structural Geology 75, 135–162. https://doi.org/10.1016/j.jsg.2015.01.010
778 Jackson, M.P., Hudec, M.R., 2017. Salt tectonics: Principles and Practice, Salt tectonics.
779 Jackson, M.P.A., Talbot, C.J., 1986. External shapes, strain rates, and dynamics of salt structures.
780 Geological Society of America Bulletin 97, 305. https://doi.org/10.1130/0016-
781 7606(1986)97<305:ESSRAD>2.0.CO;2
782 Jessell, M.W., 1986. Grain boundary migration and fabric development in experimentally deformed
783 octachloropropane. Journal of Structural Geology 8, 527–542. https://doi.org/10.1016/0191-
784 8141(86)90003-9
785 Jessell, M.W., Bons, P.D., Evans, L., Barr, T., Stüwe, K., 2001. Elle: the numerical simulation of
786 metamorphic and deformation microstructures. Computers & Geosciences 27, 17–30.
787 https://doi.org/10.1016/S0098-3004(00)00061-3
788 Jessell, M.W., Lister, G.S., 1990. A simulation of the temperature dependence of quartz fabrics.
789 Geological Society, London, Special Publications 54, 353–362.
790 https://doi.org/10.1144/GSL.SP.1990.054.01.31
791 Kern, H., 1977. Preferred orientation of experimentally deformed limestone marble, quartzite and rock
792 salt at different temperatures and states of stress. Tectonophysics 39, 103–120.
793 https://doi.org/10.1016/0040-1951(77)90091-9

Langille, J., Lee, J., Hacker, B., Seward, G., 2010. Middle crustal ductile deformation patterns in southern Tibet: Insights from vorticity studies in Mabja Dome. Journal of Structural Geology 32, 70–85. https://doi.org/10.1016/j.jsg.2009.08.009

Lebensohn, R.A., 2001. N-site modeling of a 3D viscoplastic polycrystal using Fast Fourier Transform. Acta Materialia 49, 2723–2737. https://doi.org/10.1016/S1359-6454(01)00172-0

Lebensohn, R.A., Brenner, R., Castelnau, O., Rollett, A.D., 2008. Orientation image-based micromechanical modelling of subgrain texture evolution in polycrystalline copper. Acta Materialia 56, 3914–3926. https://doi.org/10.1016/j.actamat.2008.04.016

Lebensohn, R.A., Rollett, A.D., 2020. Spectral methods for full-field micromechanical modelling of polycrystalline materials. Computational Materials Science 173, 109336. https://doi.org/10.1016/j.commatsci.2019.109336

Leitner, C., Neubauer, F., Urai, J.L., Schoenherr, J., 2011. Structure and evolution of a rocksalt-mudrock-tectonite: The haselgebirge in the Northern Calcareous Alps. Journal of Structural Geology 33, 970–984. https://doi.org/10.1016/j.jsg.2011.02.008

Linckens, J., Zulauf, G., Hammer, J., 2016. Experimental deformation of coarse-grained rock salt to high strain. Journal of Geophysical Research: Solid Earth 121, 6150–6171. https://doi.org/10.1002/2016JB012890

Llorens, M.-G., Griera, A., Bons, P.D., Lebensohn, R.A., Evans, L.A., Jansen, D., Weikusat, I., 2016a. Full-field predictions of ice dynamic recrystallisation under simple shear conditions. Earth and Planetary Science Letters 450, 233–242. https://doi.org/10.1016/j.epsl.2016.06.045

Llorens, M.-G., Griera, A., Bons, P.D., Roessiger, J., Lebensohn, R., Evans, L., Weikusat, I., 2016b. Dynamic recrystallisation of ice aggregates during co-axial viscoplastic deformation: a numerical approach. Journal of Glaciology 62, 359–377. https://doi.org/10.1017/jog.2016.28

Llorens, M.-G., Griera, A., Bons, P.D., Weikusat, I., Prior, D.J., Gomez-Rivas, E., de Riese, T., Jimenez-Munt, I., García-Castellanos, D., Lebensohn, R.A., 2022. Can changes in deformation regimes

819 be inferred from crystallographic preferred orientations in polar ice? The Cryosphere 16, 2009–2024.
820 https://doi.org/10.5194/tc-16-2009-2022
821 Llorens, M.-G., Griera, A., Steinbach, F., Bons, P.D., Gomez-Rivas, E., Jansen, D., Roessiger, J.,
822 Lebensohn, R.A., Weikusat, I., 2017. Dynamic recrystallization during deformation of polycrystalline
823 ice: insights from numerical simulations. Philosophical Transactions of the Royal Society A:
824 Mathematical, Physical and Engineering Sciences 375, 20150346.
825 https://doi.org/10.1098/rsta.2015.0346
826 Mainprice, D., Bachmann, F., Hielscher, R., Schaeben, H., 2015. Descriptive tools for the analysis of
827 texture projects with large datasets using MTEX : strength, symmetry and components. Geological
828 Society, London, Special Publications 409, 251–271. https://doi.org/10.1144/SP409.8
829 Mainprice, D., Hielscher, R., Schaeben, H., 2011. Calculating anisotropic physical properties from
830 texture data using the MTEX open-source package. Geological Society, London, Special Publications
831 360, 175–192. https://doi.org/10.1144/SP360.10
832 Mansouri, H., Prior, D.J., Ajalloeian, R., Elyaszadeh, R., 2019. Deformation and recrystallization
833 mechanisms inferred from microstructures of naturally deformed rock salt from the diapiric stem and
834 surface glaciers of a salt diapir in Southern Iran. Journal of Structural Geology 121, 10–24.
835 https://doi.org/10.1016/j.jsg.2019.01.005
836 McCrone, W.C., Cheng, P.T., 1949. Grain Growth in Octachloropropane. Journal of Applied Physics
837 20, 230–231. https://doi.org/10.1063/1.1698345
838 Means, W., 1977. A deformation experiment in transmitted light. Earth and Planetary Science Letters
839 35, 169–179. https://doi.org/10.1016/0012-821X(77)90040-1
840 Means, W.D., 1989. Synkinematic microscopy of transparent polycrystals. Journal of Structural
841 Geology 11, 163–174. https://doi.org/10.1016/0191-8141(89)90041-2
842 Means, W.D., 1983. Microstructure and micromotion in recrystallization flow of octachloropropane: A
843 first look. Geologische Rundschau 72, 511–528. https://doi.org/10.1007/BF01822080

Means, W.D., Hobbs, B.E., Lister, G.S., Williams, P.F., 1980. Vorticity and non-coaxiality in progressive deformations. Journal of Structural Geology 2, 371–378. https://doi.org/10.1016/0191-8141(80)90024-3

Means, W.D., Xia, Z.G., 1981. Deformation of crystalline materials in thin section. Geology 9, 538. https://doi.org/10.1130/0091-7613(1981)9<538:DOCMIT>2.0.CO;2

Michels, Z.D., Kruckenberg, S.C., Davis, J.R., Tikoff, B., 2015. Determining vorticity axes from grain-scale dispersion of crystallographic orientations. Geology 43, 803–806. https://doi.org/10.1130/G36868.1

Miralles, L., Sans, M., Pueyo, J.J., Santanach, P., 2000. Recrystallization salt fabric in a shear zone (Cardona diapir, southern Pyrenees, Spain). Geological Society, London, Special Publications 174, 149–167. https://doi.org/10.1144/GSL.SP.1999.174.01.09

Mises, R. V., 1928. Mechanik der plastischen Formänderung von Kristallen. ZAMM - Journal of Applied Mathematics and Mechanics / Zeitschrift Für Angewandte Mathematik Und Mechanik 8, 161–185. https://doi.org/10.1002/zamm.19280080302

Mohr, M., Kukla, P.A., Urai, J.L., Bresser, G., 2005. Multiphase salt tectonic evolution in NW Germany: seismic interpretation and retro-deformation. International Journal of Earth Sciences 94, 917–940. https://doi.org/10.1007/s00531-005-0039-5

Morales, L.F.G., Lloyd, G.E., Mainprice, D., 2014. Fabric transitions in quartz via viscoplastic self-consistent modeling part I: Axial compression and simple shear under constant strain. Tectonophysics 636, 52–69. https://doi.org/10.1016/j.tecto.2014.08.011

Pennock, G.M., Drury, M.R., Spiers, C.J., 2005. The development of subgrain misorientations with strain in dry synthetic NaCl measured using EBSD. Journal of Structural Geology 27, 2159–2170. https://doi.org/10.1016/j.jsg.2005.06.013

Piazolo, S., Bestmann, M., Prior, D.J., Spiers, C.J., 2006. Temperature dependent grain boundary migration in deformed-then-annealed material: Observations from experimentally deformed synthetic rocksalt. Tectonophysics 427, 55–71. https://doi.org/10.1016/j.tecto.2006.06.007

Prior, D.J., Wheeler, J., Peruzzo, L., Spiess, R., Storey, C., 2002. Some garnet microstructures: an illustration of the potential of orientation maps and misorientation analysis in microstructural studies. Journal of Structural Geology 24, 999–1011. https://doi.org/10.1016/S0191-8141(01)00087-6

Reddy, S.M., Timms, N.E., Pantleon, W., Trimby, P., 2007. Quantitative characterization of plastic deformation of zircon and geological implications. Contributions to Mineralogy and Petrology 153, 625–645. https://doi.org/10.1007/s00410-006-0174-4

Roessiger, J., Bons, P.D., Griera, A., Jessell, M.W., Evans, L., Montagnat, M., Kipfstuhl, S., Faria, S.H., Weikusat, I., 2011. Competition between grain growth and grain-size reduction in polar ice. Journal of Glaciology 57, 942–948. https://doi.org/10.3189/002214311798043690

Rowan, M.G., Urai, J.L., Fiduk, J.C., Kukla, P.A., 2019. Deformation of intrasalt competent layers in different modes of salt tectonics. Solid Earth 10, 987–1013. https://doi.org/10.5194/se-10-987-2019

Sarkarinejad, K., Sarshar, M.A., Adineh, S., 2018. Structural, micro-structural and kinematic analyses of channel flow in the Karmostaj salt diapir in the Zagros foreland folded belt, Fars province, Iran. Journal of Structural Geology 107, 109–131. https://doi.org/10.1016/j.jsg.2017.12.005

Schléder, Z., Urai, J.L., 2007. Deformation and recrystallization mechanisms in mylonitic shear zones in naturally deformed extrusive Eocene–Oligocene rocksalt from Eyvanekey plateau and Garmsar hills (central Iran). Journal of Structural Geology 29, 241–255. https://doi.org/10.1016/j.jsg.2006.08.014

Schléder, Z., Urai, J.L., 2005. Microstructural evolution of deformation-modified primary halite from the Middle Triassic Röt Formation at Hengelo, The Netherlands. International Journal of Earth Sciences 94, 941–955. https://doi.org/10.1007/s00531-005-0503-2

Schmid, E., Boas, W., 1950. Plasticity of crystals. F. A. Hughes & CO. LIMITED, London.

Segal, V.M., 2002. Severe plastic deformation: simple shear versus pure shear. Materials Science and Engineering: A 338, 331–344. https://doi.org/10.1016/S0921-5093(02)00066-7

Skemer, P., Katayama, I., Jiang, Z., Karato, S., 2005. The misorientation index: Development of a new method for calculating the strength of lattice-preferred orientation. Tectonophysics 411, 157–167. https://doi.org/10.1016/j.tecto.2005.08.023

Skemer, P., Warren, J.M., Kelemen, P.B., hirth, G., 2010. Microstructural and Rheological Evolution of a Mantle Shear Zone. Journal of Petrology 51, 43–53. https://doi.org/10.1093/petrology/egp057

Skrotzki, W., Helming, K., Brokmeier, H.-G., Dornbusch, H.-J., Welch, P., 1995. Textures in Pure Shear Deformed Rock Salt. Textures and Microstructures 24, 133–141. https://doi.org/10.1155/TSM.24.133

Sornette, A., Davy, P., Sornette, D., 1993. Fault growth in brittle-ductile experiments and the mechanics of continental collisions. Journal of Geophysical Research: Solid Earth 98, 12111–12139. https://doi.org/10.1029/92JB01740

Spiers, C.J., Peach, C.J., Brzesowsky, R.H., Schutjens, P.M.T.M., Liezenberg, J.L., Zwart, H.J., 1988. Long-term rheological and transport properties of dry and wet salt rocks. Office for Official Publications of the European Communities, Luxembourg.

Spiers, C.J., Schutjens, P.M.T.M., Brzesowsky, R.H., Peach, C.J., Liezenberg, J.L., Zwart, H.J., 1990. Experimental determination of constitutive parameters governing creep of rocksalt by pressure solution. Geological Society, London, Special Publications 54, 215–227. https://doi.org/10.1144/GSL.SP.1990.054.01.21

Steinbach, F., Bons, P.D., Griera, A., Jansen, D., Llorens, M.-G., Roessiger, J., Weikusat, I., 2016. Strain localization and dynamic recrystallization in the ice–air aggregate: a numerical study. The Cryosphere 10, 3071–3089. https://doi.org/10.5194/tc-10-3071-2016

Stipp, M., Tullis, J., Scherwath, M., Behrmann, J.H., 2010. A new perspective on paleopiezometry: Dynamically recrystallized grain size distributions indicate mechanism changes. Geology 38, 759–762. https://doi.org/10.1130/G31162.1

Talbot, C.J., Jackson, M.P.A., 1987. Internal Kinematics of Salt Diapirs. AAPG Bulletin 71, 1068–1093. https://doi.org/10.1306/703C7DF9-1707-11D7-8645000102C1865D

Talbot, C.J., Pohjola, V., 2009. Subaerial salt extrusions in Iran as analogues of ice sheets, streams and glaciers. Earth-Science Reviews 97, 155–183. https://doi.org/10.1016/j.earscirev.2009.09.004

ter Heege, J.H., de Bresser, J.H.P., Spiers, C.J., 2005. Rheological behaviour of synthetic rocksalt: the interplay between water, dynamic recrystallization and deformation mechanisms. Journal of Structural Geology 27, 948–963. https://doi.org/10.1016/j.jsg.2005.04.008

ter Heege, J.H., de Bresser, J.H.P., Spiers, C.J., 2004. Dynamic Recrystallization of Dense Polycrystalline NaCl: Dependence of Grain Size Distribution on Stress and Temperature. Materials Science Forum 467–470, 1187–1192. https://doi.org/10.4028/www.scientific.net/MSF.467-470.1187

Thiemeyer, N., Zulauf, G., Mertineit, M., Linckens, J., Pusch, M., Hammer, J., 2016. Microfabrics and 3D grain shape of Gorleben rock salt: Constraints on deformation mechanisms and paleodifferential stress. Tectonophysics 676, 1–19. https://doi.org/10.1016/j.tecto.2016.02.046

Truesdell, C., 1953. Two Measures of Vorticity. Journal of Rational Mechanics and Analysis 2, 173–217.

Urai, J.L., 1987. Development of microstructure during deformation of carnallite and bischofite in transmitted light. Tectonophysics 135, 251–263. https://doi.org/10.1016/0040-1951(87)90166-1

Urai, J.L., 1985. Water-enhanced dynamic recrystallization and solution transfer in experimentally deformed carnallite. Tectonophysics 120, 285–317. https://doi.org/10.1016/0040-1951(85)90055-1

Urai, J.L., Humphreys, F.J., 1981. The development of shear zones in polycrystalline camphor. Tectonophysics 78, 677–685. https://doi.org/10.1016/0040-1951(81)90036-6

Urai, J.L., Humphreys, F.J., Burrows, S.E., 1980. In-situ studies of the deformation and dynamic recrystallization of rhombohedral camphor. Journal of Materials Science 15, 1231–1240. https://doi.org/10.1007/BF00551812

Urai, J.L., Means, W.D., Lister, G.S., 1986a. Dynamic recrystallization of minerals. In: Hobbs, B.E., Heard, H.C. (Eds.), Mineral and Rock Deformation: Laboratory Studies: The Paterson Volume. American Geophysical Union, Washington, D. C., 161–199. https://doi.org/https://doi.org/10.1029/GM036p0161

945 Urai, J.L., Schléder, Z., Spiers, C.J., Kukla, P.A., 2008. Flow and transport properties of salt rocks. In:
946 Littke, R., Bayer, U., Gajewski, D., Nelskamp, S. (Eds.), Dynamics of Complex Intracontinental Basins:
947 The Central European Basin System. Springer, Berlin, 277–290.
948 Urai, J.L., Spiers, C.J., Peach, C.J., Franssen, R.C.M.W., Liezenberg, J.L., 1987. Deformation
949 mechanisms operating in naturally deformed halite rocks as deduced from microstructural
950 investigations. Geologie En Mijnbouw 66, 165–176.
951 Urai, J.L., Spiers, C.J., Zwart, H.J., Lister, G.S., 1986b. Weakening of rock salt by water during long-
952 term creep. Nature 324, 554–557. https://doi.org/10.1038/324554a0
953 Van Gent, H., Urai, J.L., de Keijzer, M., 2011. The internal geometry of salt structures – A first look
954 using 3D seismic data from the Zechstein of the Netherlands. Journal of Structural Geology 33, 292–
955 311. https://doi.org/10.1016/j.jsg.2010.07.005
956 Weijermars, R., Jackson, M.P.A., Vendeville, B., 1993. Rheological and tectonic modeling of salt
957 provinces. Tectonophysics 217. https://doi.org/10.1016/0040-1951(93)90208-2
958 Wenk, H.-R., Armann, M., Burlini, L., Kunze, K., Bortolotti, M., 2009. Large strain shearing of halite:
959 Experimental and theoretical evidence for dynamic texture changes. Earth and Planetary Science Letters
960 280, 205–210. https://doi.org/10.1016/j.epsl.2009.01.036
961 Wenk, H.R., Takeshita, T., Bechler, E., Erskine, B.G., Matthies, S., 1987. Pure shear and simple shear
962 calcite textures. Comparison of experimental, theoretical and natural data. Journal of Structural Geology
963 9, 731–745. https://doi.org/10.1016/0191-8141(87)90156-8
964 Wilson, C.J.L., 1984. Shear bands, crenulations and differentiated layering in ice-mica models. Journal
965 of Structural Geology 6, 303–319. https://doi.org/10.1016/0191-8141(84)90054-3
966 Xypolias, P., 2010. Vorticity analysis in shear zones: A review of methods and applications. Journal of
967 Structural Geology 32, 2072–2092. https://doi.org/10.1016/j.jsg.2010.08.009

Highlights:

1. Simulated halite deformation under varying deformation kinematics and temperatures
2. Deformation kinematics affect strain localization and thus microstructure
3. Microstructure is influenced by dynamic recrystallization and thus by temperature

Journal of Structural Geology

Supplement of

The influence of kinematics of deformation on polycrystalline halite dynamic recrystallization: full-field simulation of simple shear versus pure shear

Baoqin Hao[a], Albert Griera[b], Maria-Gema Llorens[c], Paul D. Bons[d], Ricardo. A. Lebensohn[e], Yuanchao Yu[a,c] and Enrique Gomez-Rivas[a]

[a] Departament de Mineralogia, Petrologia i Geologia Aplicada, Universitat de Barcelona, Spain

[b] Departament de Geologia, Universitat Autònoma de Barcelona, Spain

[c] Geosciences Barcelona, GEO3BCN-CSIC, Spain

[d] Department of Geosciences, Eberhard Karls University of Tübingen, Germany

[e] Materials Science and Technology Division, Los Alamos National Laboratory, Los Alamos, NM, USA

Corresponding author: Baoqin Hao (baoqin.hao@ub.edu, haobaoqin@hotmail.com)

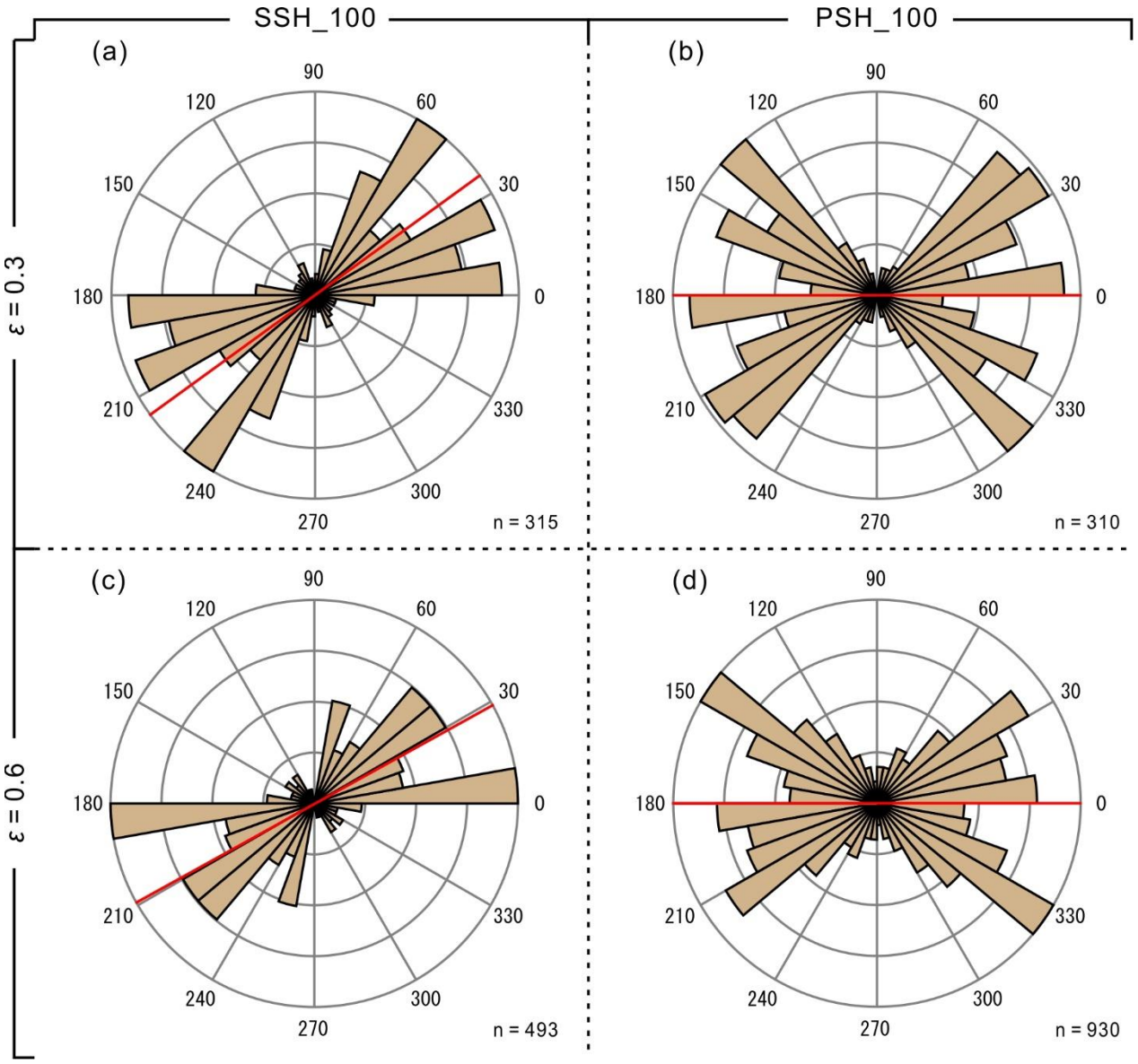

Fig. S1. Rose diagrams displaying the orientations of subgrain boundary at natural strain of ε = 0.3 and 0.6, from simulations under simple shear and pure shear at 100°C. The orientation distribution frequencies are normalized to the length of subgrain boundaries. Red lines in rose diagrams indicate the grain SPO.

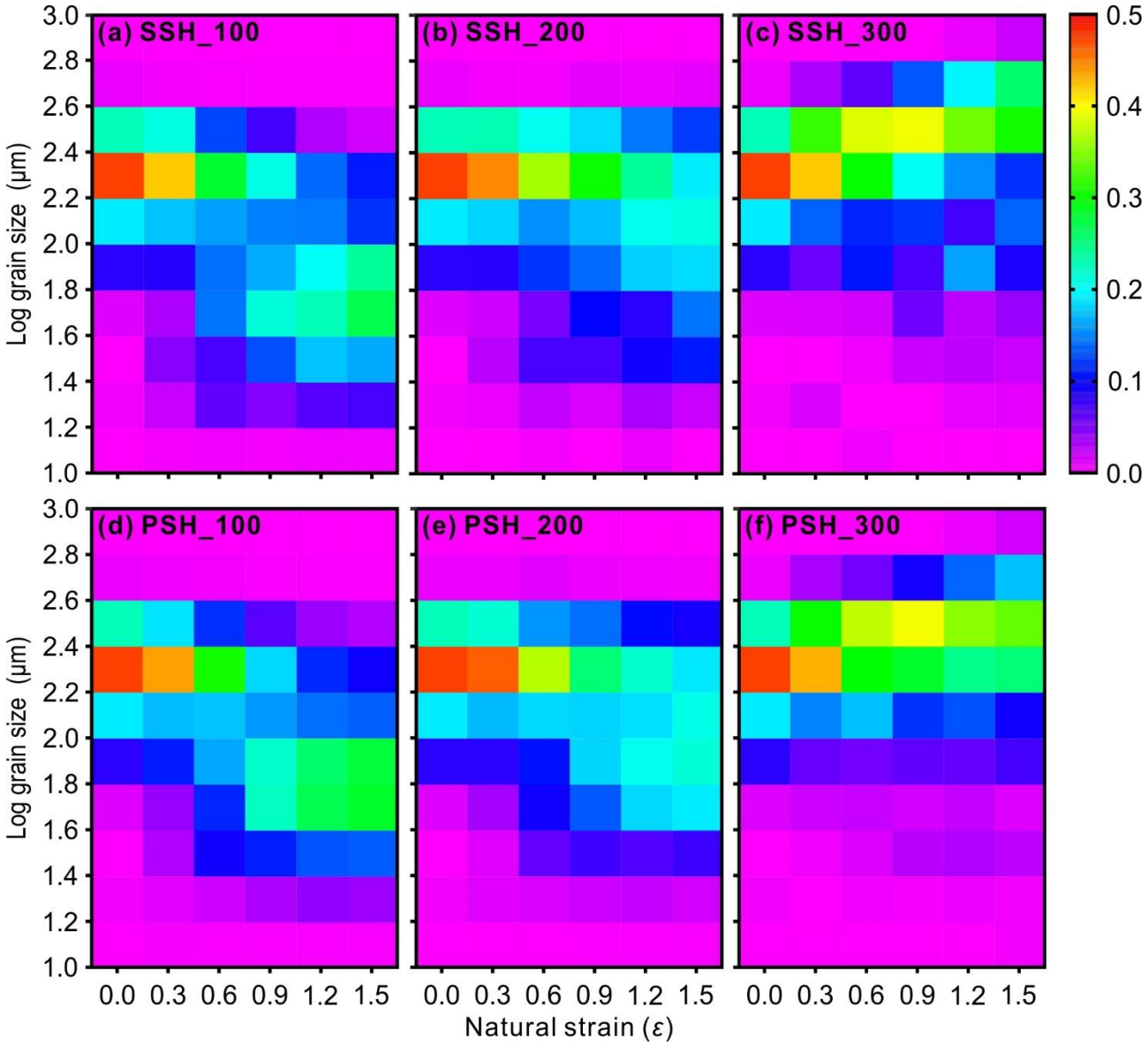

Fig. S2. Comparison of evolution of grain size distribution with natural strain increasing for simulations deformed in simple shear (SSH100/200/300) at (a) 100℃, (b) 200℃ and (c) 300℃ with that of simulations deformed in pure shear at the same temperatures (PSH_100/200/300, d-f). The grain size corresponds to the equivalent grain size (in logarithmic form, $\log_{10}$). The color bars indicate the frequency of grain size fractions (0.0-0.5).

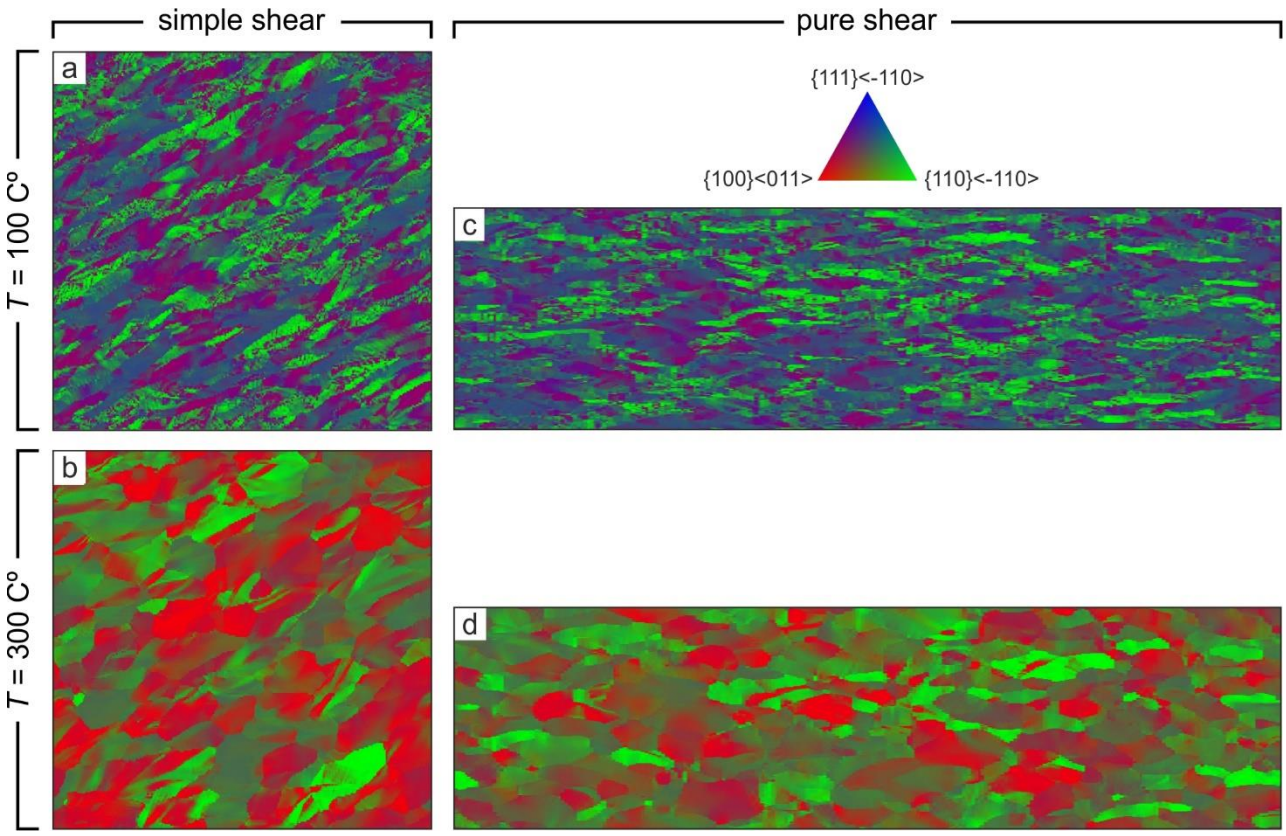

Fig. S3. Maps of distribution of slip system activity at natural strain of ε = 1.0 for simulations performed at temperatures of 100°C (a, c) and 300°C (b, d). Left-hand column shows results under simple shear, and right-hand column under pure shear deformation. Please note that the size of images corresponding to pure shear simulations (e-g) is displayed as 0.8 times that of the original images.

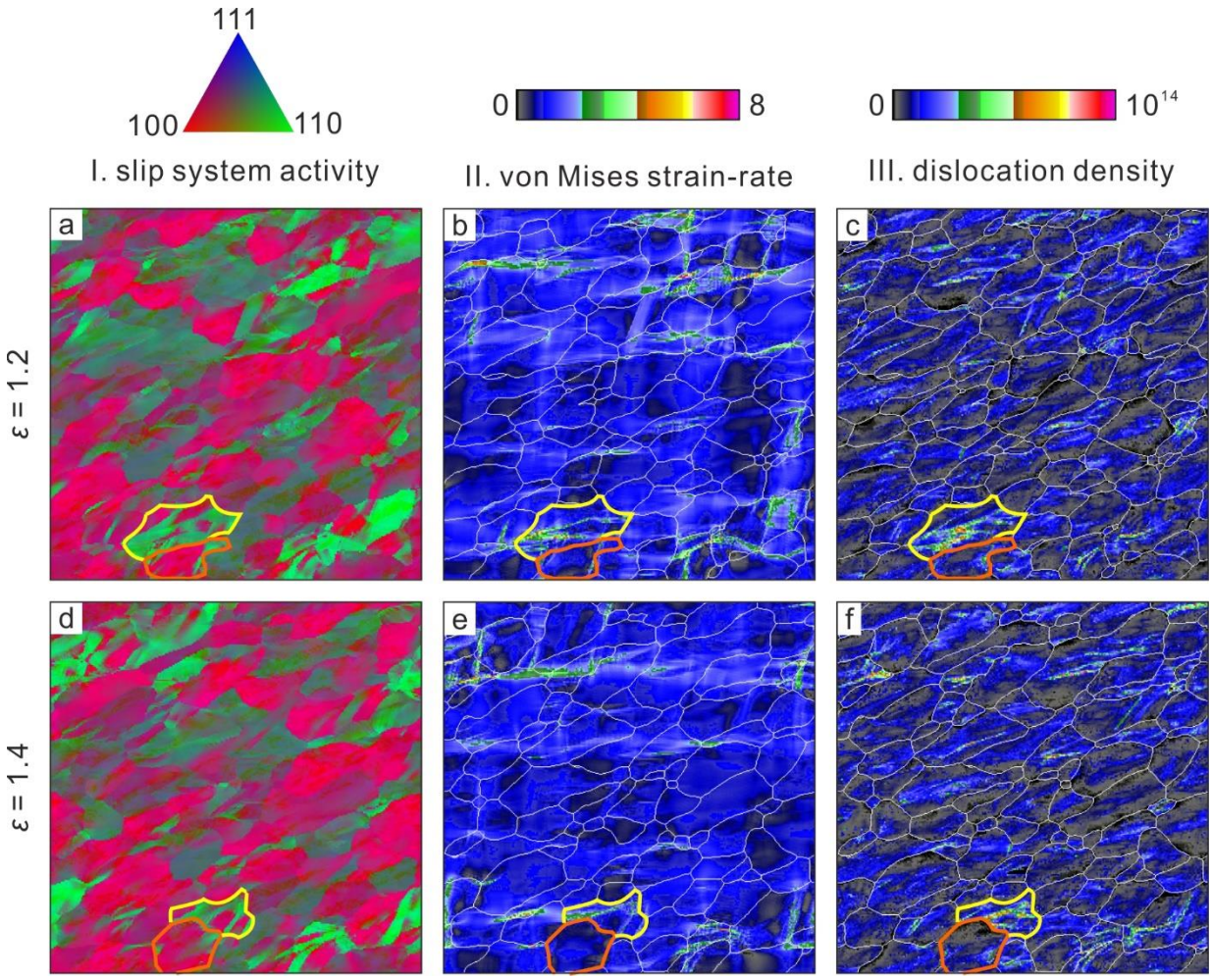

Fig. S4. Distribution of slip system activity (column I), Maps of the von Mises strain-rate field (column II) and Maps of the dislocation density distribution (column III) at natural strain of $\boldsymbol{\varepsilon}$ = 1.2 (a-c) and 1.4 (d-f) for simulations deformed in simple shear at 300°C.

Appendix 3. Conference publications

[1] Hao, B., Llorens, M.-G., Griera, A., Bons, P.D., and Gomez-Rivas, E. Full-field numerical simulation of polycrystalline halite dynamic recrystallization under simple shear conditions. Electron Backscatter Diffraction 2022 (EBSD 2022), New York, United States, June 2022.

[2] Hao, B., Llorens, M.-G., Griera, A., Bons, P. D., and Gomez-Rivas, E.:Full-field numerical simulation of dynamic recrystallisation in polycrystalline halite, 23rd International Conference on Deformation mechanisms, Rheology and Tectonics (DRT). Catania, Italy. July 2022.

[3] Hao, B., Llorens, M.-G., Griera, A., Bons, P. D., Lebensohn, R. A., Yu, Y., and Gomez-Rivas, E.: Full-Field Numerical Simulation of Halite Dynamic Recrystallization From Subgrain Rotation to Grain Boundary Migration, EGU General Assembly 2024, Vienna, Austria, 14–19 Apr 2024, EGU24-3225, https://doi.org/10.5194/egusphere-egu24-3225, 2024.

[4] Hao, B., Llorens, M.-G., Griera, A., Bons, P. D., Lebensohn, R. A., Yu, Y., and Gomez-Rivas, E.: Dynamic recrystallization during visco-plastic deformation of halite polycrystals: full-field simulation of simple shear versus pure shear, 24th International Conference on Deformation mechanisms, Rheology and Tectonics (DRT). Barcelona, Spain. July 2024.

CONFERENCE BOOKLET

Full-field numerical simulation of polycrystalline halite dynamic recrystallization under simple shear conditions

Baoqin Hao[*1], Maria-Gema Llorens[2], Albert Griera[3], Paul D. Bons[4], Enrique Gomez-Rivas[1]*

[1] Department of Mineralogy, Petrology and Applied Geology, University of Barcelona, Spain
[2] Geosciences Barcelona, CSIC, Spain
[3] Department of Geology, Autonomous University of Barcelona, Spain
[4] Department of Geosciences, Eberhard Karls University of Tübingen, Germany
[*]Email: baoqin.hao@ub.edu

The viscous flow of salt rocks leads to the development of tectonic structures such as the detachments, playing a key role in upper-crust tectonics. Moreover, evaporites are key in petroleum systems, which often control the formation of hydrocarbon traps. Therefore, understanding the mechanical behavior and microstructural processes of evaporites has key scientific and economic significance. Numerical modeling has become a useful method for the study of rock deformation processes at multiple scales. However, modeling the microstructural evolution of rock salt aggregates is challenging due to the anisotropy and complex plastic behavior of halite at the single crystal level, together with the interplay between crystal-plastic deformation and dynamic recrystallization processes.

Therefore, to explore the crystal preferred orientation (CPO) and microstructural processes of halite under viscoplastic deformation including dynamic recrystallization (DRX), we performed microdynamics numerical simulations of halite polycrystalline aggregates at different temperatures. The models are based on the approach that couples a viscoplastic deformation code (VPFFT) that simulates dislocation glide and the numerical software platform ELLE that explicitly simulates intracrystalline recovery, nucleation, and grain boundary migration. The series of simulations show how subgrain rotation recrystallization (SGR) and grain boundary migration (GBM) processes strongly influence the grain size and grain shape at different temperatures. At lower temperature (100 and 200°C), the initial grain size decreases significantly with increasing strain and an intense network of LAGB or subgrain boundaries is recognisable. At higher temperature (300ºC) the effectivity of the GBM over deformation can be observed in the final microstructure, showing larger and equidimensional grains without localisation bands. However, the development of crystallographic preferred orientation (CPO) seems to be less affected. Crystal preferred orientation and grain boundary maps show that the numerical approach can reproduce the evolution of dry halite microstructures obtained from laboratory torsion deformation experiments (based on the EBSD technique) at 100-300°C up to high shear strains of 3 and provides new insights into the dynamic evolution of polycrystalline halite during dynamic recrystallization.

https://doi.org/10.3301/ABSGI.2022.01

Catania (Italy) 4-10 July 2022

ABSTRACT BOOK

a cura della Società Geologica Italiana

DRT

Catania (Italy)

4th -10th July 2022

GEO-THINKING THE FUTURE PLANET

DRT 2022 – 23rd International Conference on Deformation mechanism, Rheology and Tectonics

Università di Catania 224

Full-field numerical simulation of dynamic recrystallisation in polycrystalline halite

Hao B.*[1], Llorens M.-G.[2], Griera A.[3], Bons P.D.[4] & Gomez-Rivas E.[1]

[1] Departament de Mineralogia, Petrologia i Geologia Aplicada, Universitat de Barcelona, Spain.
[2] Geosciences Barcelona, CSIC, Spain.
[3] Departament de Geologia, Universitat Autònoma de Barcelona, Spain.
[4] Department of Geosciences, Eberhard Karls University of Tübingen, Germany.

Corresponding author e-mail: baoqin.hao@ub.edu

Keywords: grain boundary migration, dynamic recrystallization, halite microstructure, strain localization.

The viscous flow of salt rocks leads to the development of tectonic structures such as detachments and salt diapirs. Moreover, evaporites are key in petroleum systems and are potential storage rocks for products such as hydrogen, natural gas or radioactive waste due to their low permeability and high ductility. Therefore, understanding the mechanical behaviour of evaporites are of key scientific and economic significance. Numerical modelling has become a useful method to study rock deformation processes at multiple scales. However, modelling the microstructural evolution of rock salt grain aggregates is challenging due to the anisotropy and complex plastic behaviour of halite at the single crystal level, together with the interplay between crystal-plastic deformation and dynamic recrystallisation processes.

In this contribution we present, for the first time, results of full-field numerical simulation of dynamic recrystallisation (*DRX*) of halite polycrystalline aggregates during simple shear deformation. The models are based on the approach that couples a viscoplastic deformation code that simulates dislocation glide (VPFFT) and the numerical software platform ELLE (Bons et al., 2008; Gomez-Rivas et al., 2017) that explicitly simulates intracrystalline recovery, nucleation and grain boundary migration. The simulations show that the numerical approach can reproduce the evolution of dry halite microstructures from laboratory torsion deformation experiments at 100-300°C up to high shear strains of 3 and provides new insights into the dynamic evolution of polycrystalline halite during dynamic recrystallisation. Our simulations show how subgrain rotation recrystallization (SGR) and grain boundary migration (GBM) strongly influence the microstructure (grain size and grain shape) at different temperatures and strain rates, while the development of crystallographic preferred orientation (CPO) seems to be affected less. Grain boundary migration enhances the activation of the {100} system, which leads to strain-hardening, but intracrystalline recovery processes reduces this effect. Inferring the finite strain history from the microstructure is challenging, as strain-localisation bands can be masked by high-temperature (or low strain rate) induced GBM.

Acknowledgements: Projects PID2020-118999GB-I00 and RYC2018-026335-I (Spanish Ministry of Science and Innovation (MCIN)/State Research Agency of Spain (AEI)/10.13039/5011 00011033), research group 2017SGR-824 and China Scholarship Council PhD scholarship 202006930010.

Bons P.D., Koehn D. & Jessell M.W. (2008) - Microdynamic simulation. Lecture notes in earth sciences, 106, 1-406. Berlin: Springer. https://doi.org/10.1007/978-3-540-44793-1.

Gomez-Rivas E., Griera A., Llorens M.-G., Bons P.D., Lebensohn R. & Piazolo S. (2017) - Subgrain rotation recrystallization during shearing: insights from full-field numerical simulations of halite polycrystals. Journal of Geophysical Research: Solid Earth, 122(11), 8810-8827.

EGU24-3225, updated on 29 Sep 2024
https://doi.org/10.5194/egusphere-egu24-3225
EGU General Assembly 2024

Full-Field Numerical Simulation of Halite Dynamic Recrystallization From Subgrain Rotation to Grain Boundary Migration

Baoqin Hao[1], Maria-Gema Llorens[2], Albert Griera[3], Paul D. Bons[4], Ricardo A. Lebensohn[5], Yuanchao Yu[2], and Enrique Gomez-Rivas[1]

[1]Departament de Mineralogia, Petrologia i Geologia Aplicada, Universitat de Barcelona, Spain (baoqin.hao@ub.edu)
[2]Geosciences Barcelona, CSIC, Spain
[3]Departament de Geologia, Universitat Autònoma de Barcelona, Spain
[4]Department of Geosciences, Eberhard Karls University of Tübingen, Germany
[5]Materials Science and Technology Division, Los Alamos National Laboratory, Los Alamos, NM, USA

Full-field numerical modelling is a useful method to gain understanding of rock salt deformation at multiple scales, but it is quite challenging due to the anisotropy and complex plastic behavior of halite and other evaporite minerals at the single crystal level, together with dynamic recrystallization processes. We overcome these challenges and present novel results of full-field numerical simulation of dynamic recrystallization of halite polycrystalline aggregates during simple shear deformation, including subgrain rotation and grain boundary migration recrystallization processes. The results illustrate that the approach successfully reproduces the evolution of pure halite microstructures from laboratory torsion deformation experiments at 100-300 up to shear strain of four. Temperature determines the competition between (i) grain size reduction controlled by dislocation glide and subgrain rotation recrystallization (at low temperature) and (ii) grain growth associated with grain boundary migration (at higher temperature), while the resulting crystallographic preferred orientations are similar for all cases. The analysis of the misorientation reveals that the relationship between subgrain misorientation and strain follows a power law relationship with a general exponent of 2/3. However, with progressive deformation, dynamic recrystallization leads to a gradual deviation from this relationship. Therefore, predicting strain or temperature from microstructures necessitates careful calibration.

9th-11th JULY 2024

DRT-2024 PROGRAMME AND ABSTRACT BOOK

24th International Conference on Deformation mechanisms, Rheology and Tectonics (DRT-2024)

This booklet contains the scientific programme and the abstract book of the DRT-2024 conference. We thank the members of the scientific and organising committees, the keynote speakers, session chairs, and all the participants for their contributions.
We hope you enjoy the conference and cultural delights of Barcelona.

Welcome!

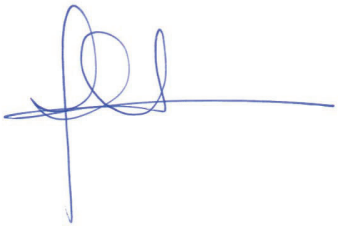

María Gema Llorens (on behalf of the organising committee)

More information at: https://drt-society.org/conferences/barcelona-2024/

Dynamic recrystallization during visco-plastic deformation of halite polycrystals: full-field simulation of simple shear versus pure shear

Hao B. *[1], Llorens M.-G.[2], Griera A.[3], Bons P. D.[4], Lebensohn R. A.[5], Yu Y.[2] & Gomez-Rivas E.[1]

[1] Departament de Mineralogia, Petrologia i Geologia Aplicada, Universitat de Barcelona, Spain
[2] Geosciences Barcelona, CSIC, Spain
[3] Departament de Geologia, Universitat Autònoma de Barcelona, Spain
[4] Department of Geosciences, Eberhard Karls University of Tübingen, Germany
[5] Materials Science and Technology Division, Los Alamos National Laboratory, Los Alamos, NM, USA

* *Corresponding email:* baoqin.hao@ub.edu

Using the full-field ELLE/VPFFT approach, we model the evolution of the microstructure and crystallographic preferred orientation (CPO) of polycrystalline anisotropic halite subjected to simple shear and pure shear, reaching a natural strain of 1.5. The simulations successfully replicate the experiments conducted at temperatures ranging from 100°C to 300°C and elucidate the temperature-dependent transition from subgrain rotation to grain boundary migration.